THE DYNAMICS OF A LONG FLEXIBLE HORIZONTAL CIRCULAR CYLINDER IN WATER WAVES

Chris-Heinz Retzler

A thesis submitted for the
degree of Doctor of Philosophy

UNIVERSITY OF EDINBURGH

1988

Abstract

This thesis examines the dynamics of a long flexible horizontal circular cylinder when immersed in water and exposed to waves. The cylinder exhibits a flexural resonance, dependent on its stiffness, which is stimulated by particular combinations of wave frequency and angle. Linearity is assumed and analysis performed in the frequency domain.

Experimental work is based on a 16 metre long 125 millimetre diameter model consisting of 40 segments with motorised joints of controllable stiffness. The bending moment and relative angular velocity are measured at each joint. The model is tested in a three-dimensional wave tank in which multiple wavefronts of specified amplitude, frequency, angle and phase can be generated. The model response to single wavefronts is displayed as an array of plots of bending moment against distance along the cylinder axis. The shape and size of the plots vary strongly with wave frequency and angle, and cylinder stiffness.

Two theoretical descriptions are explored. One treats the model as a finite continuous beam, combining beam stiffness with hydrodynamic forces in an equation which is solved analytically. The other is a more exact nodal analysis treating each segment as a rigid body, specifying the forces and moments on it, and solving by a matrix operation for all segments.

Both approaches require knowledge of the body hydrodynamics as a function of frequency. This is obtained in a set of experiments using short cylinders in a two-dimensional wave tank. Each experiment measures the wave field, the force on the cylinder and its velocity when the cylinder is driven in the water and acted on by waves. A matrix calculation is performed on the data to extract the wave force coefficient and the radiation impedance in a single operation which eliminates the masking effect of wave reflections in the tank.

When these hydrodynamic data are used with the nodal beam theory to predict bending moments in single wavefronts there is good agreement with experiment. The model is then tested in multiple-wavefront sea-states representative of the North Atlantic. The results are compared with calculations for each sea-state made by superposing the theoretical responses of the cylinder to the component wavefronts. The agreement is good enough to allow the use of nodal beam theory as a predictive tool.

Declaration

The work contained in this thesis is my own except where otherwise indicated.

Chris-Heinz Retzler
Edinburgh Wavepower Project
Department of Mechanical Engineering
University of Edinburgh
1988

Acknowledgements

My thanks are due to Stephen Salter, my supervisor and the founder of the Edinburgh Wavepower Project, on the resources of which this thesis has been based. David Jeffrey and Glenn Keller were the designers of the electronic hardware for the spine model and the sampling system; and Douglas Rogers and Matthew Rea provided much-appreciated technical support for the maintenance of apparatus. Jamie Taylor and Carn Gibson took the photographs that illustrate the text.

I would like to express my warm thanks to John Martin for his help and guidance with the mathematical content of this thesis. I am very grateful to my colleagues David Skyner and Peter Woodhead for their support and interest and practical advice as this work progressed.

Finally I want to acknowledge the dozens of people who have contributed models, instrumentation, computer software and research to the Project over the years, and made it into such a unique experimental facility.

Contents

SYNOPSIS

This thesis develops an analysis of the dynamics of a long flexible cylinder in ocean waves and compares the results with experiment. One application is for the spine of a wavepower station; others include marine pipelines and cables.

Chapter 1

Introduction

SUMMARY

Ocean waves and the extraction of energy from them is discussed.
The Edinburgh Duck wavepower device and the spine on which rows of Ducks are mounted are described.
The present work is set in the context of theoretical and experimental work on cylinders in water waves.

1.1 Background

Solar energy drives the world's weather. The sun heats the globe differentially; huge volumes of warm air rise from the tropics, spread and eventually descend many thousands of kilometres north and south of the equator. This tropical air brings not only warmth and water vapour but also momentum due to the higher tangential velocity of the Earth's spin at the equator. Satellite photographs of the world graphically demonstrate this vast transport of heat, vapour and momentum in the vortices of cloud that wreath the temperate portions of the globe. The world's rainfall and winds are concentrated in two bands between 40 and 60 degrees latitude in both the northern and southern hemispheres.

The wind dissipates itself by friction: over the ocean this frictional shear on the water surface results in the transfer of momentum to the water to form waves. Though the water itself does not travel, the waves do, carrying energy with great efficiency across thousands of kilometres of ocean. It has been esti-

mated (Curran, 1979) that of the 173 PW of solar power that strike the Earth (as a yearly average) 370 TW are converted to wind power, and 2 TW end up as wave power incident on the world's coasts.

Power produced by storms over oceans radiates out as waves to the shores, but not isotropically: more power is directed along the lines of the prevailing winds. For that reason the Atlantic seaboard of Norway, Britain and Ireland has one of the most powerful wave climates in the world. Estimates vary, but a mean figure of 70kW per metre of wave-front (Mollison, 1985) is typical 100km from the Scottish coast. Estimates for the total resource available along the 1500km seaboard of the British Isles range from 60–120 GW average per year. The fact that wave power, replenished over the whole surface of the oceans, is harvestable at its edges makes it an attractive renewable power resource. The ocean acts as an integrator of wind power in space and time, producing waves that are more constant than wind. And unlike direct solar power, it is available at night and more abundant in winter. Furthermore this is mechanical power - the first conversion from heat has been performed naturally. And unlike wind, where the translation of the medium sets an upper extraction limit (the Betz limit) of 16/27, waves merely oscillate, and 100% extraction is theoretically possible.

There has been sporadic interest over the past 150 years in the utilisation of this energy: the most recent research effort has been concentrated in Britain, Japan, Norway and Ireland from 1974 to the present. The British program was the most ambitious, setting the target of the design of a 2 GW wave power station, and spawning over a dozen projects. However, to date, the only commercial construction undertaken has been by Norwegian companies at around the 1 MW scale.

Much use was made of data collected in the two previous decades by the Institute of Oceanographic Sciences (Crabb, 1980). These indicated that there was a dominant direction for wave energy flux, a dominant frequency, and patterns of spread of these parameters which could be correlated with weather patterns.

Like most renewable resources the power varies with time in both the short and long term around these averages. Power above the limit of the notional wave energy converter must be allowed to pass, and conversely, waves which are too

weak will not overcome the starting losses of the device. These upper and lower limits depend on the device, but estimates suggest an overall effieciency of about 30%. (Davies et al, 1985)

Notable among the British devices were the Lanchester Clam, the Bristol Cylinder, the Belfast and National Engineering Laboratory versions of the Oscillating Water Column and the Edinburgh Duck. Sections of the devices are illustrated schematically in figure 1.1.

The four types shown have been chosen to represent the diversity of the technological responses to the environmental challenges. To date only models, up to 1/10 scale, of any device have been built.

The OWCs were shore-based, the rest deployed offshore. The OWCs coupled an oscillatory column of water, via an air space to an air turbine. The Clam and the Bag also had air turbines, but coupled these to air-filled rubber bags which respired under the pressure of waves. This arrangement isolated the turbines from contact with sea water and debris. The Cylinder and the Duck coupled the moving mass of their structures to hydraulic pumps.

There were three types of reaction frame. The OWCs were anchored to rock. The Cylinder was anchored to the sea bed via hydraulic pumps. The Duck contained a set of gyroscopes which in addition to providing inertial reference could also store about 3/4 hour of the Duck's full power output. All the rest used phase differences in the wave as it passed along the device to drive the power take-off. The Clam and Bag both used spines: long rigid structures comparable to the wavelength of the waves, moored into the waves in the case of the Bag, and at 35 degrees to it in the case of the Clam. The spine experienced a sum of wave phases and so underwent an average motion much less than the local wave motion at any point. This provided an inertial reference that the much smaller air bag, responding to the local wave motion, could react against. A further advantage of the crest averaging spine was that its mooring loads were reduced in proportion to the reduction of motion.

The penalty paid for these advantages is the bending moments incurred in the spine. The material and the construction must be able to resist the maximum stresses and the fatigue over the design life. The Clam and Bag devices used spines which had no joints and were not designed to yield any more than their material allowed. For this reason their lengths were kept shorter than

Figure 1.1
Sections of four wavepower devices.

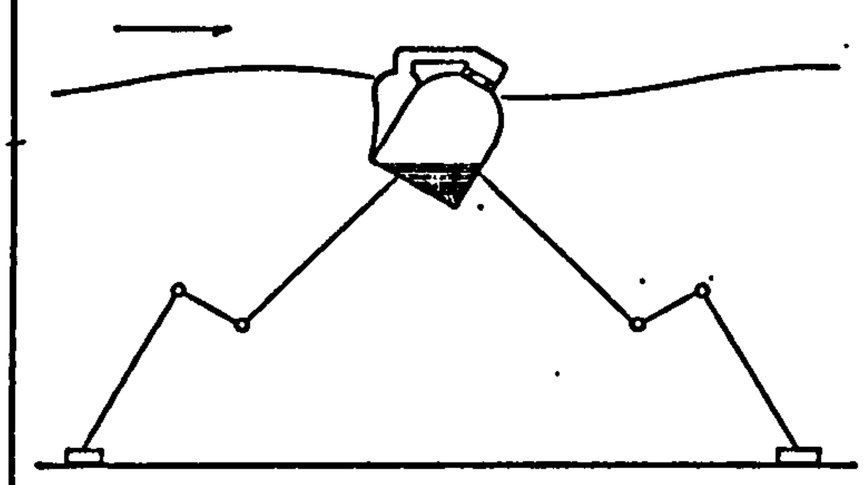

CLAM
Low freeboard respiring air bag
Sealed pneumatic power train
Bags react against a short rigid spine
Low-rate mooring, 100m depth

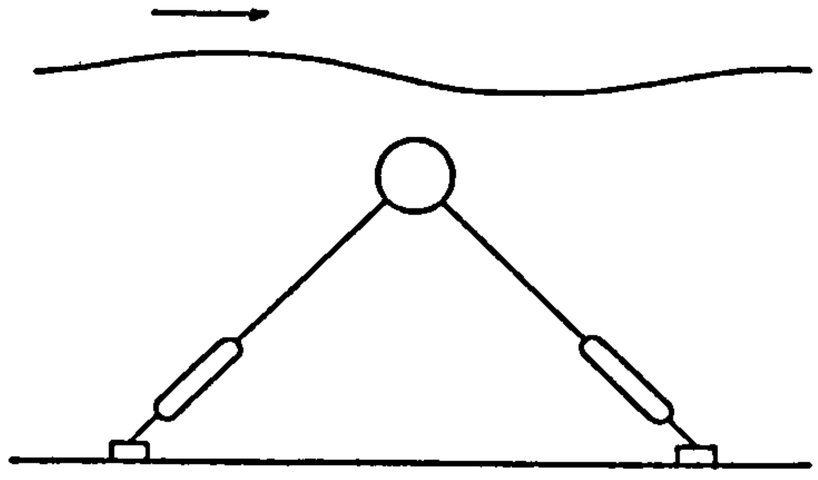

CYLINDER
Submerged tethered buoyant cylinder
Hydraulic power take-off in mooring
Tuned and damped mooring, 42m depth
point or array absorber

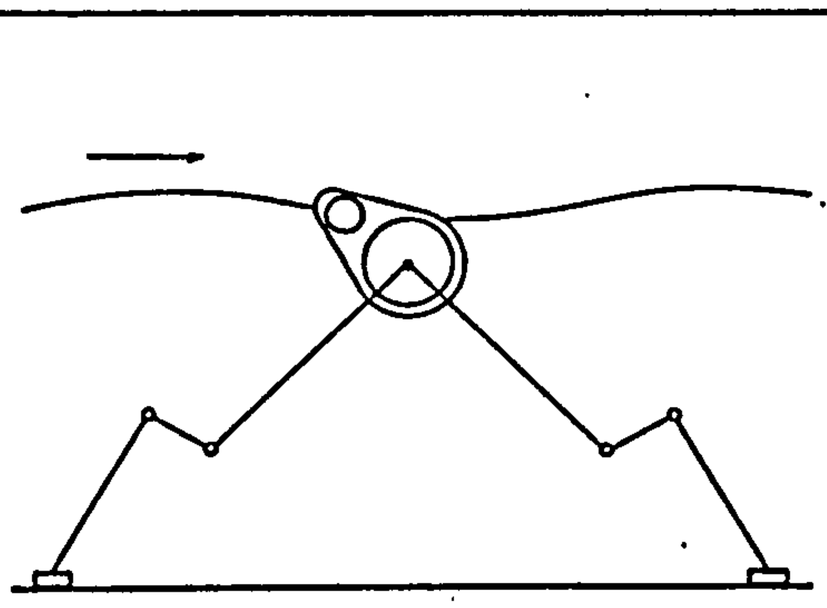

DUCK
Low freeboard pitching cam
Hydraulic power train
Gyroscopic reaction frame/energy storage
Long flexible spine
Low-rate mooring, 100m depth

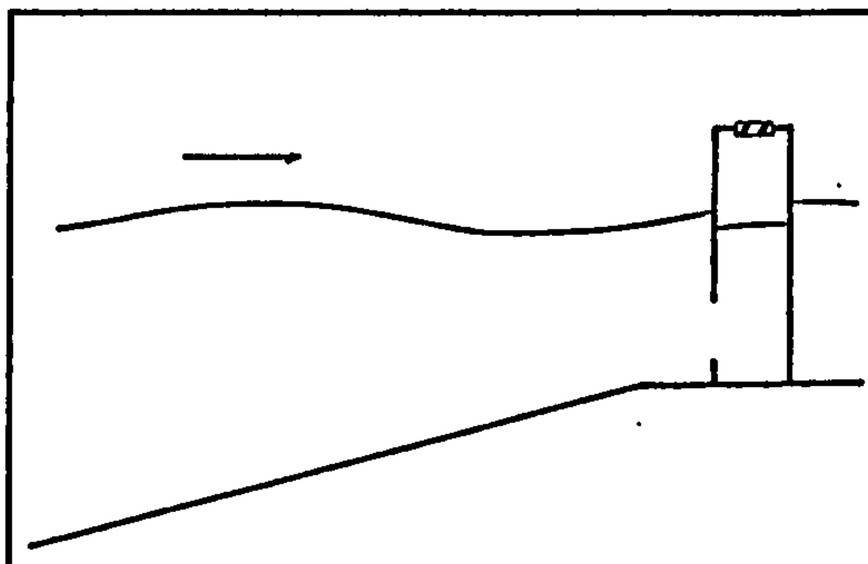

OWC
High-freeboard oscillating water column
Open pneumatic power train
Fixed to sea bed, 25m depth
Point or array absorber

one average wavelength.

The Edinburgh Duck also used a spine, but of a different structure and for different reasons. The gyroscopes in each Duck provided an internal reaction frame for *pitch*; but early experiments by Salter and Jeffrey (1978) showed that Duck productivity could be increased by appropriate *heave* and *surge* motion of the duck mounting. Salter (1985) suggests that this motion can be provided by a controllable spine. Each Duck was 40m long, and was designed to produce 2.4 MW. In order to meet the DEn 2 GW design brief, 896 were needed, with a total length of 40km. Connecting the Ducks in lines greatly reduced the mooring loads, and offered many other economies of scale, such as power conditioning and distribution. Strings of up to 100 units were envisaged with spine lengths of 4 km. There are no precedents for a marine structure like the spine which combines enormous mass with spectacular length. Supertankers have displacements up to 500 ktonnes and lengths of 500m; they therefore span many wavecrests and have a high section moment to resist the resultant bending moments. And all ships are designed to be stable, to minimize motion. Oil platforms have high mass, but deliberately place the bulk of their structure well above and below the water surface. They are designed to be transparent to waves. Wavepower devices are designed to have high interaction with waves: to be opaque to them, and to maximize motion. Calculations of the possible bending moments were high, so the spine was designed in segments which could yield to wave forces non-destructively. There is a trade-off between bending moment and motion: the spine must neither break, not bend so much it causes adjacent Ducks to collide. The Duck units absorb power, and in small and medium seas will reduce the wave forces on the spine. But above the Duck power limit, the spine is effectively on its own, and must therefore be capable of withstanding the worst possible ocean conditions.

The goal of the work described in this thesis was to develop a mathematical description of the spine which would enable engineers to calculate the maximum stresses and fatigue loading on it given the spine parameters and the necessary wave data. The experimental studies were carried out at the University of Edinburgh Wavepower Project which has a 5.8m long 2-dimensional wave tank, and a 25m wide 3-dimensional wave basin. It also has a 1/100th scale articulated spine model which is both instrumented and controllable, allowing testing over

a range of lengths and stiffnesses in a wide variety of wave conditions. This enabled the theoretical models as they were developed to be checked against experiment, with the goal of eventually replacing experiment by computation.

A description of the experimental environment is given in Chapter 2, and the force rigs and models are described in the appropriate experimental chapters. The rest of this introduction is devoted to a discussion of fluid behaviour, ocean waves, forces on objects in waves, and previous related work.

1.2 Fluid Behaviour

The Navier-Stokes equation may be written in vector form as follows:

$$\frac{\partial q}{\partial t} + q.\nabla q = \frac{1}{\rho}\nabla(p + \rho g h) + \nu \nabla^2 q \tag{1.1}$$

where q is the three-dimensional velocity vector, p is the pressure, ρ is the density of the fluid, gh is the potential due to gravity and ν is the fluid viscosity. It expresses the substantive acceleration of the fluid at a given point in terms of the forces per unit mass due to pressure, gravity and viscosity. It is a differential equation in time and space and requires initial and boundary conditions for its solution. The conditions relate to the practical situation and may be static or kinematic - the geometry of the fluid container, or the motion of an immersed object, or the deformation of a free surface of the fluid.

The Navier-Stokes equation can in general be solved numerically, but it is convenient to make simplifying assumptions both on it and the boundary conditions in order that analytic solutions may be found. These assumptions must be reasonably related to practical conditions in the fluid. This thesis concerns the behaviour of objects in water interacting with waves on a free surface.

A fluid offers no permanent resistance to shear. Consequently a practical fluid in motion will eventually exhibit some degree of chaotic behaviour. The greater the fluid velocities, the more likely this is. The Reynolds number

$$R_e = \frac{UL}{\nu} \tag{1.2}$$

where L is a characteristic length over which the velocity changes in magnitude by U, is a measure of the ratio of inertial to viscous forces. In nature and the laboratory Reynolds number can span many orders of magnitude. Above $Re = 100$ viscous forces should be insignificant in the body of fluid. However in a boundary layer adjacent to a fixed surface the velocity gradients are steep and viscous forces high. And above about $Re = 100$ the boundary layer separates from the surface and its local shear is convected into the bulk of the fluid as a vortex. When this happens repeatedly, the trail of vortices forms a wake. The qualities of this wake and of its interaction with the remaining boundary layer change with Reynolds number, and its influence on forces in the fluid

are very great. However the wake takes a finite time to appear after a flow starts. For reciprocating motion of the fluid relative to a body, or vice-versa, the wake may not have time to form before the flow reverses. Consequently a second dimensionless number is of use in determining the type of flow. The Keulegan-Carpenter number is defined (Keulegan, Carpenter, 1958)

$$K = \frac{UT}{D} = \frac{2\pi a}{D} \tag{1.3}$$

where T is the period of the motion, U is the velocity amplitude, D the body dimension and a the amplitude of motion.

For flow around a cylinder in water, Chaplin (1984) observes that there is no vortex generation until $K > 2$. At low values of K it is reasonable to make the simplification that the fluid flow is vortex-free or *irrotational*, ie the curl of the velocity vector is zero

$$\nabla \times q = 0 \tag{1.4}$$

This condition allows the definition of a *velocity potential* ϕ such that

$$q = \nabla\phi \tag{1.5}$$

A second simplification is that liquids are essentially incompressible so the dilatation can be set to zero. ie:

$$\nabla . q = 0 \tag{1.6}$$

substitution of equation 1.5 into equation 1.6 yields the Laplace equation

$$\nabla^2\phi = 0 \tag{1.7}$$

Substitution of the velocity potential from equation 1.5 into the Navier-Stokes equation, neglecting the viscosity terms because of the irrotationality condition, yields the Bernoulli equation

$$\frac{1}{2}q^2 + \frac{\partial\phi}{\partial t} + \frac{p}{\rho} + gh = 0 \tag{1.8}$$

which relates the fluid velocity to the fluid pressure.

1.3 Water waves

The solution of the Laplace equation depends upon boundary conditions. Of interest in the current work is the case where water is bounded by a surface and a rigid bottom, where small sinusoidal waves are travelling on the surface. Such a solution may be found, for example, in Newman (1977).

For horizontal coordinate x and vertical coordinate z, the linearised free surface boundary condition is

$$\frac{\partial^2 \phi}{\partial t^2} + g\frac{\partial \phi}{\partial z} = 0, \qquad z = 0, \tag{1.9}$$

and the rigid-bottom boundary condition is

$$\frac{\partial \phi}{\partial z} = 0, \qquad z = -h \tag{1.10}$$

The solution is

$$\phi = \frac{gA}{\omega}\frac{\cosh k(z+h)}{\cosh kh}\sin(kx - \omega t) \tag{1.11}$$

where A is the wave amplitude, and ω is its angular frequency given by

$$\omega^2 = gk \tanh kh \tag{1.12}$$

where $k = 2\pi/\lambda$ for a wave of length λ. The phase velocity is given by

$$V_p = \omega/k = [\frac{g}{k}\tanh kh]^{1/2} \tag{1.13}$$

In shallow water when $kh \ll 1, \tanh kh \rightarrow kh$ and

$$\omega^2 = gk^2h \tag{1.14}$$

so

$$\lambda = \frac{2\pi g}{\omega^2} \tag{1.15}$$

and

$$V_p = (gh)^{1/2} \tag{1.16}$$

V_p is therefore a constant for all frequencies. However, in deep water, $kh \gg 1$ and $\tanh kh \rightarrow 1$

$$\omega^2 = gk \tag{1.17}$$

so

$$\lambda = \frac{2\pi g}{\omega^2} \tag{1.18}$$

This result has the important consequence that for models, time scales as the square root of length scale. Also

$$V_p = g/\omega \tag{1.19}$$

So in deep water a wave travels at a velocity inversely proportional to frequency; ie, the waves are *dispersive* with frequency. The difference in V_p between deep and shallow water causes waves to refract towards the fall-line of the sea floor as they enter shallower water.

The water particles have velocities in the horizontal and vertical directions given by

$$u = \frac{\partial \phi}{\partial x} = \frac{gkA}{\omega} \frac{\cosh k(z+h)}{\cosh kh} \cos(kx - \omega t) \tag{1.20}$$

$$v = \frac{\partial \phi}{\partial z} = \frac{gkA}{\omega} \frac{\sinh k(z+h)}{\cosh kh} \sin(kx - \omega t) \tag{1.21}$$

When $kh \gg 1$ and $\tanh kh \rightarrow 1$, these expressions contract to

$$u = \frac{gkA}{\omega} e^{kz} \cos(kx - \omega t) \tag{1.22}$$

$$v = \frac{gkA}{\omega} e^{kz} \sin(kx - \omega t) \tag{1.23}$$

The horizontal and vertical water particle velocities differ by $\pi/2$ in phase, so that in water of infinite depth and for small waves the particles move in approximately circular paths with radii which decrease exponentially with depth. In water of finite depth the particles move in ellipses, which get flatter as the water gets shallower.

1.4 Ocean waves

Textbook description and laboratory observation of waves do not prepare one for the structural richness of the ocean surface. A review of ocean wave statistics and the relevance to wave energy conversion is given by Mollison (1985). Excerpts from his paper are presented in this and the next section; his convention of using wave period in addition to wave frequency is retained, where $T = 1/f$.

Most ocean wave energy is carried by waves with lengths between 50m and 300m, and the ocean is deep by comparison, so by analogy with equations 1.19 and 1.18

$$V_p = gT/2\pi \tag{1.24}$$

and

$$\lambda = gT^2/2\pi \tag{1.25}$$

An effect apparent when observing a small group of waves is that they travel at a *group velocity* which is half the phase velocity. Individual waves seem to arise behind the group, grow as they pass through it, then disappear into the calm water ahead.

The total energy per plan area of wave is

$$E = \frac{1}{2}\rho g A^2 = \rho g H^2 \tag{1.26}$$

where H is the root-mean-square wave amplitude. The water particle energy varies cyclically between kinetic and potential. Over the course of a complete wave cycle $KE = PE = E/2$. The energy in a wave travels at the group velocity. Thus energy flux (power) through a unit line is given by

$$P = EV_p/2 = \frac{\rho g^2}{4\pi} H^2 T \tag{1.27}$$

For a sea state, the individual sinusoidal components sum to a Gaussian random process. It is convenient to define a spectral distribution $S(f, \theta)$ whose overall integral is unity. This enables the definition of an *energy period* T_e which is the average value of T with respect to the distribution.

$$T_e = \iint TS(f, \theta)\, df\, d\theta \tag{1.28}$$

then

$$P = \int\int \frac{1}{2} E V_p S(f,\theta) df d\theta = \frac{\rho g^2}{4\pi} H_{rms}^2 T_e \tag{1.29}$$

where H_{rms} is the root-mean-square wave height. T_e is then the same as the period of a sinewave having the same power and H_{rms} as the distribution. It is useful also to define the mean wavelength λ_e, and the ratio H_{rms}/λ_e is then a measure of the steepness of the sea state.

The energy of a sea state increases with the *fetch*, the distance x over which the wind has been blowing. The wave height increases such that

$$H_{rms}^2 \approx 1.6 \times 10^{-7} U_{10}^2 x/g \tag{1.30}$$

where U_{10} denotes the windspeed measured at 10 metres above the sea surface.

Pierson and Moskowitz define a wave spectrum for a fully developed sea. This is one for which a steady wind has been blowing for sufficient time, and over sufficient distance or *fetch* for its spectrum to be invariant.

$$\int_0^f S(z)\, dz = H_{rms}^2 exp[-0.675(fT_e)^{-4}] \tag{1.31}$$

Its spectral width $\sigma_T = 0.28$ and its steepness $H_{rms}/\lambda_e = 1/115$ are independent of the windspeed. But windspeed—measured at 19.5 metres above the sea surface—does correlate with the following. $T_e = 0.625 U_{19.5}$, $H_{rms} = 0.0053 U_{19.5}^2$ and $V_{pe} = 0.975 U_{19.5}$. Hence $H_{rms} = 0.0136 T_e^2$. The fetch required to develop the sea is about $3000\lambda_e$.

The steady-state arises from a dynamic balance between the input of energy from the wind, due to air pressure and shear stress on the water surface, and the loss of energy as the higher-frequency waves in the sea break. They do this for steepnesses between 1/7 and 1/4 depending on the degree of focussing of the wave. Waves start small in both amplitude and wavelength, but non-linear wave interactions generate higher and lower frequencies. The lower frequencies endure, but waves of increasing frequency eventually break, and disappear. The steady state arrives when their dissipation loss equals the energy input by the wind. The process favours the production of waves with a phase velocity comparable to the wind velocity.

In practice, few seas are fully developed, and when bivariate histograms are drawn of the periods and heights of waves, there is substantial scatter around the square law line $H_{rms} = 0.0136 T_e^2$.

1.5 Angular distributions

Most early wave recordings were made by instruments which recorded only wave height with time, thus allowing only wave amplitude and frequency to be determined. More recently, buoys which record three or more degrees of freedom have enabled directional data to be acquired.

The range of wave angle is approximately equal to the angle subtended by a distant storm front at the wave-buoy. The distribution can be fitted to a function of the type

$$S(\theta) = C(s)\cos^s(\theta - \theta_0) \tag{1.32}$$

where s is an arbitrary spreading parameter, for waves due to distant storms. For more locally-generated sea-states an equation of the form

$$S(\theta) = C(s)\cos^{2s}((\theta - \theta_0/2) \tag{1.33}$$

allows the function to be positive for $-\pi <= \theta - \theta_0 <= \pi$

Mitsuyasu (1975) from measurements taken with a cloverleaf buoy measuring heave, roll and pitch, fitted the following function to the data

$$S(T,\theta) = S(T)C_m cos^m((\theta - \theta_0)/2) \tag{1.34}$$

where the spreading coefficient depends on period

$$m = 15.85\frac{T}{T_0}^{-5} \qquad T >= T_0 \tag{1.35}$$

$$m = 15.85\frac{T}{T_0}^{2.5} \qquad T < T_0 \tag{1.36}$$

and C_m is a normalizing coefficient

$$C_m = 1/\int_{-\pi}^{+\pi} cos^m((\theta - \theta_0)/2)\, d\theta \qquad -\pi <= theta - \theta_0 <= \pi \tag{1.37}$$

1.6 Body forces

The force on a cylinder immersed in an unbounded two-dimensional flow which is inviscid, unseparated and without circulation can be represented in the form (see Sarpkaya and Isaacson, 1981)

$$F = C_m \rho V \dot{U} \tag{1.38}$$

where F is the force per unit length on a cylinder of volume per unit length V. The force required to accelerate the cylinder in fluid otherwise at rest is of the same magnitude but opposite sign. The coefficient $C_m = 2$ for a circular cylinder; the disturbance caused by the presence of the cylinder in the flow is equivalent to adding a mass of fluid equal to that displaced by the cylinder.

If the fluid is bounded by a surface, the motion of the cylinder will produce waves on the surface. These carry energy away from the cylinder, damping its motion. A force appears in phase with the velocity, in quadrature with the acceleration, and C_m becomes complex and frequency dependent. This also applies to a cylinder absorbing energy by moving in waves.

For waves of length comparable to the cylinder diameter, the flow will no longer be uniform across the cylinder. There will be a phase difference, and thus a partial cancellation of the force on the cylinder. The reduction increases with the ratio D/λ. $\left(\frac{\text{diameter}}{\text{wavelength}}\right)$

It is convenient to decompose the ideal flow around an immersed object in the following form

$$\phi = \phi_i + \phi_s + \sum_{j=1}^{n} \phi_j \tag{1.39}$$

where ϕ_i represents the incident potential on the object, ϕ_s the scattered potential, and ϕ_j the potential due to the motion of the object in the j th degree of freedom. ϕ must satisfy:

1. the Laplace equation in the field;

2. a linearised boundary condition on the surface;

3. a radiation condition in the far field;

4. the normal velocity at the container bottom must be zero;

5. the normal component of fluid velocity relative to the body on the body surface is zero.

The first four conditions have been expressed in section 1.3 for the finite-depth water-wave solution. The last condition is given by

$$\frac{\partial \phi}{\partial n} = U_n \tag{1.40}$$

where U_n is the body velocity in the direction of the normal vector n. Having solved for ϕ, the pressure around the body can be obtained from the linearised form of the Bernoulli equation

$$p = \rho \frac{\partial \phi}{\partial t} \tag{1.41}$$

then the force is given by the integrated pressure over the surface of the body.

$$f = -\int_S p.n \, dS \tag{1.42}$$

Diffraction problems of this kind have been solved analytically by Ogilvie (1963) and Mehlum (1980) for fixed cylinders in waves; and by Ursell (1949) for a heaving cylinder at the water surface. In general the scattering problem for a moving body has to be solved by semi-numerical techniques, for example by boundary elements with a Green's function. This is the approach taken by Standing (1978) and Greenhow (1982) for the Duck wavepower device at the water surface; and for long cylinders in 3 dimensional waves by Battjes (1982), Garrison (1984) and Isaacson (1986).

There are also purely empirical equations. In an attempt to rationalise the data for forces on vertical piles in a variety of flows, Morison et al (1950) proposed that the total force on the pile be considered as the sum of inertial and drag forces.

$$\frac{F}{L} = C_m \rho \frac{1}{4} \pi D^2 \dot{U} + \frac{1}{2} C_d D U |U| \tag{1.43}$$

Sarpkaya (1963) derived a theoretical expression for the force on a cylinder accelerating uniformly from rest. It had an identical form to Morison's equation. Garrison (1980) provides a review of Morison's equation from experiments with cylinders in U-tubes, concluding that its form is correct but that C_m and C_d are not constant but functions of Keulegan-Carpenter number, Reynolds number,

relative roughness and phase angle of the flow. While this does complicate laboratory work, marine designers are aided by the fact that C_m and C_d vary little with Re in the region of postcritical flow.

The ratio of drag to inertia force is derived from equation 1.43 using the relationships $U = \omega A$ and $\dot{U} = \omega^2 A$ where A is the wave amplitude.

$$\frac{F_d}{F_m} = \frac{\frac{1}{2} C_d \rho D \omega^2 A^2}{C_m \rho \frac{1}{4} \pi D^2 \omega^2 A} = \frac{2 C_d A}{\pi D} = \frac{1}{\pi^2} \frac{C_d}{C_m} K \tag{1.44}$$

where K is the Keulegan-Carpenter number. Typical values for Cm and Cd are 2 and 1, so the drag force is negligible—less than 5%—if $K < 1$.

The full-scale Reynolds number is of the order of 10^7, whereas for 100th scale laboratory work it is of the order of 10^4. The drag regimes will therefore not be comparable. However, in the current work, the highest value of K is 1, so that this difference is irrelevant. This work covers a range of D/λ of 0.008 to 0.32, and wave diffraction is important. These values of K and D/λ should be compared with figure 1.2, after Isaacson (1979), with the conclusion that it should be possible to describe the forces on the spine as linear inertial forces modified by diffraction. In consequence it was decided that the most appropriate way to proceed was to determine the hydrodynamic characteristics of the spine by experiment. A discussion of non-linear effects is deferred to Chapter 7.

Figure 1.2

Wave force regimes (Isaacson, 1979)

Keulegan-Carpenter number K against diameter/wavelength.

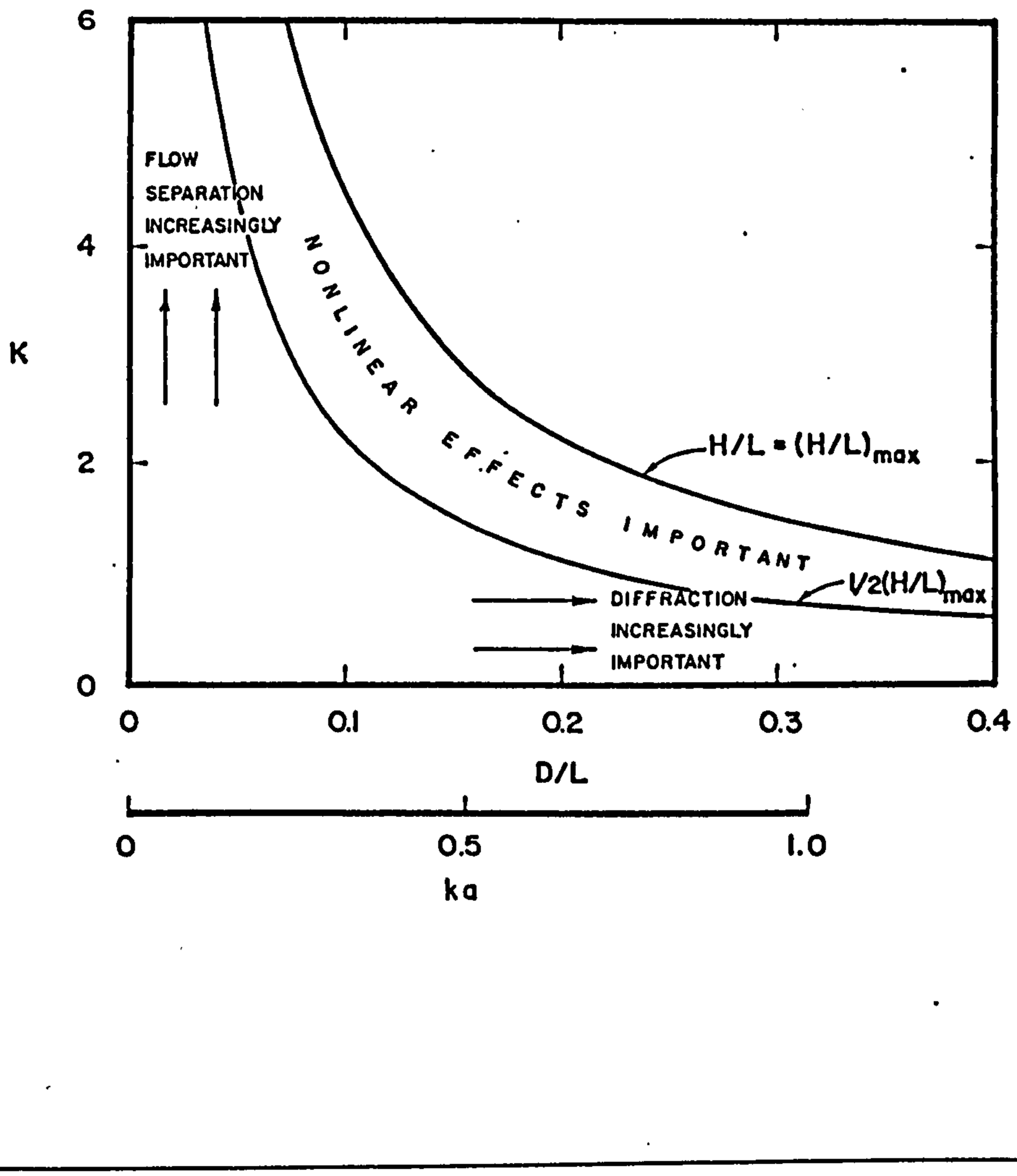

1.7 The present work in context

This present work is concerned with the theoretical and experimental modelling of a long flexible horizontal circular cylinder in ocean conditions, moored with its top just piercing the ocean surface.

As observed by Sarpkaya and Isaacson (1979) most of the experimental studies on cylinders in waves have been on vertical ones, either piles or risers. The little work that has been done on horizontal cylinders relates to bracing elements and pipelines. These are of relatively small diameter and hence the studies have been at high Keulegan-Carpenter number.

This present research builds upon and extends a body of earlier work on the spine and duck. Standing (1978) modelled the duck using potential flow theory and a source potential method. He obtained good agreement with the experimental results of Jeffrey (1978) for the efficiency of the duck in monochromatic two-dimensional waves. When Standing extended this work to include the spine (1980) in a crossed regular wave he predicted bending moments which peaked in the centre of the spine, and grew rapidly as the length of the spine was increased. Taylor (1984) assembled a large body of experimental data using the Edinburgh Wavepower Project articulated spine model. He found that bending moments increased only up to a limit, which was not exceeded however much longer the spine was made. The bending moments did peak in the middle—but only for short spines. For longer spines a central plateau of bending moment formed, somewhat lower than the peaks close to both ends. Bryden (1983) derived the beam equation, solving it analytically for the boundary condition of it being single-ended (ie semi-infinite), and numerically for the double-ended condition. For the most part, his data agreed well with Taylor's experiments on the spine at a variety of stiffnesses in a variety of Pierson-Moskowitz spectra. He also confirmed the experimental result that spine bending moments are a maximum about one crestlength in from the ends. For a spine of length equal to two crestlengths, these two maxima coincide giving the highest bending moment for all possible lengths. For the North Atlantic conditions this worst length is about 400-600 metres at full scale, increasing slightly with stiffness. Guilloud and Vignat (1979) computed the response of a pipeline using the beam equation combined with Morison's equation (including the drag term because of the high

Keulegan-Carpenter number) and solved numerically.

The purpose of this thesis is to develop a mathematical analysis which is sufficiently good to predict the performance of the spine when it is used to support a string of ducks in mixed seas, and more generally, the motion of long flexible cylinders representing pipelines, cables, etc.

In addition to the two different analyses of the cylinder developed in chapters 5 and 6, the thesis contains supporting experimentation on an articulated cylinder model of controllable stiffness in a 3D wave tank in both regular waves and mixed seas, and on short cylinders in a 2D wave tank. The experimental facilities of the Edinburgh Wavepower Project are described in chapter 2, and the author's personal contributions to this thesis begin thereafter.

In chapter 3 the hydrodynamic coefficients of cylinders are measured in the 2D wave tank over a large range of D/λ ratio, using a matrix technique which removes the effects of wave reflection in the tank. These coefficients are combined with the equations for a continuous, finite beam and solved analytically. The spine model is tested over the whole range of wave frequency and angle that the 3D tank can usefully produce, and the results compared with calculations from the continuous beam model. A further nodal analysis is made of the spine which takes its segmentation into account. This latter analysis is used to predict the spine response in a set of 46 widely ranging sea spectra representative of annual conditions in the North Atlantic. The nodal model satisfactorily predicts the variation of bending moment response down the length of the spine in both regular waves and mixed seas.

A linear treatment is adopted for the entirety of this work. It has the following advantages.

1. It is mathematically and computationally simpler.

2. Frequency-domain methods (eg Fourier analysis) can be used.

3. The superposition principle applies. The effect of waves of different frequency (and in three dimensions, different angle) can simply be added.

Chapter 7 lists its disadvantages, and gives an experimental critique, before a test of the superposition principle is carried out in Chapter 8, where the experimental spine response in mixed seas is compared with theory.

Chapter 2

The experimental environment

SUMMARY
The host computer, the sampling and control system, the 2D and 3D wave tanks and the wavegauges are described.
They are used in an experiment to determine various characteristics of the 2D wave tank, including wave reflection and attenuation.

2.1 Preamble

A large variety of experimental equipment was used: two wave tanks; wavegauge arrays; an instrumented and controllable long cylinder model; short cylinder models mounted in a force rig; sampling and control multiplex systems; and a variety of computers. All the equipment was extant: the author had no need to construct apparatus.

The scale of the wave tanks and models is nominally 1:100. Note that because of the dispersion relation, equation 1.12 time scales as the *square root* of the linear scale; a 0.1Hz ocean wave scales to a 1Hz tank wave. The short cylinder models and their force rig are described in Chapter 3, as are the wave gauges and the processing of wave data. The long active cylinder model is described in Chapter 4. This format places the model descriptions alongside the experimental descriptions and results. The rest of the experimental environment is described here.

Figure 2.1 is a schematic diagram showing the components of the experimental environment. The system is designed so that lengthy and complex experiments can be automated.

The experiment control computer is a DEC PDP-11/60, a 0.5MIP machine. It is programmed in IMP, an Edinburgh University systems programming language with similarities to C, in that it allows high-level structured programming, and efficient interfacing to the experimental environment. Direct memory access allows reading of samples without the bottleneck of serial links.

Separate programs are written for running experiments, processing data, and displaying data. This modularity helps to organize the very large amounts of data gathered, and to stay within the limits of the PDP, namely 64kB of virtual memory and 13MB of disk space allocated for sampled data.

The construction of waveforms for driving the 3D wave tank was dedicated to a real time computer, a Plessey Miproc 4 MIP machine. The PDP specifies the wavefronts required in the tank in terms of their amplitude, frequency, angle and phase. The Miproc calculates the resultant instantaneous value of the composite waveform at the refresh rate. The processor speed sets the limit on number of calculations and hence the complexity of output. The Miproc was capable of calculating 75 wavefronts for 80 wavemakers, at a rate of 20 Hz. A second Miproc was used for control of the spine model, where force command signals needed to implement the controllable stiffness were required in real time. For the experiments in the 2D tank, a purpose-built rack machine was recently added as a real time controller for both the wavemakers and the force rig drive.

A clock signal, of frequency selectable between 5Hz and 320Hz rising in powers of 2, synchronises sampling with the generated waveforms. Sampling may be delayed by an arbitrary wait time. It is normal to record a binary power of samples over an integral number of cycles so that the Fast Fourier Transform algorithm may be used to process the data.

A sampling interface handles the time-multiplexed signals from the gauges around the laboratory. Sampled data have their values passed to the PDP or real time controller when their address is selected. The real time controller can also send signals to the system.

Eight multiplex ribbon cables are provided; four are dedicated to the spine, the others may be routed anywhere in the laboratory. Sampling of up to 2048

Figure 2.1
The experimental hierarchy.

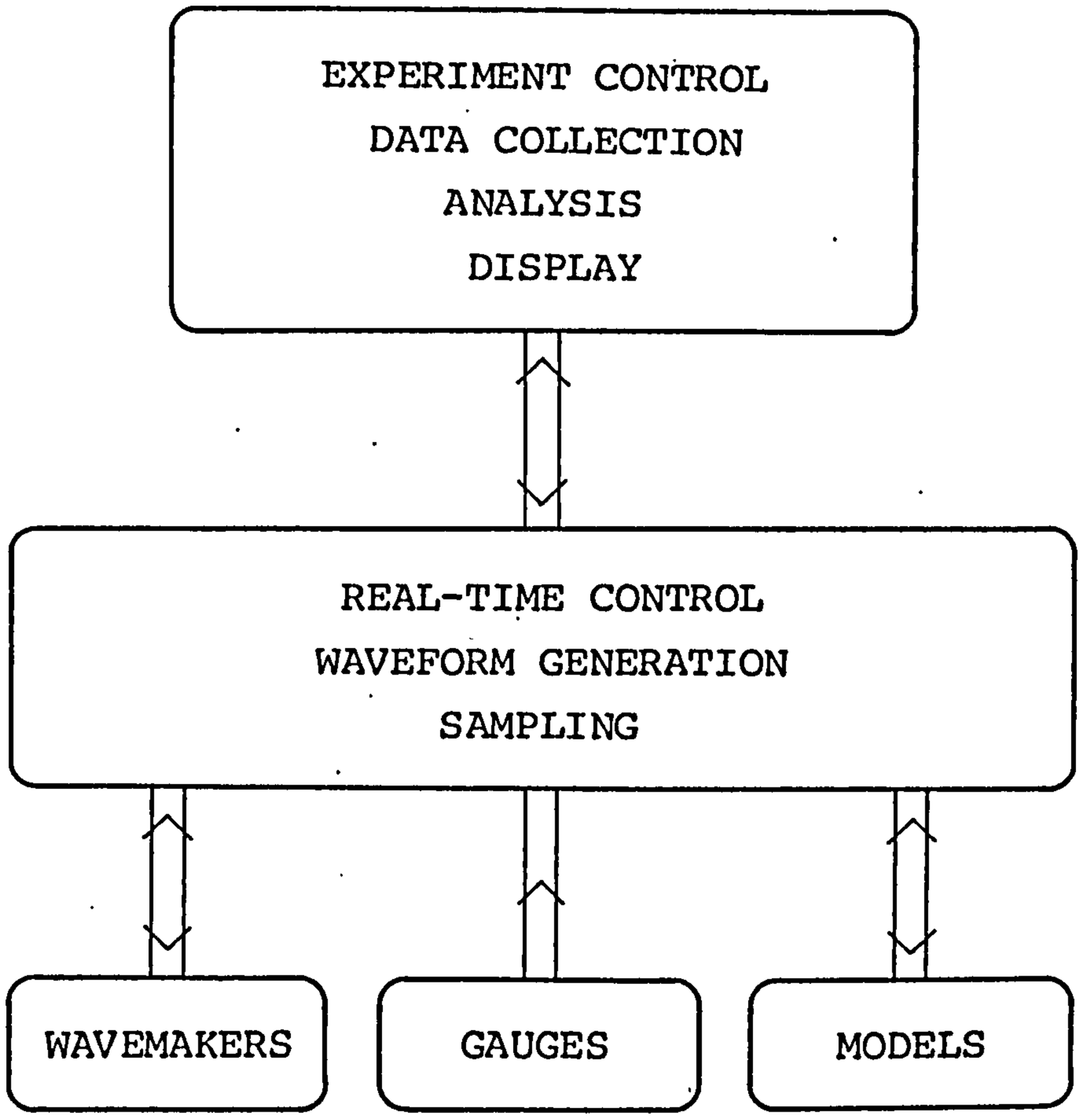

channels is possible. Signals are passed in analog form around the tank with a signal range of ±15V, and converted by a 14 bit analog-to-digital converter in the sampling interface. The size of the least significant bit is thus 2mV, setting the sampling error to ±1mV. The level of broadband noise on channels is of the order of 2–10mV.

2.2 The 3D wave tank

Figure 2.2 shows a dimensioned plan of the tank. The working area of the tank is considerably smaller than the external area due to the need to include beaches. These are passive metal-mesh triangular prisms with their apices facing into the waves to provide a gradual impedance match from the waves to the tank walls. The beaches have amplitude reflections of between 2 and 20%, absorption increasing with wave steepness. Beaches are not provided at the control end of the tank, where a glass window is mounted. Consequently, there is a local reflection field, which is avoided when positioning models in the tank.

WAVEMAKER SPECIFICATIONS	
width	300 mm
hinge depth	540mm
max angle	$\pm 15^0$
Wave amplitude maximum	
at 1 Hz	110 mm
Frequency range	
for 20 mm amplitude	0.4 - 2.0 Hz

The frequency range for a given amplitude is limited by the displacement of the wavemaker at the low-frequency end, and by wave steepness and breaking at the upper end.

The wavemakers have force and velocity feedback, enabling them to absorb spurious energy in the tank. They are of an earlier design than those in the 2D wave tank, with less open-loop gain available to counteract stiction, and hence less ability to absorb waves of low amplitude. However, the combination

Figure 2.2

The 3D tank: plan and coordinate system.

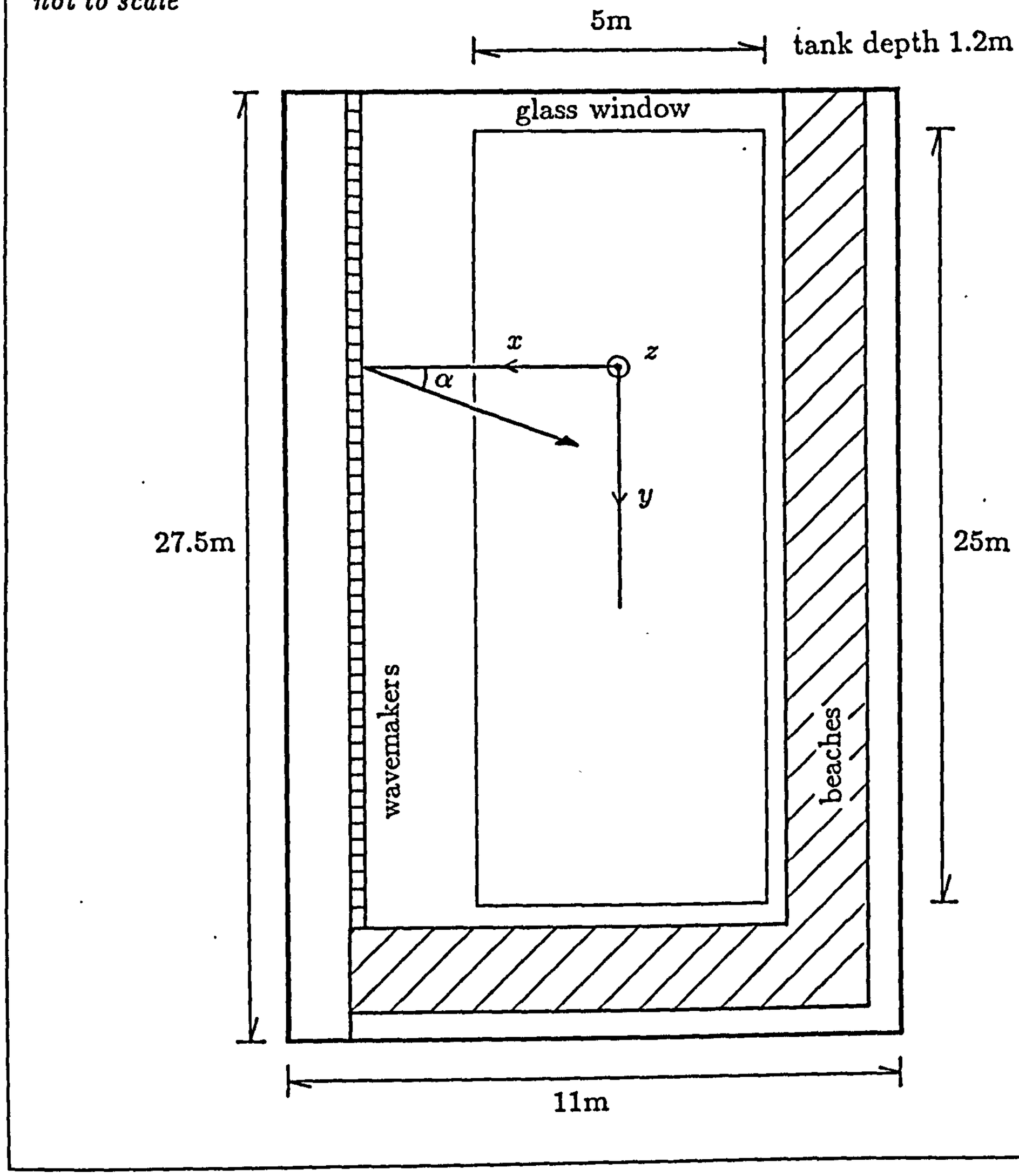

of beach and wavemaker absorption allowed the tank to adjust to new wave conditions in a settling time of about 20 seconds.

Eighty wavemakers with a pitch of 305 mm provide wave generation along a 25 metre width. They can be driven in common mode, producing parallel-crested waves up to 110 mm in amplitude at 1 Hz. When driven with a constant phase difference between paddles, they will produce angled waves, up to a maximum of 90^0. More elaborate phase difference schemes can produce, for example, a focussed circular wave with a maximum amplitude of 250 mm at 0.8 Hz.

For a wavemaker pitch of P, and a wavelength of λ a phase difference δ between wavemaker n and wavemaker $n+1$ produces an angle α

$$\alpha = \arcsin \frac{\delta \lambda}{2\pi P} \tag{2.1}$$

At higher wave frequency, an angle limitation appears. From the equation above, it is clear that for a given angle as λ decreases, δ must increase. At some point the phase difference between wavemaker n and its predecessor, wavemaker $n-1$ will be small enough to generate a wave of different angle in the other direction. The angle limit appears at 90^0 at 1.6Hz, dropping to 20^0 at 1.95 Hz.

Waves produced perpendicular to the wavemakers cover the entire work area. Angled waves leave triangular areas of calm water at the end from which the waves travel. The spine model was placed to maximise its exposure to waves, discrepancies only arising at the largest angles.

A time delay of 0.6ms appeared between adjacent wavemakers due to the multiplexing of the wavemaker drive signal. This produced a systematic error in the angle of wave propagation which can be calculated from equation 2.1 above. At 1Hz it was +0.2 degrees. The error was corrected only after this work was complete.

Skyner (1987) measured the wave reflection in the centre of the 3D tank to be about 5 to 10% between 0.8–2.0Hz. Bryden (1983) measured the root-mean-square wave amplitude over the whole surface of the tank using a travelling wavegauge array with 10 gauges spaced 0.56m apart. He discovered that the rms amplitude of a 1Hz wave propagating normally to the wavemakers varied by up to $\pm 15\%$ over the working area of the tank. In a mixed sea (a 1Hz Pierson-Moskowitz with Mitsuyasu angular spreading, principal direction normal to the wavemakers) the variation dropped to half this range. Some of the variation

may be due to an inhomogeneous wave field produced by the wavemakers, but most is likely to be reflection. Since the technique showed a large increase in energy close to the glass wall, this area was avoided during testing, and in regular wave testing the waves were given angular headings away from it.

To allow for the small evaporative losses and leaks, the tank water is topped up to the 1.2m depth before each experiment. The 300 tonnes of water is cycled through a sand filter to reduce turbidity. It is treated with a proprietory mix of corrosion inhibitor and biocide, in low enough concentration negligibly to affect the physical properties of the water.

2.3 The 2D wave tank

Figure 2.3 is a dimensioned elevation of the tank. A wavemaker is installed at each end of the tank. Their performance is measured later in this chapter. It is possible to use just one wavemaker and a passive beach to give better absorption of unwanted waves, but the twin wavemaker design allows greater flexibility of experiment design, the production of novel waves and the exact definition of a tank centre. Evaporative losses require that the tank be topped up to the 0.58m depth before each experiment.

The wavemakers control absorption of waves propagating along the tank, but cannot attenuate cross-waves. The wavemakers are attached by gussets to the side walls, and these gussets move at half the velocity of the paddle. They therefore provoke cross-waves in the tank which are undamped by the paddles, only by the viscosity and surface tension of the water. These waves constructively interfere when integral multiples of the half-wavelength coincide with the tank width. The first resonance appears at 1.58 Hz, the second at 2.2 Hz, the third at 2.7Hz and so on in accordance with the wavelength formula equation 1.18. However, models in the narrow tank are usually designed to span the tank and so will experience the average wave height. And the wavegauge arrays described below are constructed to eliminate most of the effect of cross-waves.

Figure 2.3
The 2D tank: elevation.

not to scale

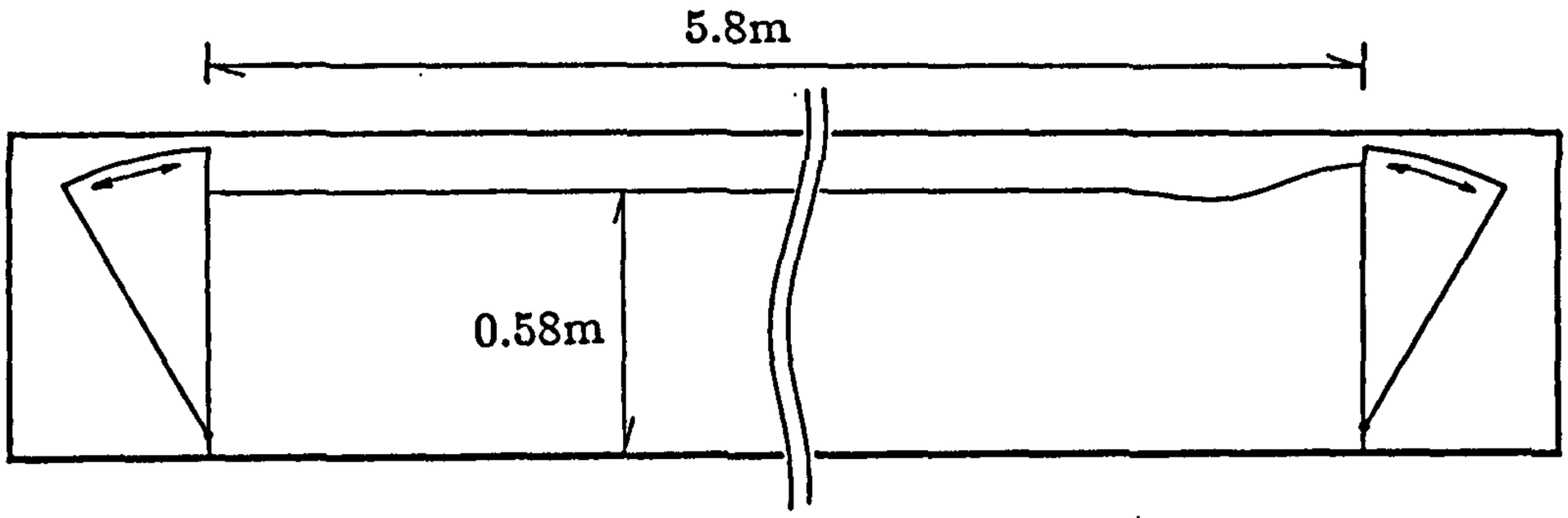

2.4 The wave gauge arrays

Twin-wire wavegauges were used of a type similar to those described by Fryer and Wilkie (1975). Those authors discovered twin-wire alternating-current resistive gauges to be considerably superior to capacitance or heaving-float gauges in their linearity and frequency response. The gauges used here offer a further improvement in being driven by constant-current sources, and hence immune to impedance effects. They also have electronic compensation for changes in water conductivity.

Photograph 2.1 shows one of the two identical wave gauge arrays. A light-alloy frame supports 4 wave gauges. The knurled discs clamp the frame in position on the glass walls of the 2d tank. Each wave gauge consists of two parallel stainless-steel rods held separate by a perspex block. The short sections of rod which protrude from the bottom of the block are used to measure and hence compensate for the effect of water conductivity. In use, the rods are mounted vertically half-immersed in the water. The conduction between the rods is measured as a voltage using a nominal 1kHz AC current source. The close proximity of the four gauges necessitated the use of 4 different drive frequencies, anharmonically related, to avoid beat interference. The wavegauges are calibrated by measuring the voltage outputs when in the rest position, and when raised 50 mm on the square-section pegs bolted to the frame.

Each wavegauge is located a quarter tank width in from the tank walls. When the signals from the pairs of gauges across the tank are added, they eliminate much of the effect of cross waves in the tank, by averaging. Consideration of the geometry shows that they average the first cross-wave to the correct mean value, and so on for all odd higher order spatial harmonics. They also correctly average out the second cross wave.

The two lateral pairs of gauges are mounted 150 mm apart, and their separation in space allows them to measure the phase difference of waves passing them. Matrix arithmetic on the two complex measurements allows the amplitude of the waves in both directions to be calculated. The method is shown below.

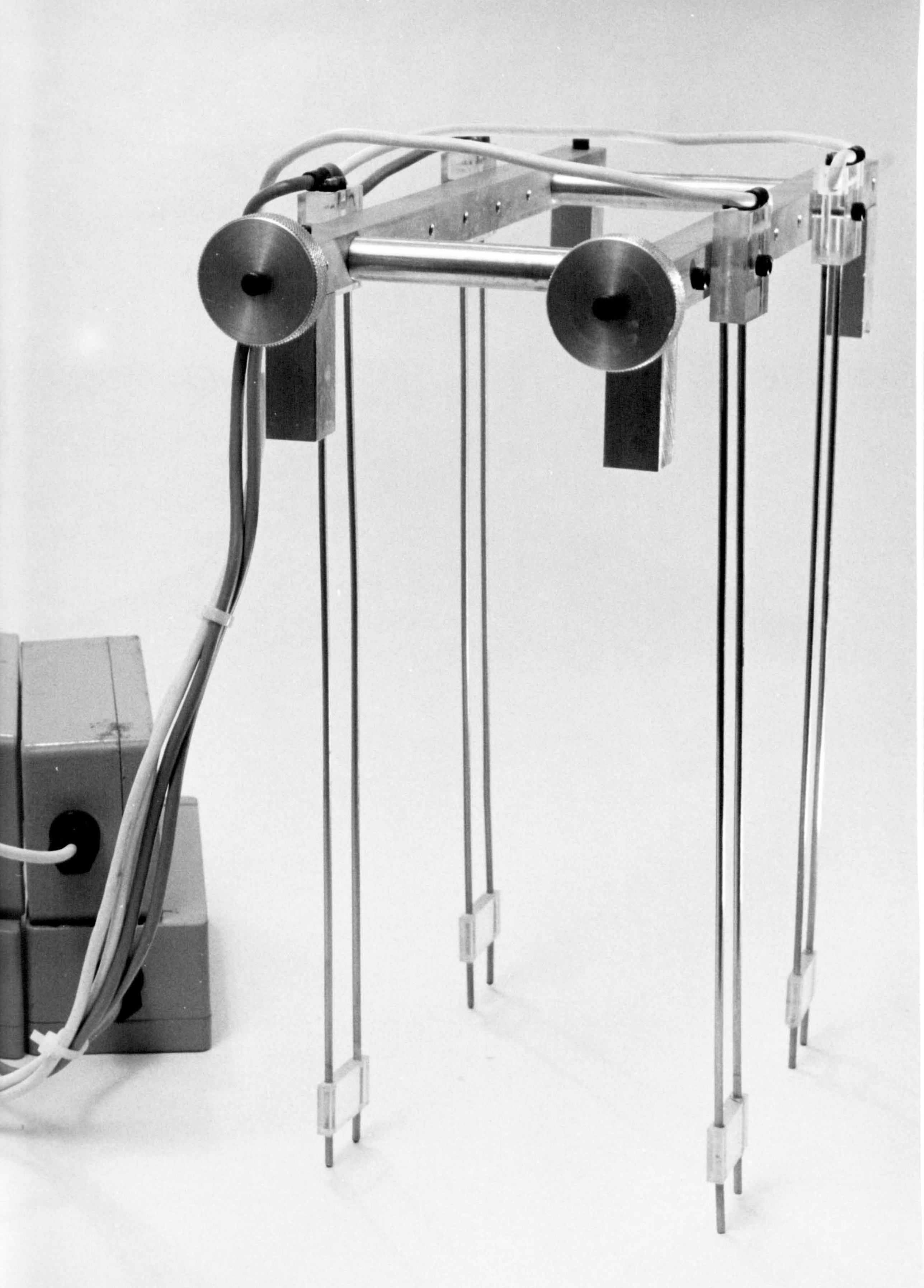

2.5 Processing wavegauge data

The wavegauge definition sketch is shown in figure 2.4; the origin is at the water surface in the middle of the tank. Two wavegauges are disposed symmetrically about the origin with a separation $2d$. Each wavegauge represents a *pair* of wavegauges *across* the tank, whose signals have been averaged to reduce the effect of cross-waves.

Waves in the tank are assumed to be linear sinusoids, hence decomposable in frequency by a discrete Fourier transform. At any one frequency there can only be two waves, travelling in the positive and negative x directions. The wavegauges measure the elevation of the water surface. For continuous sinusoidal waves of complex amplitude A, angular frequency ω and wavenumber k the instantaneous elevation varies according to

$$z_+ = \Re\{A_+ e^{i(\omega t - kx)}\} \tag{2.2}$$

$$z_- = \Re\{A_- e^{i(\omega t + kx)}\} \tag{2.3}$$

The complex amplitude G measured at each wavegauge is the local sum of the two wave trains.

$$G_0 e^{i\omega t} = A_+ e^{i(\omega t - k(-d))} + A_- e^{i(\omega t + k(-d))} = e^{i\omega t}[A_+ e^{ikd} + A_- e^{-ikd}] \tag{2.4}$$

$$G_1 e^{i\omega t} = A_+ e^{i(\omega t - k(+d))} + A_- e^{i(\omega t + k(+d))} = e^{i\omega t}[A_+ e^{-ikd} + A_- e^{ikd}] \tag{2.5}$$

Defining $P = e^{ikd}$ and $Q = e^{-ikd}$ and writing equations 2.4 and 2.5 as a matrix equation.

$$\begin{pmatrix} G_0 \\ G_1 \end{pmatrix} = \begin{pmatrix} P & Q \\ Q & P \end{pmatrix} \begin{pmatrix} A_+ \\ A_- \end{pmatrix} \tag{2.6}$$

The equation is solved for $\underline{A}$ by elimination.

The sensitivity of $\underline{A}$ to errors in $\underline{G}$ must be determined. Rewriting equation 2.6 explicitly

$$G_0 = PA_+ + QA_- \tag{2.7}$$

$$G_1 = QA_+ + PA_- \tag{2.8}$$

Subtracting Q times equation 2.8 from P times equation 2.7

$$PG_0 - QG_1 = P^2 A_+ - Q^2 A_+ \tag{2.9}$$

Figure 2.4
Wavegauge definition sketch.

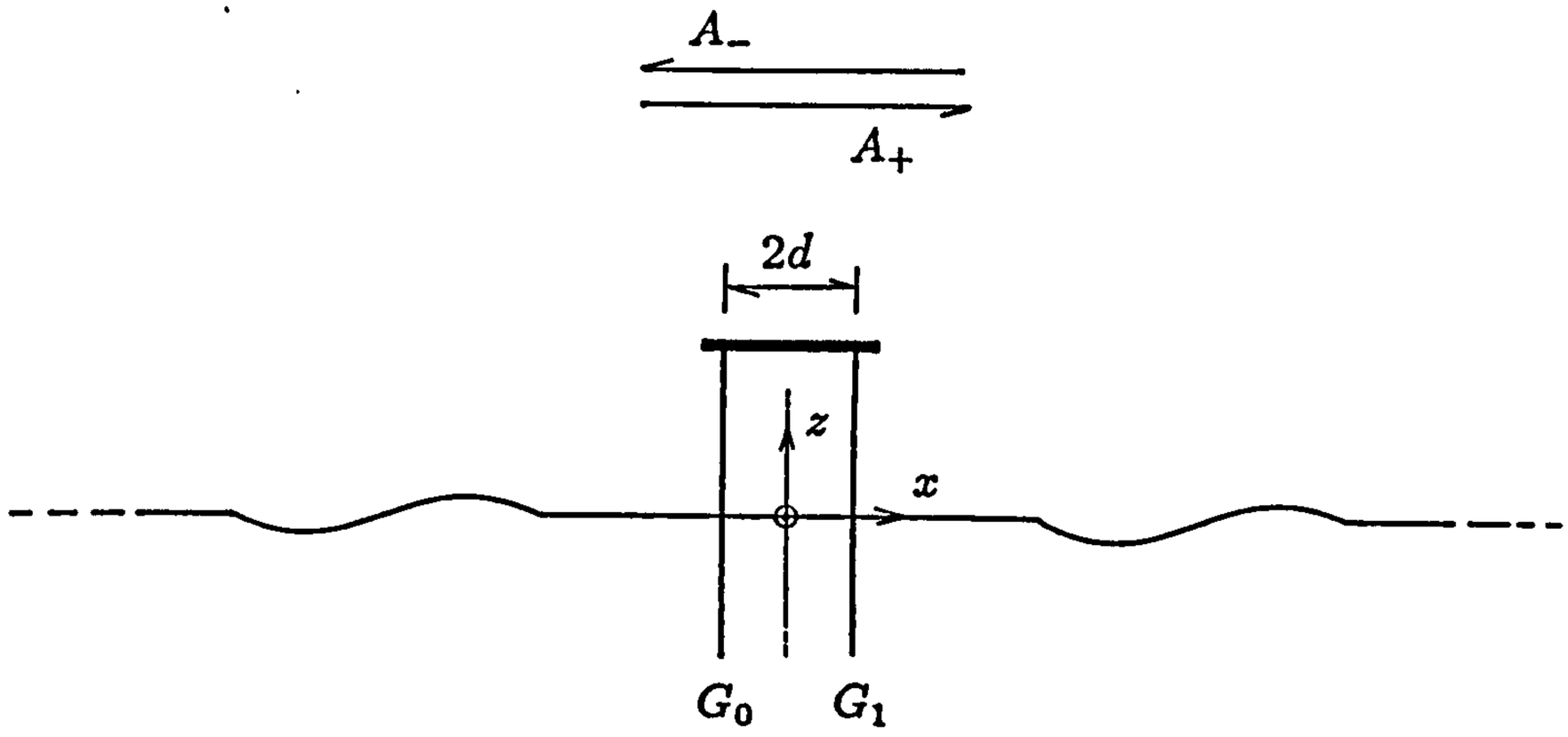

$$A_+ = \frac{PG_0 - QG_1}{P^2 - Q^2} \tag{2.10}$$

The rate of change of A_+ with respect to G_0 is given by

$$\therefore \frac{\partial A_+}{\partial G_0} = \frac{P}{P^2 - Q^2} = \frac{e^{ikd}}{e^{i2kd} - e^{-i2kd}} = \frac{\cos kd + i \sin kd}{4i \sin kd \cos kd} \tag{2.11}$$

As $kd \to 0$, $\sin kd \to kd, \cos kd \to 1$ and

$$\left|\frac{\partial A_+}{\partial G_0}\right| \approx 1/4kd \tag{2.12}$$

As $kd \to \pi/2, \cos kd \to \pi/2 - kd, \sin kd \to 1$ and

$$\left|\frac{\partial A_+}{\partial G_0}\right| \approx 1/4kd \tag{2.13}$$

So at both extremes the function tends to infinity. Clearly the other partial derivatives of amplitude with respect to gauge measurements will have the same form. If G_1 exhibits a similar (but uncorrelated) error to G_0, we can expect the total error to increase by a factor of $\sqrt{2}$ at these frequencies. This figure represents the error in the larger of the two waves and hence the limit of resolution of the smaller wave.

2.6 Wavegauge calibration

The wavegauges were calibrated by sampling the outputs for each gauge in two positions. Pegs attached to the array frame allowed the wavegauges to be raised 50 mm for this purpose. The calibrations were checked before and after each experiment. Over the course of a few hours drift was found to be of the order of 0.1%.

The dynamic calibration of the wavegauges was tested in an earlier experiment (Skyner 1987). A wavegauge was attached at various points along the length of a lever whose free end could be oscillated vertically. The wavegauge was then driven up and down in water over a range of amplitudes at 1 Hz. Its calibration at amplitudes down to 1 mm was typically within 1% of nominal — that is, within the geometrical error of the lever itself. Below 1 mm the calibration began to drop, reading 80% of nominal at 0.5 mm. The error is probably caused by the response of the water meniscus.

Fryer and Wilkie showed the frequency response of twin-wire resistive gauges to be flat over the tested range (0–2.5 Hz).

2.7 A wavegauge experiment

An experiment was run to test the 2D tank characteristics using the wavegauges set up as in figure 2.4. The experimental parameters were:

samples	2048
sampling rate	20.0Hz
frequency range	0.24 - 2.03Hz
wave amplitude	5mm

Using the matrix arithmetic of the previous section, the amplitudes and phases of the incident and reflected waves were measured as a function of frequency. The phase of the wave A_- of wavelength λ transmitted from the wavemaker was extrapolated to the position of the wavemaker (2.9m away) by adding $2\pi 2.9/\lambda$ to the phase measured at the wavegauge array. This calculated phase, and the measured wave amplitude was used to implement the 'tank transfer function' which adjusts the command signal to the wavemaker so that the wave amplitude is approximately constant and the phase approximately zero at the wavemaker, across the whole frequency band.

The experiment was then rerun using two wavegauge arrays placed symmetrically 1.5 m either side of the tank centre. This time the amplitude and phase of the transmitted and reflected waves at the two positions was used to construct graphs of the various tank characteristics.

2.8 Results

Figure 2.5 collects the wavemaker characteristics on one page. The gauge error ratio is calculated from the modulus of the expression in equation 2.11. This ratio is the factor by which the individual gauge errors must be multiplied to indicate overall error with frequency. It shows a minimum at $kd = \pi/4$ of 1/2: the error is divided between the two oppositely travelling waves. It also shows the expected rise at high and low frequency confirming the limited range of the wavegauge array. As mentioned above, individual gauge errors are of the order of 1%, and therefore their effect in the array rises to about 5% over the frequency range shown.

The wavelength error is the fractional difference between the theoretical length from equation 1.18 and the length implied by the 3m separation of the wavegauge arrays and the phase difference for the wave between the arrays. As can be seen, there is less than 1% difference over the range 0.5–2.0Hz. Below 0.5Hz the measured wave gets shorter, by about 10% at 0.25Hz. However, it is not possible to say whether this is a physical departure from linear wave theory or an error due to the wavegauges.

The wave attenuation is the fractional attenuation per metre of the wave as it passes down the tank. This is calculated from the amplitude of the wave transmitted from the wavemaker as measured at the two sites. The smoothed curve through the data suggests that attenuation is about 1%/m over most of the range. The rise in attenuation to about 5%/m suggests that the attenuating mechanism is steepness related. The large amount of scatter shows that the attenuation is of the same order as the amplitude error in wave measurement. For this reason, the effects of attenuation have been neglected elsewhere in this text.

The graph for wave reflection shows the ratio of the reflected to transmitted wave, measured at the array closest the wavemaker, and uncorrected for attenuation. Again, there is much scatter, but the smoothed curve shows a maximum of about 25% at around 1.4Hz. As will be seen, the effect of this reflection is considerable, and it is essential that it can be measured using these wavegauge arrays.

Figure 2.5
2D tank characteristics.

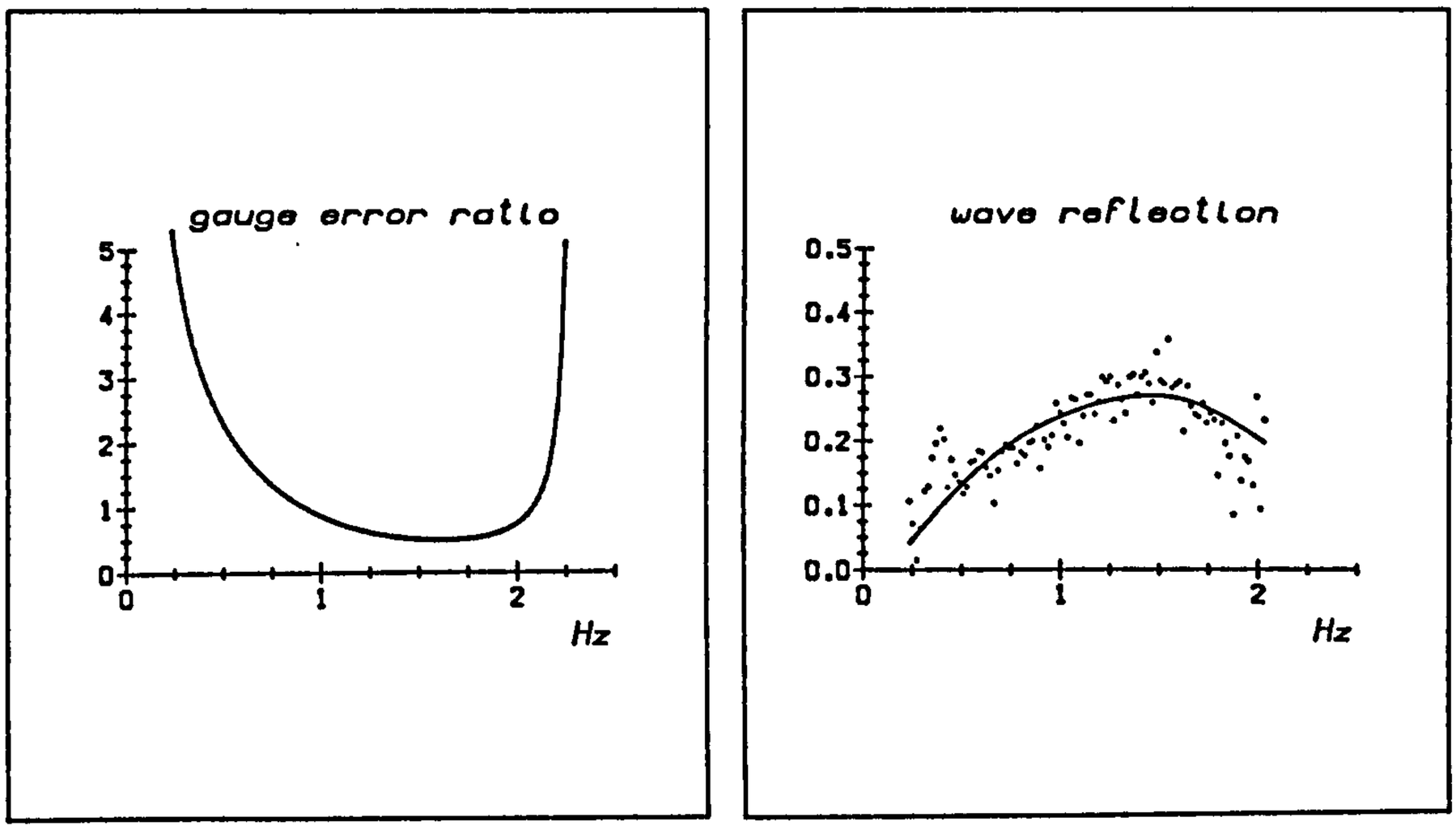

Chapter 3

Measurements on cylinders in 2 dimensions

SUMMARY

A force rig for testing the hydrodynamic characteristics of immersed cylinders is described and its intrinsic impedance measured.

Wave force coefficients and radiation impedances are determined experimentally for cylinders with a range of diameters in the 2D tank. Matrix arithmetic is used to remove the effect of tank reflections.

The data are used to calculate the equivalent values for the composite diameters of the long cylinder model.

3.1 The Pitch-Heave-Surge rig

All the experiments in this chapter were performed using the PHS rig. Photograph 3.1 shows the rig mounted on the 2D tank. It consists of a massive frame - about 40kg - resting on the rails of the tank on disc feet. Two of the feet - one is visible at the left - are eccentrically mounted to permit levelling of the frame.

A linkage projects from the frame at the left, and supports the test object, in this case a 125mm diameter cylinder. This linkage is a light and rigid space frame jointed by ball bearings and leaf springs to give a structure which allows 120mm of motion peak-to-peak in a plane parallel to the tank walls, but with little play or bearing loss. The linkage transforms motion in this plane into

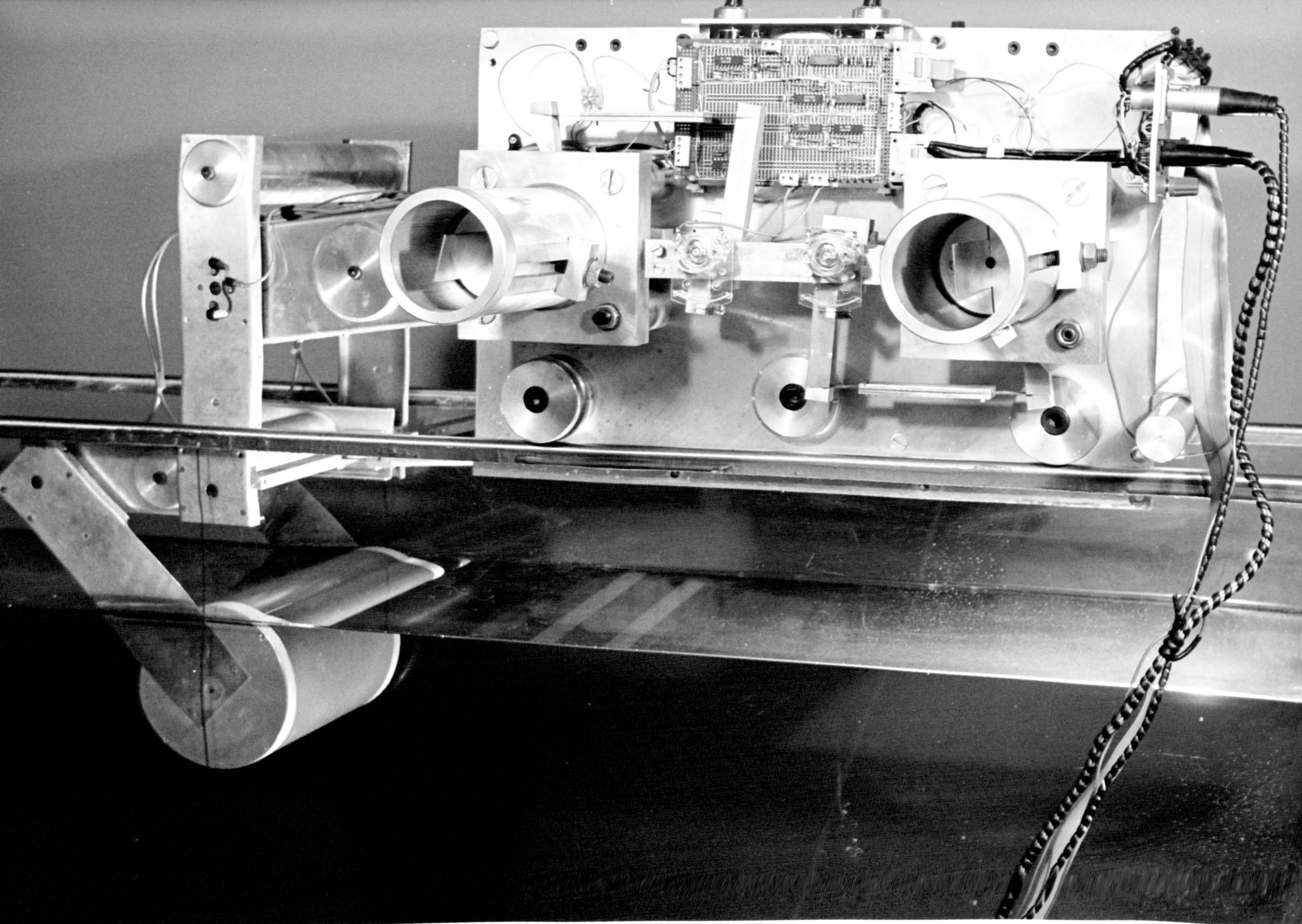

rotation about two axes; these are coaxial with the two hollow cylinders projecting from the frame out of the picture. Each cylinder contains a steel strip used as a torsion spring. These provide restoring force to the motion of the test object. Clamps sliding down the outside of the cylinder adjusts the spring rate; and rotating the cylinder from its null position provides an offset force used to cancel the buoyancy of the test object. Counterbalance weights may also be mounted inside the body for test objects which are exceptionally heavy.

Mounted in line with the springs but hidden behind them are torque motors which drive the rig under computer control. The motion of each of the axes is coupled via leaf springs to the galvanometers—used in reverse as tachogenerators—bolted to the frame next to the cylinders. Above them is a circuit board containing signal conditioning circuitry both for the velocity outputs, and for the outputs from strain gauges mounted in the prow of the linkage. The ten-turn potentiometers mounted at the top of the circuit board allow nulling of the DC offset of the strain gauge signals (which can vary considerably with the buoyancy of the test object) so that the full voltage range of the amplifiers can be used. A second set of galvanometers, strain gauges and circuitry is mounted on the far side of the rig, and the two sets of signals are combined to give a total reading. The cables at the right carry power and signals to and from the rig.

An outrigger can be attached to the linkage to measure forces and velocities in pitch. For these experiments this was not required and therefore not attached.

3.2 Rig geometry and signal processing

Figure 3.1 shows a schematic of the rig geometry. The geometry is derived from a Watt's linkage, and is designed to transform heave and surge motion of the test object into independent rotations about rig axes R_1 and R_2. These axes can be driven directly by torque motors, and they are coupled by small parallelogram linkages to galvanometers which measure the rotational velocities ν_1 and ν_2. The heave and surge velocities can be expressed in terms of the rotations by linear approximations.

$$U_s = a\nu_2 \tag{3.1}$$

$$U_h = a\nu_1 \tag{3.2}$$

Figure 3.1
Schematic diagram of the Pitch-Heave-Surge rig.

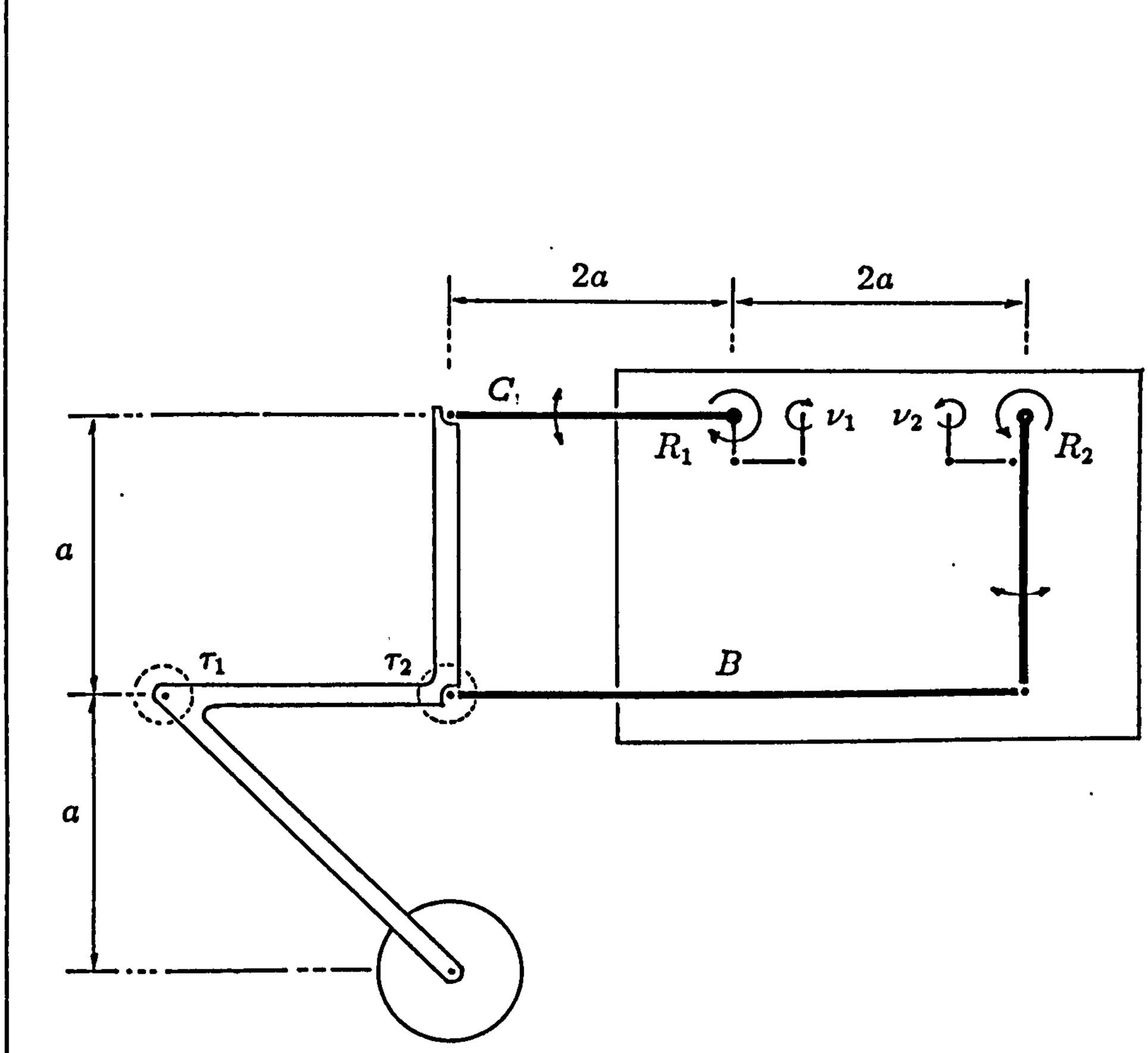

The orthogonality of these motions is only true to first order. Rotation of axis R_2 actually causes the test object to move on an arc, with spurious vertical motion of second order and higher. Rotation around axis R_1 also causes spurious horizontal motion, but because link C is half the length of link B, the even order terms cancel, leaving only third and higher order odd terms. The effects are small: 20 mm surge motion of the test object causes 1% crosstalk in heave.

Note that surge motion of the test object is accompanied by first-order pitch; motion of 20 mm amplitude will cause a 4° amplitude pitch. Heave motion will cause a spurious pitch of second-order and higher.

Torsional strain gauges are mounted at the end of the linkage, torque on them provides output. The local geometry mixes heave and surge forces in both gauges. Note from the diagram that because strain gauge τ_2 is mounted vertically above the test object, it can never experience any torque due to heave forces, but only surge. For strain gauge τ_1 the moment arm of heave and surge forces is the same, hence the reading τ_1 may simply be subtracted to leave the moment due to heave.

$$F_h = (\tau_1 - \tau_2)/a \tag{3.3}$$

$$F_s = \tau_2/a \tag{3.4}$$

The end of the linkage is a *moving* coordinate reference frame for force. This leads to a first order crosstalk term of $\sin\theta$ between channels when it is displaced by angle θ from the rest position. For a surge displacement of 20 mm this corresponds to about 7% crosstalk.

Surge motion of the test object causes an angular displacement θ of the linkage which then behaves like a pendulum with restoring force $\frac{w\sin\theta}{2a}$ where 2a is the effective pendulum length, and w is the effective weight (that is the weight of the test object minus any buoyancy). This effect appears as a spurious spring term of $\frac{w}{2a}$ when the rig is used to measure surge impedances.

The geometrical conversions given above are performed in hardware. The heave and surge velocity measurement and drives are orthogonal, but the forces must be treated to be so. The test axis is fixed and the rig driven in one mode while the force reading in the other mode is electronically trimmed to zero.

None of the cross-talk terms mentioned above is corrected: in the experiments in this thesis, amplitudes of motion in heave and surge were kept below

20 mm. The pendulum effect is appreciable however, and is corrected for when impedance graphs are drawn.

The force outputs are calibrated with known weights. The velocity outputs are calibrated by driving the test axis by an external motorised rig in a circle of known amplitude, at a measured rate. The estimated calibration error is ± 1%, in force and velocity, with a comparable calibration drift over the course of the experimental period.

3.3 The test cylinders

Three sizes were fabricated, their data are tabulated below.

length mm	diameter mm	volume litre	mass kg
295	75	1.303	1.294
295	100	2.317	2.304
295	125	3.620	4.216

3.4 Experimental parameters

For all the experiments in this chapter the following conditions were constant:

samples	2048
sampling rate	40Hz
frequency range	0.39–2.03Hz
number of frequencies	85

The frequencies are chosen so that sampling occurs over an integral number of wave cycles

3.5 Measuring the rig impedance

The strain gauges are mounted at the end of the linkage to minimise the rig's contribution to force measurements. Though small, it is not negligible, and it

was measured by driving the rig and measuring the forces on it due to the reaction of its own inertia and damping. The rig was driven in air by its own torque motors, with no test cylinder attached. The experimental parameters were as recorded above. A constant force drive signal was used and the rig motion kept below 20mm peak-to-peak at all frequencies. The forces and velocities of the test object in heave and surge were sampled.

The equation for the impedance can be written in vector form as

$$\underline{F} = \underline{\underline{Z}}\,\underline{U} \tag{3.5}$$

where all the variables are frequency dependent. Explicitly

$$\begin{pmatrix} F_h \\ F_s \end{pmatrix} = \begin{pmatrix} Z_{hh} & Z_{hs} \\ Z_{sh} & Z_{ss} \end{pmatrix} \begin{pmatrix} U_h \\ U_s \end{pmatrix} \tag{3.6}$$

To determine the 4 unknowns in Z, 2 independent experiments are required. These are: measurements in heave and surge while driving the rig in heave; and the same while driving in surge.

$$\begin{matrix} D_h & D_s \end{matrix} \qquad \begin{matrix} D_h & D_s \end{matrix}$$
$$\begin{pmatrix} F_{hh} & F_{hs} \\ F_{sh} & F_{ss} \end{pmatrix} = \begin{pmatrix} Z_{hh} & Z_{hs} \\ Z_{sh} & Z_{ss} \end{pmatrix} \begin{pmatrix} U_{hh} & U_{hs} \\ U_{sh} & U_{ss} \end{pmatrix} \tag{3.7}$$

The order of the subscripts determines the conditions of the experiment: for example, U_{hs} is the velocity of the rig in heave when driven in surge. Note that arrangement of the elements of the matrix places the largest values on the diagonal, hence maximising accuracy for a solution using matrix inversion.

The results are plotted in Figure 3.2 as a matrix graph, with the real and imaginary parts plotted for each of the elements in the array. Experimental data are drawn as points connected by straight lines. Each graph displays the frequency dependence of that element. The real part is in phase with velocity, and is damping; the imaginary part is a combination of spring and inertia. The imaginary part of Z_{hh} shows a fairly linear increase with frequency and is therefore due to mass. The imaginary part of Z_{ss} is a combination of a line for mass with a curve inversely proportional to frequency due to the negative spring of the pendulum effect. The real part of Z_{ss} shows a slight rise as frequency decreases; a true damping would remain constant. The real part of Z_{hh} is

negative over all its range; since any damping should be positive, this implies some degree of phase error and crosstalk between heave and surge. The cross-impedances Z_{hs} and Z_{sh} are non-zero because of the definition of the surge force in equation 3.4, and because of the fact that most of the mass in the end of the linkage is *between* the two force gauges, and hence the signal from τ_2 is large, and τ_1 small.

3.6 Measuring cylinder impedance in water

An experiment was performed with the 75mm cylinder to measure its impedance in water. It was mounted in the middle of the 2D tank and driven in heave and surge while recording torque and velocity signals. The impedance was calculated by the method shown above. The impedance due to the rig and the effects due to the mass of the cylinder and the negative spring due to the pendulum effect were subtracted; this process is discussed in detail in section 3.8. The results are plotted in figure 3.3. The most striking feature is the systematic ripple apparent on each graph. It can be deduced that this is due to waves transmitted from the oscillating cylinder being reflected from the imperfectly absorbing wavemakers. The frequency spacing of the spikes corresponds to an integral number of half-wavelengths fitted into the 5.8 m round trip from cylinder to wavemaker. At any frequency there will be a standing wave at the centre of the tank whose orientation in the heave-surge plane will depend upon the phase of the reflected wave with respect to the transmitted wave, and hence will depend upon frequency. Consequently the ripple on Z_{hh} is in antiphase with that of Z_{ss}. The ripple almost completely masks the data. Clearly a means of eliminating it is essential for obtaining usable impedance curves.

This is done by taking account of the effect of the waves generated by the motion of the cylinder. To do this requires knowledge of the wave force coefficient, determined by measuring the forces on the cylinder in waves—which also will be corrupted by the effect of reflections. However the wave field at the position of the cylinder can be extrapolated from measurements made with the wave gauge arrays. The calculation for the wave force coefficient on the cylinder and the impedance of the cylinder can then be performed in a simultaneous matrix operation.

Figure 3.2
PHS rig impedance against frequency.

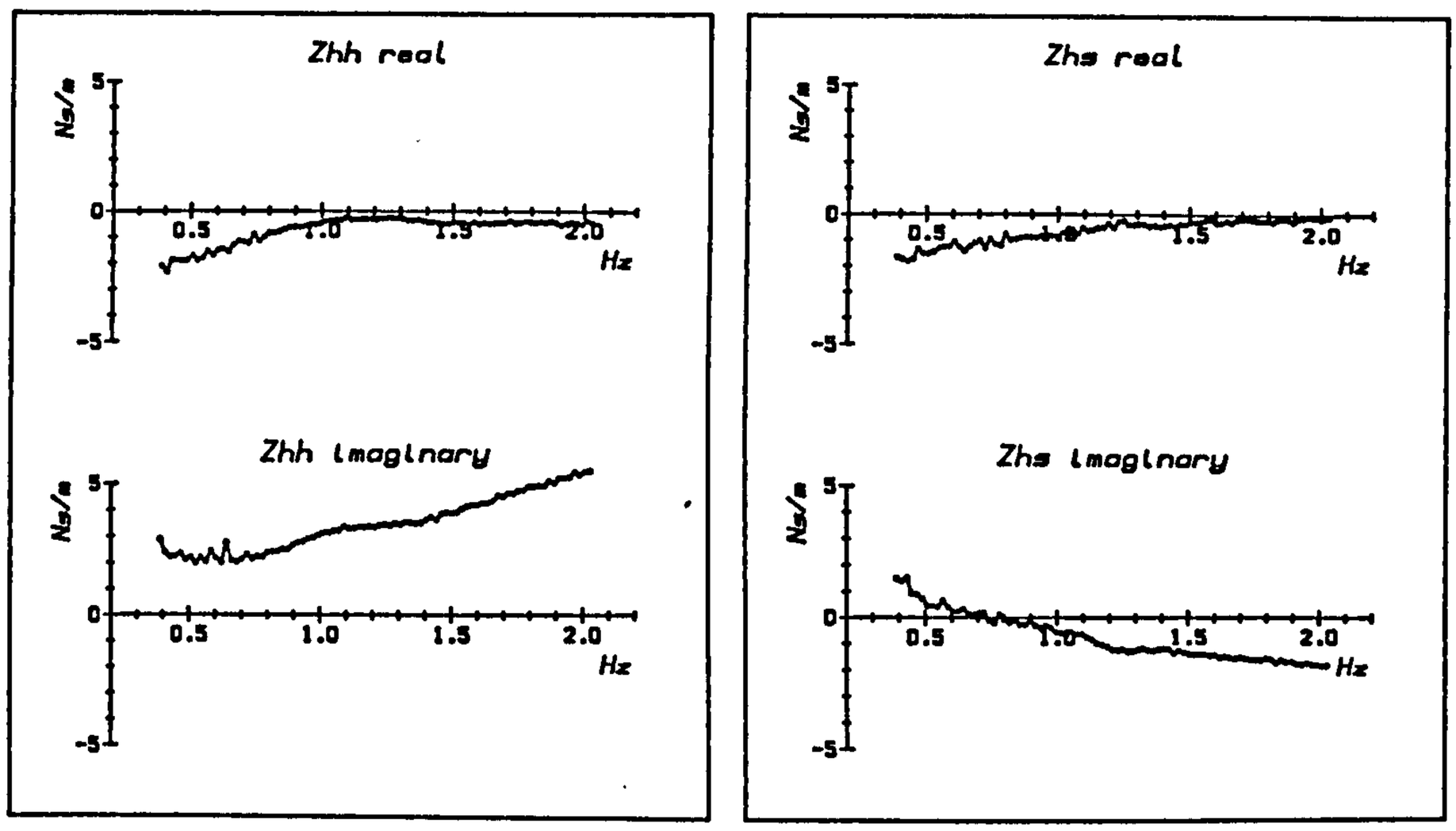

Figure 3.3
Impedance of the 75mm diameter cylinder, freeboard -20mm showing the effect of wave reflections.

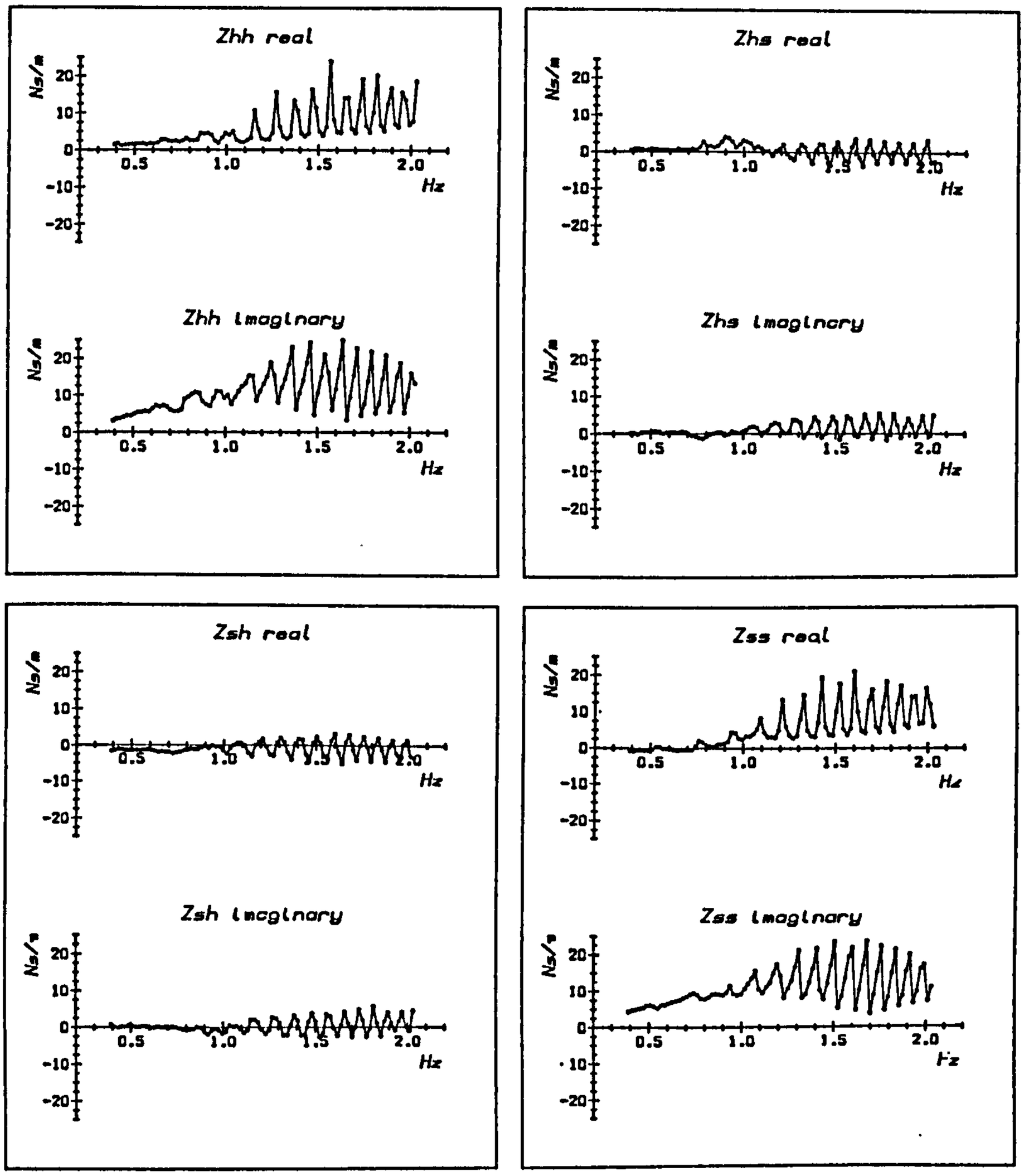

3.7 The extrapolated wave field

Figure 3.4 shows an elevation of the narrow tank with the cylinder model halfway between the two wavemakers. The wavegauge arrays are symmetrically disposed either side of the cylinder. Each cross-tank pair of gauges is represented as a single line, and their readings are assumed averaged to a single value in the treatment which follows.

The gauge-gauge distance $2d$ is 150 mm, the array-cylinder distance S centre-to-centre, is 1.5 m. The waves are assumed sinusoidal and linear, and hence may be separated by Fourier transformation. Considering a single frequency, there are four waves in the tank: their directions and complex amplitudes are shown in the diagram, and their specifications in time and space are:

$$A_{h+}e^{i(\omega t-kx)}$$

$$A_{h-}e^{i(\omega t+kx)}$$

$$A'_{h+}e^{i(\omega t-kx)}$$

$$A'_{h-}e^{i(\omega t+kx)}$$

The gauges measure the vector sum of the pairs of waves

$$G_0 = e^{i\omega t}[A_{h+}e^{ik(S+d)} + A_{h-}e^{-ik(S+d)}] \tag{3.8}$$

$$G_1 = e^{i\omega t}[A_{h+}e^{ik(S-d)} + A_{h-}e^{-ik(S-d)}] \tag{3.9}$$

$$G_2 = e^{i\omega t}[A'_{h+}e^{ik(S-d)} + A'_{h-}e^{-ik(S-d)}] \tag{3.10}$$

$$G_3 = e^{i\omega t}[A'_{h+}e^{ik(S+d)} + A'_{h-}e^{-ik(S+d)}] \tag{3.11}$$

Setting $P = e^{ik(S+d)}$ and $Q = e^{ik(S-d)}$, then

$$\begin{pmatrix} G_0 \\ G_1 \\ G_2 \\ G_3 \end{pmatrix} = e^{i\omega t} \begin{pmatrix} P & 1/P & 0 & 0 \\ Q & 1/Q & 0 & 0 \\ 0 & 0 & 1/Q & Q \\ 0 & 0 & 1/P & P \end{pmatrix} \begin{pmatrix} A_+ \\ A_- \\ A'_+ \\ A'_- \end{pmatrix} \tag{3.12}$$

which may be solved for A by elimination.

Figure 3.4
Wave extrapolation definition sketch.

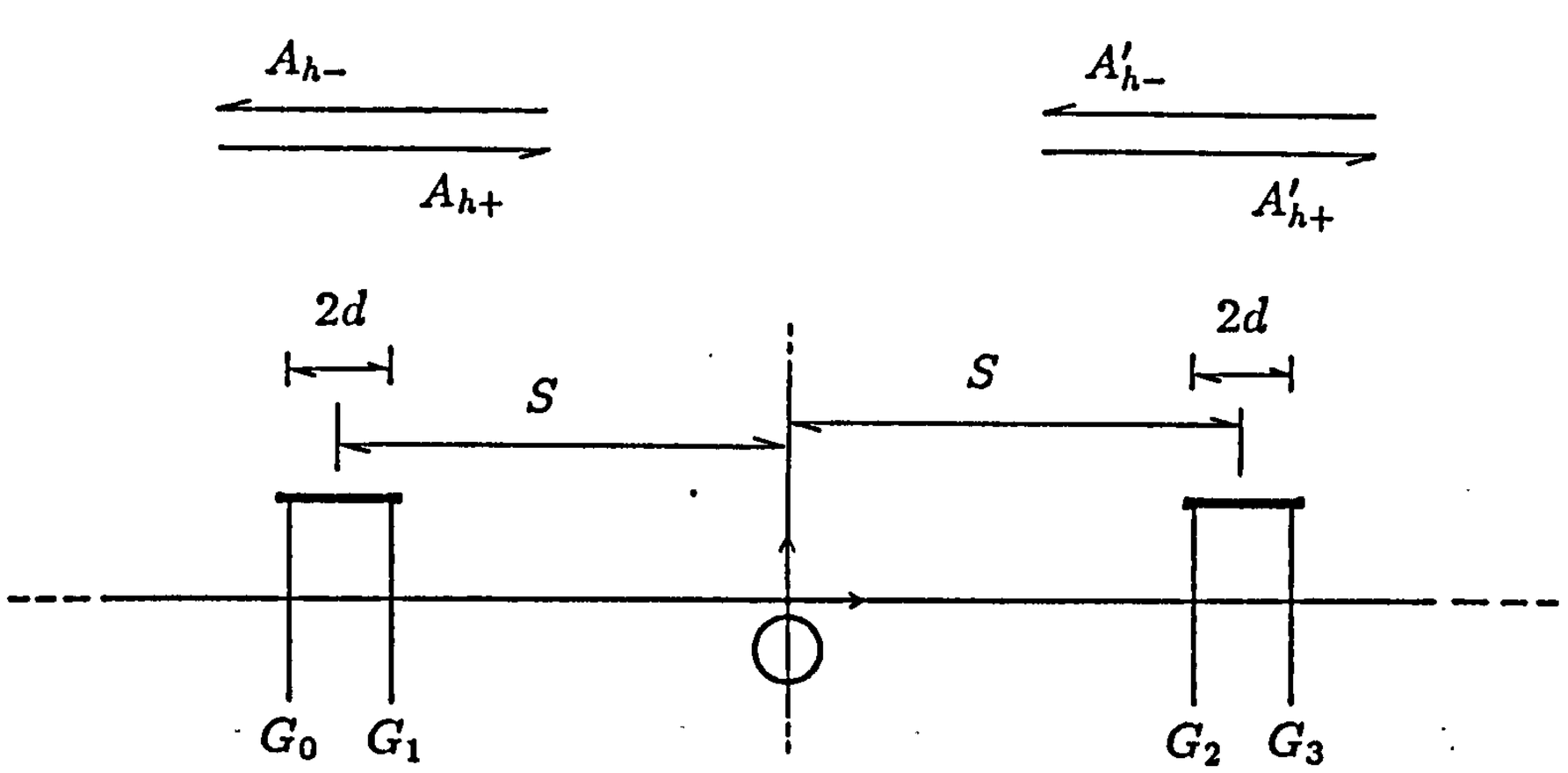

The surge component of positive direction waves lags heave by $\pi/2$ radians, while the surge component of negative direction waves leads heave by $\pi/2$ radians. Therefore

$$A_{s+} = A_{h+}e^{i(\omega t - kx - \pi/2)} = A_{h+}e^{i\pi/2} = iA_{h+} \tag{3.13}$$

and

$$A_{s-} = A_{h-}e^{i(\omega t + kx + \pi/2)} = A_{h-}e^{-i\pi/2} = -iA_{h-} \tag{3.14}$$

The cylinder will only be affected by waves travelling towards it from either direction, hence the resultant heave and surge components of the waves impinging on the cylinder can be written

$$A_h = A_{h+} + A'_{h-} \tag{3.15}$$

$$A_s = iA_{h+} - iA'_{h-} \tag{3.16}$$

The heave resultant is the complex sum of the components; the surge resultant is the complex difference.

3.8 Processing experimental data

Following Evans (1979) the hydrodynamic forces on the cylinder are treated as the sum of two parts: the force on the body when held fixed in an incident wave; and the force on the body assuming it to be oscillating with its induced motion in absence of the incident wave.

Writing a vector equation of motion equating the sum of the forces on the cylinder to its mass times acceleration.

$$\underline{F} - \underline{\underline{W}}\,\underline{A} - \underline{\underline{Z}}\,\underline{U} = \underline{\underline{M}}i\omega\underline{U} \tag{3.17}$$

where the force F measured by the rig is exerted by the rig on the cylinder. W is the waveforce coefficient, Z is the radiation impedance and U the cylinder velocity and M is the cylinder mass in both degrees of freedom. This can be rewritten

$$\underline{F'} = \underline{\underline{W}}\,\underline{A} + \underline{\underline{Z'}}\,\underline{U} \tag{3.18}$$

where a new impedance Z' incorporates the cylinder inertial force, also the rig impedance and the rig pendulum effect. These latter two effects also result in the modification of the force to F'. Rewriting the matrices explicitly:

$$\begin{pmatrix} F'_h \\ F'_s \end{pmatrix} = \begin{pmatrix} W_{hh} & W_{hs} & Z'_{hh} & Z'_{hs} \\ W_{sh} & W_{ss} & Z'_{sh} & Z'_{ss} \end{pmatrix} \begin{pmatrix} A_h \\ A_s \\ U_h \\ U_s \end{pmatrix} \tag{3.19}$$

To determine the 8 unknowns in W and Z 4 independent experiments are required. These are: waves in the two directions; and the cylinder driven in x and y.

$$\begin{matrix} & A_+ & A_- & D_h & D_s \\ \end{matrix}$$
$$\begin{pmatrix} F'_{h+} & F'_{h-} & F'_{hh} & F'_{hs} \\ F'_{s+} & F'_{s-} & F'_{sh} & F'_{ss} \end{pmatrix} =$$

$$\begin{matrix} & & & & A_+ & A_- & D_h & D_s \end{matrix}$$
$$\cdot \begin{pmatrix} W_{hh} & W_{hs} & Z'_{hh} & Z'_{ss} \\ W_{sh} & W_{ss} & Z'_{sh} & Z'_{ss} \end{pmatrix} \begin{pmatrix} A_{h+} & A_{h-} & A_{hh} & A_{hs} \\ A_{s+} & A_{s-} & A_{sh} & A_{ss} \\ U_{h+} & U_{h-} & U_{hh} & U_{hs} \\ U_{s+} & U_{s-} & U_{sh} & U_{ss} \end{pmatrix} \tag{3.20}$$

Which as before is solved for the hydrodynamic coefficients by elimination. For reasons of symmetry it is only necessary to perform one of the wave experiments, A_-. The result of A_+ is synthesised by reversing the horizontal forces, velocities, and wave displacements measured for the A_- experiment. When the experiment is performed, and the data processed in the above way, the correct $\underline{\underline{W}}$ is produced. However, the composite value for the impedance matrix results, and from this must be subtracted

- the rig impedance
- the effect of cylinder mass $mi\omega$
- the pendulum effect of the cylinder $\frac{(m-\rho V)g}{2ai\omega}$

3.9 Measurements on cylinders

Cylinders were mounted in the PHS rig in the middle of the tank. They were exposed to waves over a range of frequency, and the rig was driven in heave and surge over the same range of frequency. The experimental parameters were as tabulated at the beginning of this chapter, and the wave amplitude was 5 mm. The following variables were measured:

heave and surge forces
heave and surge velocities
fore and aft incident and reflected waves

Each experiment was composed of 255 tests (85 frequencies in each of the three wave or drive conditions). The order of the tests was randomised so that any systematic errors in the experiment also became random, appearing merely as extra scatter in the graphs, and could not be misinterpreted. So, for example, the small changes which occur due to the evaporation of a millimetre or so of water from the tank during the course of the experiment do not appear as a systematic change with frequency.

It is possible to lock each undriven mode in the PHS rig so that, for example, the cylinder could have been fixed while experiencing forces on it due to waves, or have been driven in heave while locked in surge. However, the data processing used, which is a matrix operation applied at any given frequency to all the degrees of freedom of the system, make this unnecessary. Furthermore, leaving the whole system free allowed the experiment to be fully automated and the randomization of tests referred to above.

An experiment was performed with the 75 mm diameter cylinder, with a freeboard of -20 mm. The full matrix calculation of equation 3.8 was used. The results of the impedance calculation are plotted in figure 3.5. They can be compared with figure 3.3, in which only the force and velocity measurements from this experiment were used, noting that the scale is identical. It is clear that the ripple due to reflection has been virtually eliminated. Drawing a smooth curve through the data points is now justifiable.

Figure 3.5

Impedance of the 75mm diameter cylinder, freeboard -20mm

Corrected for wave reflections

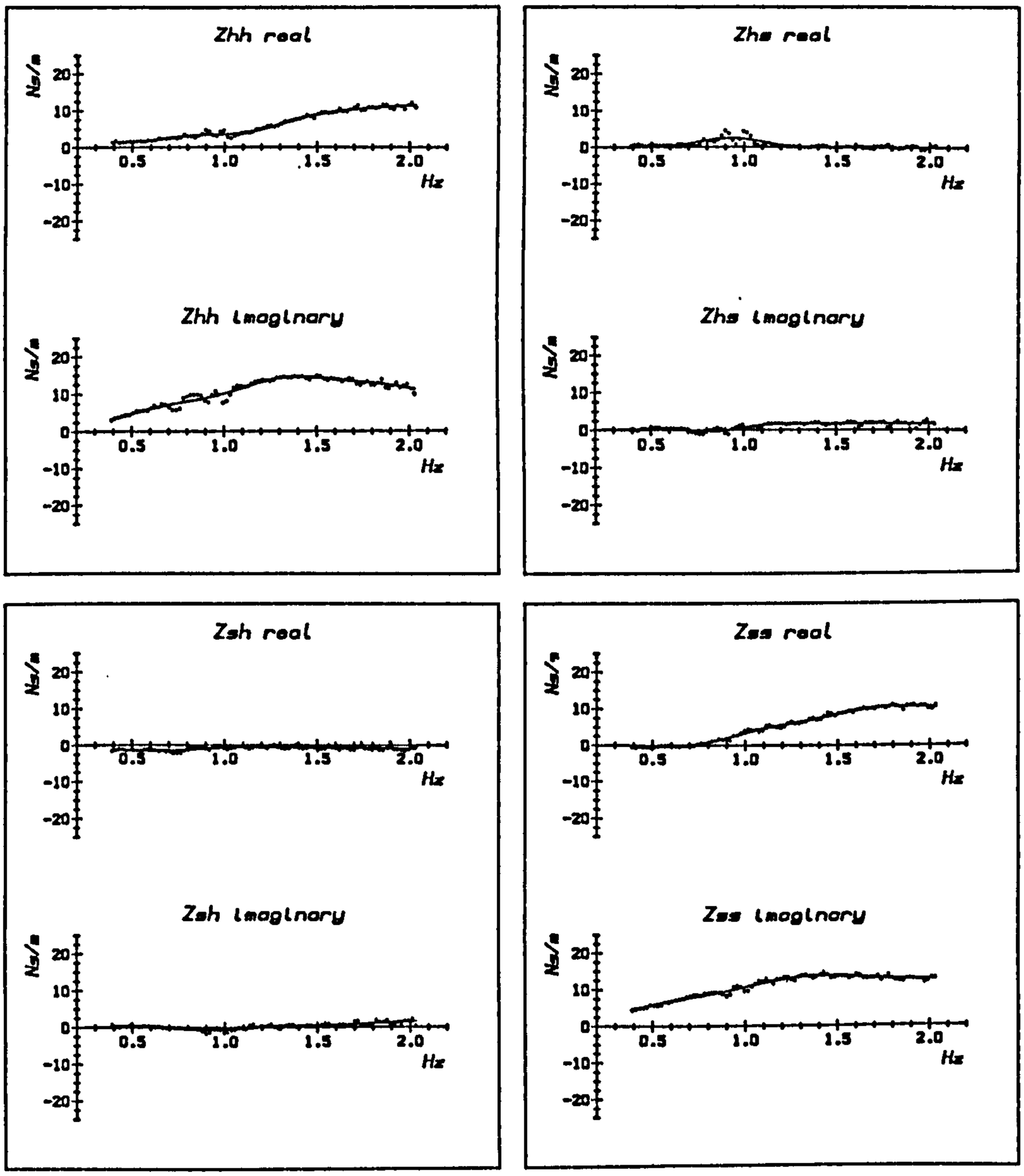

The cross-impedances Z_{hs} and Z_{sh} are very close to zero over most of their range. This suggests that the heave and surge axes are orthogonal both geometrically and fluid dynamically. The anomalies between 0.7 and 1.0 Hz are probably due to the resonances of the rig compliance coupled to the cylinder mass. The amplitude of cylinder motion will increase at these points, increasing the possibility of non-linear crosstalk. Z_{hh} and Z_{ss} would be identical in an unbounded fluid. In these graphs they are very similar, showing that the influence of the surface even only 20mm away from the top of the cylinder is small.

Figure 3.6 shows the wave force coefficient. The elements are identified by their subscripts: for example W_{hs} is the force experienced in heave due to surge displacements of the wave. Again the cross-terms are small. Because the different amplitudes of the waves in heave and surge have been accounted for, the two curves are again very similar.

Impedance results for another experiment, the 125 mm diameter cylinder at a freeboard of +20 mm are shown in figure 3.7. Note the change of scale. The volume of the cylinder has increased by a factor of 2.8. The freeboard has produced a radical difference between the heave and surge impedances. In heave, the real part of the impedance has dropped to very low values, implying that the cylinder radiates only very small waves when vibrated in heave. The imaginary part is now dominated by the negative spring due to buoyancy.

Similar radical changes are apparent in the graphs for the wave force coefficient in figure 3.8. It is clear that large changes result from changes in cylinder size and freeboard. The spine model contains sections of different lengths and freeboards, and it is essential to determine accurate values of W and Z.

3.10 Cylinder diameter and freeboard

A set of experiments was performed to determine the effects of cylinder diameter and proximity to the surface. Nine experiments were performed with three diameters and three freeboards.

Freeboards were impossible to set by trying to locate the top of the cylinder at the required distance below the surface because of the effects of surface

Figure 3.6

Wave force coefficient of 75mm diameter cylinder, freeboard -20mm.

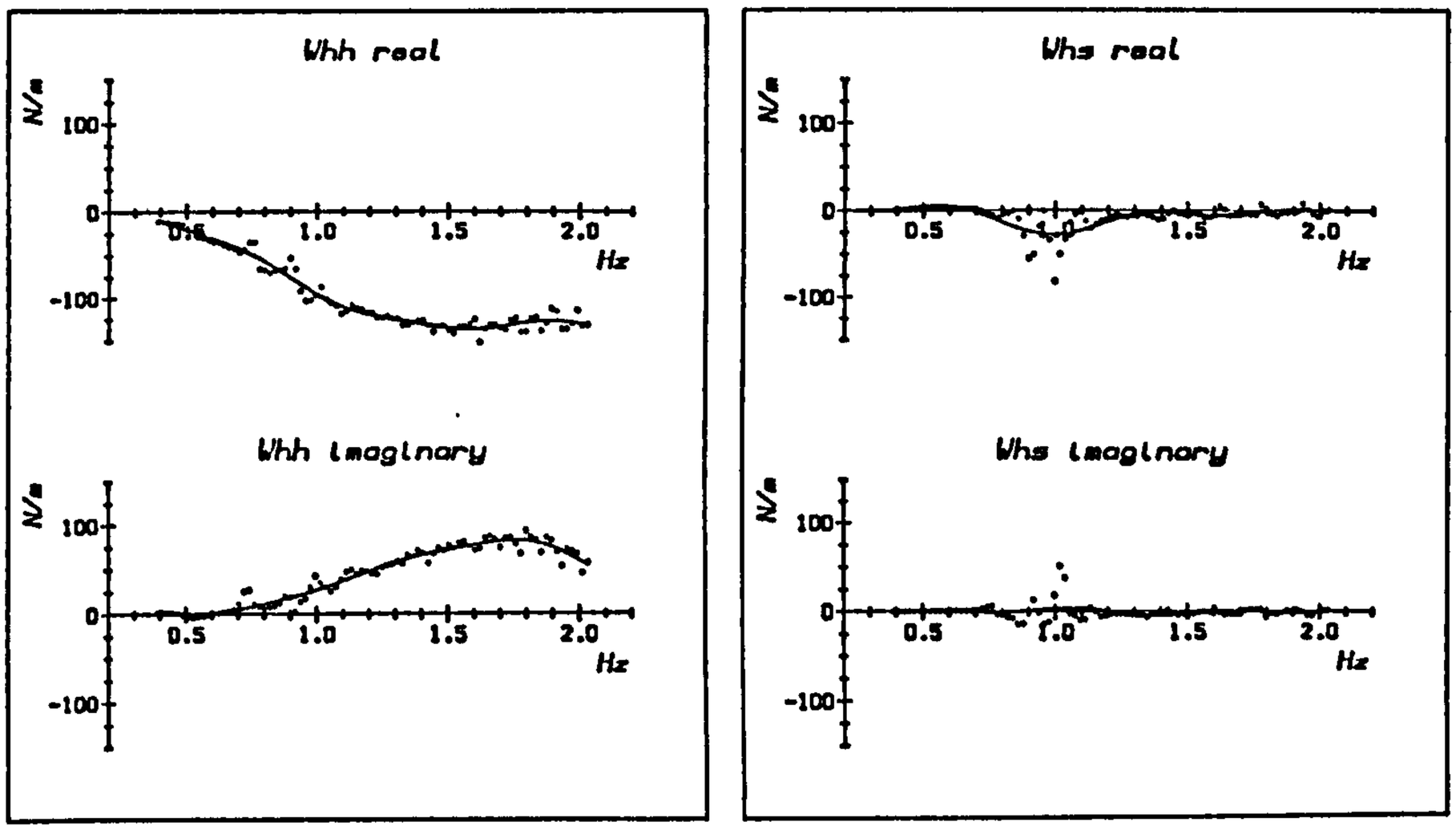

Figure 3.7

Impedance of 125mm diameter cylinder, freeboard +20mm.

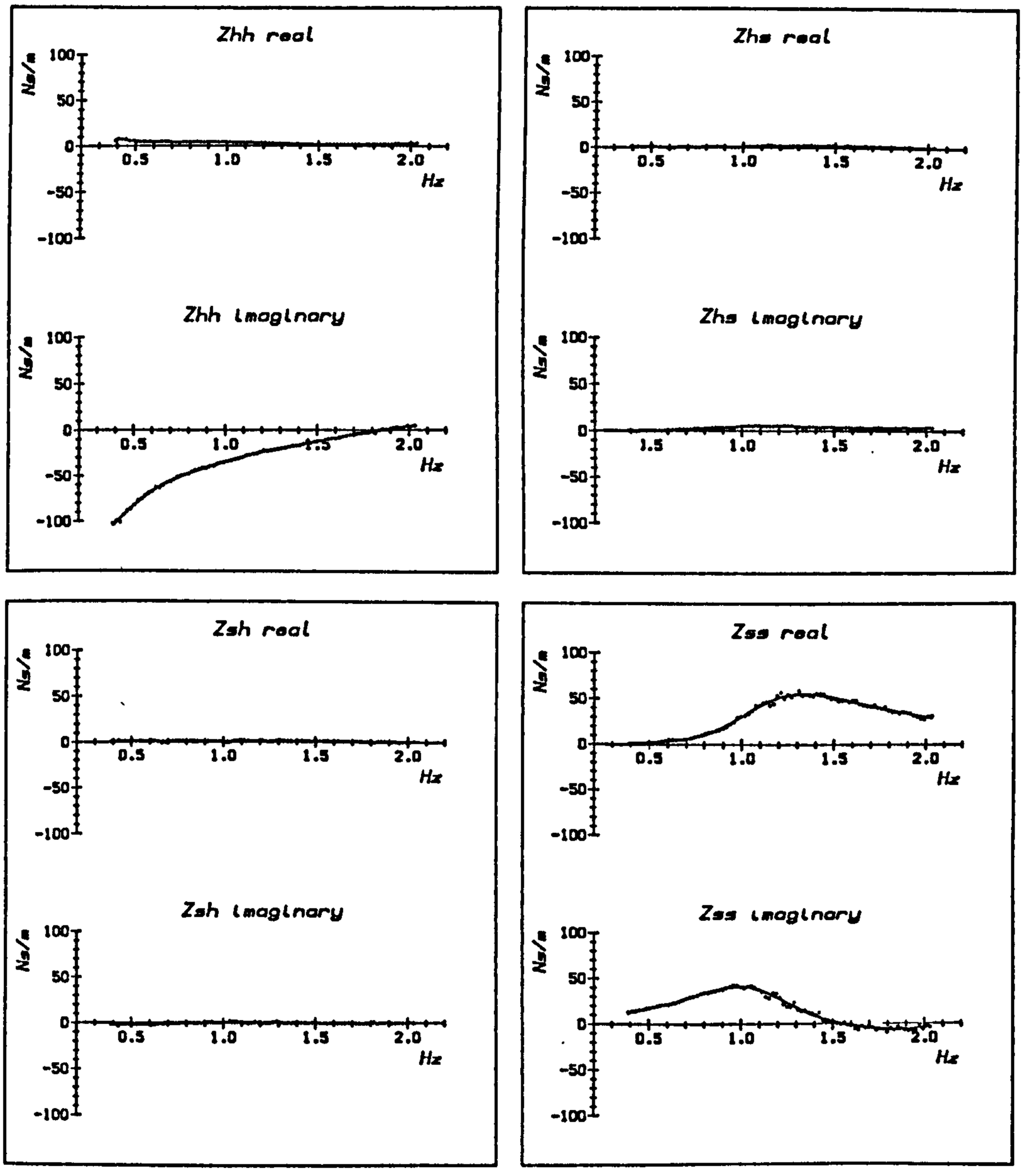

Figure 3.8
Wave force coefficient of 125mm diameter cylinder,
freeboard +20mm.

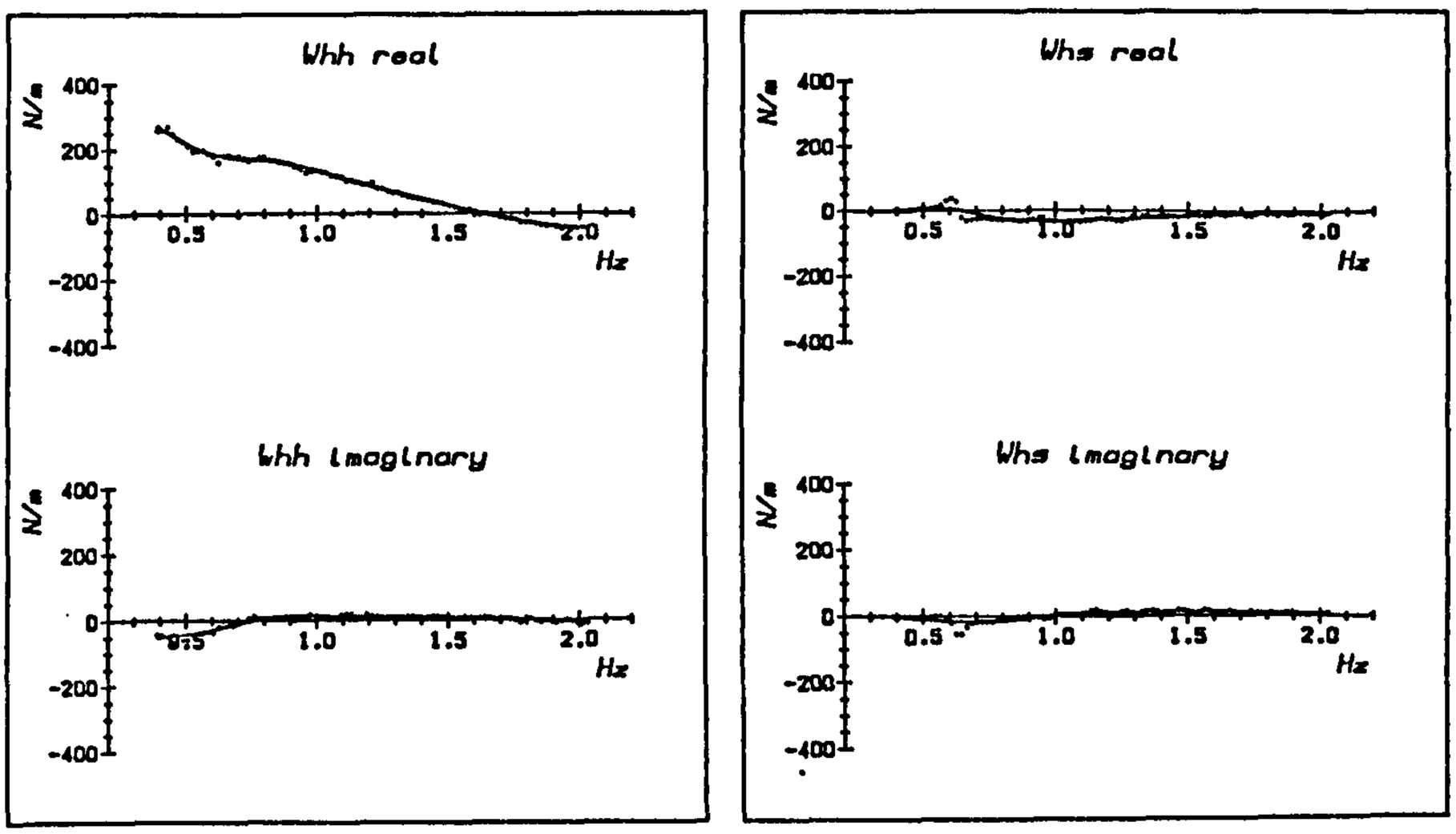

tension, which caused the water surface to run up the sides of the cylinder. Therefore the cylinder axis was set at the corresponding distance below the surface, so that the correct freeboard was attained. Freeboards were set by adjusting the offset of the torsion springs on the rig. In the case of the 125mm cylinder, additional counterbalance weights were set inside the rig.

The spring rates kept constant, and consequently the resonance due to the mass of the cylinder coupled to the spring varied with the cylinder size. The 100mm cylinder had a surge resonance of 0.6Hz and a heave resonance (when fully immersed) of 0.8Hz. For positive freeboard the additional spring due to buoyancy will raise the resonance. It is clear that all the cylinders have resonances in the frequency band used. However care was taken that in none of the experiments did the amplitude of cylinder motion exceed 20mm. Typically it was around 2–5mm.

The results are plotted in the four figures 3.9 to 3.12. Because the cross-terms are small they have not been plotted. The figures consist of 4 pages for W and Z in heave and surge, and on each are the 9 cylinder plots in real and imaginary. The effects due to the rig, and the pendulum effect due to non-neutral buoyancy have been subtracted from the impedance curves. Smoothed curves have been drawn through all the data.

Figures 3.9 and 3.10 show the impedance in heave and surge. The real part of the impedance, representing the extent to which energy is radiated away from the cylinder as it moves, of course never drops below zero. But the imaginary part, representing the added mass and spring, can be of either sign.

One effect of the variation of cylinder size can be seen most clearly for the -20mm freeboard case. As diameter increases, so does the overall size of the impedance curve; and the peak of the curve shifts to lower frequencies. A larger cylinder can make waves of larger amplitude; but diffraction effects reduce the efficiency with which shorter waves are produced.

The most dramatic effects on the graphs are those due to a change in freeboard. These seem out of all proportion to the freeboard range, which is less than a third of the largest cylinder diameter. In heave, there is only a slight change in the curves in going from -20 to 0mm freeboard—and then a profound one as soon as the top surface of the cylinder is clear of the water surface. At +20mm freeboard the real part of the impedance is very low, implying that

Figure 3.9

Heave impedances.

3 cylinder diameters; 3 freeboards

frequency 0.2–2.2Hz; impedance ±100Ns/m.

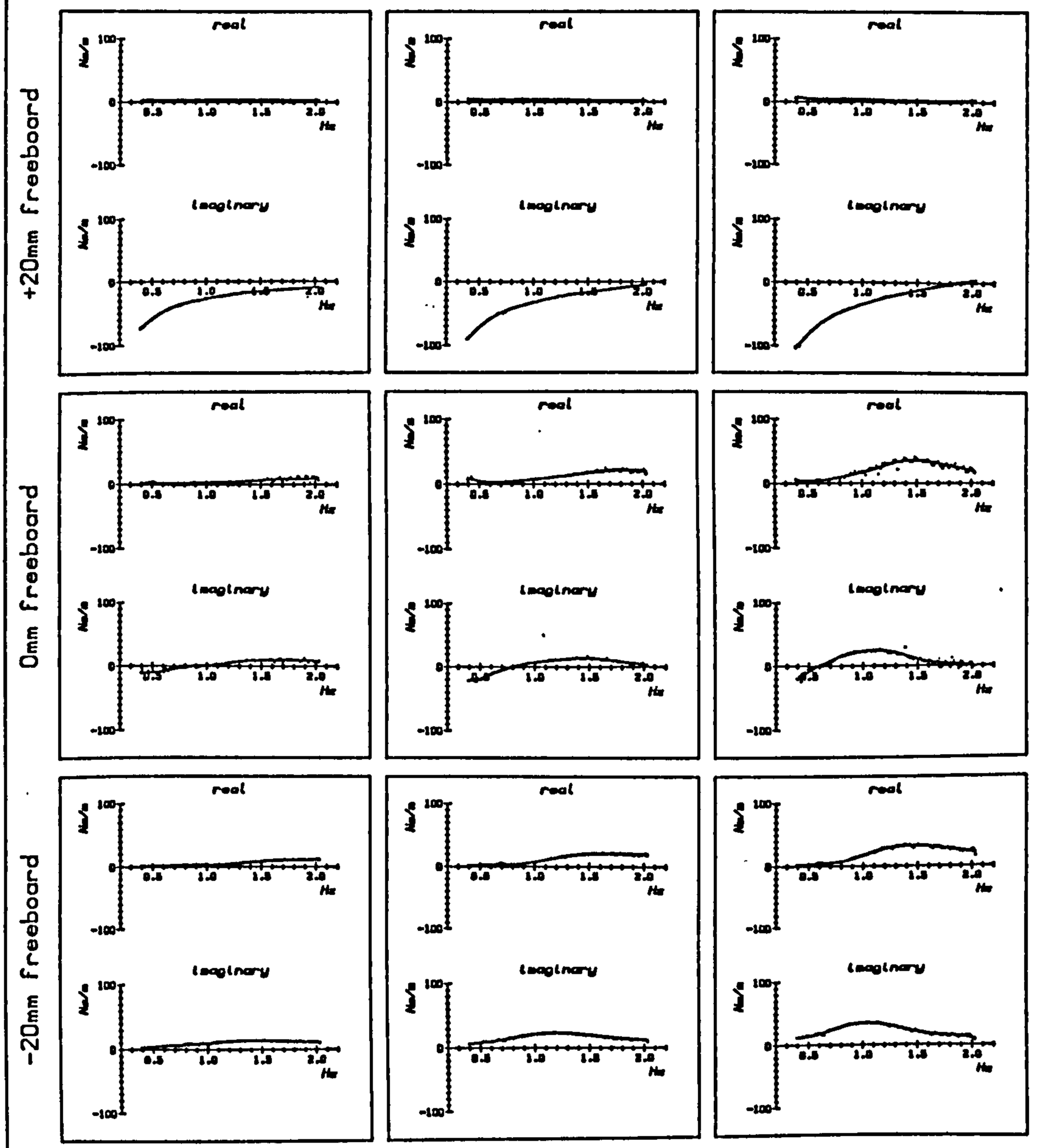

Figure 3.10

Surge impedances.

3 cylinder diameters; 3 freeboards

frequency 0.2–2.2Hz; impedance ±100Ns/m

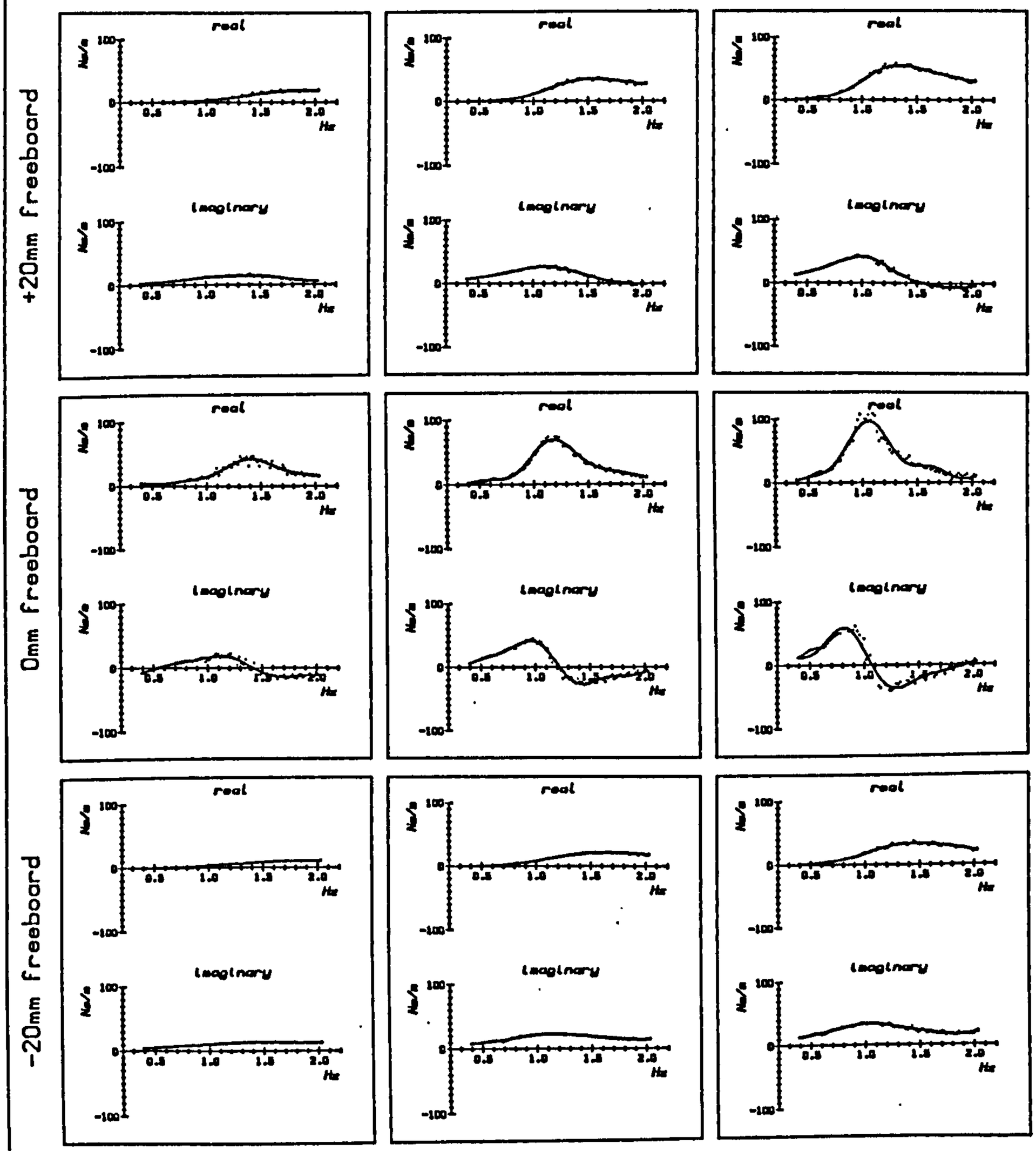

the cylinder is much less capable of radiating wave energy. The imaginary part demonstrates the effects of buoyancy. Since the freeboard is constant, an increase in cylinder diameter increases the waterline area, hence increasing the spring due to buoyancy. The curves therefore show a steady increase in negative spring with cylinder diameter.

In surge the results for the +20 and -20mm freeboard cases are not dissimilar. But at the surface, there is a large change in magnitude and in the *difference* between the real and imaginary curves with frequency, implying rapid changes in the phase of the impedance for the surface-grazing condition.

Similar observations can be made for the graphs of wave force coefficient in figures 3.11 and 3.12 . Again, the consequences of increase in cylinder diameter are well behaved and explicable. And with cylinder size the curves increase in size and shift to lower frequencies. At +20mm freeboard in heave, the effect of freeboard (which is to produce an upward force for an upward displacement of the water) increases with cylinder diameter and waterline area, and the slope of the curve increases. In surge the same dramatic features noted for the impedance curves reappear.

3.11 Synthesizing impedances and waveforce coefficients

The spine model, described in detail in chapter 4, is composed of segments predominantly of one diameter, but with short joining sections of reduced diameter. Ideally one would test a complete segment, but at 400mm they are too wide for the 2D tank. The alternative is to test cylinders of the same diameter and at the same freeboard as the various sections, and then combine the results to predict the hydrodynamic parameters for the spine. The spine segments are composed of three sections:

diameter	length	length fraction	freeboard	axis depth ratio
125 mm	293mm	0.733	+ 7.5 mm	0.88
110 mm	55mm	0.138	0.0 mm	1.00
88 mm	52mm	0.130	-11.0 mm	1.25

Figure 3.11

Heave wave force coefficients.

3 cylinder diameters; 3 freeboards

frequency 0.2–2.2Hz; force coefficient ±600N/m.

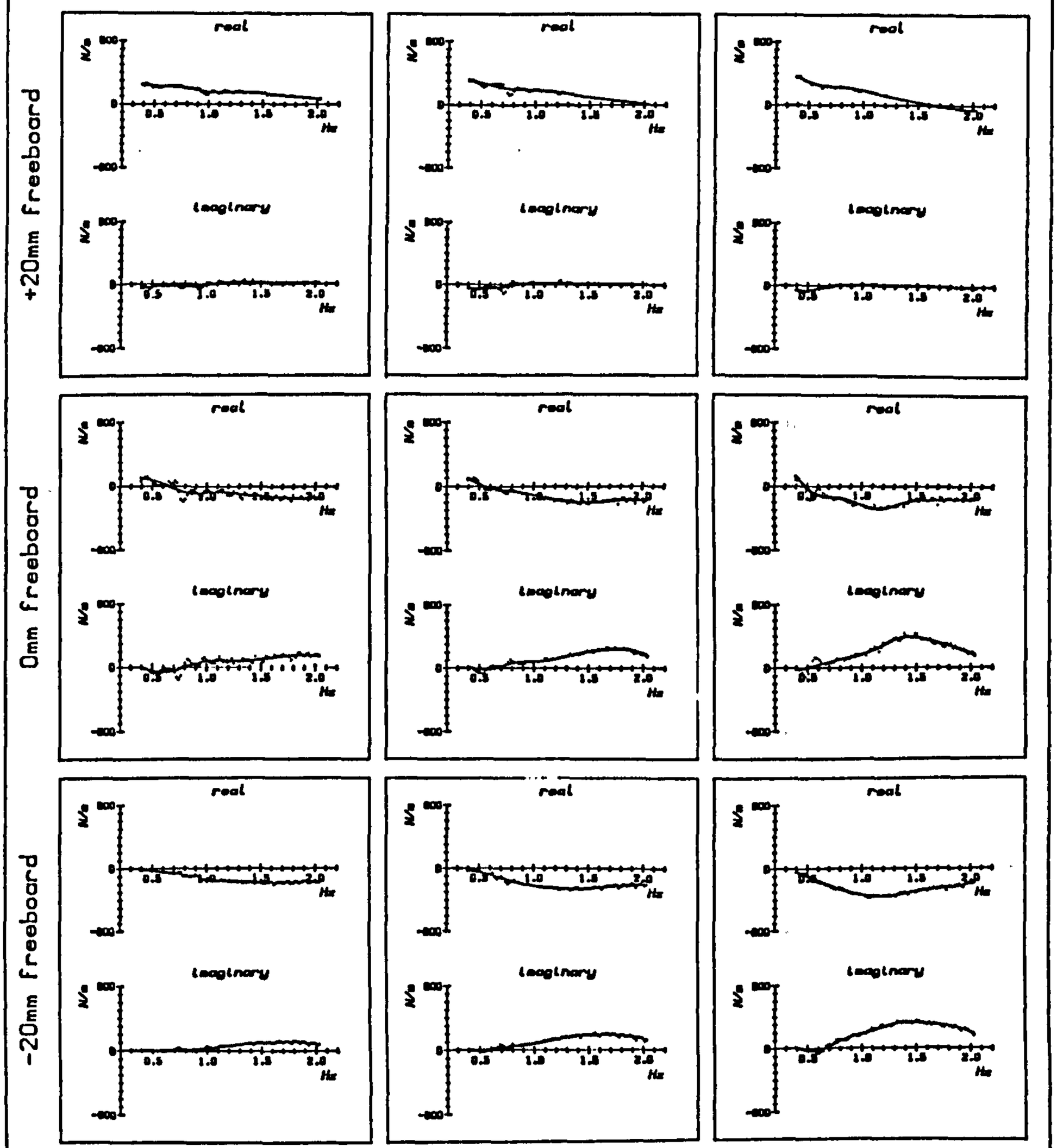

Figure 3.12

Surge wave force coefficients.

3 cylinder diameters; 3 freeboards

frequency 0.2–2.2Hz; force coefficient ±600N/m.

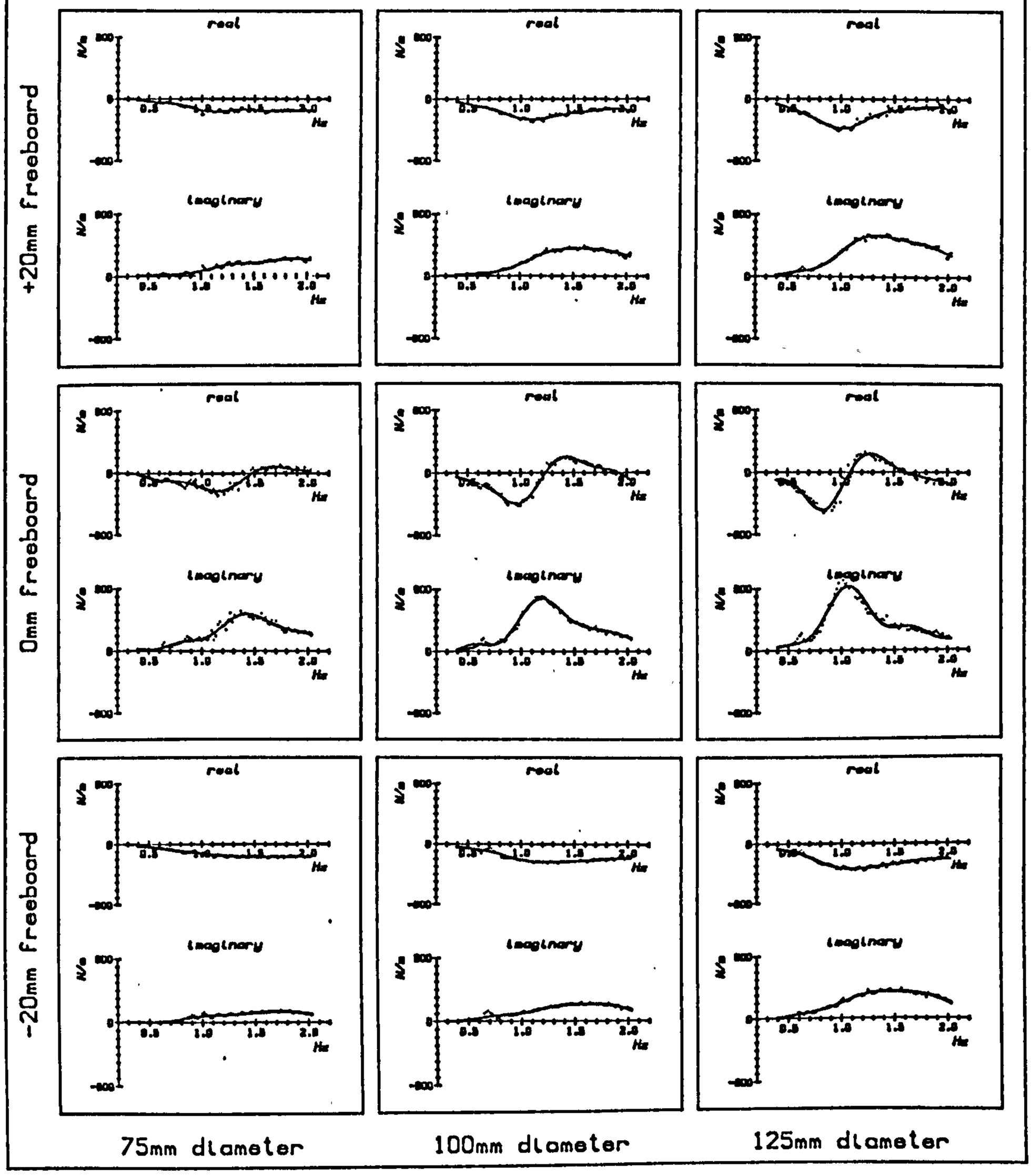

In the following experiments, the 125, 100, and 75mm diameter sections which were available, were tested at the above axis depth ratios. The axis *height* ratio, referred to the tank bottom, is about ten times greater, and so the effect of the tank bottom is negligible compared to that of the water surface. The results were rescaled, and used to generate a composite cylinder impedance and wave force coefficient.

The experimental parameters were otherwise the same as for the previous set of experiments. Only 5 experiments were necessary: a cylinder of the required 125mm diameter can be tested directly at an axis depth ratio of 0.88; for each of the other two axis depth ratios the two cylinder diameters which bracket the required cylinder diameter are tested. And since the axis depth ratio of 1.0 corresponds to the zero freeboard cases already tested, only three extra experiments needed doing.

The results are shown in figures 3.13 to 3.16. The three new experiments fall within the range of freeboard previously tested, and they show no unexpected features.

The results are then normalized in the following way. The impedances are divided by the product of the displaced mass of water and by the angular frequency:

$$Z_n = \frac{Z}{\rho V \omega} \tag{3.21}$$

The wave force coefficients are normalized by the product of the displaced mass of water and the square of the angular frequency:

$$W_n = \frac{W}{\rho V \omega^2} \tag{3.22}$$

These normalized quantities are plotted on the ordinate against a new abscissa kD, where k is the wavenumber corrected for depth (given by equation 1.12), and D is the cylinder diameter.

The goal is to calculate W and Z for intermediate values of cylinder diameter. Hence in the following graphs, sets of normalized data for the two diameters which bracket the required diameter are overplotted. Rather than overplot the data points which have already been recorded, simply the smoothed curves are

Figure 3.13

Heave impedances.

3 cylinder diameters; 3 axis depth ratios;

frequency 0.2–2.2Hz; impedance ±100Ns/m.

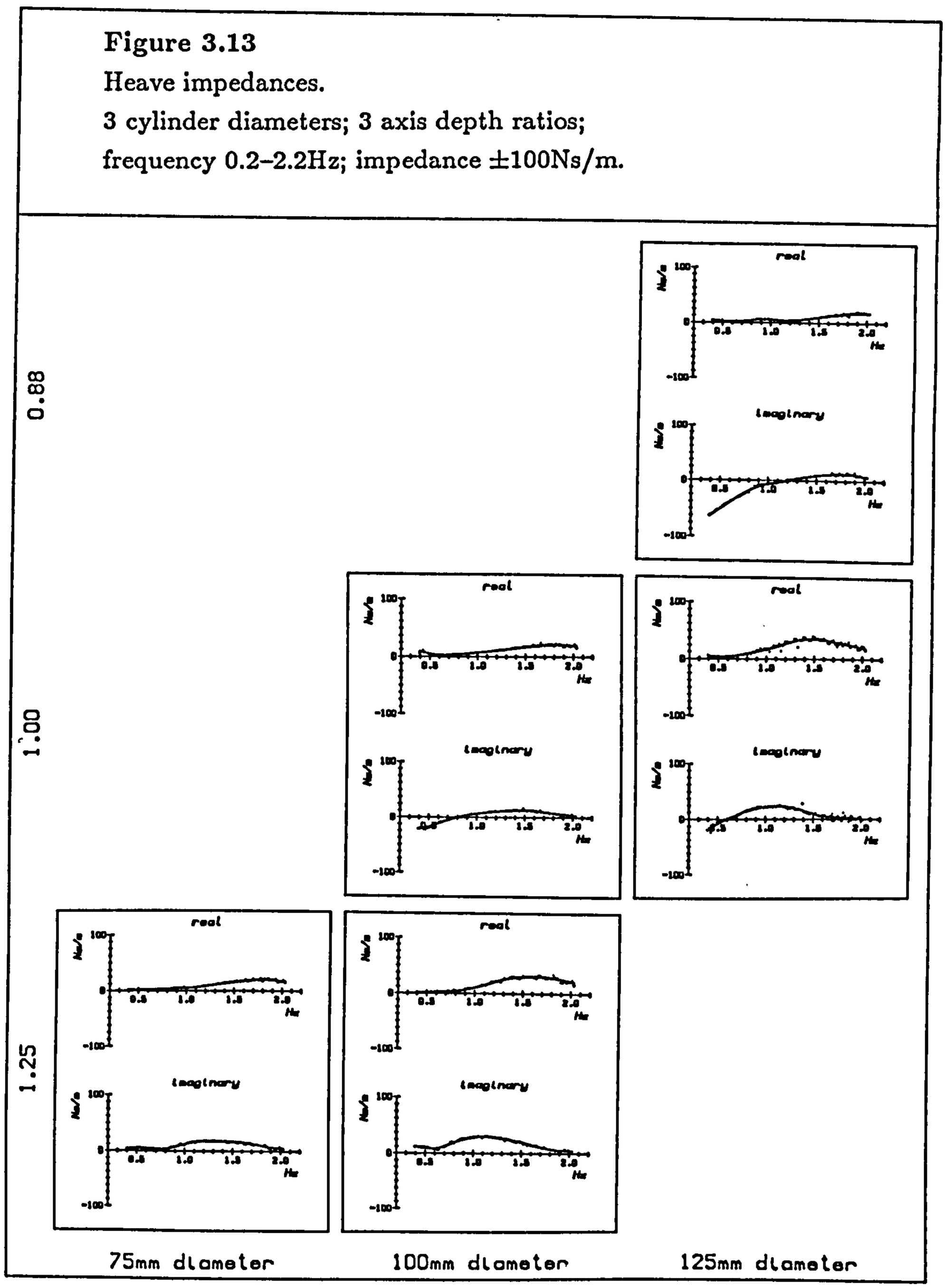

Figure 3.14

Surge impedances.

3 cylinder diameters; 3 axis depth ratios;

frequency 0.2–2.2Hz; impedance ±100Ns/m.

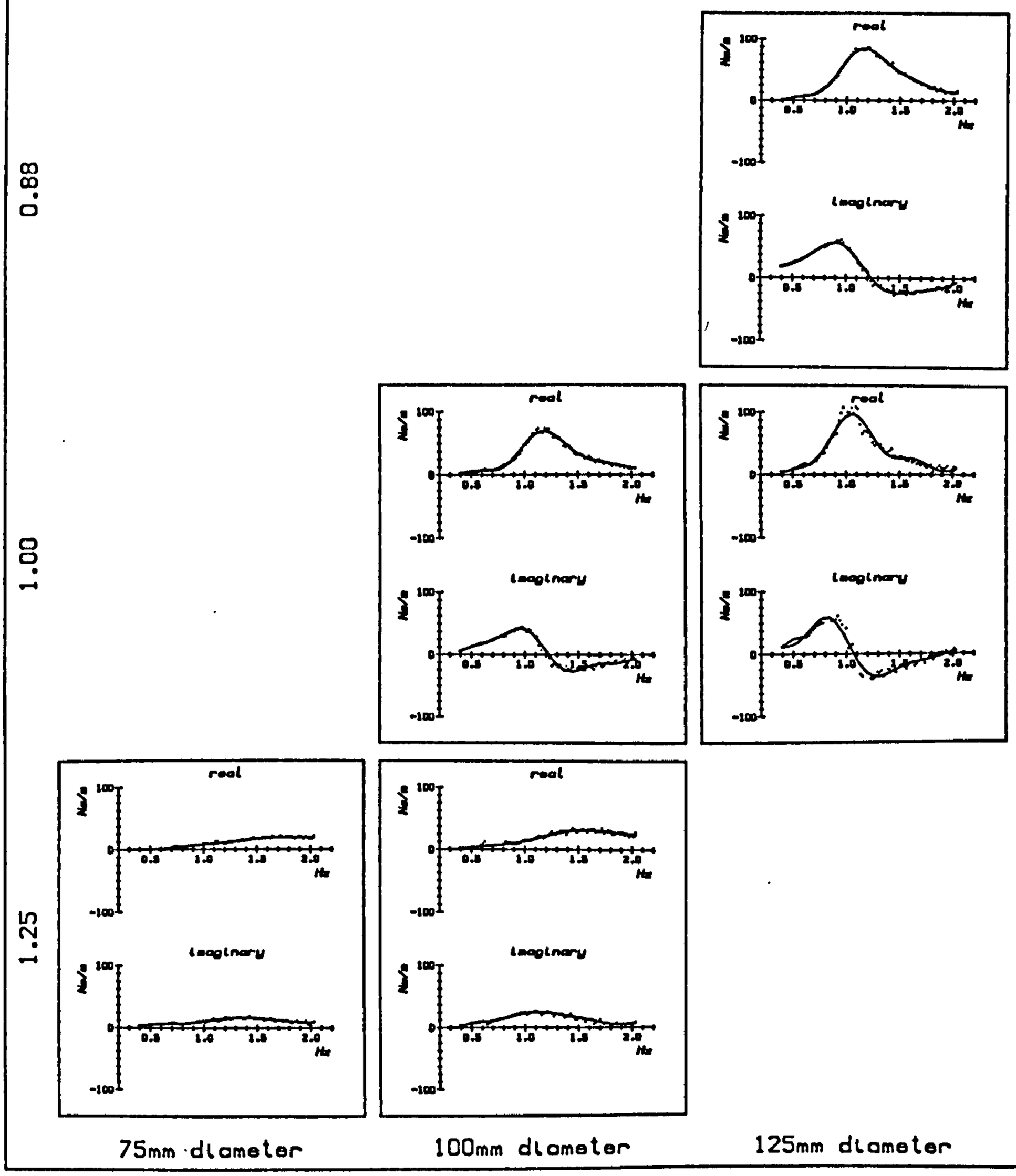

Figure 3.15

Heave wave force coefficients.

3 cylinder diameters; 3 axis depth ratios;

frequency 0.2–2.2Hz; force coefficient ±600N/m

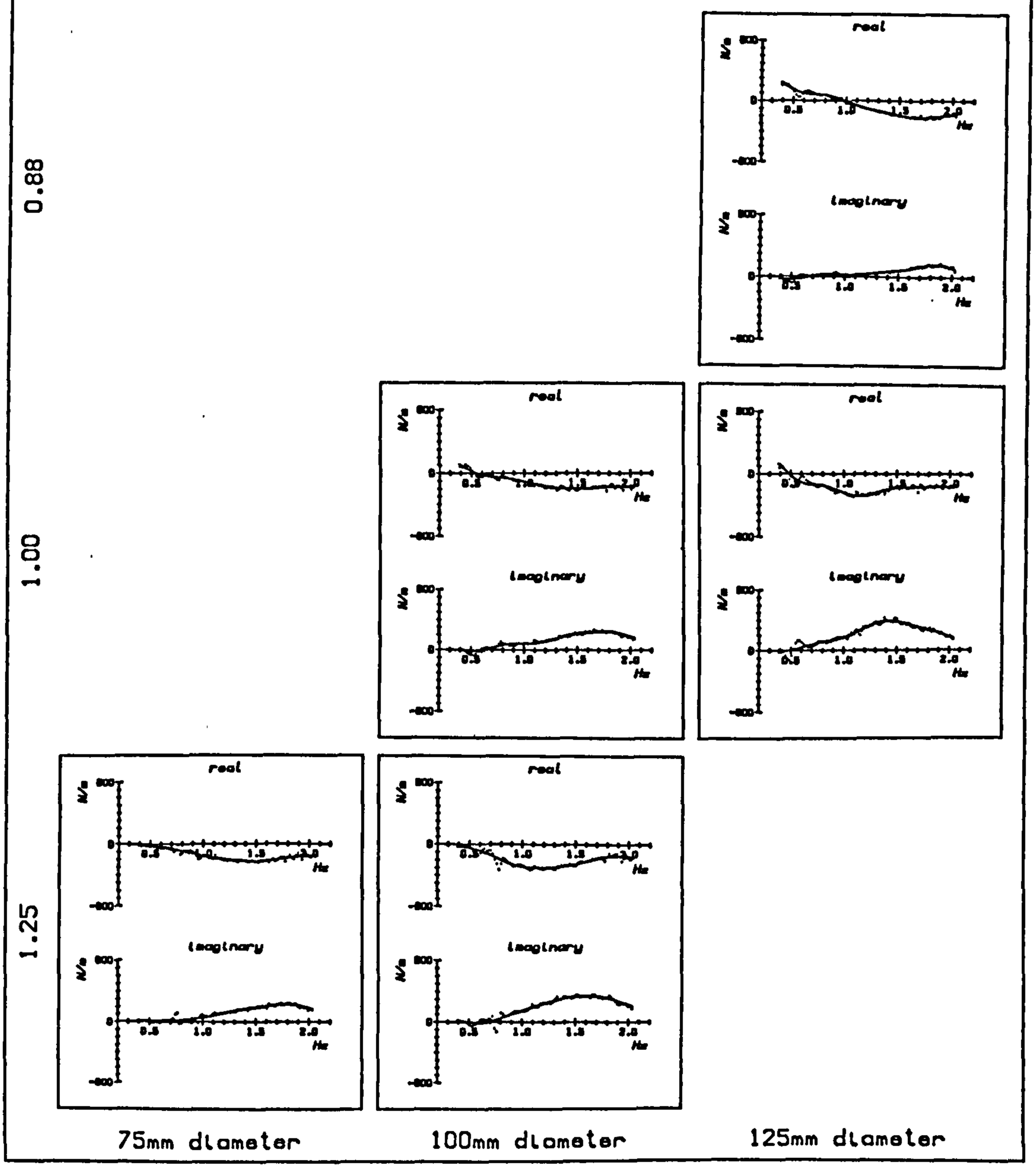

Figure 3.16

Surge wave force coefficients.

3 cylinder diameters; 3 axis depth ratios;

frequency 0.2–2.2Hz; force coefficient ±600N/m

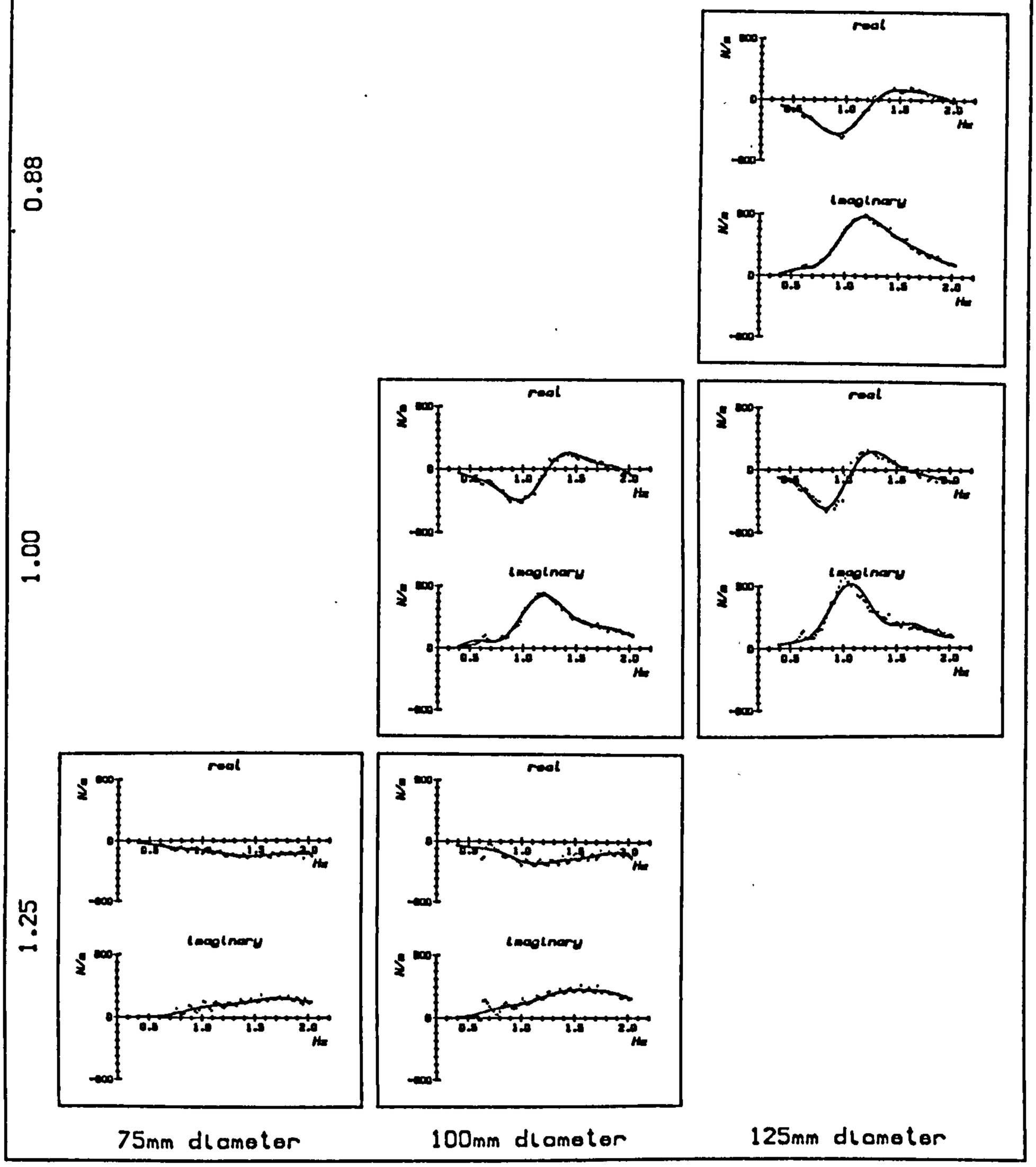

drawn, making the comparison of results easier to interpret. In each figure curves for heave and surge, real and imaginary are drawn.

Figures 3.17 and 3.18 show the results for impedance for two sets of cylinder sizes. The curves coincide very well in terms of peak position and height, and overall shape. The close fit suggests that interpolating from such non-dimensionalized graphs will be valid.

The results for the wave force coefficients is shown in figures 3.19 and 3.20. Again the graph features have scaled appropriately, and the overplots are very close. However, in some cases they are not as close as those in the impedance curves because the normalization divides by ω^2 which generates more extreme slopes which the curve smoothing algorithm handles less well.

Jefferys (1983), in a slightly different context, points out that interpolation of hydrodynamic complex quantities is better done in the magnitude/phase domain than in real/imaginary because the curvature of the graphs is less extreme. In this case however, the data are far less sparse than in Jefferys' case, and the calculations for the final part of this section were made without using a smoothing algorithm, and any error that may introduce.

In these four figures, the pairs of overplotted curves were averaged to a single curve (using not the smoothed curves but the normalized data) and these curves transformed to W and Z curves for 88mm and 110mm diameter cylinders by rescaling the dimensionless quantities as the reverse of the process above. These calculated quantities were then combined with the measured quantities for the 125mm diameter cylinder pro rata with length to yield values for the composite cylinder per metre of length. The results are shown in figures 3.21 to 3.24. These final quantities are used in the theoretical models of Chapters 5 and 6.

Figure 3.17

Normalized impedance against kD.

75mm and 100mm diameter cylinders; axis depth ratio 1.25.

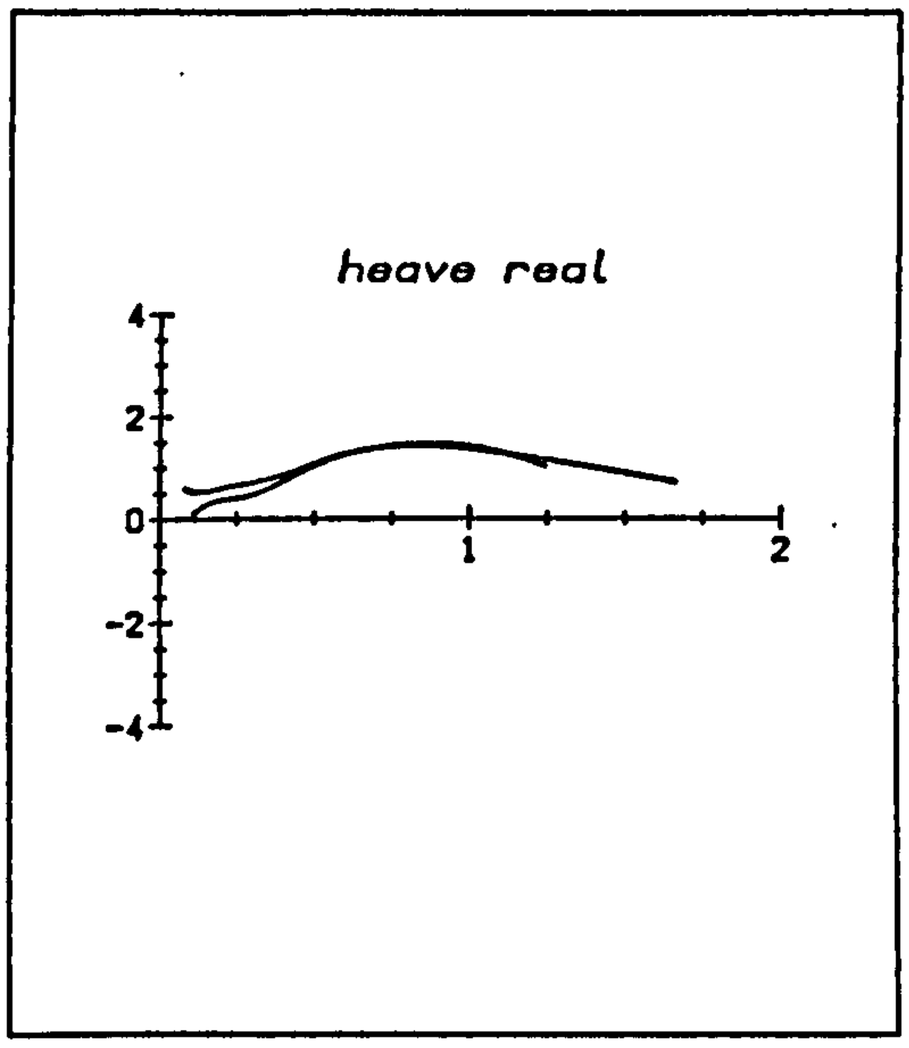

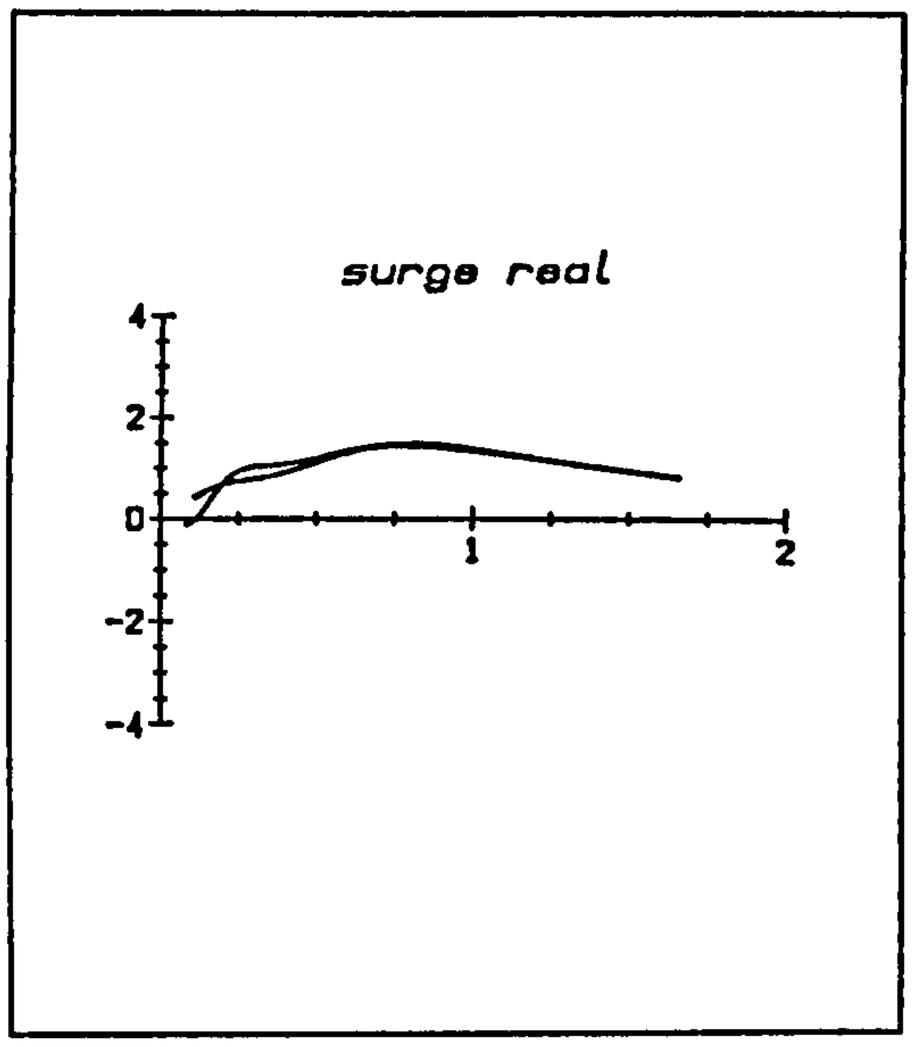

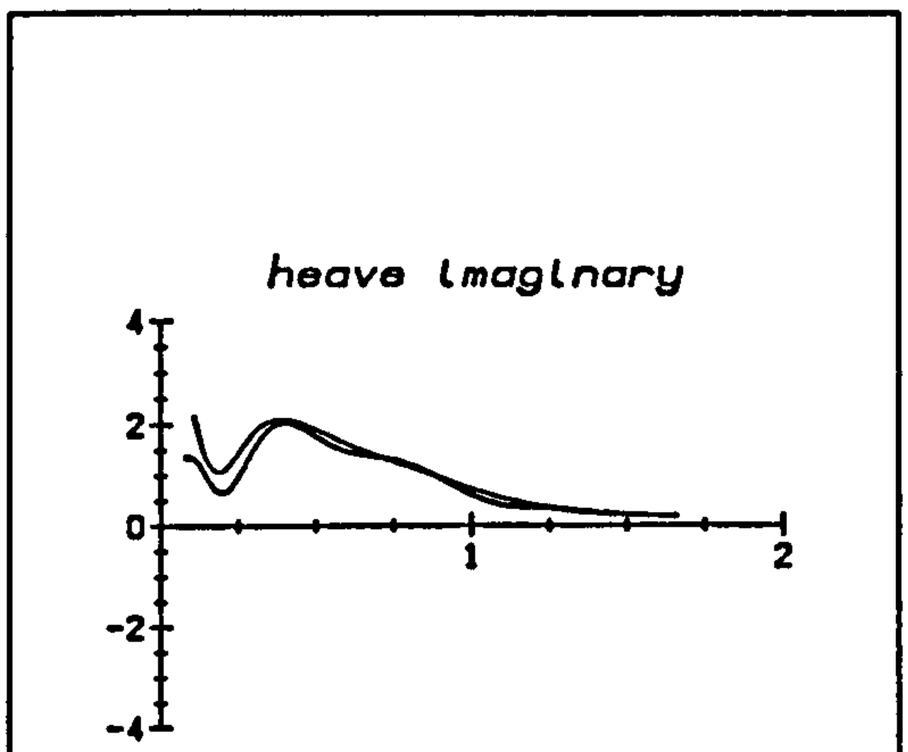

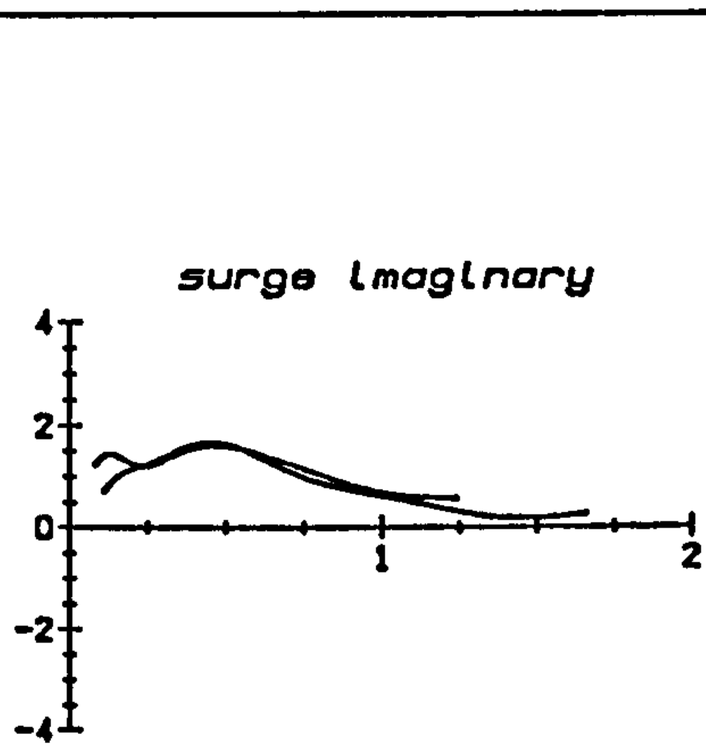

Figure 3.18

Normalized impedance against kD.

100mm and 125mm diameter cylinders; axis depth ratio 1.00

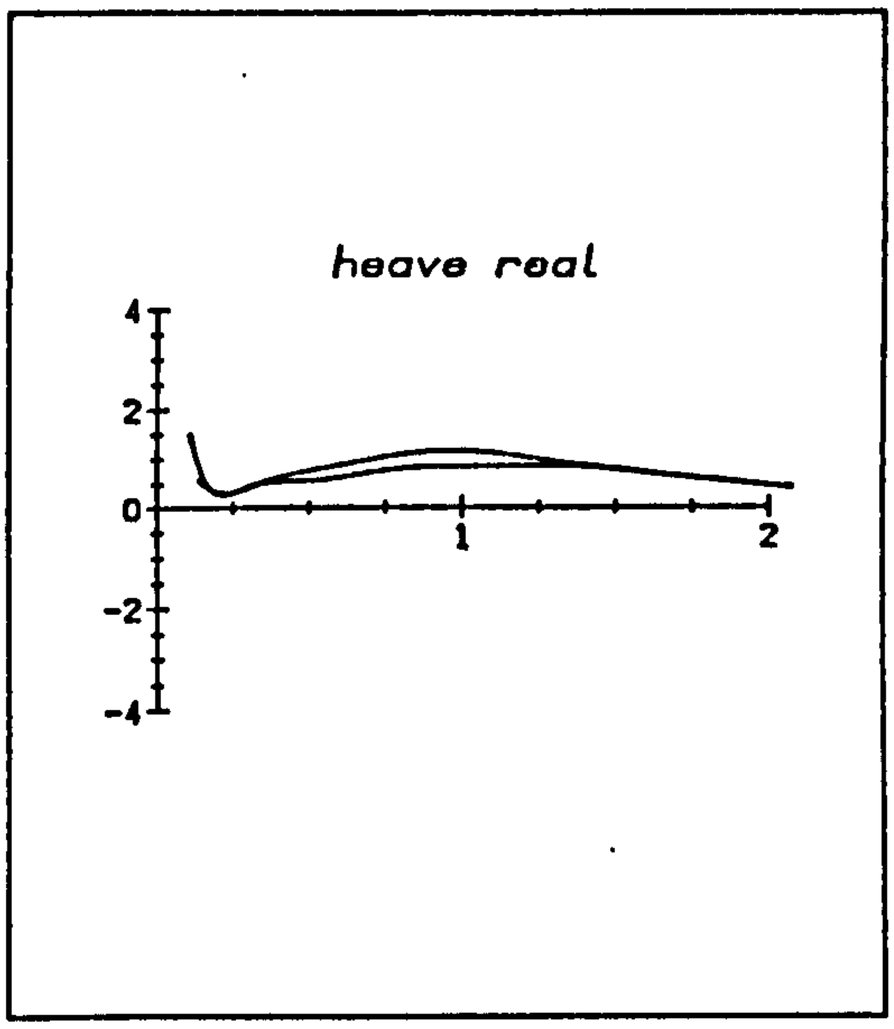

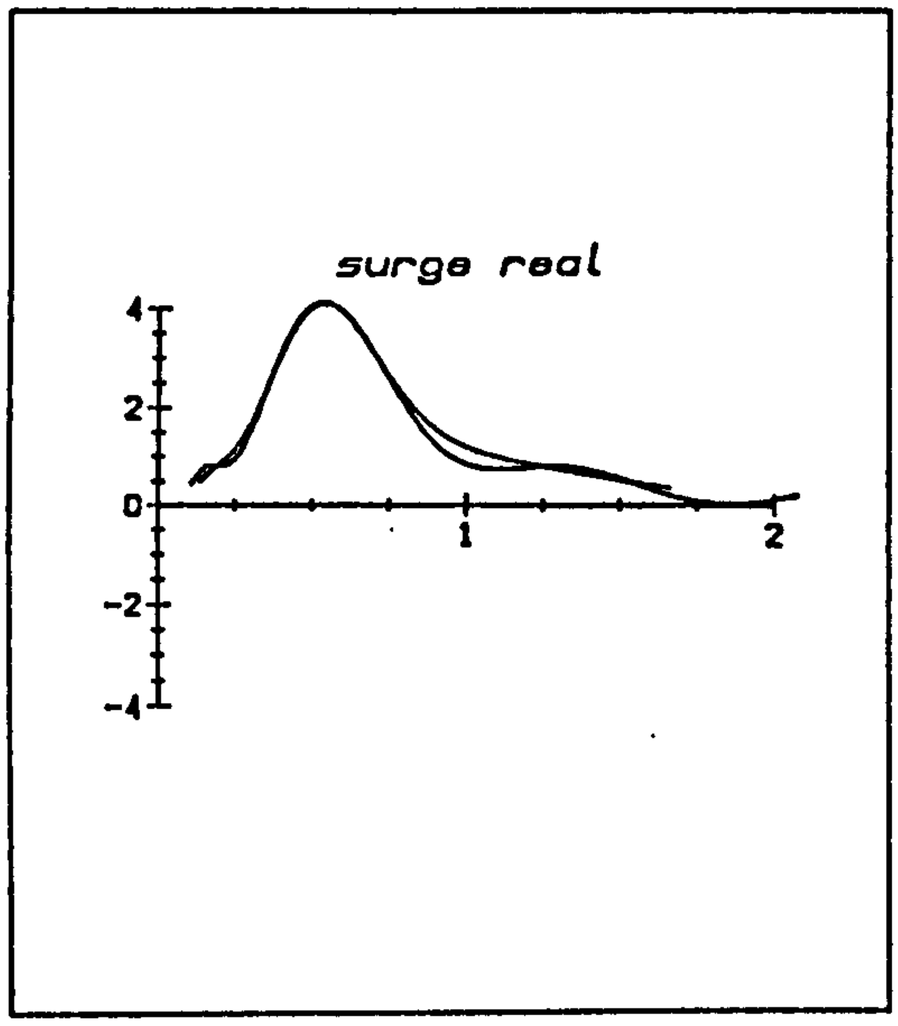

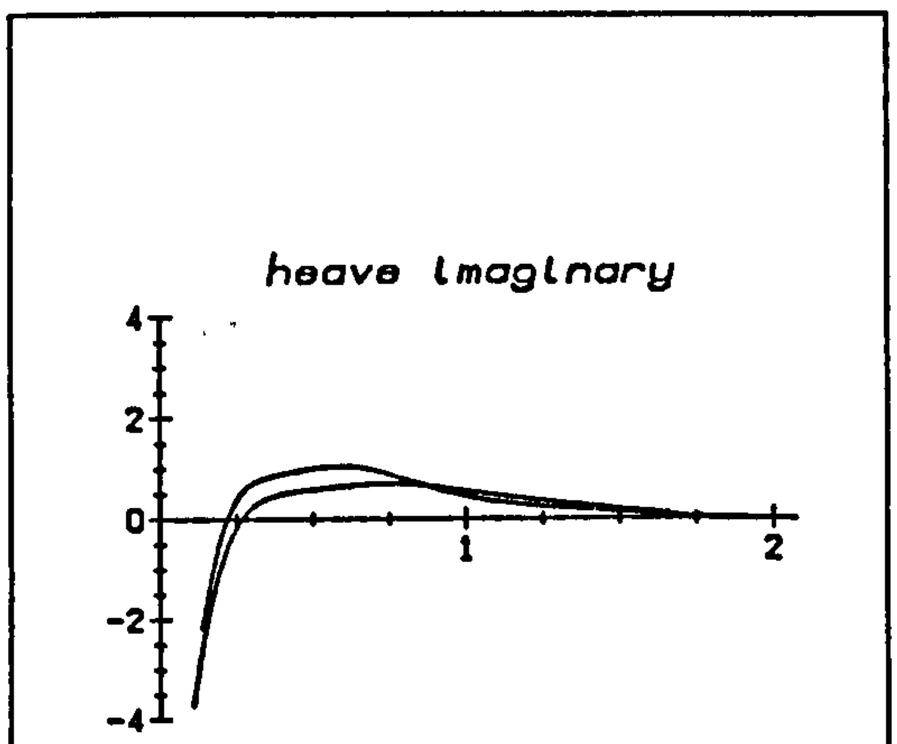

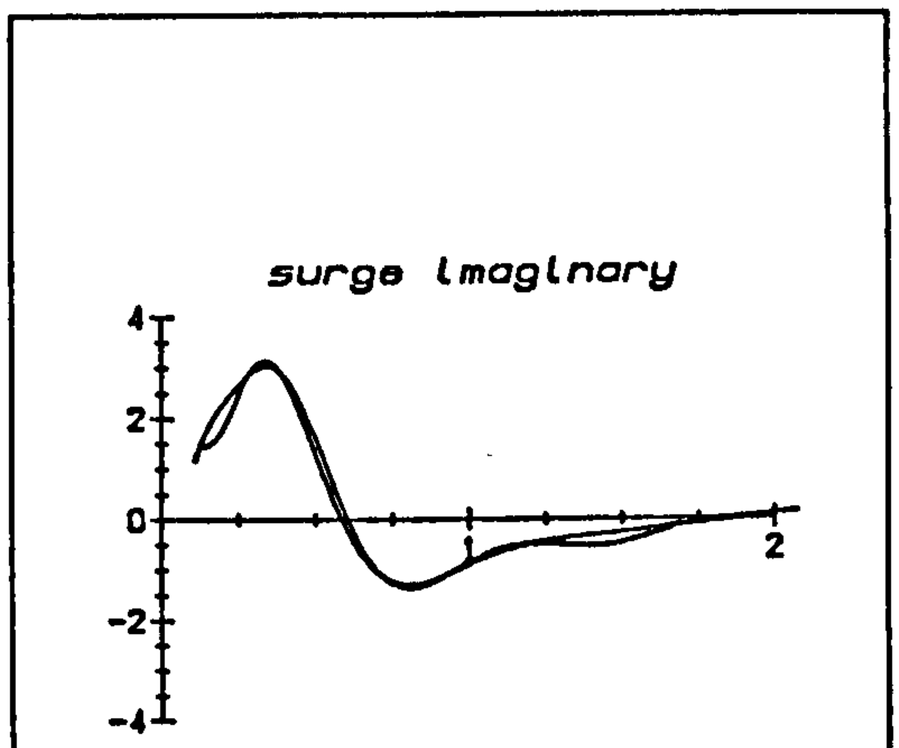

Figure 3.19

Normalized wave force coefficient against kD.

75mm and 100mm diameter cylinders; axis depth ratio 1.25

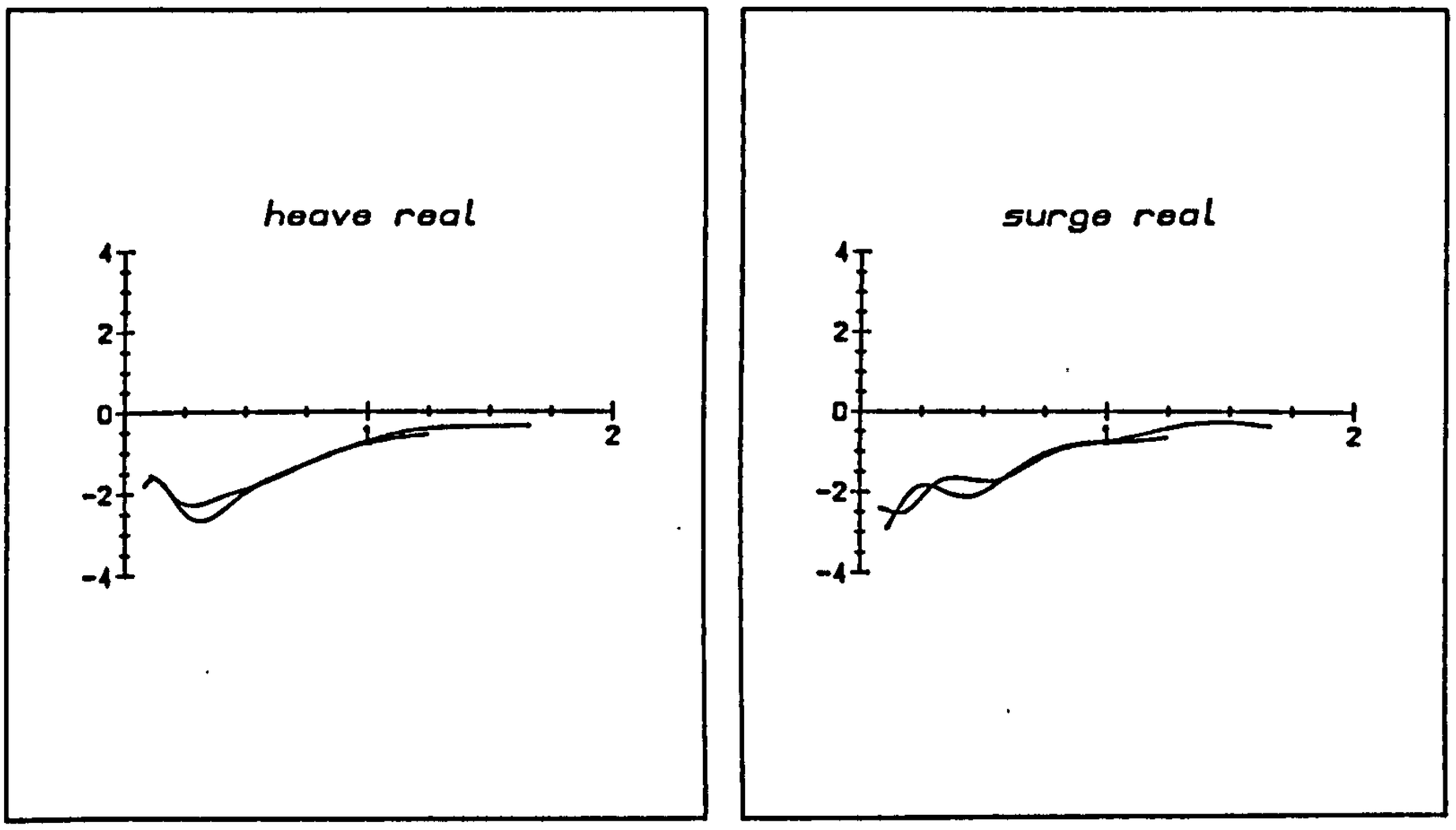

Figure 3.20

Normalized wave force coefficient against kD.

100mm and 125mm diameter cylinders; axis depth ratio 1.00

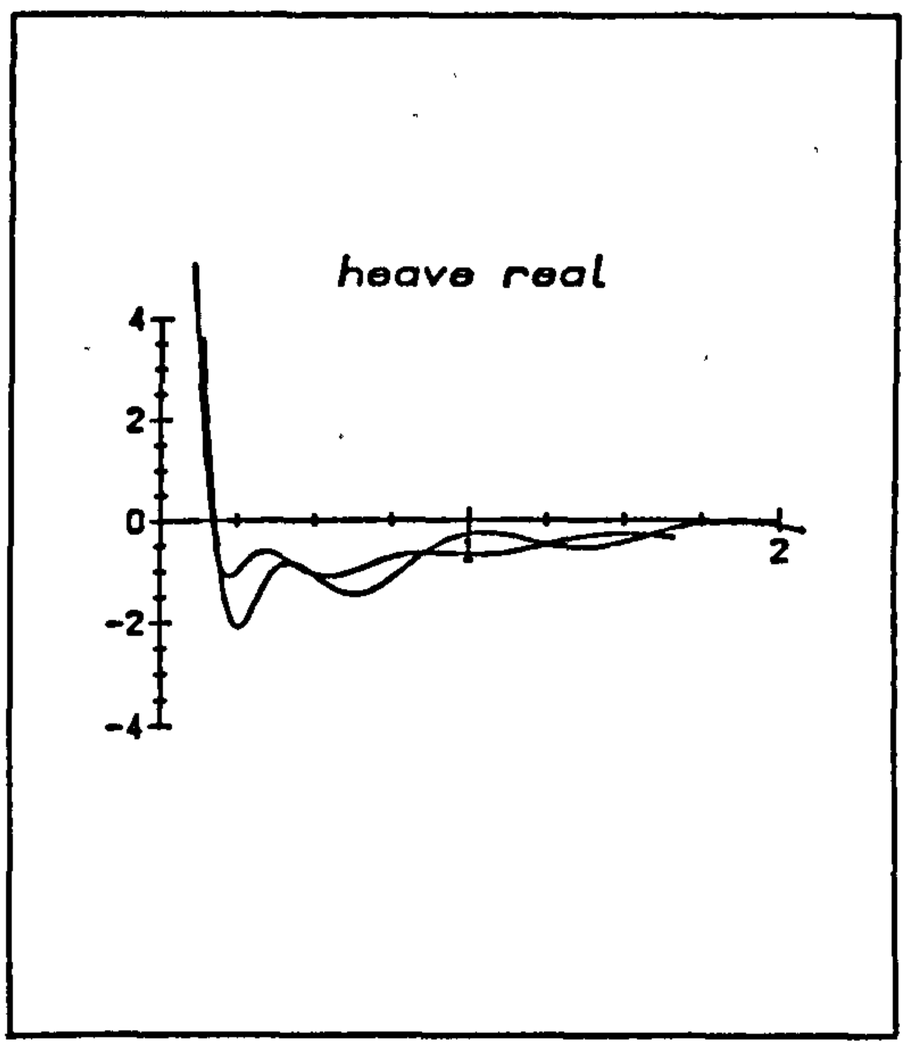

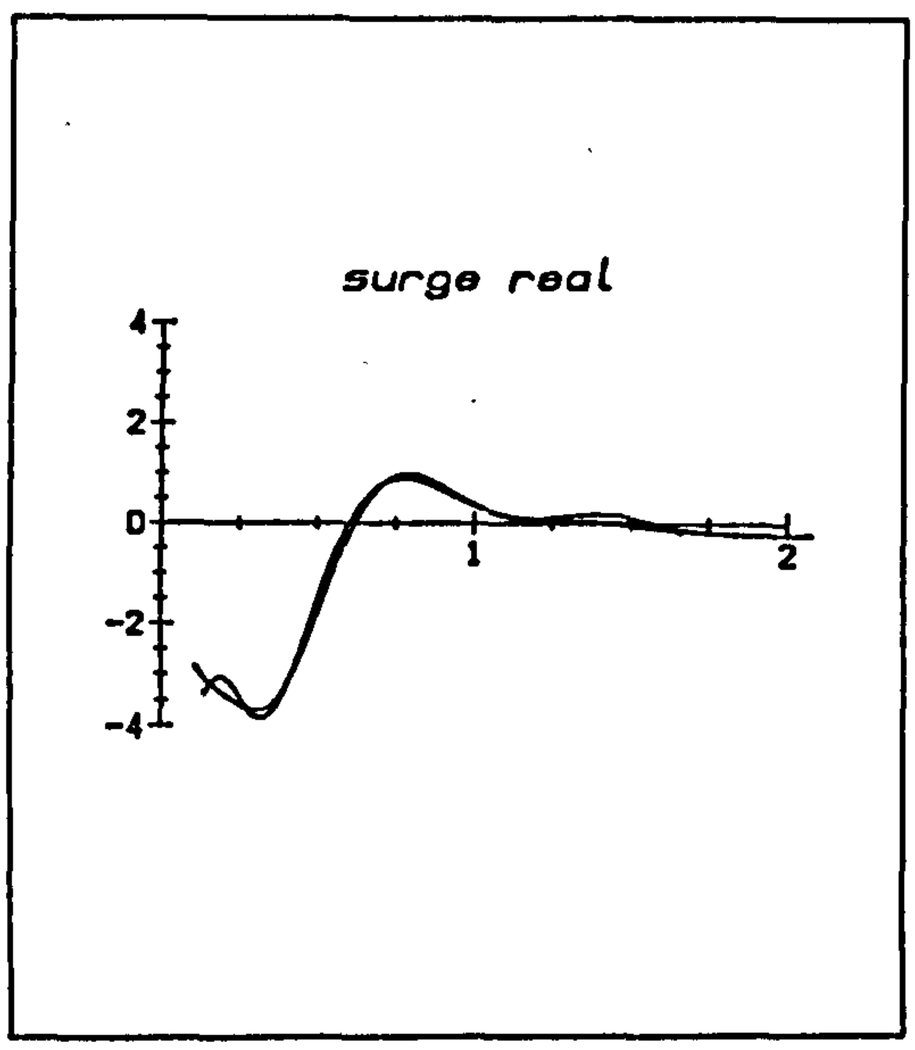

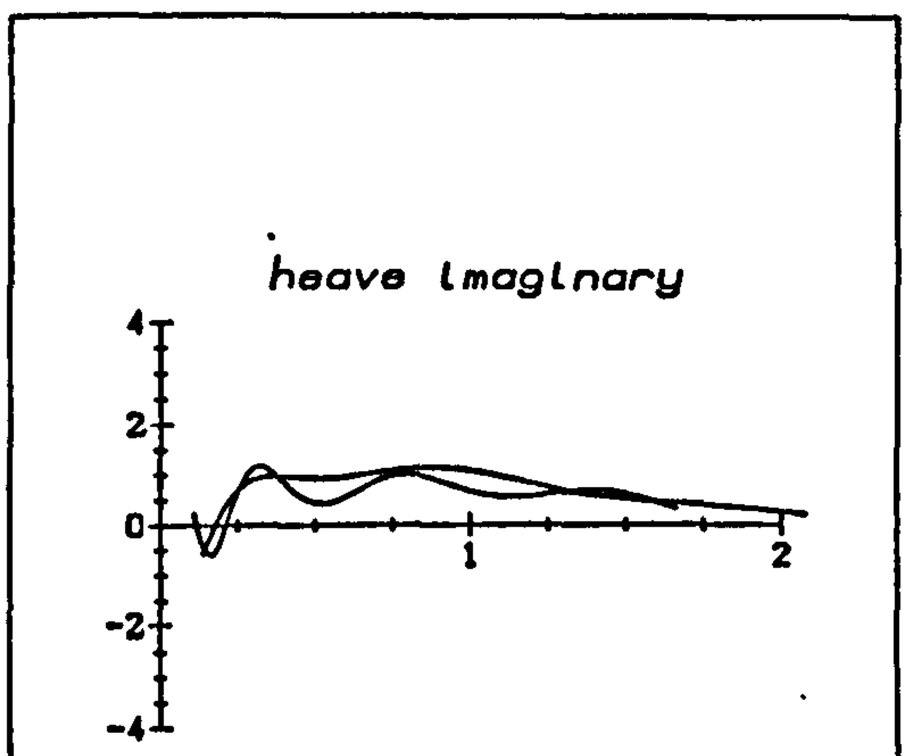

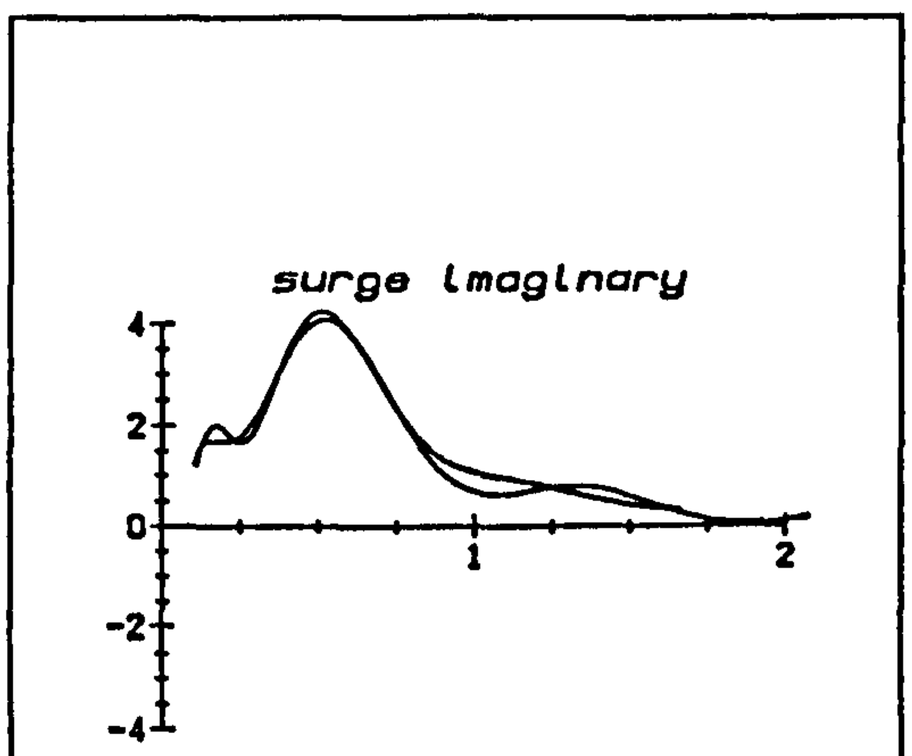

Figure 3.21
Heave impedance for:
the contributing cylinders, 295mm long;
the composite cylinder, 1000mm long.

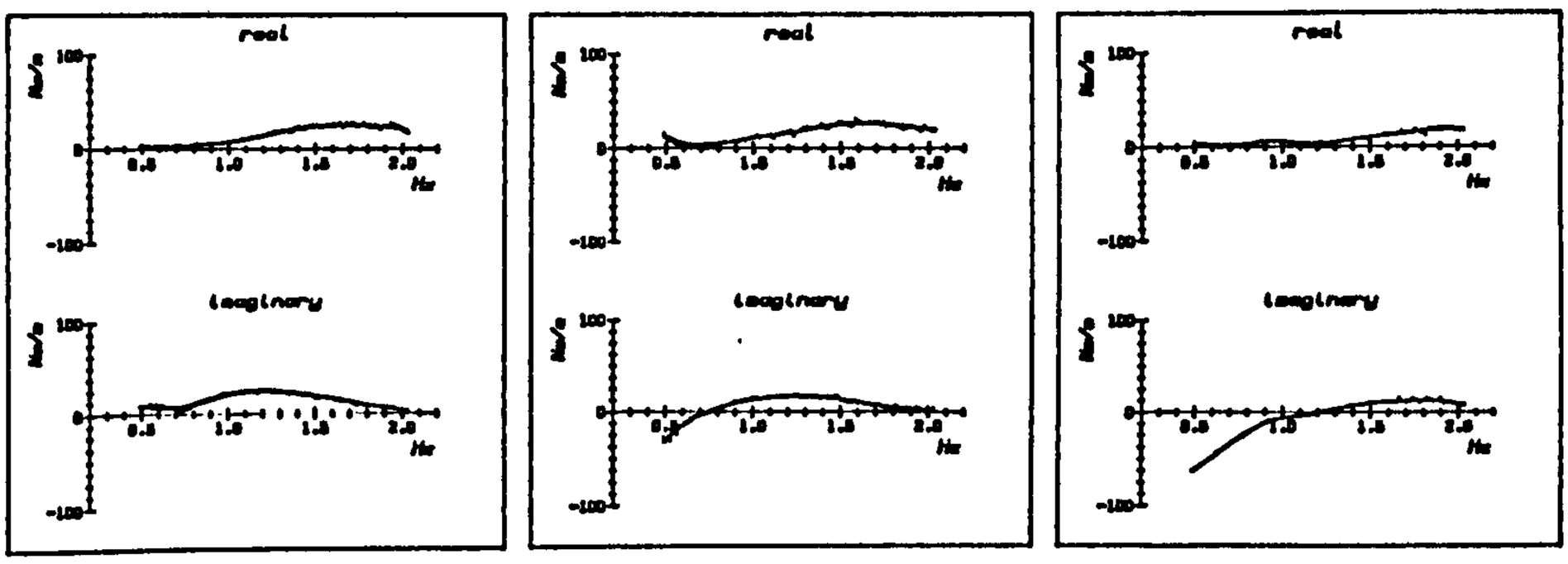

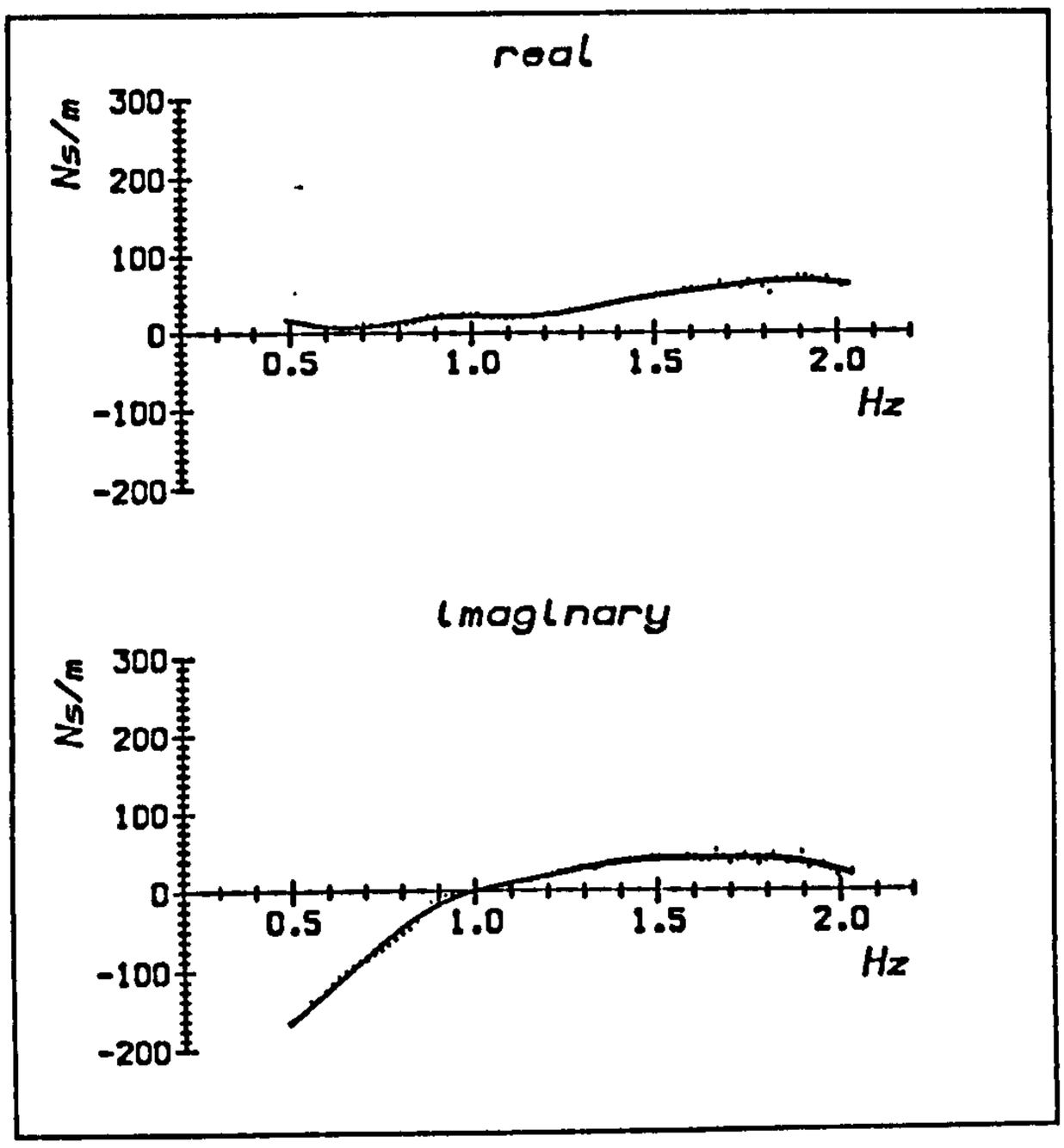

composite diameter

Figure 3.22

Surge impedance for:

the contributing cylinders, 295mm long;

the composite cylinder, 1000mm long.

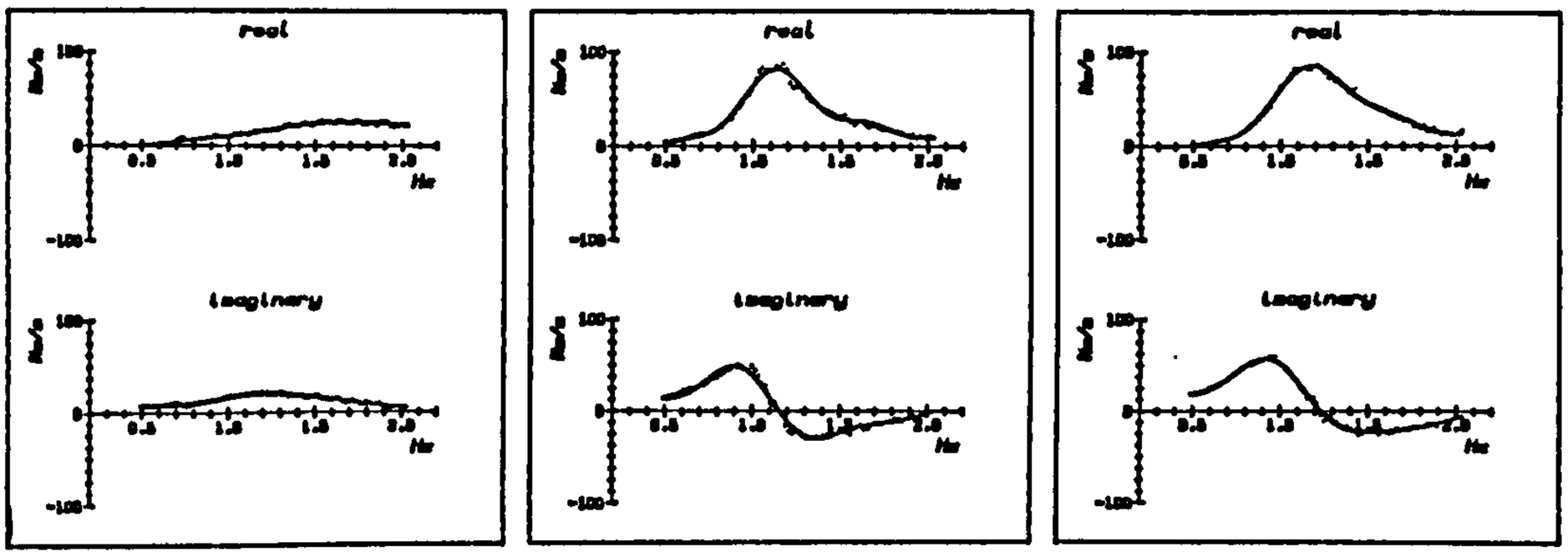

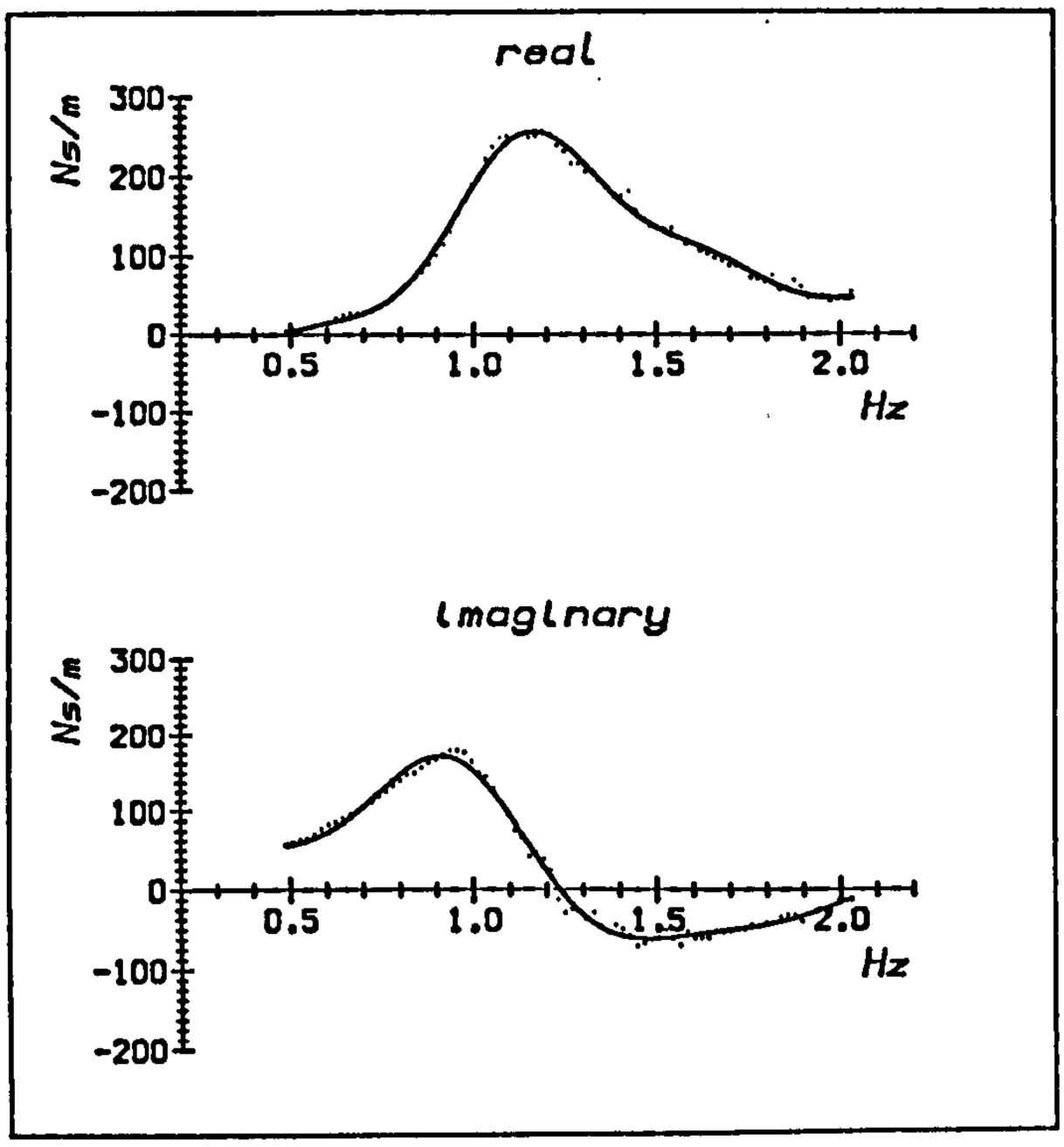

composite diameter

Figure 3.23
Heave wave force coefficient for:
the contributing cylinders, 295mm long;
the composite cylinder, 1000mm long.

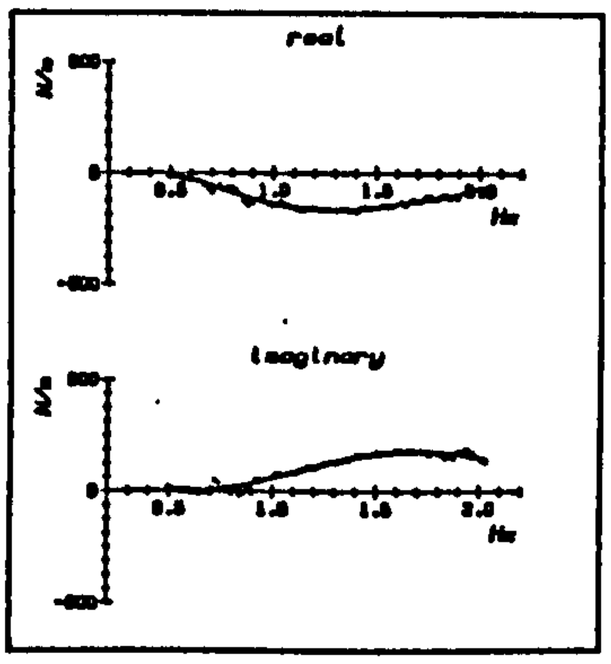

88mm diameter

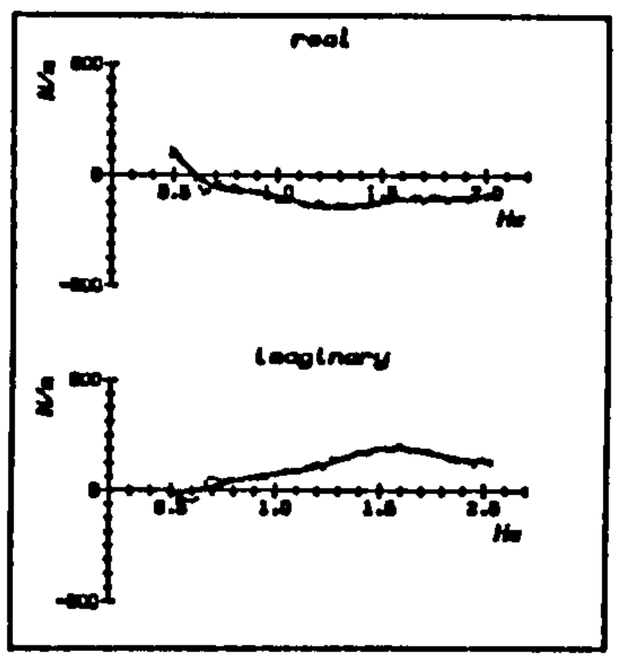

110mm diameter

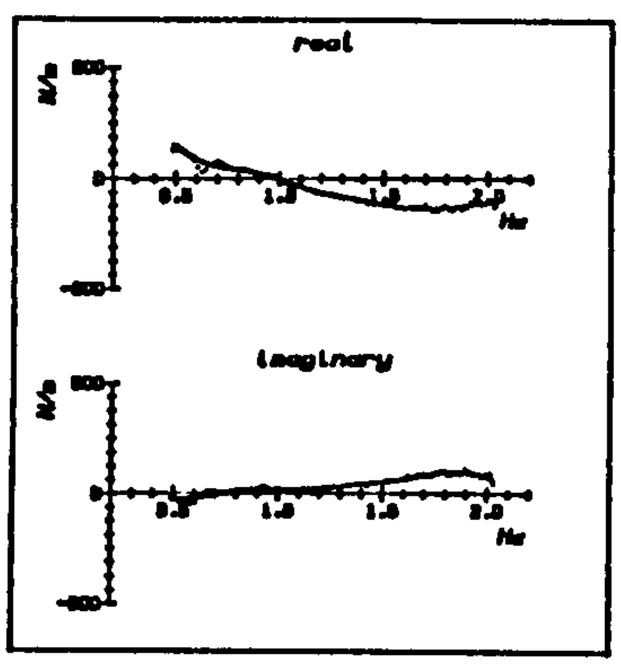

125mm diameter

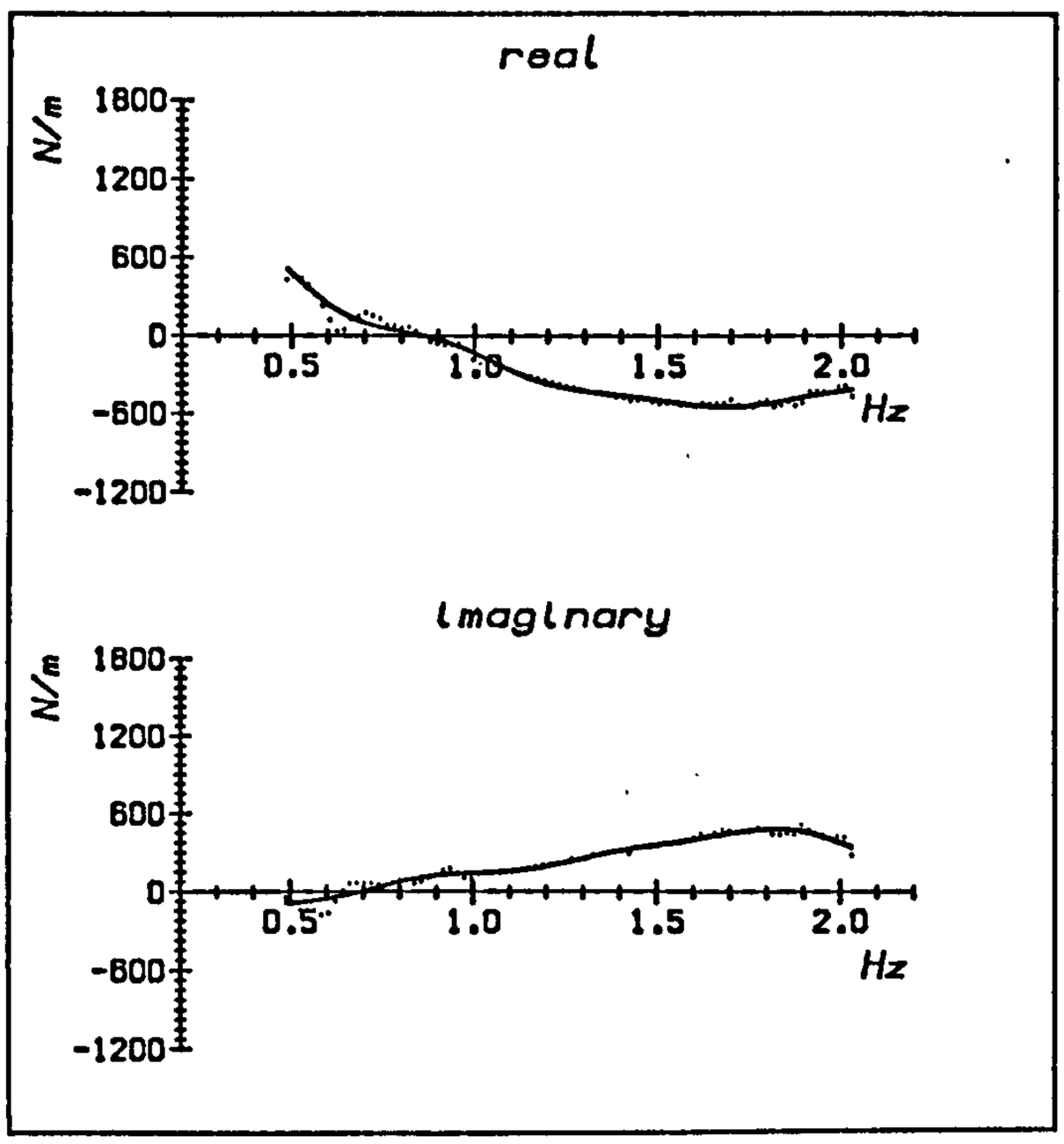

composite diameter

Figure 3.24
Surge wave force coefficient for:
the contributing cylinders, 295mm long;
the composite cylinder, 1000mm long.

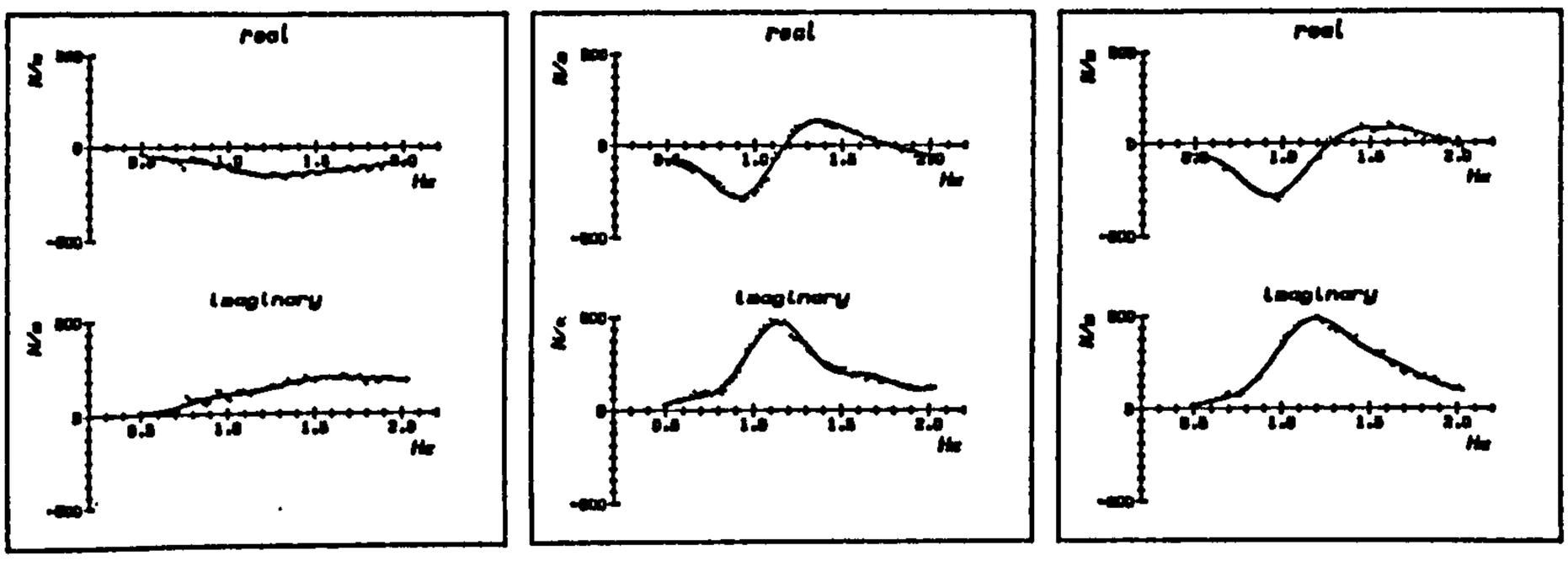

88mm diameter 110mm diameter 125mm diameter

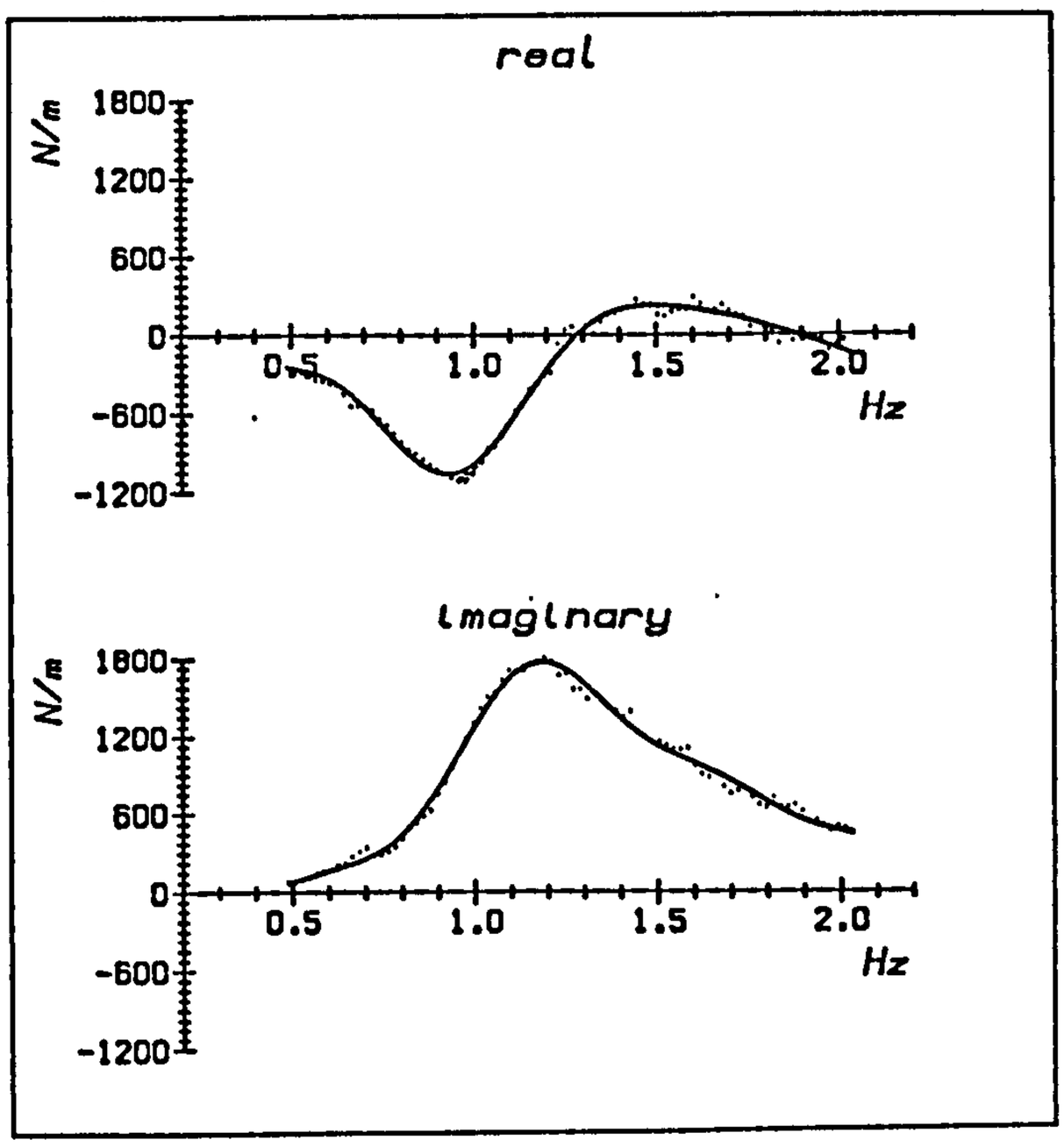

composite diameter

3.12 Conclusions

A force rig was used with a 2D wave tank to determine the hydrodynamic characteristics with frequency of a range of cylinder sizes at different freeboards. Care is required in specifying the geometry of the rig, and where possible removing effects due to it. The intrinsic impedance of the rig was measured, and subtracted from subsequent measurements on test cylinders.

1. The effect of wave reflections in the tank is very large, rendering data useless if left uncorrected.

2. Force and velocity data from the rig can be combined with extrapolated wave data in a matrix calculation which yields the wave force coefficient W, and the hydrodynamic impedance Z in a single operation which allows for the effect of tank reflections.

3. Crosstalk between axes is small at small amplitudes; some crosstalk appears in high amplitude conditions such as rig/cylinder resonance, implying a non-linear response.

4. The effect of the surface is large. It can alter the radiation impedance by a factor of 2, and introduces buoyancy forces comparable with inertial wave forces.

5. Over the range tested, W and Z obey the expected scaling laws. Their non-dimensionalized plots for different cylinder sizes can be superimposed with good agreement. It is therefore possible to construct with confidence equivalent curves for other sizes of cylinder.

Chapter 4

Measurements on cylinders in 3 dimensions

SUMMARY
The spine model is described, and its control, instrumentation and performance are discussed.
An experiment is carried out to determine the spine response in regular waves over a range of frequency and angle.

4.1 The spine model

Photograph 4.1 shows the model in the 3D tank in a 1 Hz, 20 degree wave. Bending of the spine in response to the wave is very obvious. In the lee of the spine, high frequency radiated waves are visible— these are partly due to the segmentation of the spine and the presence of sharp corners. Most of the spine length is made up of the dark 125 mm diameter segments. Between them are short lengths of reduced diameter which form the joints. These allow bending about one axis only and are therefore alternated to allow heave and surge bending. The joints do not permit shear.

A triangular section steel space-frame hangs from the roof on an electric hoist, one of whose four chains is visible. Nylon ropes drop from it to attachment rings on every second spine segment, and these take the weight of the spine when it is lifted out of the water. The space-frame also carries interface electronics for

the spine. On the right are 3 light-alloy busbars carrying a ±27 volt, 500 amp power supply from a transformer whose 3 phases are combined to provide a low ripple supply without the need for massive smoothing capacitors. The line of boards fixed on top of the busbars carry small capacitors for local decoupling, both for the spine and the circuit boards on the left of the frame. The latter multiplex signals to and from the spine into ribbon cables which connect via the sampling interface to the direct memory access boards on the PDP 11 computer. A group of 7 boards serves a 'gang of four' spine segments. In the picture a downlead, composed of a wound group of signal and power cables sheathed in silicone rubber can be seen descending to each gang of four. Each segment in a gang of four is daisy-chained to the next with a similar cable. The plug and socket at each joint is protected with a silicone rubber sleeve packed with silicone grease. All the spine segments are identical; any one can replace any other simply by rotating to provide the correct heave or surge orientation. Segments have an individual serial number stuck on them so that the history of their faults and performance can be recorded, but when connected in the spine are identified by their position. Likewise, the multiplex boards are identical in hardware, and in use, are differentiated by the setting of their address switches, which allow access to any channel within any spine segment.

The spine mooring is a float and sinker arrangement providing a low-rate spring. Some floats are visible on the waveward side of the spine. The arrangement finally used in the experiments had floats and sinkers 3 times smaller in displacement and spaced 4 times less frequently than in the photograph. They were also set lower in the water to incur less wave loading. During experiments the space-frame was lowered until the support cords were slack, then moved slightly back to minimise the interference of the cable on the motion of the spine. A quick test in which the frame was moved first fore then aft of the spine showed that the extra force due to the presence of the cords and cables is about a fifth of that due to the whole mooring assembly. The spine mooring is described in more detail in section 4.6.

Beneath the walkway at the left of the picture are the metal mesh beaches. The experimental area of the tank is 5 metres wide and 25 metres long marked off at 1 metre intervals; the markings are just visible through the water. The wavemakers are 2 metres beyond the walkway on the right.

Photograph 4.2 shows a spine segment with its outer tube removed. The following description proceeds from the left of the photo to the right.

At the extreme left is a gimbal ring which can pivot in the ball-bearings mounted in the bulkhead. It contains two finger clamps whose tightening screws pull them outwards, to engage with the interior bevel of a joiner ring (not shown), which connects them to the next segment. The electrical signal and power leads to the segment enter through a hole in the joiner ring.

Between the clamps is a beryllium-copper strip which acts as a torsion spring, providing a restoring force for the spine segments in parallel with the active spring provided by the spine control.

Rods which are shrouded by waterproof bellows connect the gimbal ring through the bulkhead to the triangular torque-plate. Strain gauges are cemented with epoxy resin to the plate next to T-shaped slots which concentrate the strain beneath the gauges. A thin film of silicone rubber over the gauges protects them from moisture. The arrangement is reflected on the bottom side of the plate and the four gauges connected in a bridge which provides a difference signal for bending moments in the plane of the plate and a common-mode signal— cancelled in the amplifier—for out of plane bending.

The apex of the plate is clamped to a steel-reinforced polyurethane belt driven via an epicyclic reduction gearbox by the motor beneath the plate. A tachogenerator is connected to the motor so its velocity, and hence the velocity of the joint, can be measured. The torque-plate senses fluid loads on the segment, and the motor can drive the joint until these loads match the specified function of joint displacement and velocity.

The cover tube fits between the bulkheads and is sealed with a rubber 'O' ring and silicone grease. A strip of blotting paper between two electrodes fits on the inner surface of the tube; its change of conductivity when damp is used to detect leaks. A supply of filtered dry air was pumped through the model in order to purge water vapour; additionally, its slight overpressure helped to prevent leaks.

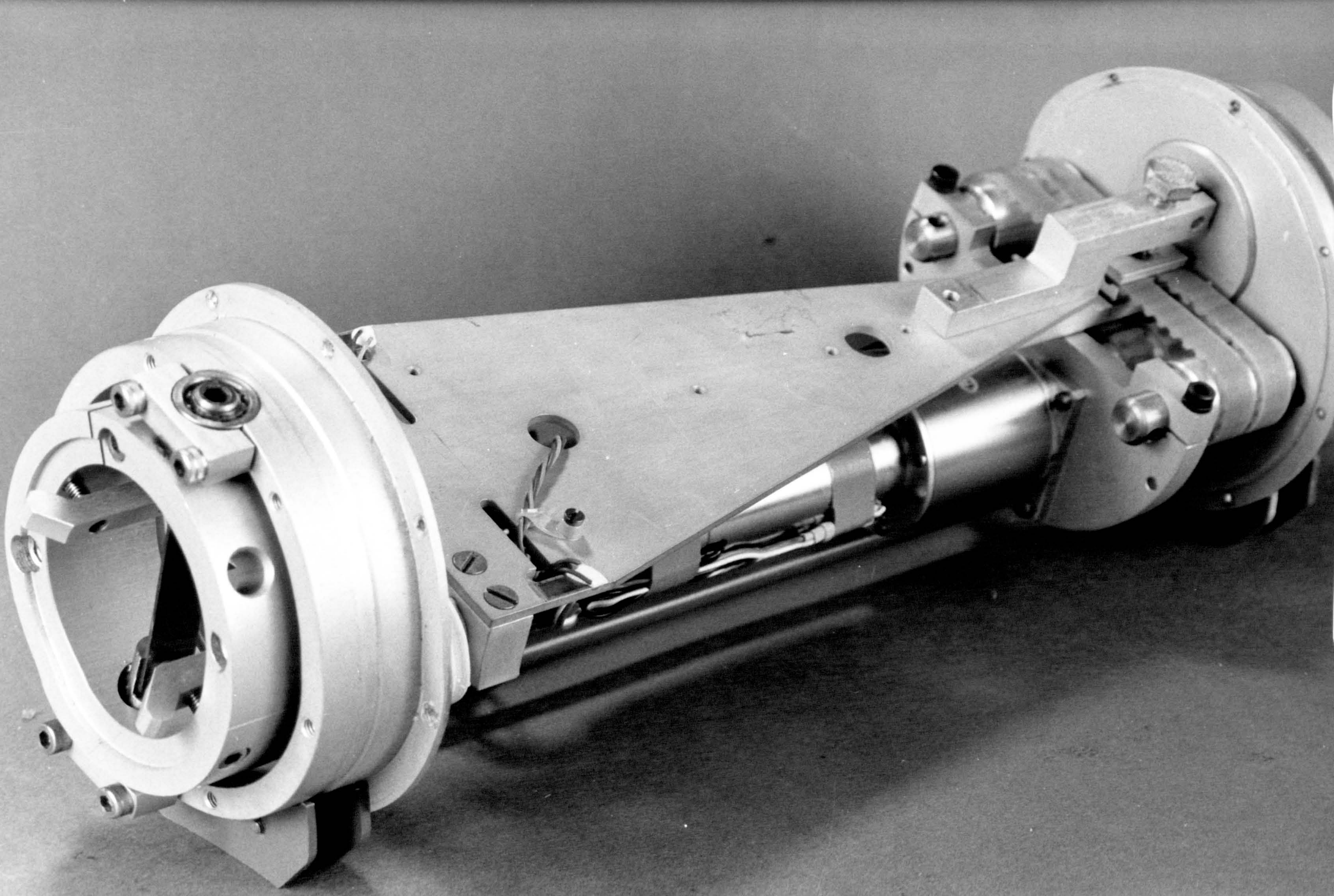

Photograph 4.3 shows a spine segment with its control board in place over the torque plate. The double-sided printed circuit board is through-connected where necessary with soldered pins; it is tinned but not lacquered. The board is centrally braced down its length with a 6 mm square light-alloy beam. At its left end are four plastic power transistors mounted on a light-alloy plate. This makes good thermal contact with the bulkhead, which when immersed in water acts as an excellent heat sink. The transistors are part of two power amplifiers, one of which drives the spine segment, the other being available to drive a Duck model when attached. The large chip in the middle is a 16 channel bi-directional multiplexer which allows the transmission of torque and velocity signals to the computer, and the reception of command signals from the computer to the servo-motor. On the far right of the board are three trimming potentiometers which adjust the torque and velocity calibration, and the torque offset. When the segment is fully assembled they can be adjusted by a screwdriver through the circular hatch visible in the adjacent bulkhead.

In front of the segment are the torque plate and the components of the belt drive. The belt is tightened by rotating the eccentric cores of the rollers on which it bears.

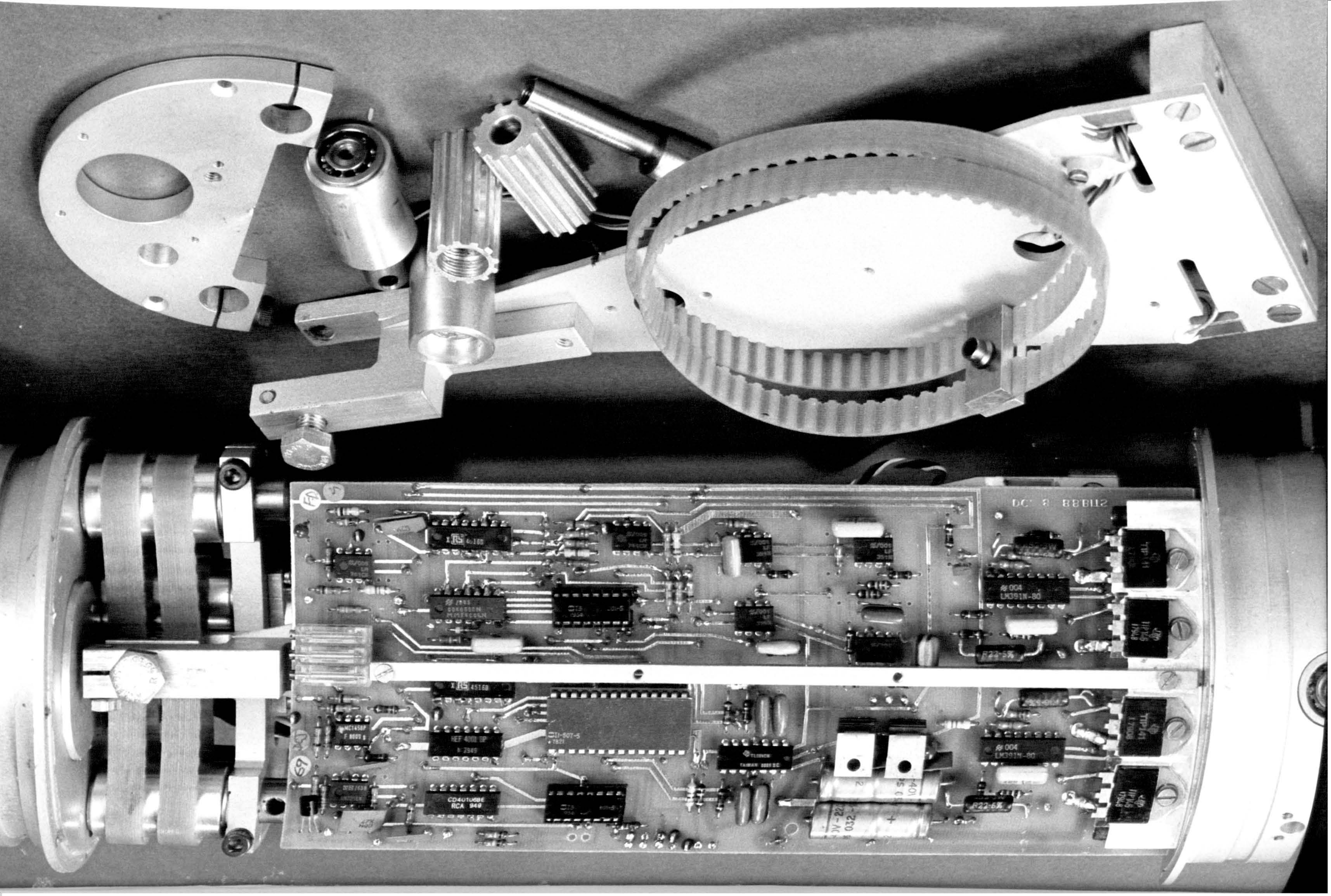
HEF 4001 BP
CD4011UBE
RCA 949
LM391N-80
LM391N-80

4.2 Spine specification

SEGMENT DIMENSIONS			
segment mass	3.9 kg		
segment volume	4.0 litres		
freeboard	7.5 mm		
segment pitch	400 mm		
section diameters	125 mm	110 mm	88 mm
section lengths	293 mm	55 mm	52 mm

SEGMENT CALIBRATIONS	
Velocity	0.1 rad/s/V
Torque	10 Nm/V
Torque command	10 Nm/V
Motor current	1.0 A/V

4.3 The control loop

The model contains computer-selectable gain levels for the servo loop connecting the strain gauges to the motor.

gain 0	signal circuits on, motor off
gain 2.7	motor on
gain 8.3	motor on

These gain levels indicate the factor by which distortion is reduced due to the feedback loop. They are a measure of how well any externally applied function—stiffness, damping, etc—will be met. All the calculation is done by the control computer: velocity signals are integrated to angular displacement, and a control signal calculated to drive the motor until the torque signal equals the angle times the stiffness set for the test. Provision is made for damping, but this never worked in practice - the spine became unstable even for very

low levels. In these experiments the damping was therefore always set to zero. Again because of instability, the high gain of 8.3 can only be used for low values of stiffness.

4.4 Calibration

The spine is calibrated when stripped down. Torque is adjusted to its calibration value of 10 Nm/V with the aid of a 60 N weight attached over a pulley to alternate sides of the torque plate. Velocity is calibrated by swinging the spine segment between externally mounted end-stops, and trimming until the integrated velocity signal reaches the calibration value of 0.1 radians/V. It was possible to perform these calibrations to a repeatability of better than 1%. Torque offset is adjusted through the hatch when the segment is fully powered up and the motor drive is operative, first at low gain, then at high gain, until the segment shows less than 1mm offset from the central position, that is, about 0.1^0. Belt tension has a substantial effect on the amount of current consumed by the motor, and on unwanted damping. It is set to an optimum value by driving the motor with a 1Hz signal and tightening the belt until there is an abrupt rise in the motor current. The belt is then tight enough to avoid backlash, but not so tight as to cause undue friction.

4.5 Faults and maintenance

Despite the mechanical complexity of the spine model, virtually all the faults were electronic in origin. With a total of 320 circuit boards to control the model this is perhaps unsurprising. However, electronic failures (calculated per integrated circuit) were some ten times higher than for the adjacent wavemaker control boards. Failures within the spine segments occurred at twice the rate of the associated external signal circuitry. There were three main reasons for this:

- The segments were sealed for the first time with a silicone rubber which released acetic acid as it cured. This caused extensive corrosion when it penetrated integrated circuits.

- The inside of spine segments were occasionally exposed to water.
- Unlike the spine electronics, the wavemaker signal circuitry power supply was derated from 15 volts to 7 and better protected from voltage transients.

Because of this high level of faults a microcomputer was dedicated to the task of continually monitoring the spine; it was also used to check the state of health of the model before and after every experiment. In the course of preparing for a typical experimental run there would be three faults which required the removal of a board or a segment. Careful setting up ensured that none of these took place *within* an experiment. Before launching, the model was checked for: wet segments; voltage offsets on the torque or velocity amplifiers; faulty motors. The model was then launched and moored and straightened by minimising all the motor currents. (The straightness thus relies upon the correct fitting of the beryllium-copper torsion springs in the joints.)

It was then subjected to a pseudo-random sea and the torque and velocity signals analysed statistically to check that spine stiffness was as specified, and that damping was low, and that torque and velocity signals had an approximately normal distribution (deviations here usually indicating a sticky joint). This same test was repeated at the end of an experimental run, but for the experiments recorded here, never showed any anomaly. Monitoring was continual throughout the experiments. If the computer detected any fault condition, such as an instability in the control loop leading to mechanical oscillation of the spine, it would stop that section of the experiment and then restart.

4.6 The spine mooring

A full description of the spine mooring, and a set of experiments upon it, is given in an earlier work (Retzler 1986). A brief description is given here. At every eighth spine joint there is a mooring assembly shown in elevation in figure 4.1. The float and sinker arrangement acts as a low-rate spring allowing large displacements. The spine remains tightly coupled to the water surface by buoyancy forces, so the displacements in heave are comparable with the local wave motion. In surge however, the mooring provides the only restoring force

Figure 4.1
Elevation of the spine mooring.

not to scale

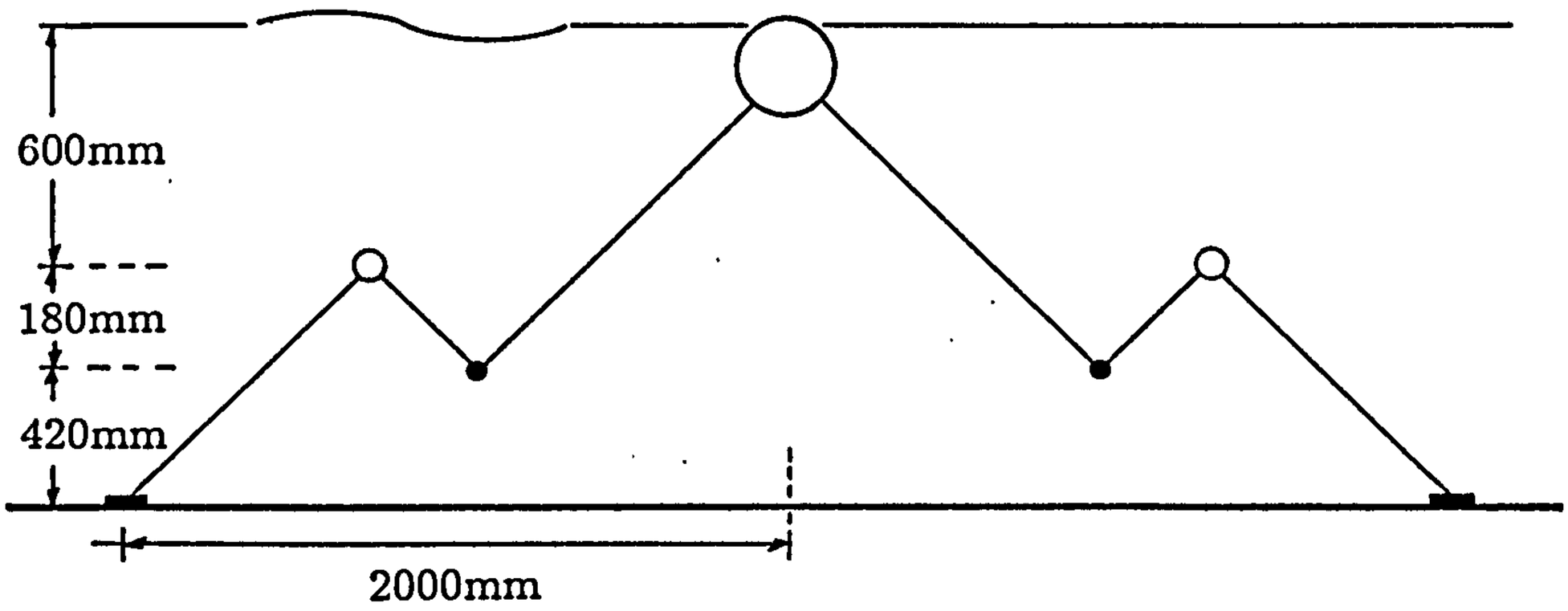

to displacement. The resonance of the spring of the mooring with the mass of the spine must be well below the wave frequency so the spring rate must be low, but not so low to cause problems with the range of displacement. The float and sinker mooring meets these requirements. It is a non-linear spring, stiffening rapidly at high stretch, but with a large central linear region. The model mooring, with a base length of 2 m, has a virtually linear central range of ±200mm, and a spring rate of 1N/m. Five of these springs coupled to the spine mass gave a resonance at 50mHz, far below the wave frequency range.

However, even if the spine is fixed, the float and sinker can resonate in a number of modes in three dimensions. The mode with highest frequency is an in-plane, in-phase motion of the sinker and float which was calculated by Langrangian method, and confirmed by experiment, to be about 0.34Hz, again below the range of wave frequencies used.

Moreover, because of the low rate of the mooring, the mooring forces exerted for spine displacements of the order of the wave height are negligible—about a thousand times less than those due to buoyancy.

In the mixed sea states described in chapter 8, some low frequency excursions of the order of 50 mm, were noted at around the spine-mooring resonance frequency. The resultant forces (around 50mN at any moored joint) are a hundred times smaller than the forces due to spine bending, and for the analyses of chapters 5 and 6 have been neglected.

4.7 Tank and model performance

The validity of the experiments is dependent upon the accuracy of calibration of the sensors and low drift thereof, and also upon the accuracy of tank and model control and the stablility of the model, and waves in the tank.

The spine segment sensors were calibrated to an accuracy of about 1%, and since they were checked frequently, their drift was known to be not worse than 2% over a period of about a month. Wavegauges were calibrated before and after each experiment. Their accuracy is estimated to be about 1% and their drift to be less than this within the course of the experiment. The tank transfer function (wave amplitude against frequency) was checked infrequently, and found to change by no more than 5% at any one frequency over the course

of a year.

As stated in chapter 2, the energy of the wave field in the tank is known to be inhomogeneous, mainly due to reflections. But because the spine intercepts waves over a considerable length of the working area, and because energy is transmitted down the spine by flexure, the effects of the wave amplitude variation will be mitigated.

A further test of the tank and model performance and stability can be made by repeatability tests. Figure 4.2 shows superimposed time traces taken ten minutes apart for a wavegauge and for the torque at a spine joint, taken in a mixed sea (a 1Hz Pierson-Moskowitz with Mitsuyasu angular spreading) The repeatability is good, and the error is high frequency, implying that when Fourier filtering is used error should be even less. In the long term - over many months - the bending moment response of the spine changed at the worst by 10%, which in many cases included complete segment replacement.

Figure 4.2

Repeatability in the 3D tank.

Two superimposed wave records.

Two superimposed torque records.

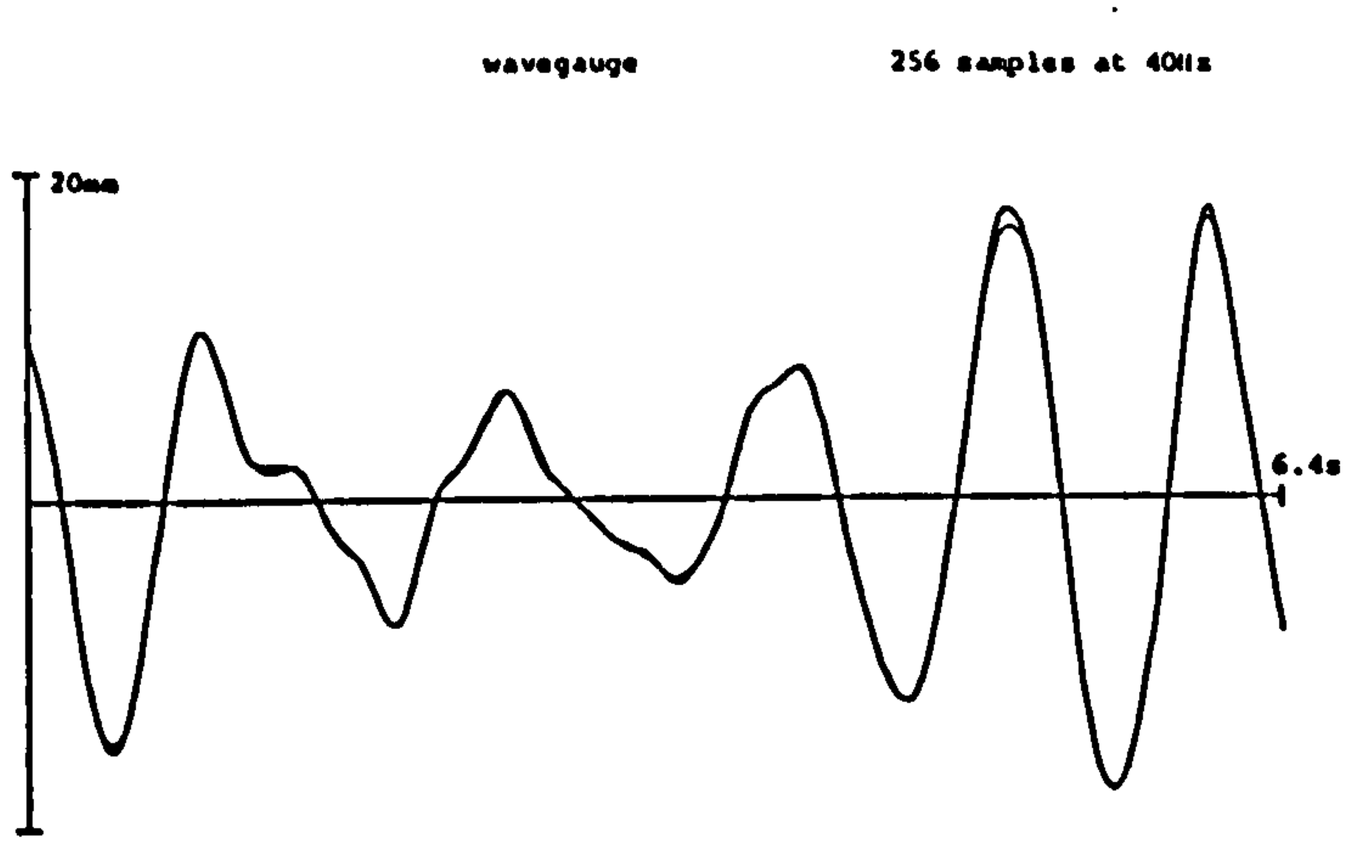

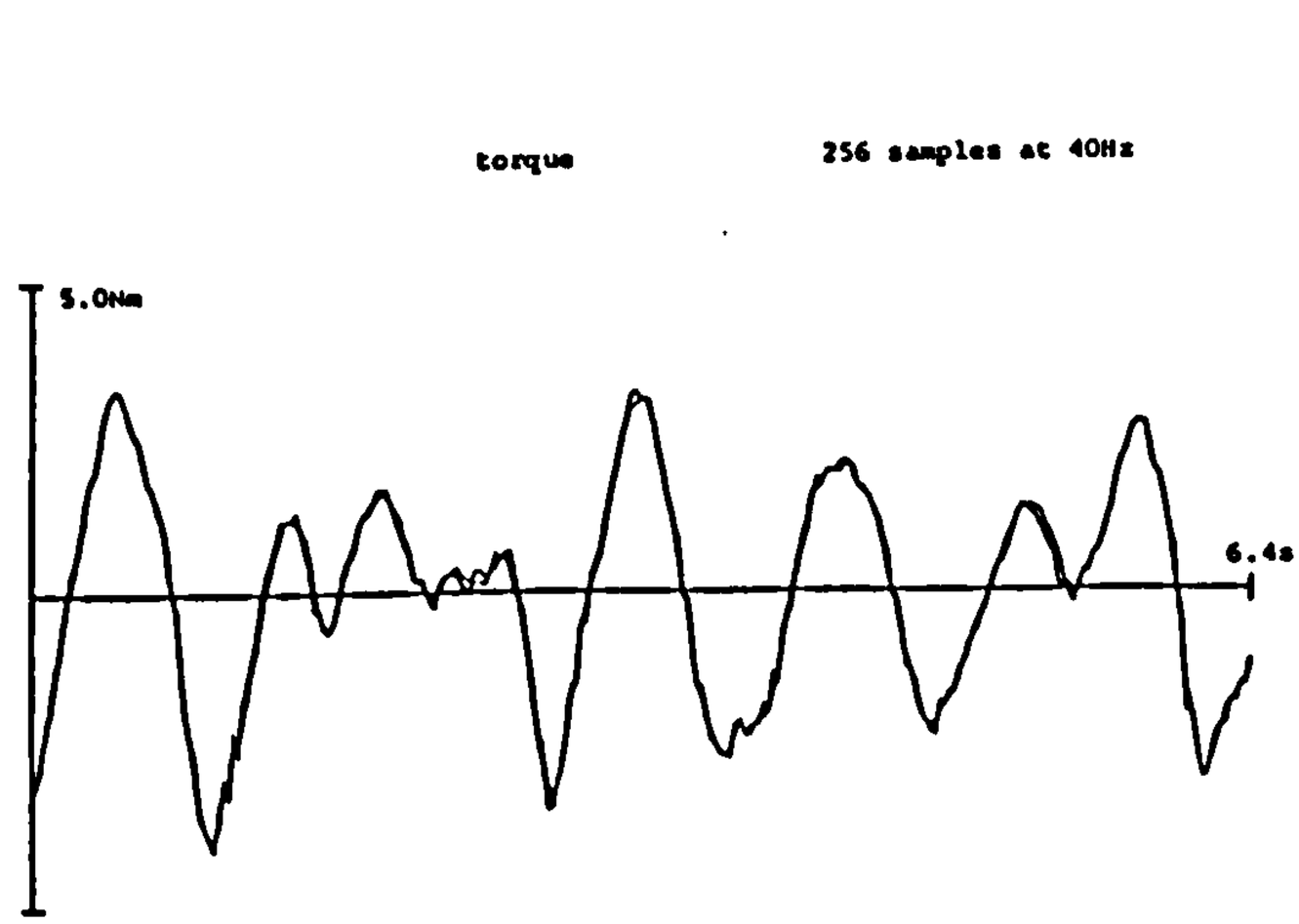

4.8 Experiments

The spine was assembled from 40 segments, giving 19 heave joints alternated with 20 surge joints. Its length was 16 metres. It was moored in the centre of the tank working area, thus leaving about 5 metres of clear water at either end, about 3 metres behind before waves were absorbed by the beach, and about 4.5 metres foreward to the wavemakers allowing for full development of waves. Location error in the x and y directions was about $\pm$20mm. Waves propagating at zero angle have their crest parallel to the spine. Positive angles of wave only were used in the experiments to avoid the bad area of reflection around the glass. The experimental parameters were as follows:

sampling rate	20Hz
number of samples	256
wave amplitude	10mm
frequency range	0.47 - 1.95 Hz
angle range	0 - 70 degrees

The wave frequencies were chosen so as to give a whole number of cycles (from 6 to 25) within the sampling time. A wait time of 30 seconds was taken after the start of the wave and the powering up of the spine to allow the starting transients of the tank and spine to dissipate, and both to reach a steady state before sampling was started.

The finite depth of the tank reduces the wavelength of low-frequency waves in accordance with equation 1.12. In these experiments, the angle of the waves was therefore also reduced at low frequency in order to maintain the crest length down the length of the spine at the deep water value. The experimental results are thus presented as if the tests were performed at the nominal wave angles in deep water. The most extreme change was at 0.47Hz, when the nominal angle is 70 degrees, the actual angle used was 55 degrees.

The spine was tested at two stiffnesses: 100Nm/rad and 1000Nm/rad. The lower stiffness was tested at loop gain 8.3, the high stiffness at loop gain 2.7. The torque and velocity records from each spine joint were Fourier transformed, and the amplitude and phase of the components at the wave frequency were abstracted. As a check that the spine control loop was functioning correctly, the

torque was divided by the integrated velocity to yield the effective stiffness for each joint. In the region where the spine dynamic response was high the average stiffness in the spine agreed with the commanded stiffness to typically 5%. In areas of low bending moment response the agreement worsened appreciably. The torque signal was also divided by the velocity to yield a damping value. Though commanded to be zero, it was not. In the areas of high spine response it was inversely proportional to frequency. It was also dependent upon the spine stiffness and loop gain.

loop gain	stiffness	formula
8.3	100 Nm/rad	10/f Nm/rad/s
2.7	1000 Nm/rad	50/f Nm/rad/s

The implications for this failure of the spine control loop need to explored. If the joint does not yield sufficiently to fluid forces on the segment, then the effective stiffness will be greater than that specified; if it does not yield fast enough, the damping will be higher than specified.

A closer look at the data showed that in the areas of high bending moment the peak bending moment did not change much with frequency; therefore (because the stiffness was constant) neither did the angular displacements. And therefore the angular velocities were proportional to frequency, and the force in phase with angular velocity was approximately constant.

This is not due to phase error in the controller: the implementation of the software control loop was checked and gave negligible error down to 0.1Hz. And it was independent of the hardware loop gain.

There are mechanical components within the feedback loop of the spine segments themselves which could contribute to the anomaly. For example the drive belts will require energy to deform them; but this should appear as a true damping, with no frequency dependence.

The most likely explanation is that there is stiction in the system—for example, backlash in the gearbox is about 1°. For small displacements, ie sufficient to change the polarity of the stiction force, the force will be in quadrature with the displacement and in phase with velocity, and hence be measured as a damping. It is of course non-linear, the force stays constant with velocity. This then

agrees with the observed frequency dependence of the measured damping. It also agrees with the observed change with loop gain and stiffness: the increased loop gain used at the lower stiffness will act to decrease the damping error; and as stiffness decreases the amount of spine motion increases, but the stiction force will stay the same, thus apparently decreasing the damping.

4.9 Results

The bending moment response of the spine in surge at a stiffness of 100Nm/rad is plotted in figure 4.3. In this discussion, the term *plot* refers to the individual miniature graphs of bending moment amplitude at each joint against position in the spine. The term *array* refers to the 20 by 15 grid of these miniatures. Note that the boxes for the 32 high frequency/large angle waves that the wavemakers are unable to produce have been left blank. The plots are drawn as blocked in histograms (the data are also replotted as points later in the text.) This style of presentation allows the shape of the plots to be seen clearly in silhouette; while the overall *density* of the bending moment response across the whole array is also clear.

The response across the array appears as an arc from high frequency and small angle to low frequency and large angle. It is clear that for *any* wave frequency in the array the spine exhibits a resonance provided that the wave angle is right. There is no reason to suspect a sudden change outside the limits of the array, although it should be noted that the position of the resonance shifts to larger and larger angle as the frequency decreases and at some point must approach the limiting value of 90 degrees.

The position of the resonance maximum with crestlength down the spine rather than wave angle shows less variation: from a crestlength of 2.4m at 1.95Hz, to 3.9m at 0.7Hz.

The width of the response area increases as the frequency drops. At high frequencies the width of the response is very sharply defined, with very little bending moment for wave frequencies and angles away from the resonance.

At any frequency the response at an angle of zero degrees—a beam wave—should be zero because all the spine segments should move in common, with no joint movement at all. On the figure, though the 0 degree response is very small, it does exist. The highest bending moment for any joint is about 1Nm, though most are well below. There are several possible explanations for this:

1. electrical noise in the spine or sampling system;

2. mechanical noise in the spine;

3. angular error in the wavemakers;

Figure 4.3

Surge bending moments.

Spine stiffness 100Nm/rad.

Wave frequency 0.47–1.95Hz, wave angle 0–70 degrees.

Bending moment 0–5Nm versus joint position 0–16m.

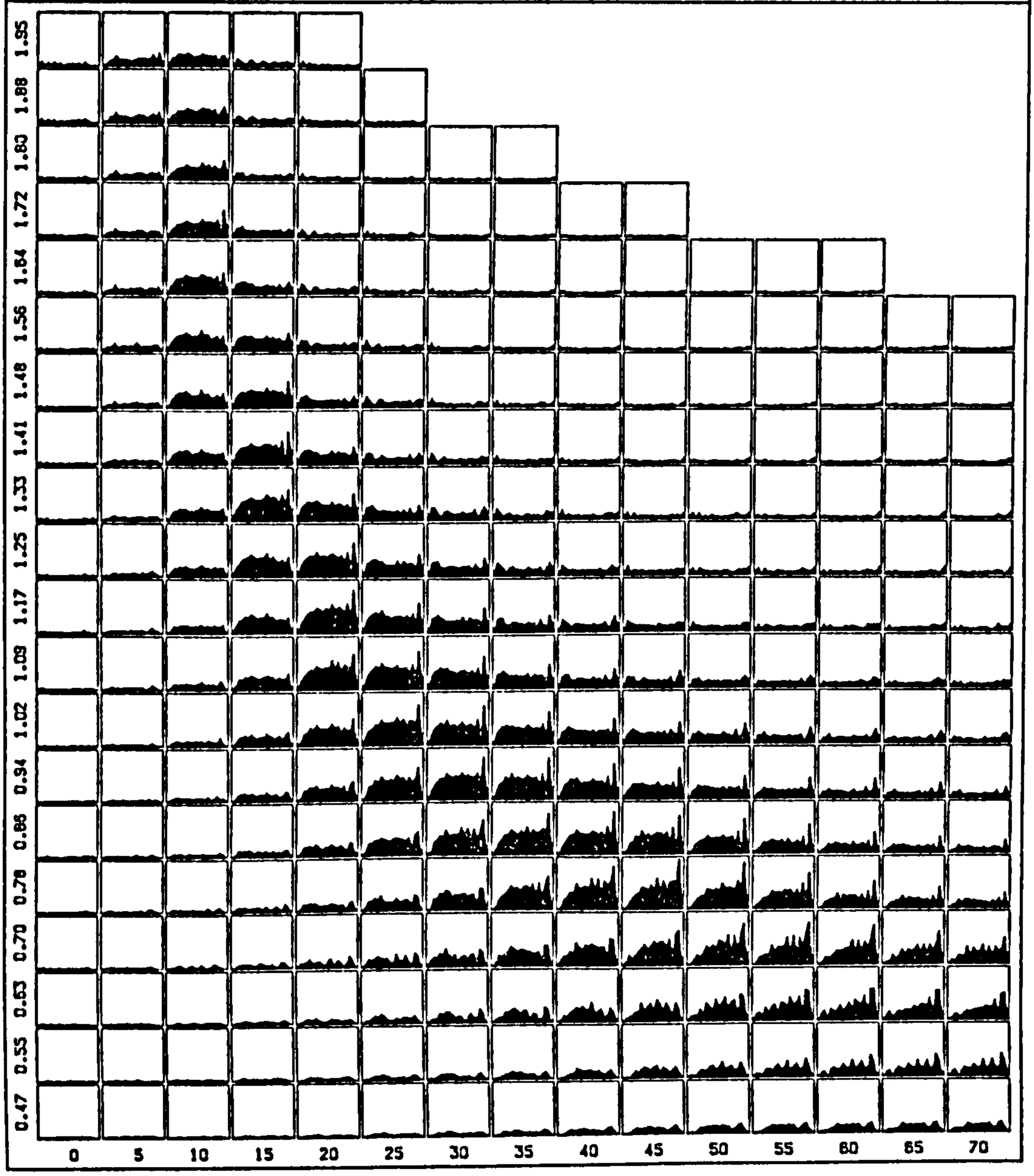

4. angular error in the spine alignment;

5. inhomogeneous wave field.

The first two possibilities can be ruled out because the root-mean-square signal recorded for the spine at rest in the tank with no waves is of the order of 0.05 Nm - and most of that is high-frequency noise that will be removed by the Fourier filtering process. Items 3 and 4 have been mentioned previously: there is a systematic wavemaker angle error which is +0.2 degrees at 1Hz; and the angular error in the spine alignment is of the order of 0.1 degrees. One would expect the importance of angular error to rise with frequency, as the resonance shifts to smaller angles; and indeed, bending moment at zero degrees does rise with frequency. However, the most likely source of corruption is inhomogeneity of the wave field in the tank. The reflection results of Bryden (1983) are quoted above: the anisotropy of energy in the tank implies the existence of reflections both normal to the wavemakers and at other angles. These are probably sufficient to cause the observed spurious signal. Bryden's tests with monotonic waves all used waves propagating at zero degrees; it is probable that waves at other angles produce similar amounts of reflection. The bending moments for the spine in 0 degrees waves therefore indicate the degree of error that is possible for any other plot in the array.

For any particular frequency, the size and shape of the plots changes radically with angle. For the 1.02Hz case, the plots steadily increase in magnitude as the wave angle increases, reaching a maximum at about 25 degrees. At this angle, a sharp peak appears in the plot at the downwave end of the spine. As the wave angle increases further, this peak gradually reduces and broadens, and a smaller smoother peak also appears at the upwave end. This pattern is repeated at lower frequencies - for example, 0.78Hz - but at still lower frequencies, large numbers of peaks appear in the plots. At higher frequencies resonance occurs over a much narrower band of angle and providing less chance for close examination of changes in shape. Some other parameter, such as wave crest length, or crest velocity may be a more appropriate axis than angle.

Figure 4.4 shows the bending moment response of the spine in heave at a stiffness of 100Nm/rad. Note the change in scale - heave results are about half the magnitude of surge. While showing the same broad arc of resonance of the surge case, the array density is markedly different. The greatest density is now between 0.94 and 1.33Hz. The resonance area is outlined less crisply than in the surge case, with more signal at low and high angles - note the size of the 0 degrees cases. Noise can be expected to be relatively greater due to the much lower overall level of signal.

The position of resonance is found to be at smaller angles than for surge. For example, at 1.02Hz, the largest plot is found at 20 degrees, compared with 25 degrees for surge. At lower frequencies the difference is greater - at 0.78Hz it is about 40-45 degrees in surge, but only 30 degrees in heave. As angle decreases so crest length increases and the moment must increase. If more moment is required to bend the spine it implies that it must be stiffer. A crude calculation for the stiffness that buoyancy adds to the spine suggests that it is of the same order - say 60 to 120 Nm/rad - as the programmed stiffness, which could account for the observed shift in resonance.

The shapes of the plots are also very different. In heave, the plots for 0.78Hz are very peaky compared to surge, whereas at 0.55Hz they are smoother.

Figure 4.4

Heave bending moments.

Spine stiffness 100Nm/rad.

Wave frequency 0.47–1.95Hz, wave angle 0–70 degrees.

Bending moment 0–3Nm versus joint position 0–16m.

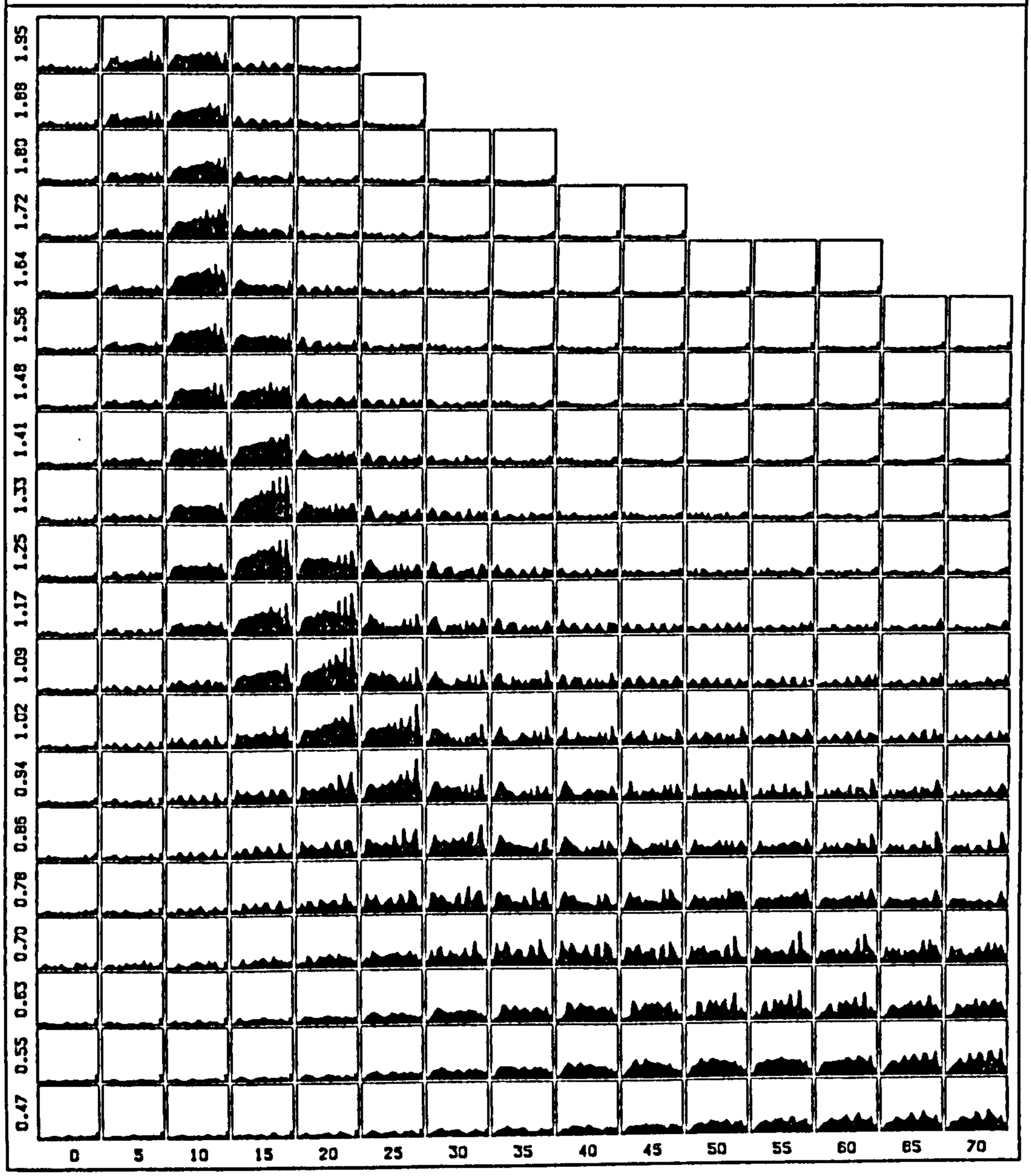

Figure 4.5 shows results for the spine in surge at a stiffness of 1000Nm/rad. Compared with the array for surge at 100Nm/rad stiffness, there are many striking differences. Firstly note the change in scale —the magnitude of the plots is 3 to 4 times larger than for the low stiffness case. The resonance has narrowed in angular spread. This narrowing probably accounts for the apparent reduction of resonance amplitude between 1.56 and 1.88Hz—it is likely that the angle for which the resonance is at a maximum is now very sharply defined and lies *between* 5 and 10 degrees. There has been a considerable shift of the resonance to smaller angles compared to the low stiffness case. For example, at 1.33Hz it has shifted from 15 to 10 degrees; at 1.02Hz from 25 to 15 degrees; and at 0.70Hz from 50 to 30 degrees. There appears to be a larger low frequency resonance than for the low stiffness case, but this could just be that more of the resonance now appears within the angular limits of the array, due to the shift to smaller angles. The shapes of the plots are very different from those of the low stiffness case. There are fewer peaks, and the peaks are lower and better defined.

Figure 4.5

Surge bending moments.

Spine stiffness 1000Nm/rad.

Wave frequency 0.47–1.95Hz, wave angle 0–70 degrees.

Bending moment 0–20Nm versus joint position 0–16m.

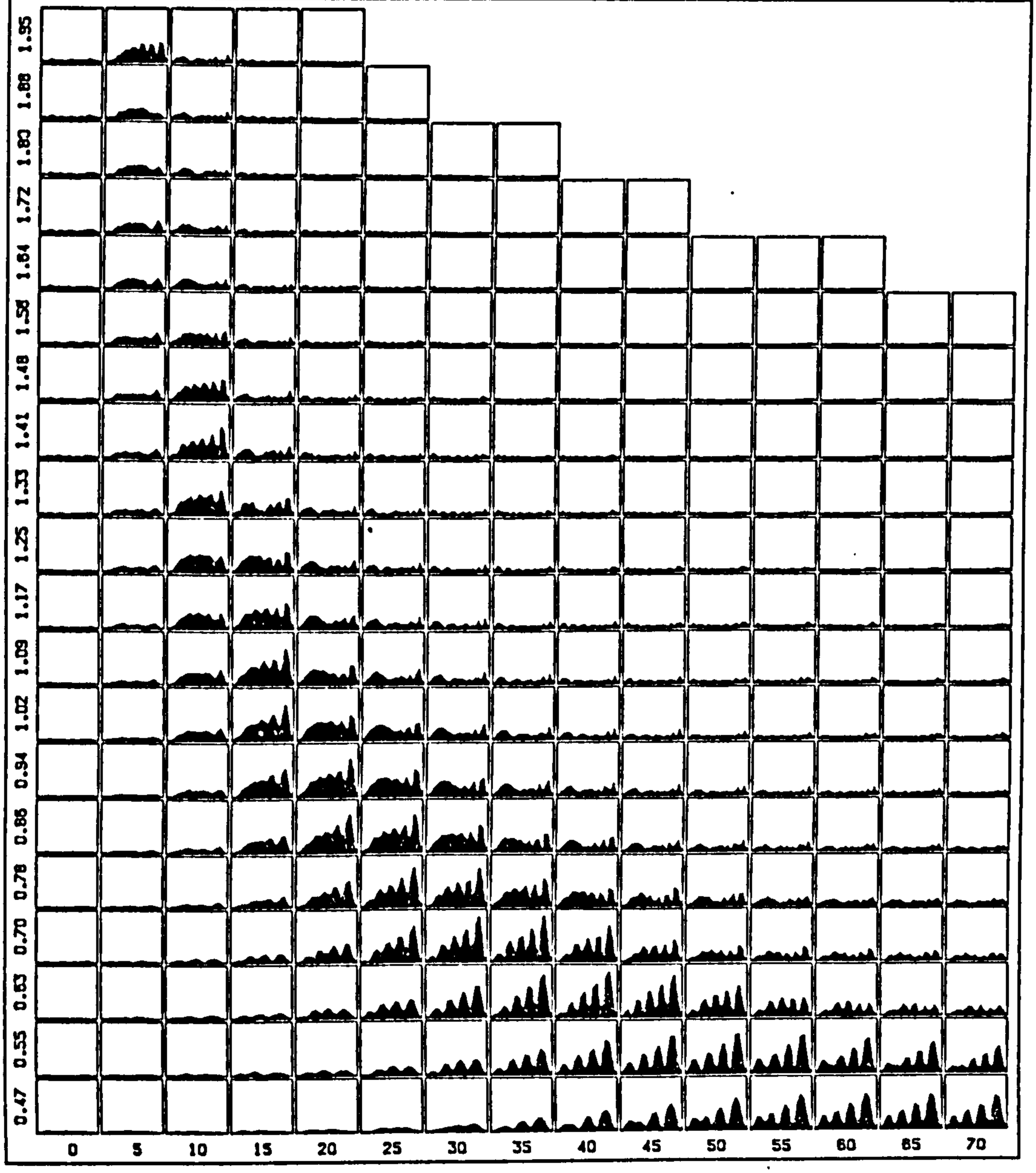

Figure 4.6 shows the results for the heave response of the spine at a stiffness of 1000Nm/rad. Again, the overall magnitude of the response is some 3 to 4 times greater than for the low stiffness in heave. And the plots have the same sparser, better defined peakiness as in surge. Unlike the low stiffness case, there is no noticeable shift of the resonance to smaller angles due to buoyancy.

Figure 4.6

Heave bending moments.

Spine stiffness 1000Nm/rad.

Wave frequency 0.47–1.95Hz, wave angle 0–70 degrees.

Bending moment 0–10Nm versus joint position 0–16m.

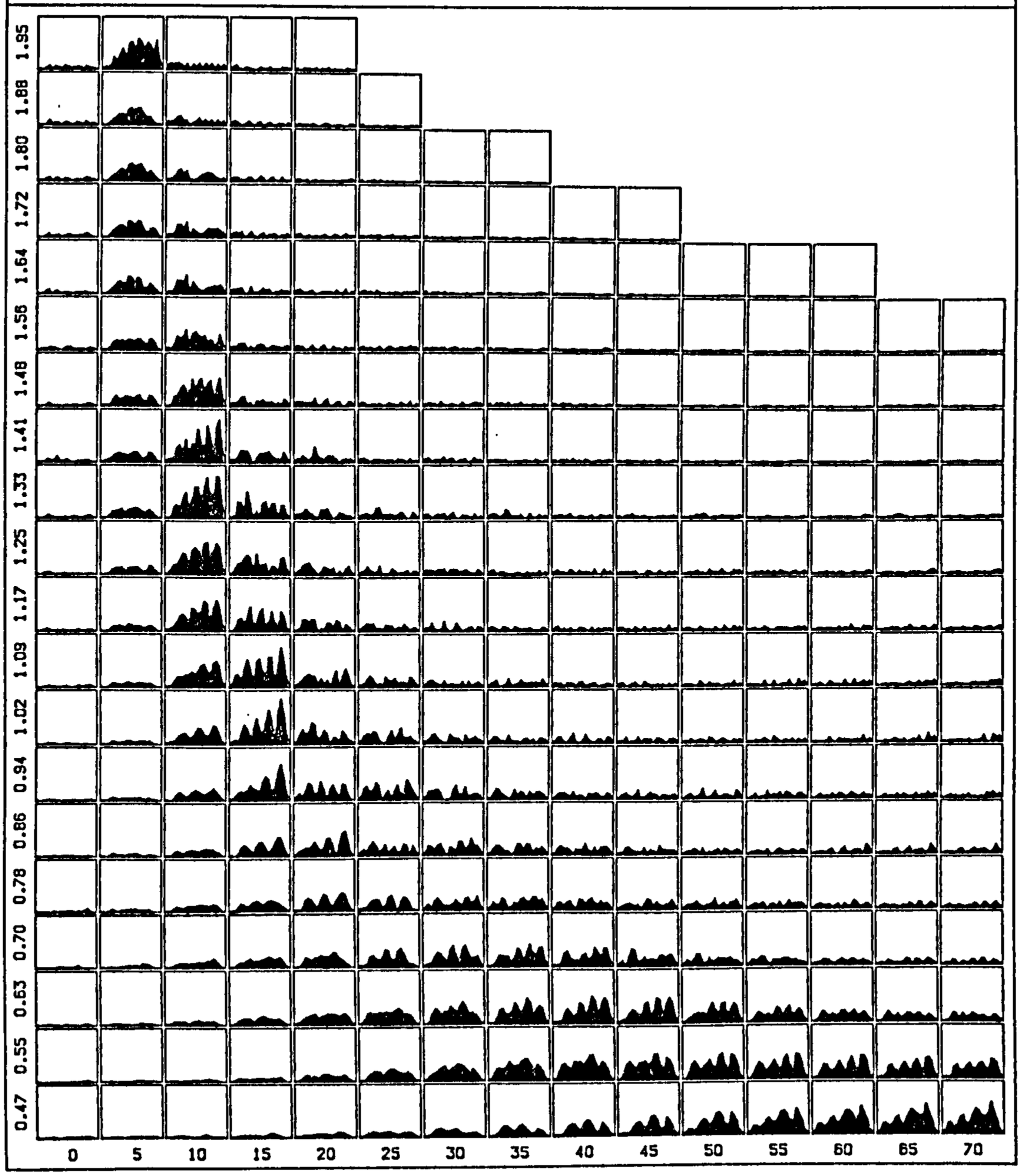

Figure 4.7 is a photoreduced page of the 4 bending moment arrays to display the heave and surge bending moments at the two different stiffnesses. It clearly shows the narrowing and shift of the resonance as stiffness increases and the differences between heave and surge with frequency.

Figure 4.7

Heave and surge bending moments.

Spine stiffness 100 and 1000Nm/rad.

Wave frequency 0.47–1.95Hz, wave angle 0–70 degrees.

Not to same scale.

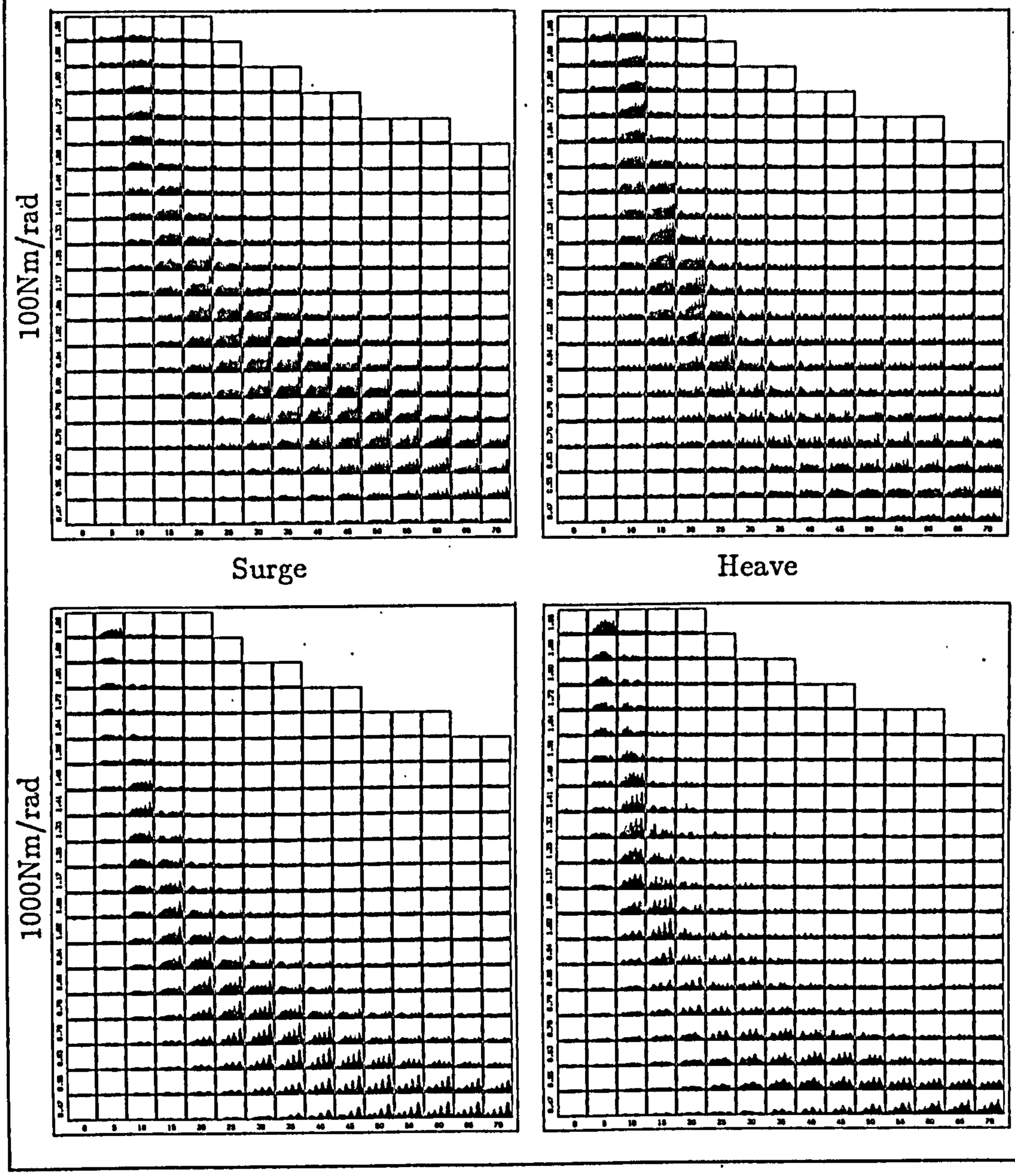

4.10 Conclusions

1. For each wave frequency in the tested range there is a wave angle for which the spine exhibits a resonance.

2. The wave angle at the resonance maximum decreases as frequency increases.

3. The size and shape of the bending moment plots is critically dependent upon the frequency and angle of the wave.

4. When the spine stiffness is increased by a factor of 10, the overall bending moment magnitude increases by a factor of 3 to 4.

5. As the stiffness increases:

   a the spine resonance shifts to smaller angles;

   b the angular width of the resonance decreases;

   c the number of peaks in the bending moment plots decreases.

6. The overall bending moment magnitude is greater in surge than heave by about a factor of 2. This appears to be independent of spine stiffness.

7. The magnitude of the response with frequency is very different in heave and surge.

8. The effect of buoyancy on the spine is to add stiffness in heave. The effect is very marked at low stiffness. The value of added stiffness is about 100Nm/rad.

Chapter 5

A continuous beam model of the spine

SUMMARY

The equation of motion for a finite continuous beam in water waves is developed. The equation is combined with experimental hydrodynamic data and used to calculate bending moments. The predictions are compared with experiment.

5.1 Preamble

A successful theory must account for the following:

1. The spine resonance and its relationship with wave frequency and angle.
2. The variation in magnitude of the resonance maximum with frequency.
3. The increase of bending moment with spine stiffness.
4. The shift of the resonance to smaller wave angles as the spine stiffness is increased.
5. The differences between heave and surge response.
6. The bending moment with respect to position in the spine, and the origin of peaks in these spatial plots.

5.2 The beam equation

Timoshenko (1974) discusses the equation for a prismatic beam whose cross-section is small compared with its length. Using the coordinate system defined in Chapter 2 with the length of the spine along the y axis and specifying all quantities to be per unit length of the beam, the force opposing horizontal bending of a beam of elasticity E and sectional moment of inertia I is

$$F = -EI\frac{\partial^4 x}{\partial y^4} \tag{5.1}$$

Combining this force with the hydrodynamic forces on the beam in the x direction, and equating to the mass times acceleration

$$-W_{xx}A_x - Z_{xx}U_x - EI\frac{\partial^4 x}{\partial y^4} = m\dot{U}_x \tag{5.2}$$

Writing U_x as $\dot{x}$ and the fourth partial derivative of x wrt y as x^{iv}; taking exogenous terms to the right, endogenous to the left; and neglecting subscripts

$$-m\ddot{x} - Z\dot{x} - EIx^{iv} = WA \tag{5.3}$$

This fourth-order linear non-homogeneous equation in x can be solved by the method of undetermined coefficients. Assuming steady-state sinusoidal conditions, the forcing function is of the form $WA_0e^{i(\omega t - ky)}$ where W is the wave force coefficient per unit length, A_0 the wave amplitude, ω the wave angular frequency and k the wave number along the y axis given by

$$k = \frac{2\pi \sin\alpha}{\lambda} \tag{5.4}$$

where λ is the wavelength, and α is the wave angle to the x axis. The displacement response of the spine and its time and space derivatives can be written

$$x = x_0e^{i(\omega t - ky)} \tag{5.5}$$

$$\dot{x} = i\omega x \tag{5.6}$$

$$\ddot{x} = -\omega^2 x \tag{5.7}$$

$$x^{iv} = k^4 x \tag{5.8}$$

Equation 5.3 can therefore be written

$$m\omega^2 x - Zi\omega x - EIk^4 x = WA \tag{5.9}$$

and

$$m\omega^2 x_0 - Zi\omega x_0 - EIk^4 x_0 = WA_0 \tag{5.10}$$

so

$$x_0 = \frac{WA_0}{m\omega^2 - Zi\omega - EIk^4} \tag{5.11}$$

This is the particular integral of equation 5.3. It indicates a resonance in the beam when the inertia of the beam is cancelled by its spring. Note that the imaginary part of Z contains the hydrodynamic added mass and added spring for the beam and this too affects the position of the resonance. The Q of the resonance is governed by the value of the real part of Z.

The homogeneous equation

$$m\omega^2 x - Zi\omega x - EIx^{iv} = 0 \tag{5.12}$$

can be solved by substituting $x = x_0 e^{\mu y}$

$$m\omega^2 x_0 e^{\mu y} - Zi\omega x_0 e^{\mu y} - EI\mu^4 x_0 e^{\mu y} = 0 \tag{5.13}$$

Giving

$$\mu = \sqrt[4]{\frac{m\omega^2 - Zi\omega}{EI}} \tag{5.14}$$

The four complex roots $\mu_{1,2,3,0}$ are determined by De Moivre's theorem, and combined with the particular integral, equation 5.11, to form the general solution, equation 5.15

$$x = x_0 e^{i\omega t}[e^{-iky} + \sum_{j=0}^{3} C_j e^{\mu_j y}] \tag{5.15}$$

5.3 End conditions

For a finite beam of length L the four coefficients $C_{0,1,2,3}$ are determined by making use of the boundary conditions of the beam. These are that at the ends of the beam, the bending moments and the shears must be zero. Respectively,

$$EI\frac{\partial^2 x}{\partial y^2} = 0, \qquad z = 0, L \tag{5.16}$$

$$EI\frac{\partial^3 x}{\partial y^3} = 0, \qquad z = 0, L \tag{5.17}$$

These four conditions allow the solution of the four unknowns in C.

$$\frac{\partial^2 x}{\partial y^2}|_0^L = x_0[-k^2 e^{-iky} + \sum_{j=0}^{3} C_j \mu_j^2 e^{\mu_j y}]_0^L = 0 \tag{5.18}$$

$$\frac{\partial^3 x}{\partial y^3}|_0^L = x_0[ik^3 e^{-iky} + \sum_{j=0}^{3} C_j \mu_j^3 e^{\mu_j y}]_0^L = 0 \tag{5.19}$$

which can be expressed in matrix form

$$\begin{pmatrix} k^2 \\ k^2 e^{-ikL} \\ -ik^3 \\ -ik^3 e^{-ikL} \end{pmatrix} = \begin{pmatrix} \mu_0^2 & \mu_1^2 & \mu_2^2 & \mu_3^2 \\ \mu_0^2 e^{\mu_0 L} & \mu_1^2 e^{\mu_1 L} & \mu_2^2 e^{\mu_2 L} & \mu_3^2 e^{\mu_3 L} \\ \mu_0^3 & \mu_1^3 & \mu_2^3 & \mu_3^3 \\ \mu_0^3 e^{\mu_0 L} & \mu_1^3 e^{\mu_1 L} & \mu_2^3 e^{\mu_2 L} & \mu_3^3 e^{\mu_3 L} \end{pmatrix} \begin{pmatrix} C_0 \\ C_1 \\ C_2 \\ C_3 \end{pmatrix} \tag{5.20}$$

which is of similar form to that derived by Bryden (1983).

The values of C are determined by elimination, and then substituted with μ in the general solution of equation 5.15, to give the value of x as a function of time and distance y down the spine. The solution for z has a similar form. For each axis the frequency dependent values of W and Z need to be substituted into the equation, along with the values for the mass and elasticity of the beam, and the wave parameters of ω, A, and k. The latter is calculated from the deep-water formula

$$k = \frac{\omega^2 \sin\alpha}{g} \tag{5.21}$$

in order to match the experimental results of chapter 5, where the wave angles were depth corrected.

The value of the wave amplitude A in heave is constant, but in surge it is multiplied by the cosine of the wave angle.

$$A_s = A_h \cos\alpha \tag{5.22}$$

There is the important question of whether it is appropriate to use two-dimensional measurements of W and Z when the spine experiments are performed in three dimensions. Garrison (1984) points out that strip-theory analysis of immersed cylinders uses two-dimensional coefficients on the assumption that each strip is unaffected by its neighbour. This is valid until incident or

radiated wave angles are such that crest-length down the axis of the cylinder is of the same order as the cylinder diameter. The spine experiments showed a resonance at a crest-length of around 5 metres—ie, 40 times the spine diameter. Garrison calculates numerically the impedances in heave and surge for a semi-immersed cylinder. For the frequencies and angles important to spine resonance, they show between 0 and 20% difference from the two dimensional values. Given that cylinder hydrodynamic coefficients change far more dramatically with small changes of freeboard in the vicinity of the water surface, and Garrison's results were for *semi*-immersed cylinders, it was decided simply to use the experimentally determined values of chapter 4.

The spine model stiffness and dampings are specified for a joint, whereas the beam stiffness EI, and W and Z are defined per metre. A means of converting between the two specifications is required. From beam theory the moment M in a beam is given by

$$M = \frac{EI}{R} \tag{5.23}$$

where R is the radius of curvature of the beam and is large. Suppose the angle of a spine joint to be θ, and the pitch of the joints to be h; then

$$\theta = \frac{h}{R} \tag{5.24}$$

Also, if the spine has stiffness σ Nm/rad

$$M = \sigma\theta \tag{5.25}$$

then

$$MR = \sigma\theta\frac{h}{\theta} = \sigma h = EI \tag{5.26}$$

similarly, if joint damping $= \delta$, then beam damping $= \delta h$.

In principle the bending moments in the spine are calculated from

$$EI\frac{\partial^2 x}{\partial y^2} = \frac{EIWA_0}{m\omega^2 - Zi\omega - EIk^4}[-k^2 e^{-iky} + \sum_{j=0}^{3} C_j \mu_j^2 e^{\mu_j y}] \tag{5.27}$$

but the practical values of springs and dampings in the spine model must be taken into account.

These are: the 15 Nm/rad reference spring s_r; the commanded spine stiffness σ_s; and the in trinsic stiffness of the spine segment, s_t, with a value of 14000

Nm/rad. The latter was measured by Taylor (1984), and acts to increase the compliance of the spine - ie, the spine bends more than the tachogenerator registers.

The aggregate value for flexural rigidity is then given by

$$EI = h[s_r + 1/(1/\sigma + 1/s_t)] \tag{5.28}$$

and this is the value which is used in the calculation of the spine displacements.

The spurious (but real) damping imposed by the motors described in chapter 5, δ, must be taken into account when deriving the spine bending moments. The final equation used for deriving bending moments was

$$M = (\sigma + i\omega\delta)h\frac{\partial^2 x}{\partial y^2} \tag{5.29}$$

5.4 Discussion

Equation 5.11 informs us that there will be resonance in the spine when spring terms cancel inertial terms. Remembering that the value of Z also has an effect a resonance will occur for all values of $m\omega^2$ for which a countervailing EIk^4 term occurs. The value of k increases with the angle of incidence of the wave. Therefore as frequency drops, the position of resonance moves to larger angles of incidence. An upper limit for k is at $\alpha = \frac{\pi}{2}$ implying that below some limit in frequency, a resonance will no longer occur.

Equation 5.15 gives the form of the displacement with time and position in the spine. The whole expression is multiplied by $x_0 e^{i\omega t}$, indicating that the displacement is periodic in time uniformly throughout the spine. The first term in the square brackets shows that there is a spatially periodic wave down the spine with the same crest length as the forcing wave. The summation term shows that in addition there are four spatial waves, composed of periodic and exponential terms, which for a given ω have a fixed spatial frequency, derivable from equation 5.14. How these endogenous waves react with the exogenous one stimulated by the water wave depends upon the spine length.

Equation 5.18 shows that when $k = 0$ then the coefficients C_j must also equal zero (since all μ_j are non-zero, and the overall sum of terms must equal zero). And when these results are substituted in equation 5.27 it is clear that the bending moment at zero wave angle must also be zero.

Equation 5.27 can be used to show how bending moment changes with spine stiffness. At resonance (m+added mass)ω^2 = (EI+added spring)k^4 and hence $k^2 \propto 1/\sqrt{EI}$. Also, from equation 5.14 all $\mu_j \propto 1/\sqrt{EI}$. Combining these results with equation 5.27 shows that the bending moment at resonance is $\propto \sqrt{EI}$.

5.5 Results

In the following four figures, the calculated beam response is compared with experiment. The form of the figures is similar to those of chapter 4 with plots of bending moments against spine length arranged in a 20 by 15 array of frequency and angle. The experimental data are plotted as points, while the calculated response is overplotted as a continuous line. Note that the high frequency/large angle corner of the array, disallowed in experiment, has now been calculated.

Figure 5.1 shows the results for the spine at a stiffness of 100Nm/rad in surge. Note firstly that the scale is twice that for the equivalent figure in chapter 5. The eye is drawn immediately to the area of greatest mismatch between theory and data, between 0.70 and 0.86Hz. The calculated response is both greater in overall magnitude - about twice the data - and the individual plots are considerably more peaky in shape. The attraction of the eye to this region is perhaps a little unfair - elsewhere the match of theory and data is quite close. Overall the position of resonance is correctly predicted, likewise the width of the resonance with angle. And in many places even the shape of the plots is correct. For example, 0.63Hz at 60 degrees, where the seven peaks are correct in size and shape and position. At higher frequencies, 1.64 - 1.95Hz, the smooth plot with one or two peaks at the downwave end is also correctly predicted in size and shape.

Figure 5.1

Continuous beam response; experimental data overplotted.
Surge bending moments. Spine stiffness 100Nm/rad.
Wave frequency 0.47–1.95Hz, wave angle 0–70 degrees.
Bending moment 0–10Nm versus joint position 0–16m.

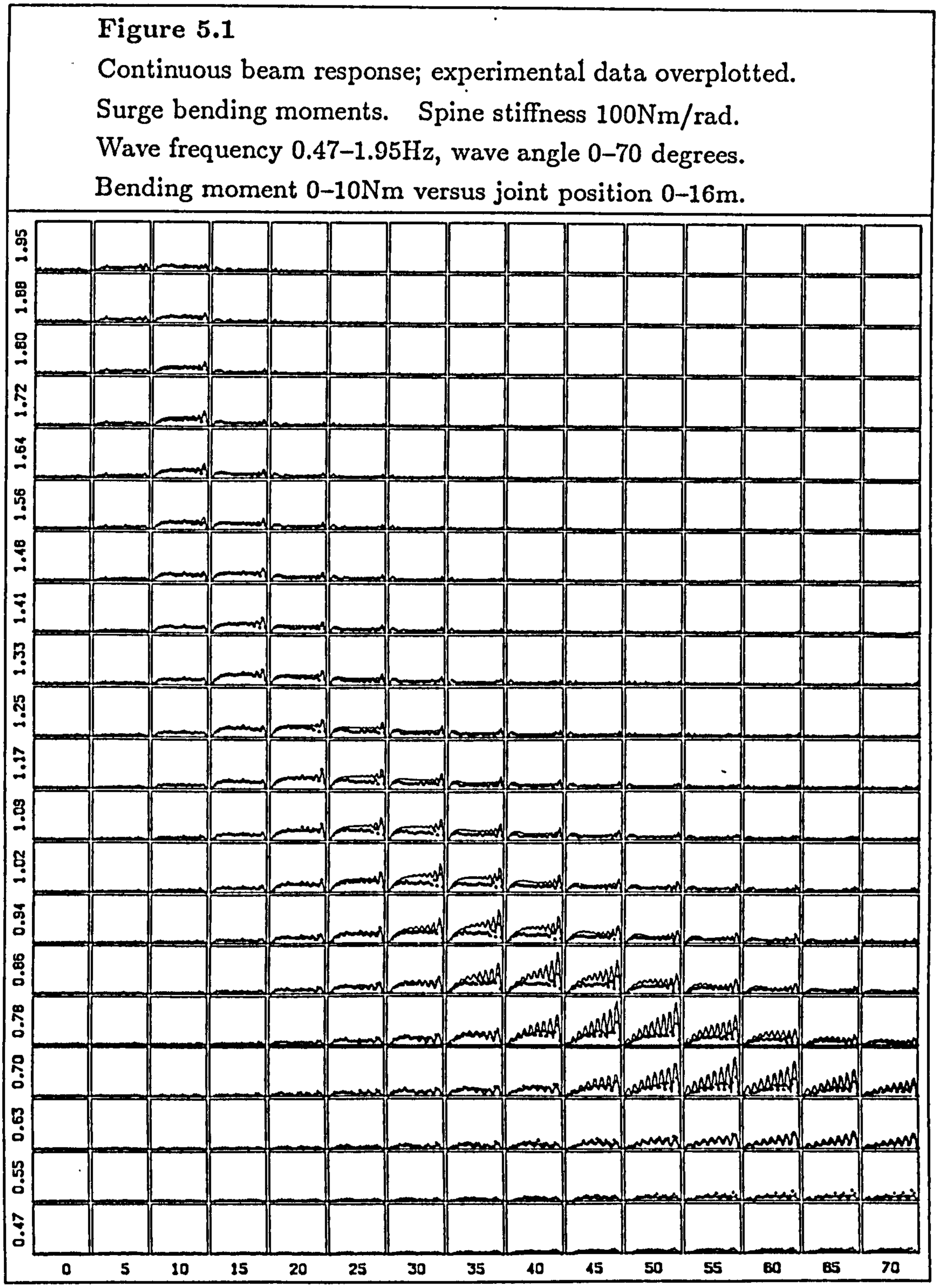

Figure 5.2 shows results for heave bending moment at 100Nm/rad stiffness. Note the scale: again theory overpredicts in places by a factor of two. Note that for a particular plot when the theory overpredicts the magnitude it also overpredicts the peakiness.

Overall the position and shape of the resonance in the array is correctly predicted, implying that the inclusion of buoyancy spring in the impedance of the cylinder has correctly influenced the calculation.

However, in general, the prediction of plot shapes is poor. The worst mismatch is around 1.41Hz, and as for the surge case, the mismatch is worst when a large number of peaks in the response are predicted. It should be remembered that the spine model is not continuous but segmented, with 19 heave joints and 20 surge. 19 joints is exactly sufficient to show 9 peaks - and no more. The implication is that the segmented spine is reaching the limit of its ability to resolve the spatial detail of the response.

Figure 5.2

Continuous beam response; experimental data overplotted.

Heave bending moments. Spine stiffness 100Nm/rad.

Wave frequency 0.47–1.95Hz, wave angle 0–70 degrees.

Bending moment 0–5Nm versus joint position 0–16m.

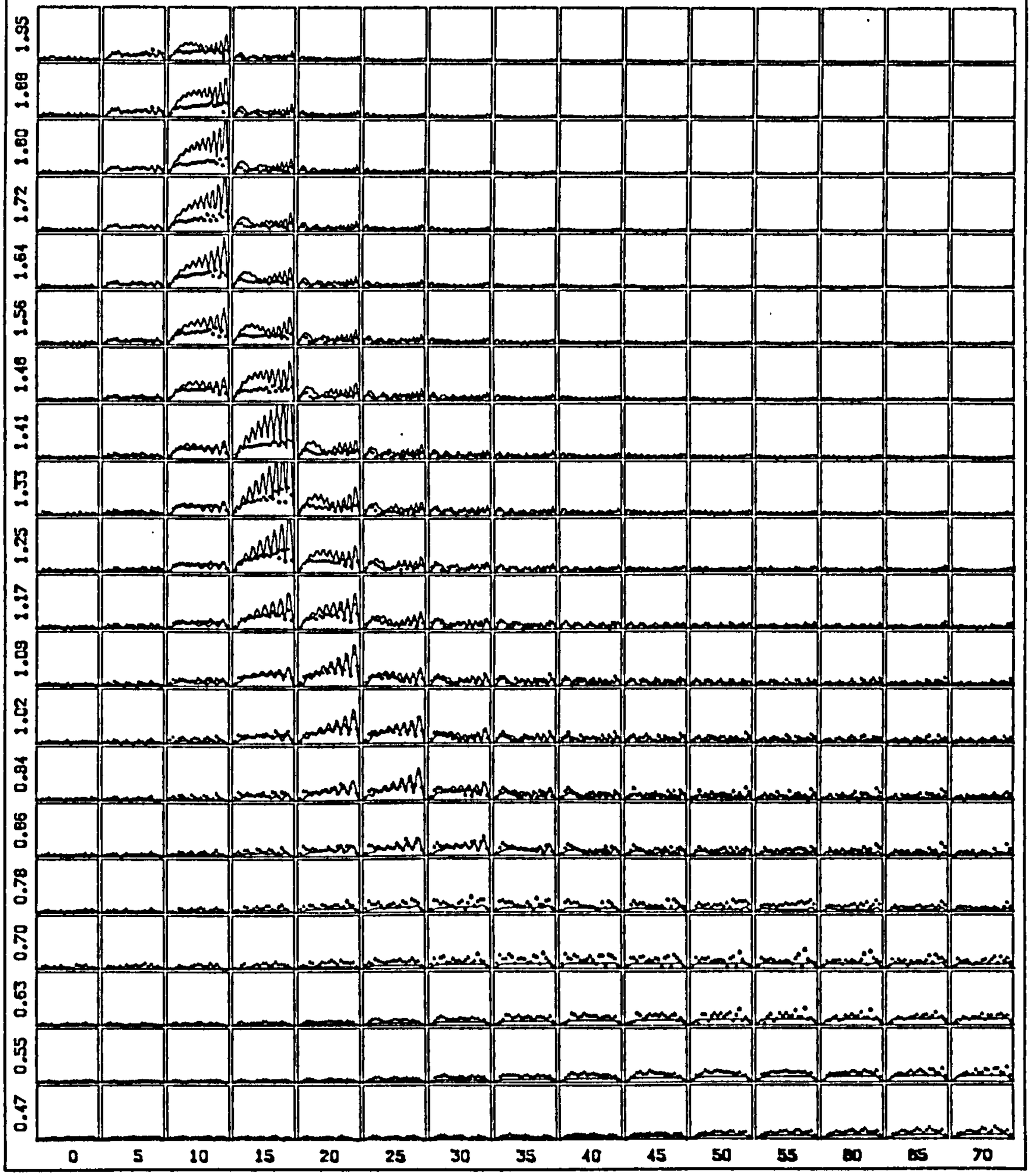

Figure 5.3 shows results for the spine at a stiffness of 1000Nm/rad in surge. Overall there is good correspondance between theory and data for the size and shape of the resonance in the array.

For the most part the agreement for the individual plot shapes is also good, although there is a conspicuous failure at 0.47Hz.

Figure 5.3

Continuous beam response; experimental data overplotted.

Surge bending moments. Spine stiffness 1000Nm/rad.

Wave frequency 0.47–1.95Hz, wave angle 0–70 degrees.

Bending moment 0–25Nm versus joint position 0–16m.

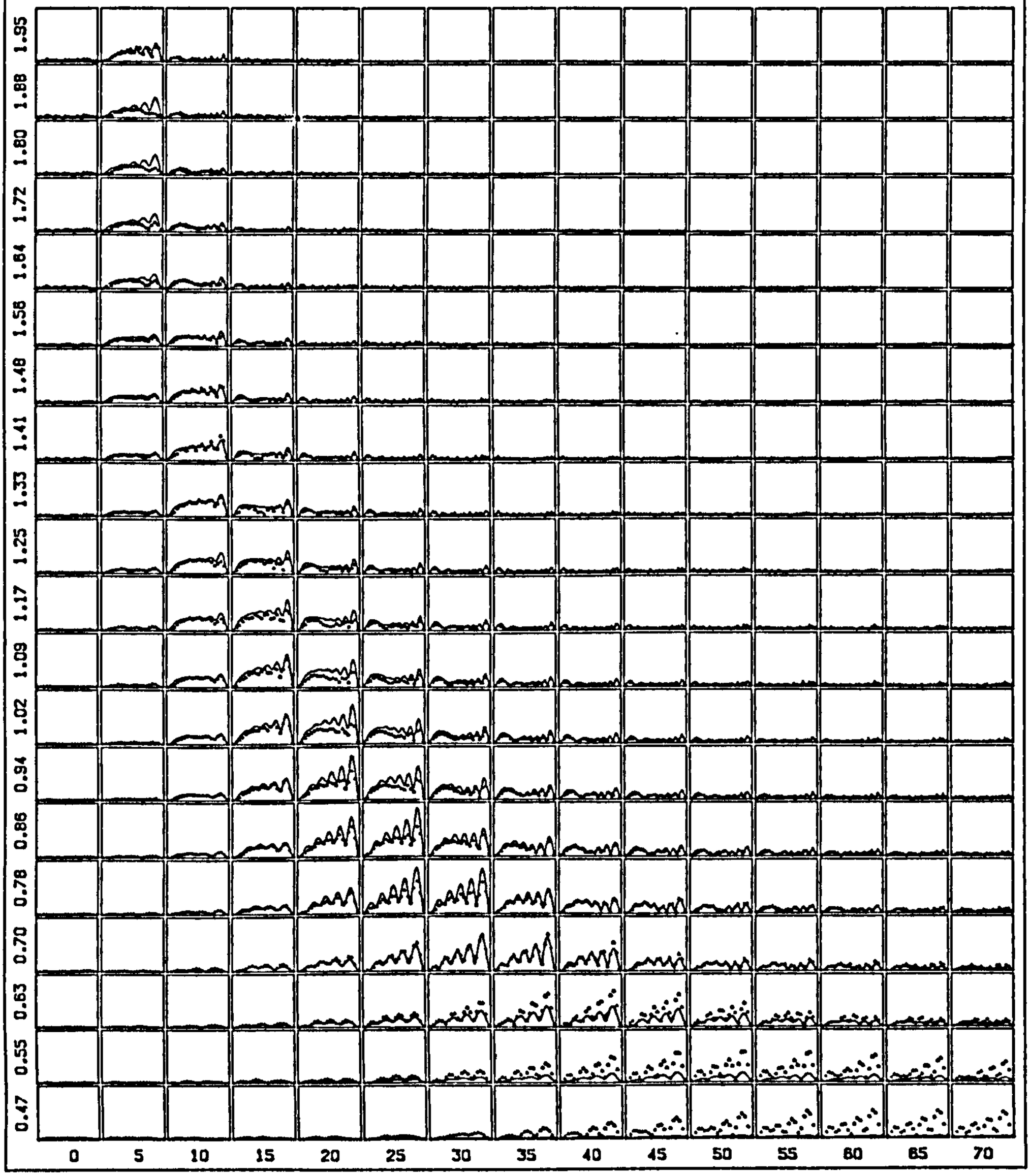

Figure 5.4 shows the results for the high stiffness case in heave. The agreement between theory and data for the position of the resonance in the array is good. However, the prediction of individual plot shape is worse than for surge. Note that, as before, when the theory overpredicts the magnitude of a plot - as at 1.80Hz - it also overpredicts the peakiness. And when it underpredicts magnitude - as at 0.47Hz - it predicts a smoother response than it should.

Figure 5.4

Continuous beam response; experimental data overplotted.
Heave bending moments. Spine stiffness 1000Nm/rad.
Wave frequency 0.47–1.95Hz, wave angle 0–70 degrees.
Bending moment 0–10Nm versus joint position 0–16m.

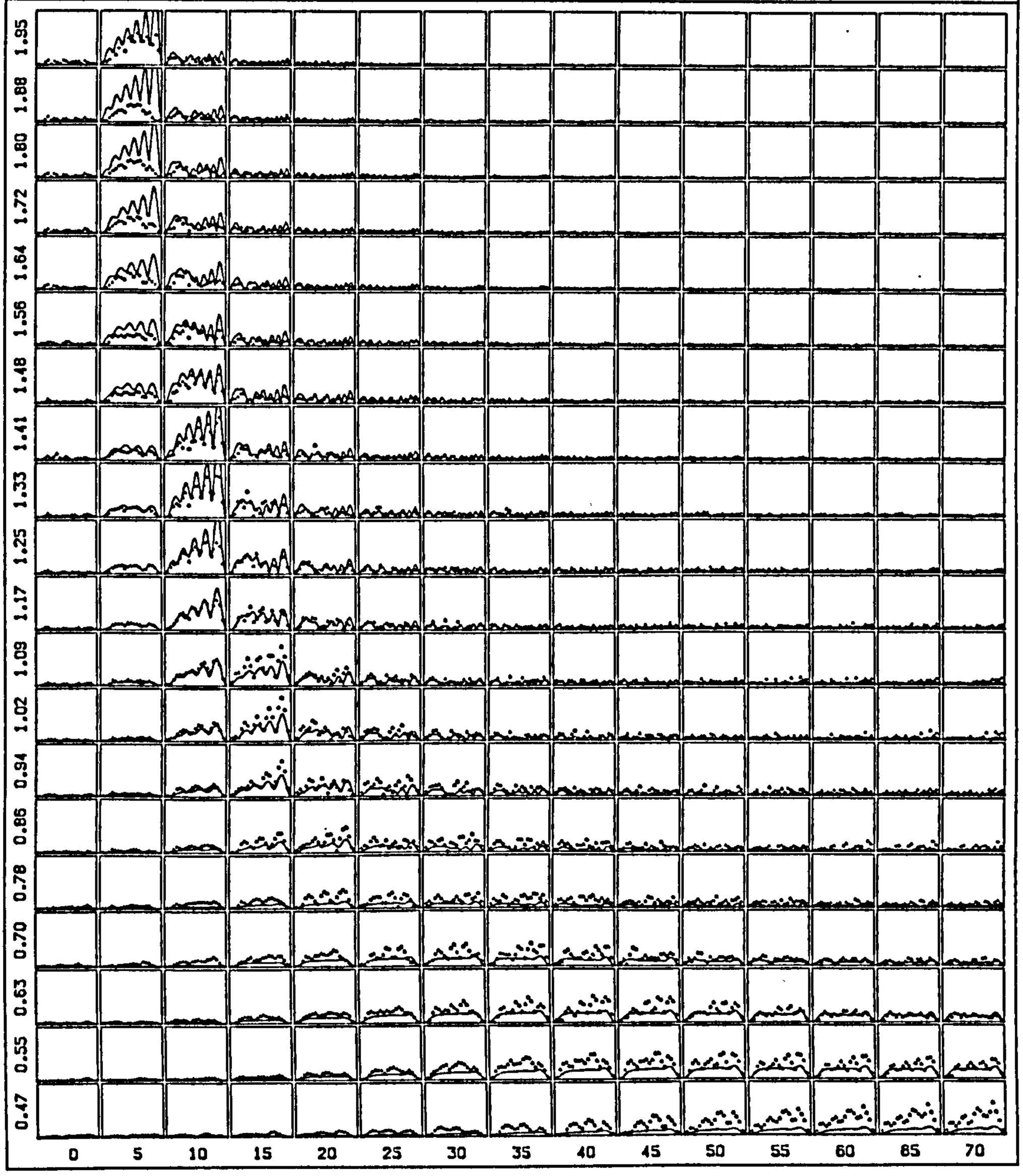

5.6 Conclusions

The continuous beam theory was combined with experimentally derived values of impedance and wave force coefficients for cylinders. The theory was used to calculate the bending moments in the spine over the same range of wave frequency and angle as used in chapter 4.

1. The beam theory accounts for the presence of a spine resonance at all frequencies in the range covered.

2. It shows how the wave angle which causes the resonance must increase as frequency decreases.

3. It predicts well the position and shape of the beam resonance with respect to wave frequency and angle.

4. It shows how the resonance must shift to smaller angles as the spine stiffness increases.

5. It correctly predicts the difference in the position of the beam resonance between heave and surge, suggesting that the incorporation of buoyancy forces into the cylinder impedance can increase the heave stiffness by significant amounts.

6. The theory indicates that the bending moment at resonance rises as the square root of beam stiffness. This agrees with the observed 3–4 fold increase in bending moment for the spine when its stiffness is increased from 100 to 1000 Nm/rad.

7. The theory predicts zero bending moment at zero degrees. It predicts no discernable bending moment for the high frequency/large angle waves that the tank is unable to produce.

8. The theory describes the displacement of the spine as a combination of travelling and standing waves. The standing waves account for the shape of the bending moment response down the length of the spine.

9. The continuous beam theory predicts plot shape fairly well. In some cases it fails because it predicts more detail than the segmented model can produce.

Chapter 6

A nodal model of the spine

SUMMARY

A discrete mathematical model of the spine is developed by consideration of the dynamics of one joint, then solving for the displacement of all joints in a matrix operation.

The model is combined with experimentally determined hydrodynamic coefficients, and bending moments are calculated which are compared with experiment.

6.1 Preamble

Chapter 5 compared spine experiments with analytic beam theory. The beam was assumed to be continuous, and slender. Timoshenko (1975) extends the theory by corrections for the rotation and shear of elements of the beam. In this chapter a discrete model of the spine will be developed which takes into account the facts that the spine is segmented not continuous; is not slender and therefore the rotational inertia must be accounted for; and that the joints can only bend, they cannot shear.

6.2 Definitions

Figure 6.1 shows a definition sketch of a portion of the spine in the plane x, y of the water surface. This notional spine is composed of N segments and $N+1$ joints, where joints 0 and N are the free ends. The following analysis treats each segment as a rigid body and determines the displacement x of the joints with respect to distance y along the spine. We begin by defining terms.

Each segment is of length h, mass μ and moment of inertia J. Z_T and Z_R are the translational and rotational hydrodynamic impedances of each segment. T_n and R_n are the translational and rotational wave forces on the nth segment. u_n is the velocity of the centre of the nth segment, θ_n is the angle the nth segment makes with the y axis and β_n is the angle the nth segment makes with the $(n-1)$th segment. Note that angles are positive clockwise. σ and δ are the stiffness and damping of each joint. F_n and M_n are the force and moment on the nth joint due to the $n+1$th. x_n is the displacement of the nth joint. The wave angle is α.

The impedance Z used in chapter 5 was a translational impedance per metre. Therefore, using the strip theory approximation

$$Z_T = Zh \tag{6.1}$$

and

$$Z_R = Z\int_{-h/2}^{h/2} y^2\,dy = \frac{Zh^3}{12} \tag{6.2}$$

The segment moment of inertia must take into account its finite radius. For a cylinder of radius r the moment of inertia about its centre is

$$J = \mu(h^2 + 3r^2)/12 \tag{6.3}$$

In chapter 3 weighted average values for W and Z were calculated for the spine; similarly, a composite radius is used in this calculation.

The spine is assumed to be exposed to a sinusoidal wave of angular frequency ω, whose direction of propagation makes an angle α with the x axis, and wavenumber k along the y axis. The spine is assumed to have reached a steady state, and so

Figure 6.1
Definition sketch for the spine nodal analysis.

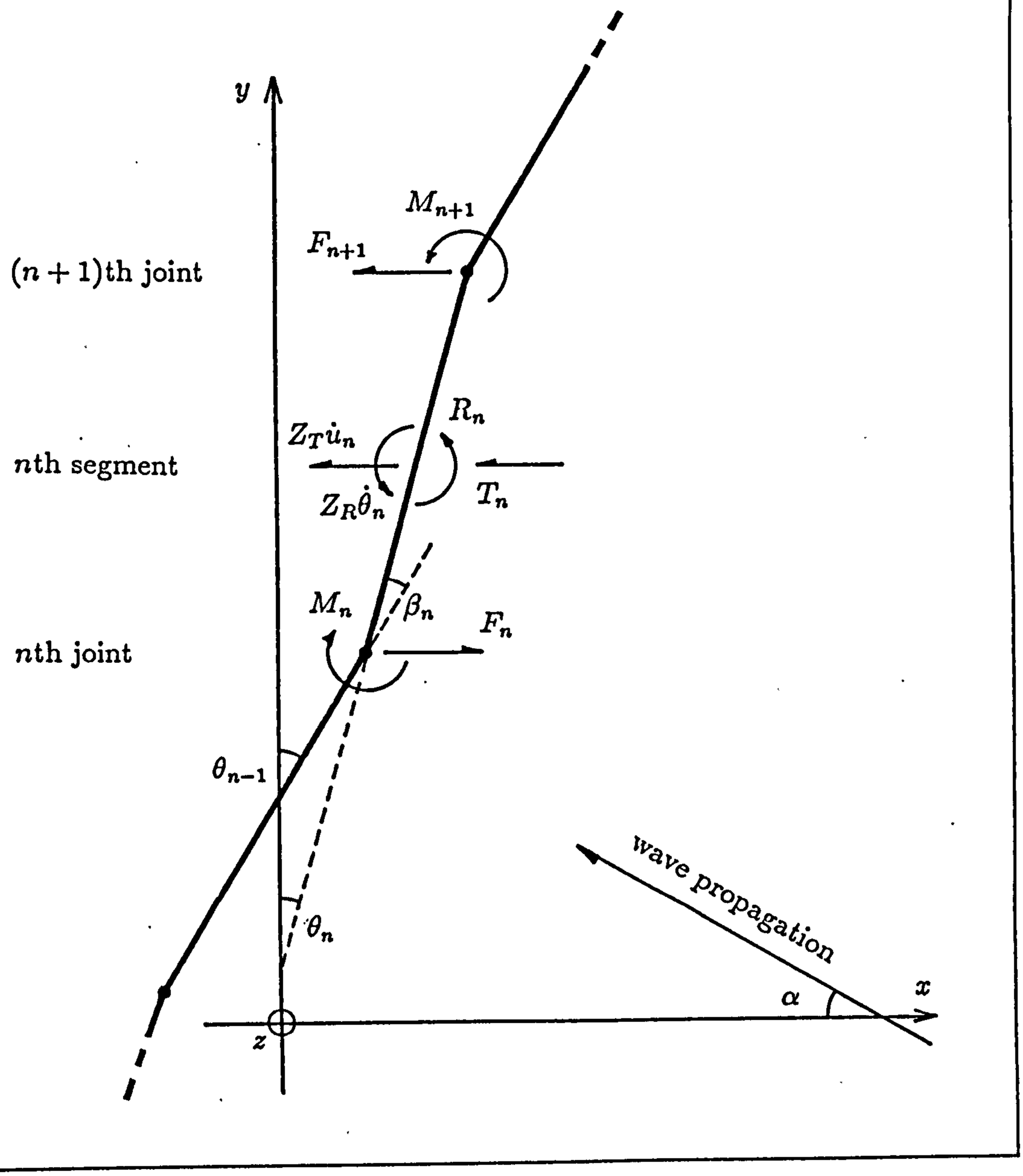

$$x_n = e^{i\omega t}\mathcal{F}(y) \tag{6.4}$$

$$\dot{x}_n = i\omega x_n \tag{6.5}$$

$$\ddot{x}_n = -\omega^2 x_n \tag{6.6}$$

$$u_n = i\omega(x_n + x_{n+1})/2 \tag{6.7}$$

These algebraic expressions for the time derivatives also apply to angle. Making the approximation for small angles the following definitions arise.

$$\theta_n = (x_{n+1} - x_n)/h = \frac{1}{h}\Delta x_n \tag{6.8}$$

$$\beta_n = \theta_n - \theta_{n-1} = (x_{n+1} - 2x_n + x_{n-1})/h = \frac{1}{h}\Delta^2 x_n \tag{6.9}$$

$$M_n = -(\sigma\beta_n + \delta\dot{\beta}_n) = -(\sigma\beta_n + \delta i\omega\beta_n) = \frac{\gamma}{h}\Delta^2 x_n \tag{6.10}$$

where $\gamma = -(\sigma + i\omega\delta)$

6.3 The equations of motion

Writing force and moment equations of motion for the nth segment

$$-F_{n+1} + F_n - Z_T u_n - T_n = \mu\dot{u}_n \tag{6.11}$$

and

$$-M_{n+1} + M_n - Z_R\dot{\theta}_n - R_n - \frac{h}{2}(F_n + F_{n+1}) = J\ddot{\theta}_n \tag{6.12}$$

F is the only quantity which cannot be calculated or expressed in terms of x, we proceed to eliminate F. Multiplying equation 6.11 by $h/2$ and subtracting equation 6.12 from it

$$\frac{h}{2}[2F_n - Z_T u_n - T_n] + M_{n+1} - M_n + Z_R\dot{\theta}_n + R_n = \frac{h}{2}\mu\dot{u}_n - J\ddot{\theta}_n \tag{6.13}$$

and multiplying equation 6.11 by $h/2$ and adding equation 6.12

$$\frac{h}{2}[-2F_{n+1} - Z_T u_n - T_n] - M_{n+1} + M_n - Z_R\dot{\theta}_n - R_n = \frac{h}{2}\mu\dot{u}_n + J\ddot{\theta}_n \tag{6.14}$$

But equation 6.14 also holds for $(n-1)$th segment, when $2 <= n <= N-2$.

$$\frac{h}{2}[-2F_n - Z_T u_{n-1} - T_{n-1}] - M_n + M_{n-1} - Z_R\dot{\theta}_{n-1} - R_{n-1} = \frac{h}{2}\mu\dot{u}_{n-1} + J\ddot{\theta}_{n-1} \tag{6.15}$$

and adding equation 6.13 to equation 6.15 to eliminate F

$$-\frac{h}{2}[Z_T(u_n+u_{n-1})+T_n+T_{n-1}]+M_{n+1}-2M_n+M_{n-1}+Z_R(\dot{\theta}_n-\dot{\theta}_{n-1})$$

$$+R_n-R_{n-1}=\frac{h}{2}\mu(\dot{u}_n+\dot{u}_{n-1})-J(\ddot{\theta}_n-\ddot{\theta}_{n-1}) \qquad (6.16)$$

Writing $\frac{h}{2}[T_n+T_{n-1}]-R_n+R_{n-1}=L_n$, and replacing M_n by $\gamma\beta_n$,

$$-\frac{h}{2}[Z_T(u_n+u_{n-1})]+\gamma[\beta_{n+1}-2\beta_n+\beta_{n-1}]+Z_R(\dot{\theta}_n-\dot{\theta}_{n-1})$$

$$-\frac{\mu h}{2}(\dot{u}_n+\dot{u}_{n-1})+J(\ddot{\theta}_n-\ddot{\theta}_{n-1})=L_n \qquad (6.17)$$

Replacing all time differentials with their appropriate algebraic substitutes, and all angles by difference expressions in x

$$-\frac{h}{2}[\frac{i\omega}{2}Z_T(x_{n+1}+2x_n+x_{n-1})]+\frac{\gamma}{h}\Delta^4x_n+\frac{i\omega}{h}Z_R\Delta^2x_n$$

$$+\frac{\omega^2\mu h}{4}(x_{n+1}+2x_n+x_{n-1})-\frac{\omega^2}{h}J\Delta^2x_n=L_n \qquad (6.18)$$

Writing $p=\gamma/h$, $q=(i\omega Z_R-\omega^2J)/h$, $r=\frac{h}{4}(\omega^2\mu-i\omega Z_T)$ and writing (by analogy with the difference operator) $\Sigma^2x_n=x_{n+1}+2x_n+x_{n-1}$ equation 6.18 becomes

$$p\Delta^4x_n+q\Delta^2x_n+r\Sigma^2x_n=L_n \qquad (6.19)$$

This may be written more explicitly as:

$$p[x_{n+2}-4x_{n+1}+6x_n-4x_{n-1}+x_{n-2}]$$
$$+q[x_{n+1}-2x_n+x_{n-1}]$$
$$+r[x_{n+1}+2x_n+x_{n-1}]=L_n \qquad (6.20)$$

and grouping terms in each x_n

$$px_{n+2}+\overbrace{(-4p+q+r)}^{s}x_{n+1}+\overbrace{(6p-2q+2r)}^{v}x_n+\overbrace{(-4p+q+r)}^{s}x_{n-1}+px_{n-2}=L_n \qquad (6.21)$$

for $2 <= n <= N-2$

6.4 End conditions

These are the same as in Chapter 5, namely that the moments and shears at the ends of the beam must be zero. $M_0 = M_N = F_0 = F_N = 0$.

MOMENTS

Rewriting equation 6.19

$$M_{n+1} - 2M_n + M_{n-1} + q\Delta^2 x_n + r\Sigma^2 x_n = L_n \tag{6.22}$$

and setting $n = 1$

$$M_2 - 2M_1 + 0 + q\Delta^2 x_1 + r\Sigma^2 x_1 = L_1 \tag{6.23}$$

but $2M_1 = p(2x_2 - 4x_1 + 2x_0)$, and $M_2 = p(x_3 - 2x_2 + x_1)$, so

$$\begin{aligned} &-p[2x_2 - 4x_1 + 2x_0] \\ &+p[x_3 - 2x_2 + x_1] \\ &+q[x_2 - 2x_1 + x_0] \\ &+r[x_2 + 2x_1 + x_0] = L_1 \end{aligned} \tag{6.24}$$

and grouping terms in each x_n

$$px_3 + \overbrace{(-4p + q + r)}^{s} x_2 + \overbrace{(5p - 2q + 2r)}^{a} x_1 + \overbrace{(-2p + q + r)}^{b} x_0 = L_1 \tag{6.25}$$

For the other end of the beam, setting $n = N - 1$

$$0 - 2M_{N-1} + M_{N-2} + q\Delta^2 x_{N-1} + r\Sigma^2 x_{N-1} = L_{N-1} \tag{6.26}$$

But $2M_{N-1} = p(2x_N - 4x_{N-1} + 2x_{N-2})$; and $M_{N-2} = p(x_{N-1} - 2x_{N-2} + x_{N-3})$

$$\begin{aligned} &-p[2x_N - 4x_{N-1} + 2x_{N-2}] \\ &+p[x_{N-1} - 2x_{N-2} + x_{N-3}] \\ &+q[x_N - 2x_{N-1} + x_{N-2}] \\ &+r[x_N + 2x_{N-1} + x_{N-2}] = L_{N-1} \end{aligned} \tag{6.27}$$

or

$$bx_N + ax_{N-1} + sx_{N-2} + px_{N-3} = L_{N-1} \tag{6.28}$$

The shear end-condition is used to rewrite equation 6.11 and 6.12. Setting $n = 0$

$$-F_1 + 0 - Z_T u_0 - T_0 = \mu \dot{u}_0 \tag{6.29}$$

and

$$-M_1 + 0 - Z_R \dot{\theta}_0 - R_0 - \frac{h}{2}(0 + F_1) = J\ddot{\theta}_0 \tag{6.30}$$

multiplying equation 6.29 by $h/2$ and subtracting equation 6.30

$$-\frac{h}{2}[Z_T u_0 + T_0] + M_1 + Z_R \dot{\theta}_0 + R_0 = \frac{h}{2}\mu \dot{u}_0 - J\ddot{\theta}_0 \tag{6.31}$$

Replacing time differentials by the algebraic equivalent in ω, and taking exogenous terms to the right-hand-side.

$$-\frac{h}{4} i\omega Z_T(x_1 + x_0) + \frac{\gamma}{h}\Delta^2 x_1 + \frac{i\omega}{h} Z_R(x_1 - x_0) + \frac{h}{4}\omega^2 \mu(x_1 + x_0)$$

$$-\frac{\omega^2}{h} J(x_1 - x_0) = \frac{h}{2} T_0 - R_0 \tag{6.32}$$

Substituting p, q, r as before

$$p[x_2 - 2x_1 + x_0]$$

$$q[x_1 - x_0]$$

$$r[x_1 + x_0] = \frac{h}{2} T_0 - R_0 \tag{6.33}$$

giving

$$p x_2 + \overbrace{(-2p + q + r)}^{b} x_1 + \overbrace{(p - q + r)}^{c} x_0 = \frac{h}{2} T_0 - R_0 \tag{6.34}$$

Similarly, at $n = N - 1$

$$0 + F_{N-1} - Z_T u N - 1 - T_{N-1} = \mu \dot{u}_{N-1} \tag{6.35}$$

$$-0 + M_{N-1} - Z_R \dot{\theta}_{N-1} - R_{N-1} - \frac{h}{2}(F_{N-1} + 0) = J\ddot{\theta}_{N-1} \tag{6.36}$$

multiplying equation 6.35 by $h/2$ and adding equation 6.36

$$-\frac{h}{2}[Z_T u_{N-1} + T_{N-1}] + M_{N-1} - Z_R \dot{\theta}_{N-1} - R_{N-1} = \frac{h}{2}\mu \dot{u}_{N-1} + J\ddot{\theta}_{N-1} \tag{6.37}$$

Replacing the time differentials by the algebraic terms in ω, and taking exogenous terms to the right-hand-side

$$-\frac{h}{4}i\omega Z_T(x_N + x_{N-1}) + \frac{\gamma}{h}\Delta^2 x_{N-1} - \frac{i\omega}{h}Z_R(x_N - x_{N-1}) + \frac{h}{4}\omega^2\mu(x_N + x_{N-1})$$

$$+ \frac{\omega^2}{h}J(x_N - x_{N-1}) = \frac{h}{2}T_{N-1} + R_{N-1} \tag{6.38}$$

and substituting p, q, r

$$p[x_N - 2x_{N-1} + x_{N-2}]$$

$$q[-x_N + x_{N-1}]$$

$$r[x_N + x_{N-1}] = \frac{h}{2}T_{N-1} + R_{N-1} \tag{6.39}$$

giving

$$cx_N + bx_{N-1} + px_{N-2} = \frac{h}{2}T_{N-1} + R_{N-1} \tag{6.40}$$

6.5 Wave loading

The experimentally determined value of the wave force coefficient, W, allows for the phase averaging of the wave around the circumference of the cylinder. In a three-dimensional wave it is also necessary to sum the phase variation over the length of the spine segment. In heave, the wave force per unit length of the cylinder is WA_0, and in surge, in a wave of angle α, it is $WA_0 \cos\alpha$. Representing the latter as F_s, expressions for the integrated force and moment on each spine segment are developed below.

Neglecting the small angle θ that the spine segment makes with the y axis, for the *force* on the nth segment

$$T_n = \int_{y_n}^{y_{n+1}} F_s e^{i(\omega t - ky)}\, dy = F_s e^{i\omega t} \int_{y_n}^{y_{n+1}} e^{-iky}\, dy \tag{6.41}$$

Taking the middle of the spine segment as a new origin, and changing variables

$$T_n = F_s e^{i\omega t} e^{-ikh(n+1/2)} \int_{-h/2}^{h/2} e^{-ik\eta}\, d\eta \tag{6.42}$$

$$T_n = F_s e^{i\omega t} e^{-ikh(n+1/2)} [-\frac{1}{ik}(e^{-ikh/2} - e^{ikh/2})] \tag{6.43}$$

giving

$$T_n = F_s e^{i\omega t} e^{-ikh(n+1/2)} \frac{2\sin(kh/2)}{k} \tag{6.44}$$

For the *moment* on the nth segment

$$R_n = \int_{y_n}^{y_{n+1}} [y - (y_n + y_{n+1})/2] F_s e^{i(\omega t - ky)}\, dy \tag{6.45}$$

As before, changing variables and integrating about the middle of the segment.

$$R_n = F_s e^{i\omega t} e^{-ikh(n+1/2)} \int_{-h/2}^{h/2} \eta e^{-ik\eta}\, d\eta \tag{6.46}$$

Integration of this product is simplified by recalling the earlier result

$$\frac{2\sin(kh/2)}{k} = \int_{-h/2}^{h/2} e^{-ik\eta}\, d\eta \tag{6.47}$$

And by differentiating with respect to k to give the required integral.

$$-i \int_{-h/2}^{h/2} \eta e^{-ik\eta}\, d\eta = \frac{d}{dk} \frac{2\sin(kh/2)}{k} = \frac{2k\frac{h}{2}\cos\frac{kh}{2} - 2\sin\frac{kh}{2}}{k^2} \tag{6.48}$$

So

$$\int_{-h/2}^{h/2} \eta e^{-ik\eta}\, d\eta = \frac{1}{-i}[\frac{h}{k}\cos\frac{kh}{2} - \frac{2}{k^2}\sin\frac{kh}{2}] \tag{6.49}$$

Giving

$$R_n = F_s e^{i\omega t} e^{-ikh(n+1/2)}[\frac{ih}{k}\cos\frac{kh}{2} - \frac{2i}{k^2}\sin\frac{kh}{2}] \tag{6.50}$$

The aggregate wave loading is given by

$$L_n = \frac{h}{2}(T_{n-1} + T_n) + R_{n-1} - R_n \tag{6.51}$$

$$\begin{aligned} L_n &= F_s e^{i\omega t}\frac{h}{k}\sin\frac{kh}{2}[e^{-ikh(n-1/2)} + e^{-ikh(n+1/2)}] \\ &\quad + F_s e^{i\omega t}\frac{ih}{k}\cos\frac{kh}{2}[e^{-ikh(n-1/2)} - e^{-ikh(n+1/2)}] \\ &\quad - F_s e^{i\omega t}\frac{2i}{k^2}\sin\frac{kh}{2}[e^{-ikh(n-1/2)} - e^{-ikh(n+1/2)}] \end{aligned} \tag{6.52}$$

But

$$e^{-ikh(n-1/2)} + e^{-ikh(n+1/2)} = e^{-ikhn}[e^{ikh/2} + e^{-ikh/2}] = e^{-ikhn}2\cos\frac{kh}{2} \tag{6.53}$$

$$e^{-ikh(n-1/2)} - e^{-ikh(n+1/2)} = e^{-ikhn}[e^{ikh/2} - e^{-ikh/2}] = e^{ikhn}2i\sin\frac{kh}{2} \tag{6.54}$$

and substituting these results in equation 6.52

$$\begin{aligned} L_n &= F_s e^{i\omega t}\frac{h}{k}\sin\frac{kh}{2}e^{-ikhn}2\cos\frac{kh}{2} \\ &\quad + F_s e^{i\omega t}\frac{ih}{k}\cos\frac{kh}{2}e^{-ikhn}2i\sin\frac{kh}{2} \\ &\quad - F_s e^{i\omega t}\frac{2i}{k^2}\sin\frac{kh}{2}e^{-ikhn}2i\sin\frac{kh}{2} \\ &= F_s e^{i\omega t}e^{-ikhn}\frac{4}{k^2}\sin^2\frac{kh}{2} \end{aligned} \tag{6.55}$$

Applying the end-conditions $T_{-1} = R_{-1} = T_N = R_N = 0$

$$L_0 = \frac{h}{2}T_0 - R_0 = F_s e^{i\omega t}e^{-ikh/2}[\frac{h}{k}\sin\frac{kh}{2} - \frac{ih}{k}\cos\frac{kh}{2} + \frac{2i}{k^2}\sin\frac{kh}{2}] \tag{6.56}$$

$$L_N = \frac{h}{2}T_{N-1} + R_{N-1} = F_s e^{i\omega t}e^{-ikh(N-1/2)}[\frac{h}{k}\sin\frac{kh}{2} + \frac{ih}{k}\cos\frac{kh}{2} - \frac{2i}{k^2}\sin\frac{kh}{2}] \tag{6.57}$$

6.6 Solving the equations

The equations are written in matrix form

$$\begin{pmatrix} L_0 \\ \vdots \\ \\ \\ \\ \\ \\ \vdots \\ L_N \end{pmatrix} = \begin{pmatrix} c & b & p & & & & & & \\ b & a & s & p & & & & & \\ p & s & v & s & p & & & & \\ & \ddots & \ddots & \ddots & \ddots & \ddots & & & \\ & & \ddots & \ddots & \ddots & \ddots & \ddots & & \\ & & & p & s & v & s & p & \\ & & & & p & s & a & b & \\ & & & & & p & b & c & \end{pmatrix} \begin{pmatrix} x_0 \\ \vdots \\ \\ \\ \\ \\ \\ \vdots \\ x_N \end{pmatrix} \tag{6.58}$$

which can be solved by elimination for all x_n

Making the appropriate changes in L, W and Z, the vertical displacements $z_0....z_N$ may similarly be calculated. The bending moments are then calculated from equation 6.10.

Note that the experimental model has 19 heave joints separating 20 segments each 0.8 m long. It is modelled as 21 nodes with a pitch of 0.8 m. In surge however there are 20 joints in the same spine length. To be exact, it should be modelled as 22 nodes, with the outer two nodes set at half the normal pitch from their neighbours. This would require rewriting the end-conditions for the equation, and instead the spine was modelled as 21 nodes, and the values for the 20 surge joints were interpolated.

6.7 Results

In the following four figures, the experimental data of chapter 4 are compared with the results predicted by the discrete spine theory.

Firstly it should be noted that the scales of the figures are the same as those of their counterparts in chapter 4. In other words, the overall predicted magnitude of the resonance is correct.

Figure 6.2 shows the results for surge bending moment at stiffness 100Nm/rad. The theory shows an excellent match with the data. The position of the resonance and its width match at every frequency. The shapes of the individual plots match the data extremely well except at the very lowest frequencies. The theory shows a noticeable failure to predict the single high peak in bending moment of the penultimate spine joint at the downwave end. This may be a consequence of the interpolation when calculating bending moments in surge. The anomaly is not apparent in heave.

Figure 6.3 shows the results for heave at low stiffness. The overall position and shape of the resonance within the array is correct, showing that again the difference from surge due to buoyancy is accounted for. The theory shows a rather poorer match for the individual plot shapes than in surge, but for both heave and surge, the discrete model does a good job of predicting plot peakiness, and the anomalies of the continuous beam theory are not repeated.

Figure 6.2

Discrete beam response; experimental data overplotted.

Surge bending moments. Spine stiffness 100Nm/rad.

Wave frequency 0.47–1.95Hz, wave angle 0–70 degrees.

Bending moment 0–5Nm versus joint position 0–16m.

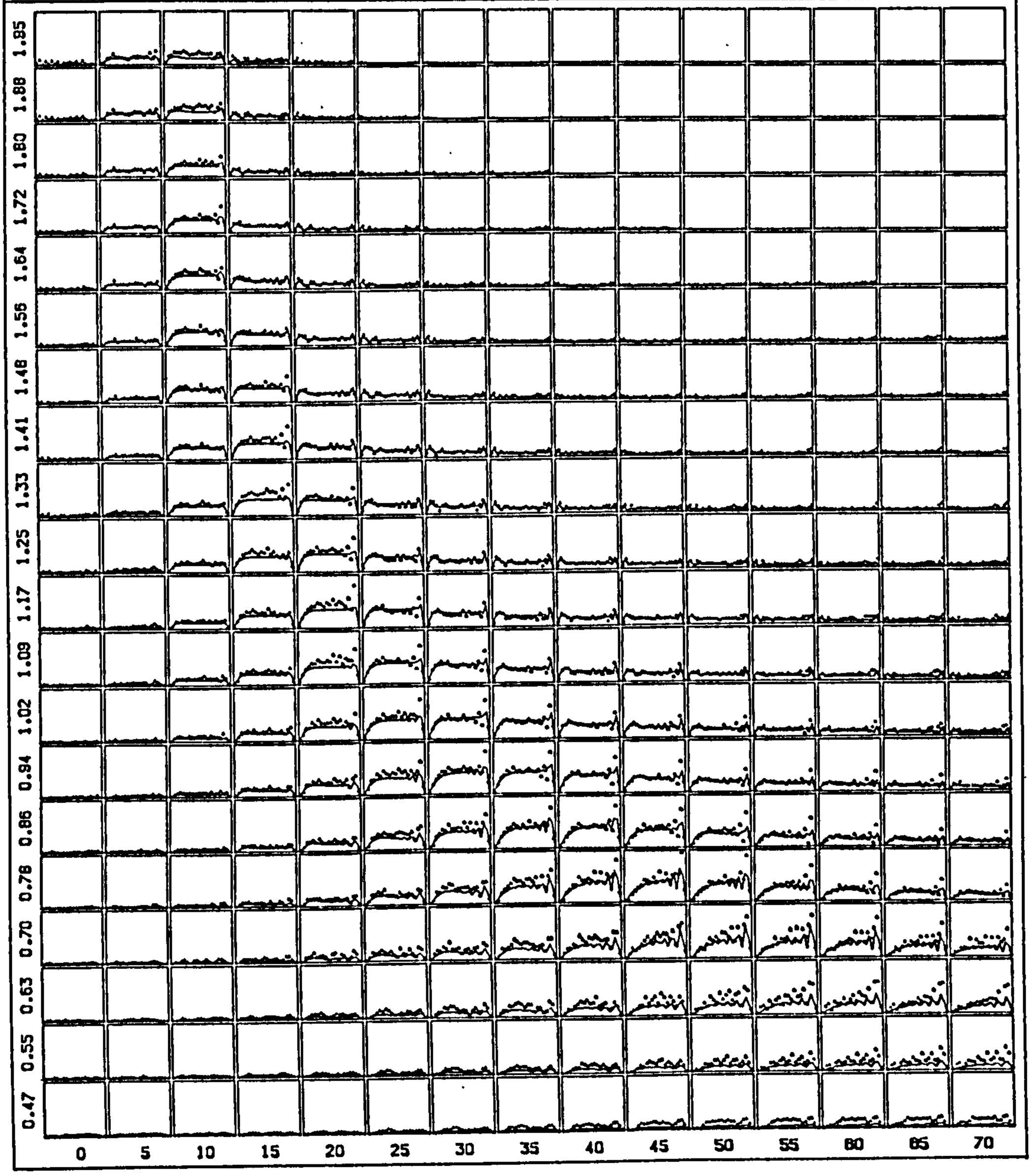

Figure 6.3

Discrete beam response; experimental data overplotted.
Heave bending moments. Spine stiffness 100Nm/rad.
Wave frequency 0.47–1.95Hz, wave angle 0–70 degrees.
Bending moment 0–3Nm versus joint position 0–16m.

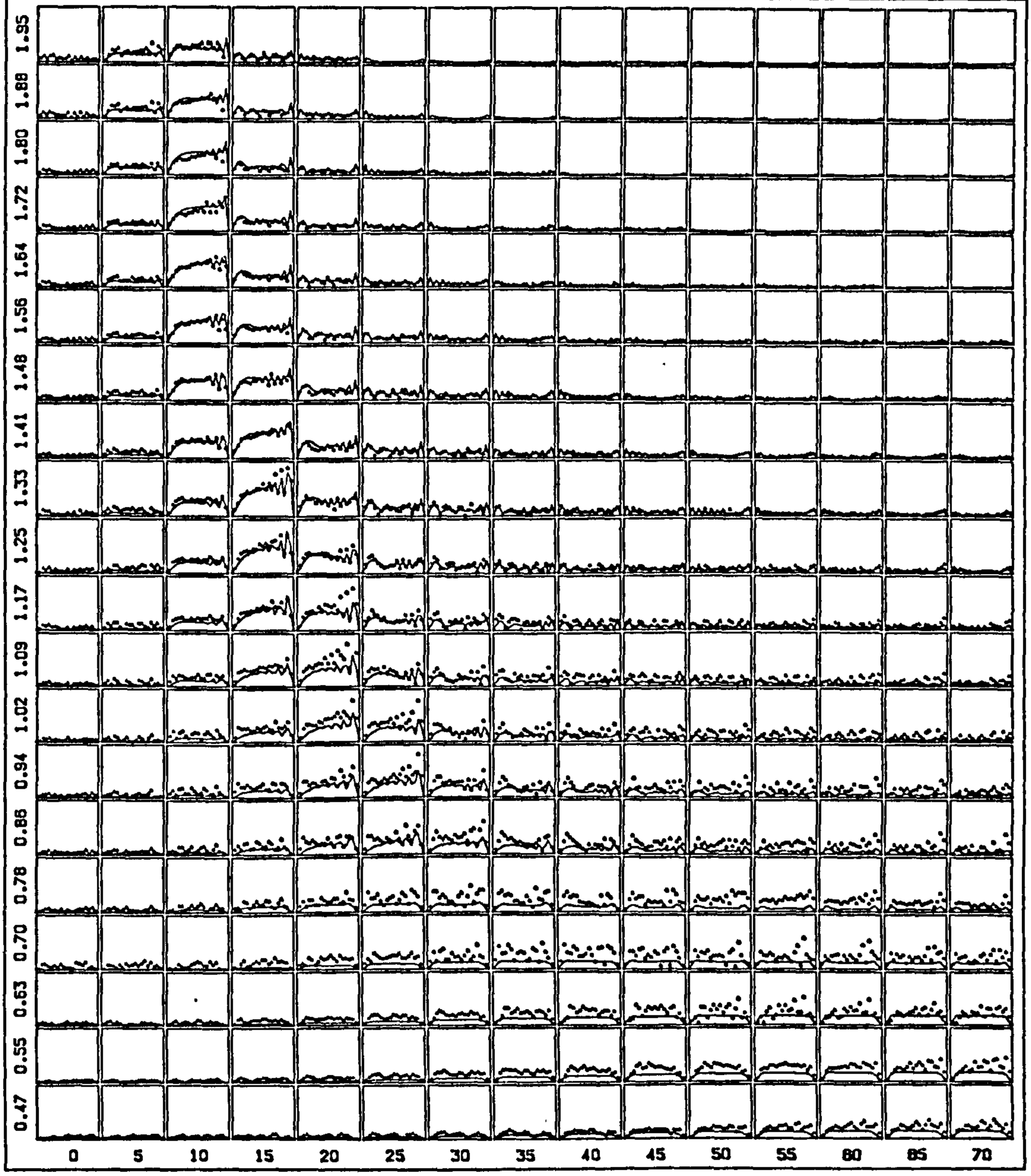

Figures 6.4 and 6.5 show the results at the higher stiffness of 1000Nm/rad. Again the fit is good, though somewhat better in surge. The mismatch in plot shape is greater at the very low frequencies, and as for the continuous beam theory, when the magnitude of a plot is overpredicted, then so is the peakiness. Because the position of the resonance in the array is correct, the inference is that all springs and added springs, masses and added masses have been correctly accounted for and it is the damping used in the prediction which is wrong. Theory underpredicts the magnitude and peakiness of the very low frequency plots, suggesting that the damping value used was too high.

Figure 6.4

Discrete beam response; experimental data overplotted.

Surge bending moments. Spine stiffness 1000Nm/rad.

Wave frequency 0.47–1.95Hz, wave angle 0–70 degrees.

Bending moment 0–20Nm versus joint position 0–16m.

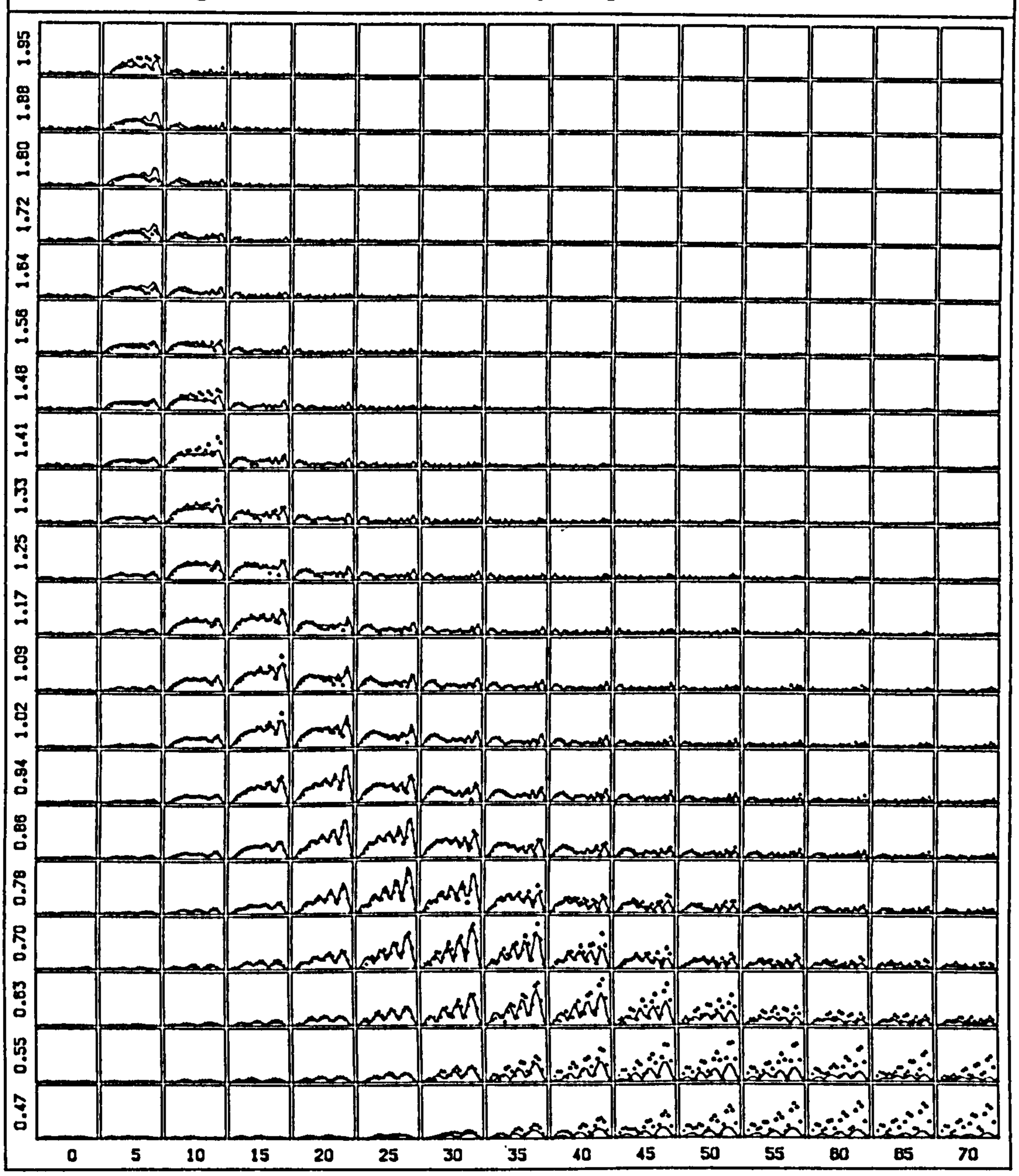

Figure 6.5

Discrete beam response; experimental data overplotted.

Heave bending moments. Spine stiffness 1000Nm/rad.

Wave frequency 0.47–1.95Hz, wave angle 0–70 degrees.

Bending moment 0–10Nm versus joint position 0–16m.

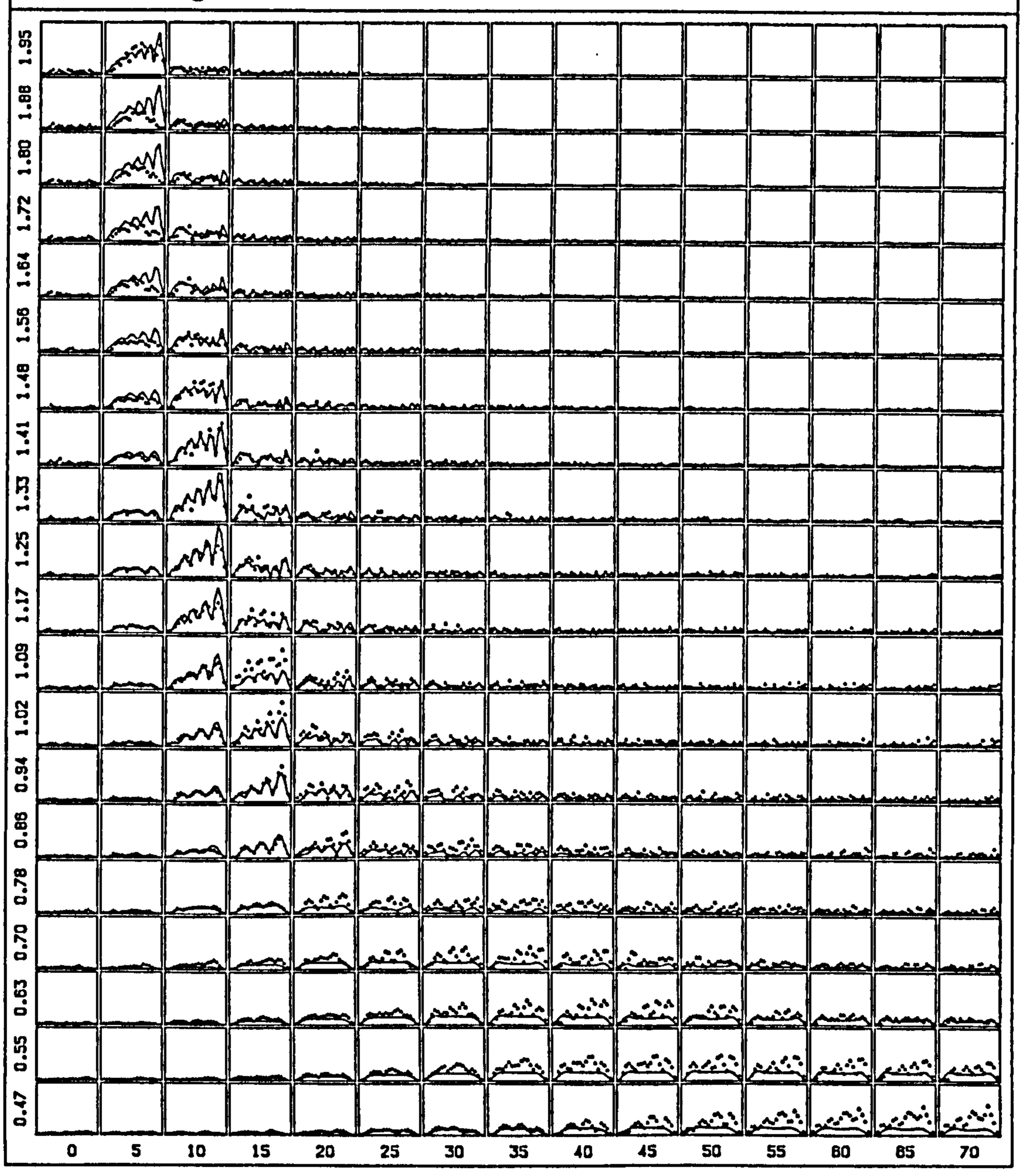

6.8 Conclusions

1. The nodal beam theory matches the performance of the continuous beam theory in predicting:

   a the position and shape of the spine resonance with frequency and angle;

   b the change in spine resonance with stiffness;

   c the differences between heave and surge.

2. It is much better than continuous beam theory at predicting the variation in bending moment down the length of the spine.

3. It correctly predicts the magnitude of the resonance, failing only at very low frequencies.

4. The failure of prediction at low frequencies is probably due to to a spurious non-linear damping in the spine model.

Chapter 7

An assessment of linearity

SUMMARY
Some non-linear contributions to forces on bodies in water are described. Linearity experiments in the 2D and 3D tanks are performed on fixed and moving cylinders.

7.1 Sources of non-linearity

The Laplace equation is linear, but often the boundary conditions applied to it are not. In Chapter 1, the free-surface boundary condition was linearised so that the treatment could proceed. It is possible to integrate the potential up to the true position of the free surface, and because orbital motions are larger at the crest than in the trough, there is a second-order drift force in the direction of wave travel. It is described by Stokes, and by Longuet-Higgins (1977). This is just one of many non-linear effects.

There are a number of non-linear theories—Stokes, cnoidal, stream function etc—which produce analytic or semi-analytic solutions for velocities in an irrotational fluid. The non-linearities are concentrated near the surface and bodies near the surface—such as the spine—will experience them more strongly. They are however small for small wave steepnesses. In this current work the wave steepness A/λ for the regular wave experiments ranged from 0.002 to 0.05 - compared with the wave-breaking limit of 0.14. In the mixed sea experiments of chapter 8 there was some wave breaking as waves of differing frequency and

angle instantaneously reinforced each other. Also waves were frequently caused to break due to the presence of the spine, thus producing high local fluid velocities.

Mehlum (1980) in his linear analysis of wave forces on a fixed cylinder notes a dramatic change in force as the cylinder approaches the free surface. This implies that for any finite amplitude wave, there will be non-linearity. This is corroborated by the results for the wave force coefficients in Chapter 3 where the shape and size of the graphs changes radically as the cylinder approaches and pierces the surface. This alerts us to potential non-linearity.

A surface piercing cylinder experiences buoyancy forces. Dixon et al (1979) show how the changing waterline area of a cylinder in finite waves results in a non-linear periodic buoyancy force. This predominantly second order force opposes the vertical inertial force on the cylinder, producing a mean downward force. Since the buoyancy force is enough to cancel the inertial force in heave at some frequencies, the relative nonlinear contribution at these frequencies will be high. The authors included the effect of the varying immersed volume of the cylinder (which will also affect surge forces) but did not pursue the analysis beyond zero freeboard, ie for overlapping waves, in order not to introduce a discontinuity in the derivative of force.

When the immersed volume of the cylinder changes, then so will the added mass. In their investigation of slamming forces on cylinders in the wave splash zone, Greenhow et al (1987) make use of the force equation due to the rate of change of added mass with vertical displacement.

$$F = -\frac{d}{dt}M\dot{z} = -\frac{dM}{dz}\dot{z}^2 - M\ddot{z} \tag{7.1}$$

which is non-linear. However, at the velocities and frequencies of waves in this work, slamming forces are some three orders of magnitude smaller than the inertial forces.

Chaplin (1984) found for an immersed cylinder whose axis depth equalled its diameter and whose non-dimensionalized radius $kD = 0.41$, that the wave force coefficent, when normalized by displaced mass, could be represented by

$$C_m = 2.25 - 0.58K^2 \tag{7.2}$$

where K = Keulegan-Carpenter number. The effect is due to fluid streaming

around the circumference of the cylinder and reacting with the fluid velocity due to the waves to produce a lift at right-angles to the velocity and in opposition to the wave inertial force. Only the smallest diameter section of the spine can permit circumferential streaming, and that only up to amplitudes of 11mm, $K = 0.78$, when the wave trough no longer covers that section of the spine and circulation is thus broken. The kD value of 0.41 implies a wave frequency of 1.08Hz. At the maximum amplitude this would therefore imply a 15% reduction in C_m—and that over only 13% of the spine length.

The non-linear part of Morison's equation, the force due to drag, should be negligible below K=1, because no vorticity should be generated. However, there are two instances in which the spine will generate vortices. The spine model is a series of cylinder segments, with sharp edges and protruding tubes and cables. The local K will be high, and vortex-shedding can be expected. These components however occupy relatively little volume. The second instance is more serious. The low spine freeboard allows early wave overlapping - earlier than one might guess because momentum carries water up the shallow slope of the spine top surface for wavè amplitudes well below the 7.5 mm freeboard. This rapid flow over the top of the cylinder meets flow of lower or even opposite velocity on the far side, and considerable vorticity can be observed in the cylinder lee. This vorticity is not only non-linear, but may also generate orthogonal force components - ie differences in horizontal velocity may generate vertical lift forces, or even axial ones if the vorticity is non-uniform along the cylinder axis. The presence of the cylinder is forcing a similar condition to wave breaking.

While there are numerical schemes which can model the behaviour of the water surface in breaking waves (eg Cokelet 1979) and their effects on objects at the surface (Greenhow et al 1982) because they are based on irrotational flows they cannot proceed beyond wave breaking. And again, while there are numerical solutions of the Navier-Stokes equation for rotational flow, these also fail for breaking waves and overlapping of immersed bodies because of difficulties in defining the boundaries of the computational volume.

7.2 An experimental assessment of non-linearity

An experiment to test linearity was performed in the 2D tank. The 125 mm cylinder was clamped rigidly at a freeboard of +7.5mm, the same as for the free-floating spine in the 3D tank. It was exposed to a range of amplitudes at 5 different frequencies, the latter spanned the frequency range previously used.

The parameters of the experiment are tabulated below.

Cylinder diameter	125 mm
Axis depth	55 mm
Number of samples	2048
sampling rate	40Hz
wait time	150 s
wave amplitude range	0.5 - 20 mm in 0.5mm steps
frequencies	0.39,0.78,1.17,1.56,1.95 Hz

As in previous narrow tank experiments, the order of tests was randomized. The long time between tests was required because of the mix of large and small amplitude experiments.

The 20 mm maximum wave amplitude was the largest possible for the lowest frequency with the constraint of wavemaker displacement, and also for the highest frequency with the constraint of wave breaking.

The wave force coefficient was calculated from the matrix equation

$$\underline{F} = \underline{\underline{W}}\,\underline{A} \tag{7.3}$$

Explicitly,

$$\begin{pmatrix} F_h \\ F_s \end{pmatrix} = \begin{pmatrix} W_{hh} & W_{hs} \\ W_{sh} & W_{ss} \end{pmatrix} \begin{pmatrix} A_h \\ A_s \end{pmatrix} \tag{7.4}$$

Which can be solved by measuring forces and wave amplitudes in two orthogonal experiments, ie two directions of wave.

$$\begin{matrix} & A_+ & A_- \\ \begin{matrix} \\ \\ \end{matrix} & \begin{pmatrix} F_{h+} & F_{h-} \\ F_{s+} & F_{s-} \end{pmatrix} \end{matrix} = \begin{pmatrix} W_{hh} & W_{hs} \\ W_{sh} & W_{ss} \end{pmatrix} \begin{matrix} \begin{matrix} A_+ & A_- \end{matrix} \\ \begin{pmatrix} A_{h+} & A_{h-} \\ A_{s+} & A_{s-} \end{pmatrix} \end{matrix} \tag{7.5}$$

Where, as in Chapter 3, the second set of experiments, ie, that with the wave direction reversed, was constructed by reversing the sign of the second column and second row in the force and amplitude matrices. Note that this construction forces the cross-terms of the wave force coefficient to be zero.

The modulus of the wave force coefficient was calculated for heave and surge at each of the 40 amplitudes and 5 frequencies. The results are plotted in Figure 7.1. Since the cross-terms are zero they are not shown. Waveforce coefficient is plotted against wave amplitude, for each of the 5 frequencies. If the system were linear, the coefficient would have a constant value.

The results for surge indicate that only the lowest frequency shows linearity. The other curves show a deviation from constancy beginning above an amplitude of about 4 mm, and is greatest for the 1.17 Hz case. The curves show a sharp drop, which tends to level out with higher amplitude, as though the wave force coefficient were tending towards a new constant value, some 50% of the initial value in the 1.17Hz case. The 4mm amplitude level was the point at which waves began to overlap the cylinder.

In heave, the picture is more complicated. The curves show less deviation from constancy (about 25%) than for surge, but in many cases the coefficient actually increases. The most striking example of this is the 1.17Hz case, which starts and ends around zero, but has a positive value of 50N/m around the 7.5mm mark. The curve for the 0.78Hz case is almost the inverse, showing a minimum at 7.5mm wave amplitude. The other curves show a steady decline with amplitude.

It is probable that there will be similar non-linear effects on the impedance of the cylinder to motion in the fluid. And it is also possible that when the cylinder is allowed to move when exposed to waves, there will be a change—possibly even a reduction—in the non-linearity of the cylinder response because the difference between the instantaneous wave elevation and the position of the cylinder is no longer maintained.

In order to discover how much the spine bending moments deviate from linearity with wave amplitude, two experiments were performed. In the first experiment, the spine was exposed to a wave of constant frequency and angle, but rising amplitude.

Figure 7.1

Linearity: wave force coefficient against wave amplitude.

125mm diameter cylinder, 295mm long, +7.5mm freeboard.

Wave frequencies: 0.39Hz, 0.78Hz, 1.17Hz, 1.56Hz, 1.95Hz.

+ × △ □ ○

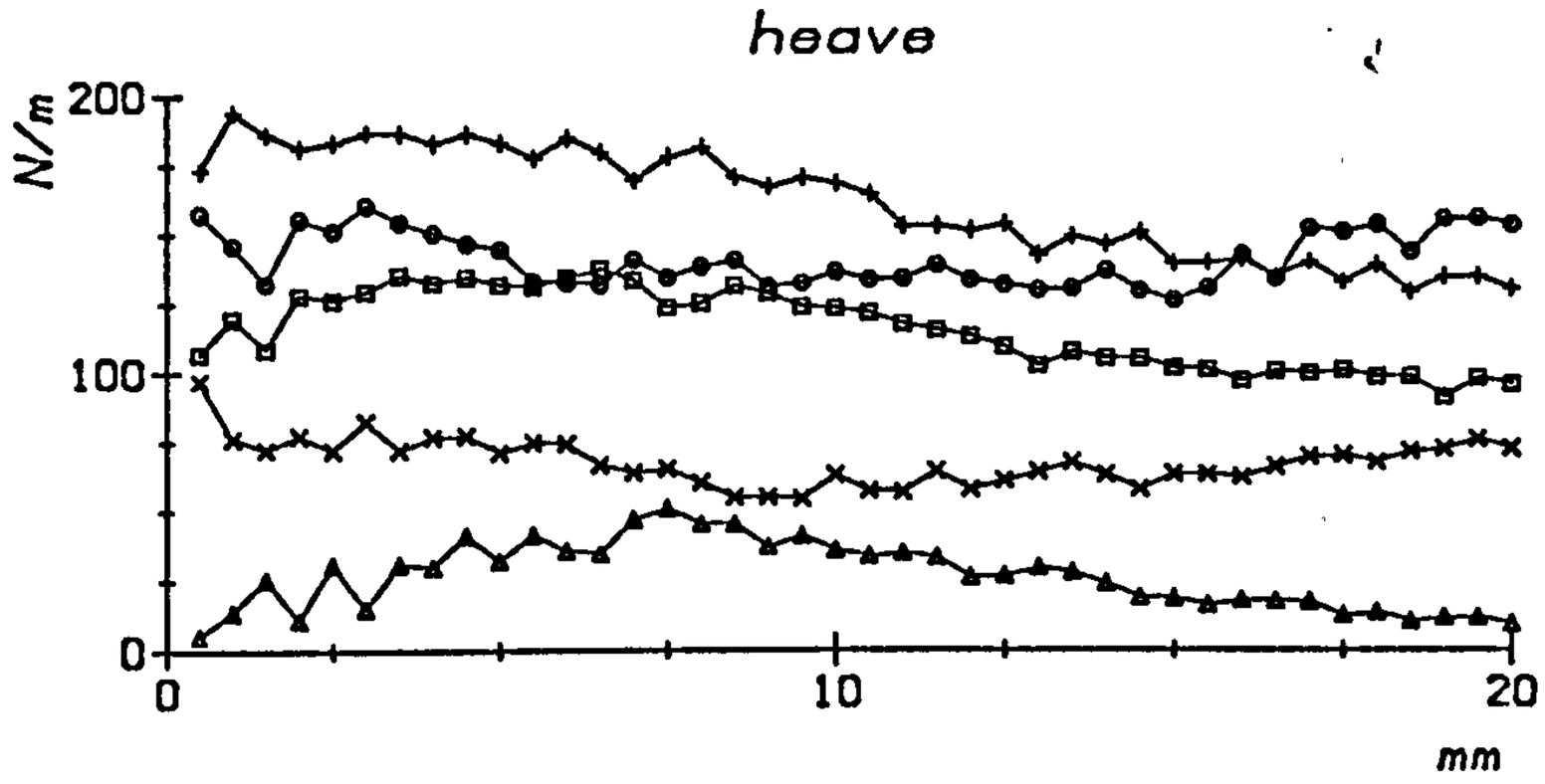

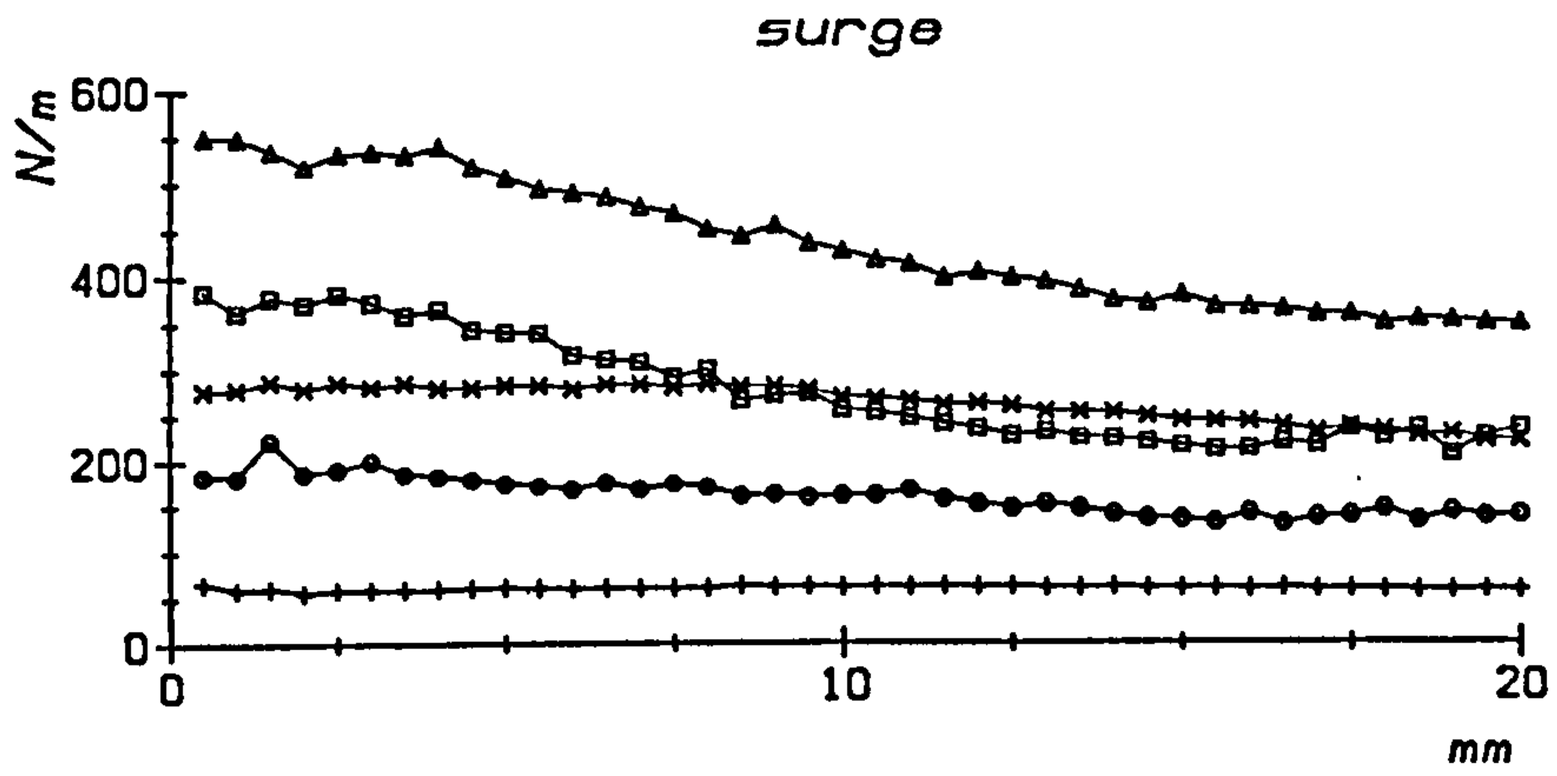

The experimental parameters are recorded below.

number of samples	256
sampling rate	20Hz
wait time	30 s
spine stiffness	1000 Nm/rad
wave frequency	1.016 Hz
wave angle	18 degrees
wave amplitude	1.25 - 40.0 mm in 1.25 mm steps

The samples were Fourier transformed, and the response at the same frequency as the exciting wave calculated. An average was taken of the bending moments over the whole length of the spine, separately in heave and surge, and divided by the wave amplitude. In this and the next experiment the wave amplitudes were measured with the waves rerun and the spine out of the water.

The results are plotted in Figure 7.2. The plot for heave shows a shallow peak around 20mm amplitude. The variation is about ±25%. By contrast, the surge plot shows a steady decline to about 60% of its low amplitude value.

Figure 7.2

Linearity: average spine bending moment against wave amplitude.
Wave frequency 1.02Hz.

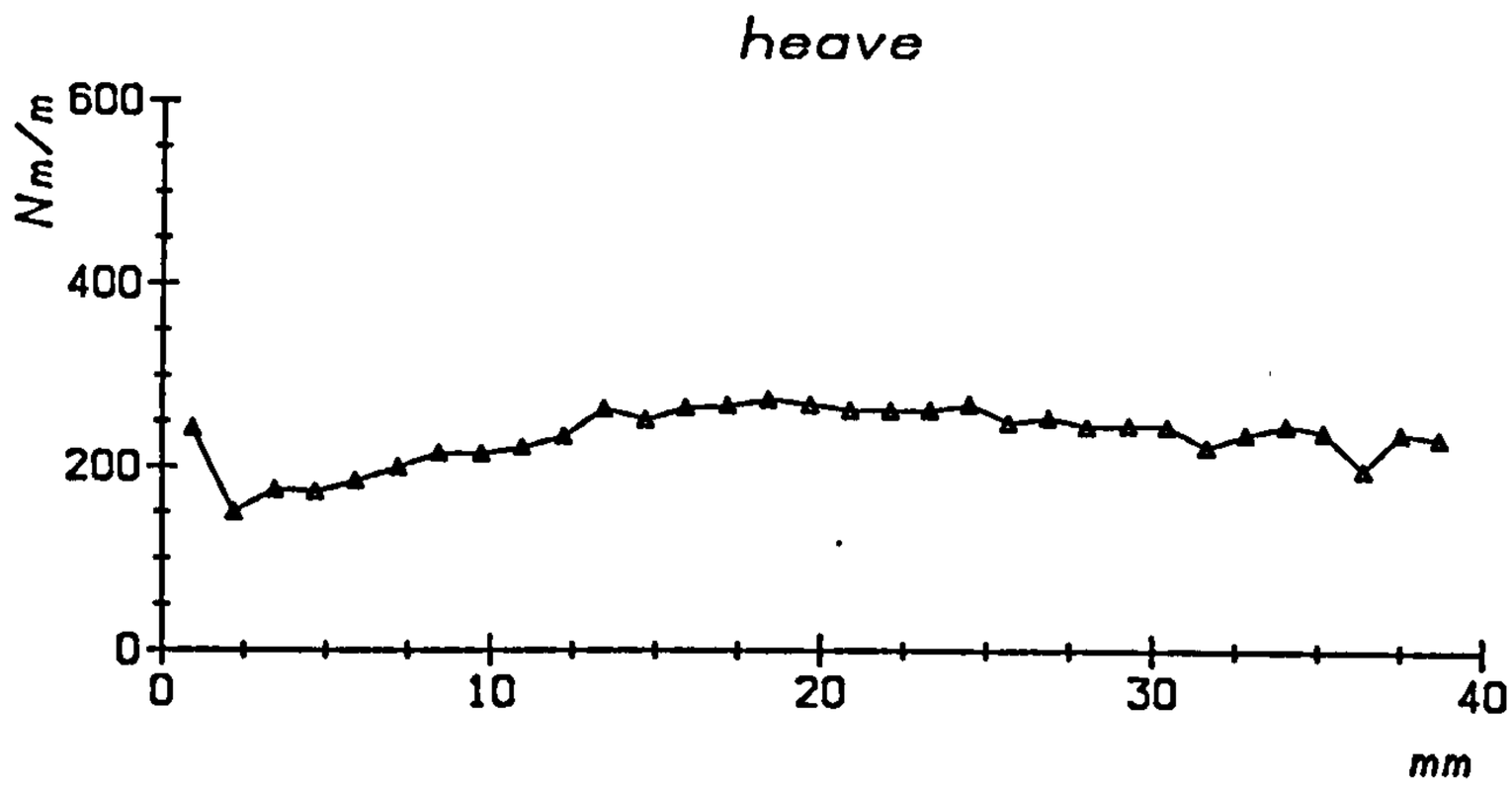

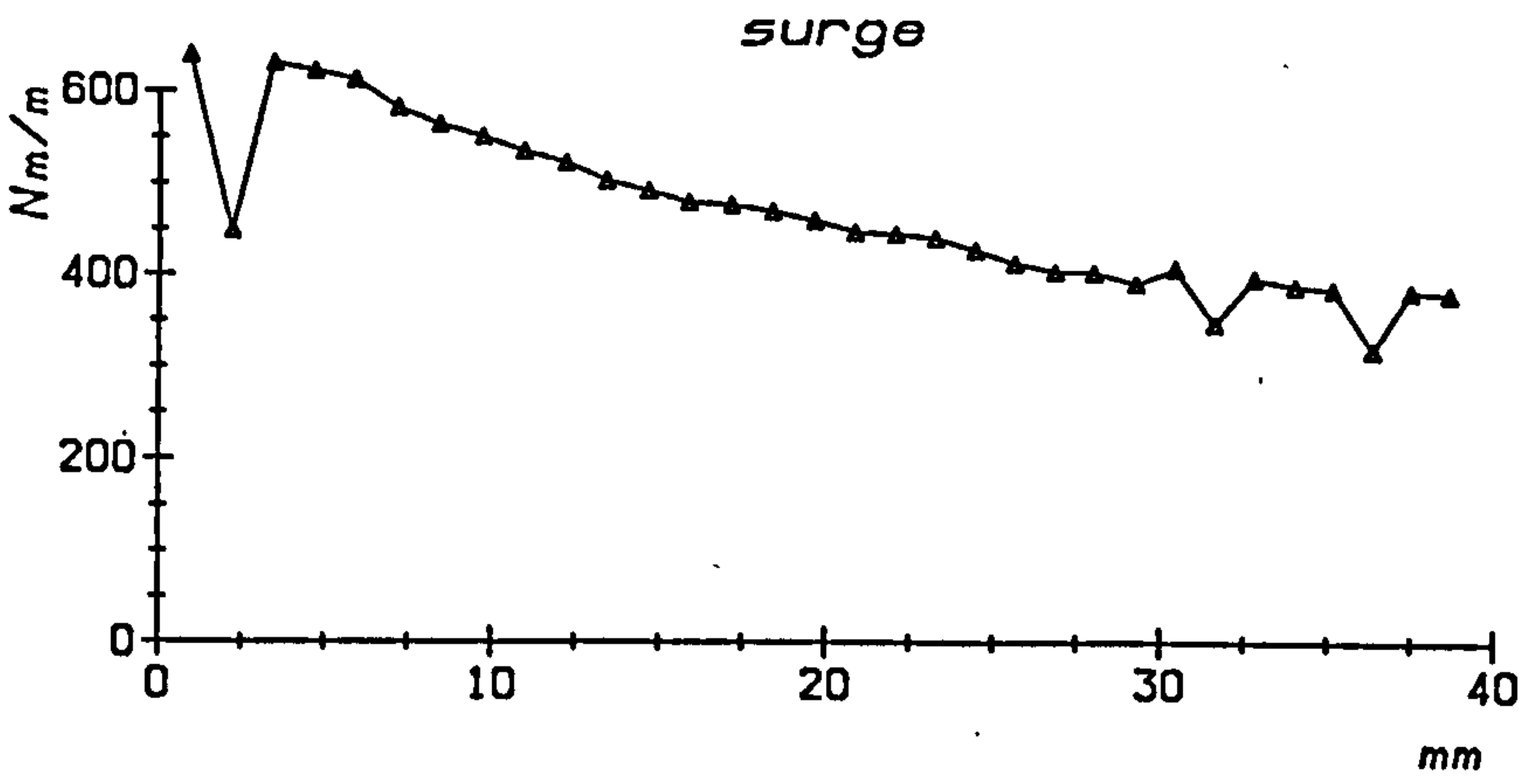

A final experiment exposed the spine to a mixed sea of increasing amplitude. The sea chosen was a Pierson-Moskowitz with a cosine squared directional spreading function, which provided a large number of components in the high response region of the spine.

The experimental parameters are recorded below.

number of samples	256
sampling rate	20Hz
wait time	30 s
spine stiffness	1000 Nm/rad
sea type	1 second Pierson-Moskowitz
directional spreading	$\cos^2(\theta - \theta_0)$
sea amplitude range	0.88 - 28.2 mm rms

The range of the root-mean-square of the wave amplitude was designed to approximate that of the previous experiment. The H_{rms} of the largest amplitude is twice the Pierson-Moskowitz norm for that T_e.

In this case a Fourier analysis is inappropriate, and the root-mean-square bending moment is calculated for each spine joint, and the rms for all the joints, separately in surge and heave taken for the spine. The plot of rms bending moment divided by rms wave amplitude is shown in figure 7.3.

The curve for heave shows a rapid initial drop, then a fairly constant level over most of the range. It is essentially linear. The curve for surge shows a consistent decrease with wave amplitude, ending at about 50% of its low amplitude value, indicating substantial non-linearity.

Figure 7.3

Linearity: average spine bending moment against H_{rms}.

1 second Pierson-Moskowitz sea; cosine-squared angular spread.

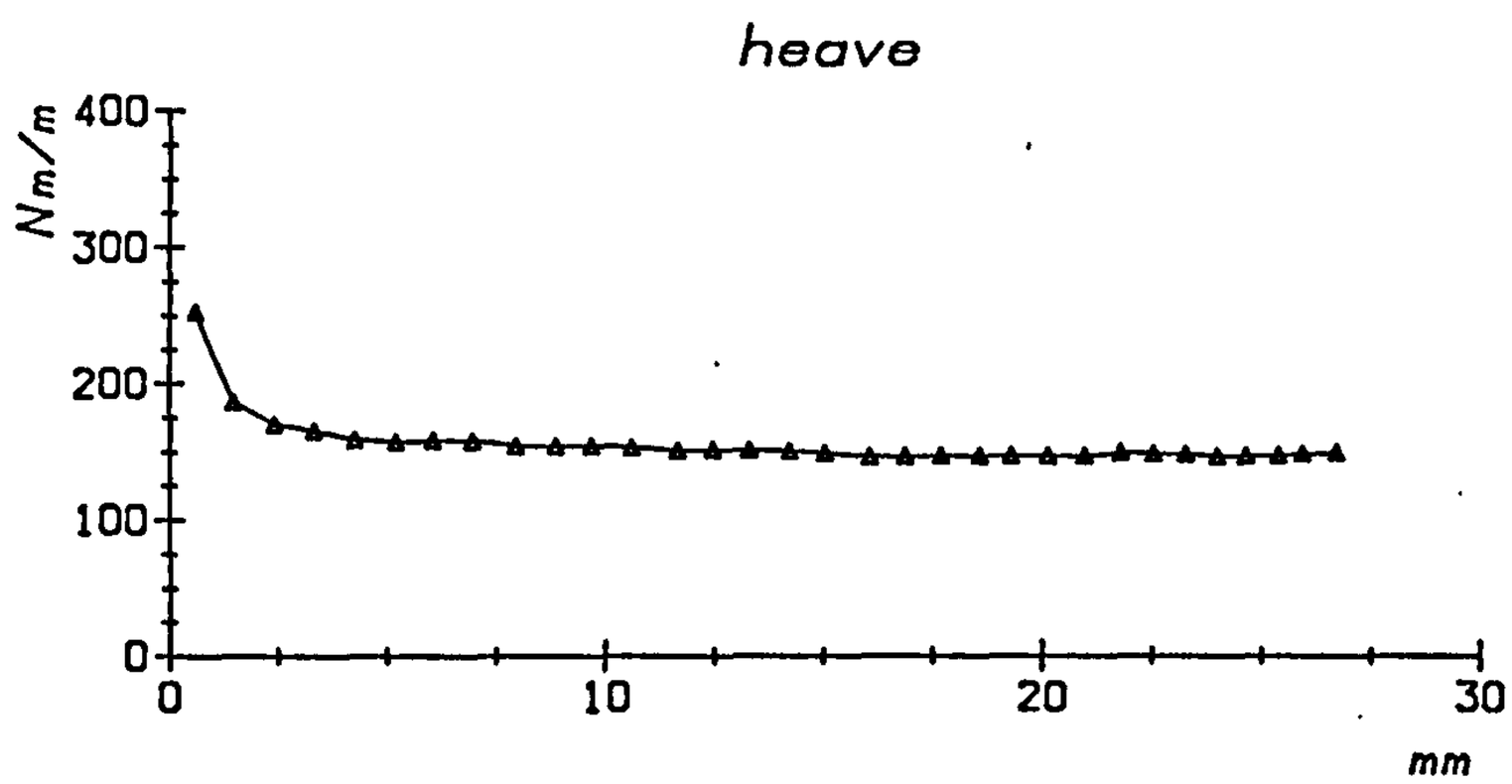

7.3 Conclusions

1. The wave force coefficients in heave and surge for a fixed cylinder in a number of regular wave frequencies are amplitude dependent.

2. The probable main cause of the non-linearity is wave-overlapping. The effect is apparent for wave amplitudes above 4mm, the point at which overlapping was observed to occur.

3. Bending moments in the spine when subjected to a 1Hz angled wave and allowed to move also show non-linearity in heave and more in surge.

4. Bending moments in the spine allowed to move in a mixed sea show a smoother change with amplitude.

5. In the mixed sea, the spine shows good linearity in heave. In surge the bending moments in the largest sea are about half that expected from a linear extrapolation from the smallest.

Chapter 8

The spine response in mixed seas

SUMMARY
The synthesis and selection of a set of directional wave spectra from observed ocean conditions are described.
Experiments and computer modelling of the spine response in this set of mixed seas are carried out.

8.1 Wave data

In March 1976 the Institute of Oceanographic Sciences deployed a Datawell Waverider buoy in 42 m of water 13 km west of South Uist in the Outer Hebrides. Wave height data were recorded in 1024 second samples at 3 hourly intervals. The buoy did not measure directional data.

Nearby, at the Benbecula anemograph station, wind speed and direction data were recorded as hourly mean values. In addition, sets of bivariate histograms describing the distribution of hourly mean wind speed and direction based on ten years sets of data, and broken down by seasons were available.

The three categories of data were combined to produce an estimate of the distribution of wave heights with frequency and direction intended as a representation in the long-term. The synthesis is described by Crabb (1980), and is summarised here.

The wind histograms were used as the basis of data selection. The frequency of occurrence in each wind speed/direction cell was multiplied by 400 in order

to produce 100 representatives per season. The closest match to these representatives was then found in the hourly wind data for that season. The nearest wave sample in time to that was then chosen as the wave representative. If no valid wave data existed, another wind representative was chosen.

Each wave sample was Fourier analysed, and its spectrum correlated with associated meteorological information. Three types of sea were identified.

- Local wind sea: the local wind was assumed to have generated a spectrum down to a lower frequency limit dependent on its scale in space and time. Waves lower in frequency were regarded as non-local. Local wind sea was deemed to have Mitsuyasu directionality.

- Old wind sea: if the wind had recently changed significantly in speed or direction the wind sea spectrum was assigned to previous local conditions.

- Swell: waves of low frequency and low directional spread, due to distant storms. These were identified by a low frequency associated with a change over time in that low frequency due to dispersion. The extent of the dispersion indicated the distance of the storm, and this was then checked with large-scale meteorological data to assign a probable generating storm, and hence direction for the swell. The angle subtended by the storm front at the location of the buoy determined the angular spread.

The consequence of using the long-term wind histograms is to weight the wave data also towards the long-term for wind seas. The inclusion of swells is random, but probably annually typical because of the seasonal selection of wind data.

The process of selection resulted in 399 evenly weighted spectra (1 less than 400 due to rounding errors) representative of the annual South Uist wave climate.

8.2 The 46 spectra

Subsequently the IOS produced a subset of the 399 spectra for the Department of Energy to facilitate wave energy research. Sea states which contributed little to the annual energy available were excluded. The 267 remaining spectra were sorted into a 4 dimensional histogram whose variates were:

- frequency width
- direction width
- energy period
- power density

This resulted in 46 occupied cells. One representative was chosen from each cell, resulting in 46 spectra, which appropriately weighted accounted for 76.5% of the total energy of the 399 spectra.

Mollison (1983) recalculates this data for four water depths, accounting for the effects of the sea bottom topography and friction on wave energy and direction.

Clearly the calculation and production of the 46 spectra from the water surface elevation raw data through to implementation in the 3D tank is a process of estimation and approximation. The spine bending moments are a function of the amplitude, frequency, and direction of the wave, so relying on sea state data whose directionality is not measured but hindcast is unsatisfactory. However, if the experiments with the spine in mixed seas can be shown to agree well with a theoretical model, then that model can be used with better data when it arrives.

The 46 spectra can be taken as representative of most South Uist conditions, but extreme waves have been excluded.

8.3 The 46 spectra in the 3D tank

The scale chosen is 107.7:1. Mollison's 1983 recalculation of the data for 100m water depth is used. This is not quite appropriate since the 3D tank is 1.2m deep, equivalent to 129m water depth. Pierson-Moskowitz spectra (equation 1.31) are used to represent each of the sea types (wind or swell). These are modified by a frequency compression factor which adjusts the spectral width to match that in the spectrum specified by IOS. The directional spreading is deemed to be Mitsuyasu (equation 1.34) for new wind seas. For old wind sea and for swell the spreading function is given by

$$S(\theta) = C(s)\cos^{2s}(\frac{\theta - \theta_0}{2}) \tag{8.1}$$

where θ_0 is the directional heading of the sea and $C(s)$ is a normalization coefficient given by

$$C(s) = 1/\int_{-\pi}^{+\pi} \cos^{2s}(\frac{\theta - \theta_0}{2}) \tag{8.2}$$

For old wind sea $s = 6$, and for swell s varies from 6 to many thousands. In general, s increases from new wind sea through old wind sea to swell, and the energy period, T_e, also increases.

The implementation is discrete, with 74 or 75 frequencies (depending on rounding) being assigned to each spectrum, with one angle assigned to each frequency. The frequency range is 0.5 to 3.0Hz, and -70 to +70 degrees. Portions of the spectra which are outside the frequency/angle limits of the wavemakers will generate secondary fronts. However, there are relatively few of these and their effects are small.

Figure 8.1 shows wavefront plots of the 46 spectra with frequency and angle. At the top left of each graph is the IOS sea number, at top right is its root-mean-square wave height (H_{rms}) in mm at tank scale. Each wavefront on a plot is represented by a blob whose area is proportional to the wave amplitude; the density of the plot thus gives an indication of the sea size. For many of the sea states their composition of more than one sea type is clearly apparent. For example sea 360 shows a broad wind sea and a compact swell. It is clear that while the H_{rms} of the spectra follows a general rise with IOS number, the frequency and angle distributions are very varied.

8.4 Experiments

The experimental procedure was similar to that described in Chapter 4, with the same attention paid to the condition of the spine before any test was undertaken.

Figure 8.1

The South Uist 46 spectra: wavefront plots.

Frequency 0.5–3.0Hz; angle -70→+70 degrees.

IOS number top left; model scale H_{rms} top right.

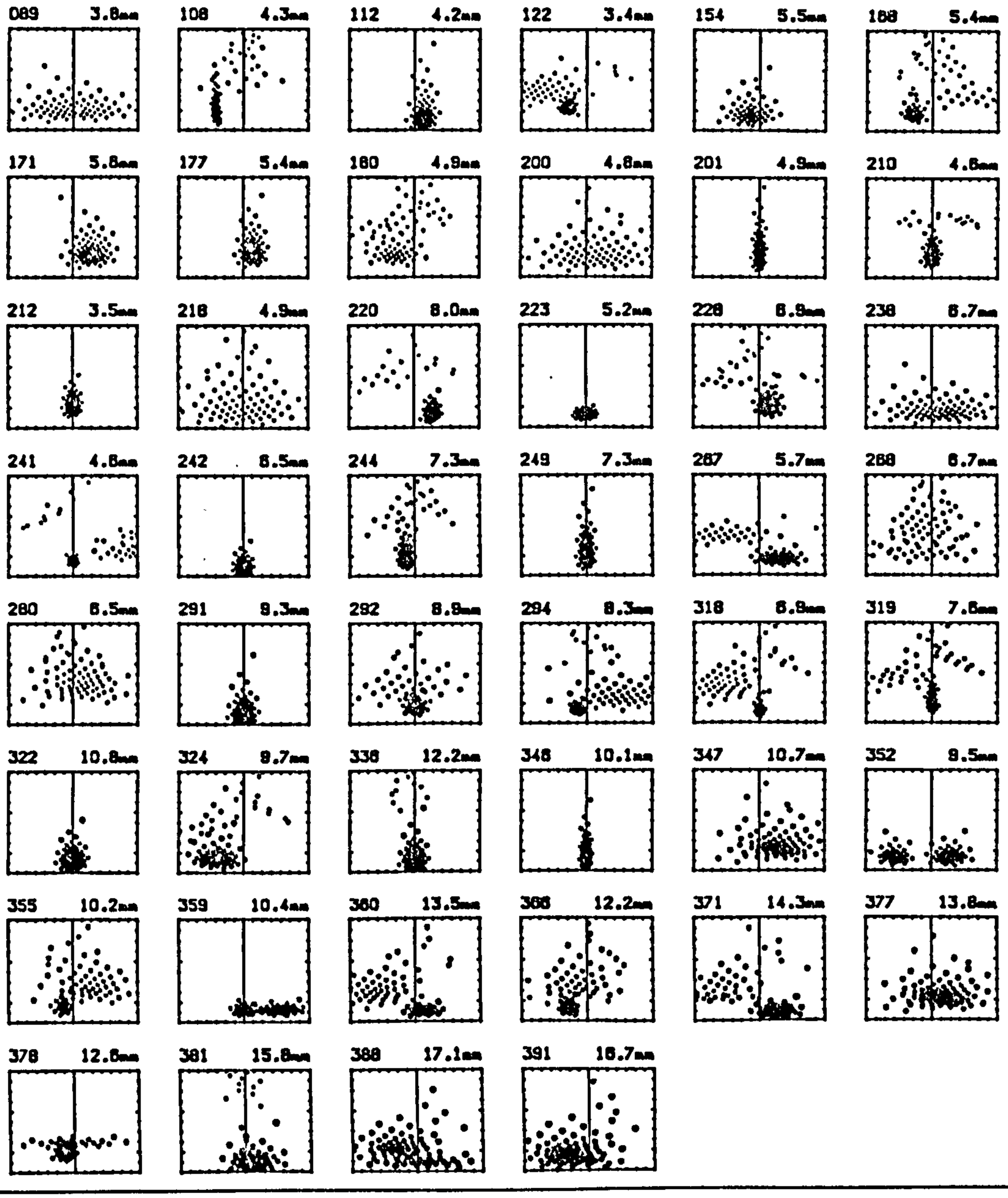

The experimental parameters are recorded below.

number of samples	1024
sampling rate	20Hz
spine stiffness	100 and 1000 Nm/rad
sea type	46 spectra
wait time	20 s

Because the nature of these seas is pseudo-random, a long sampling period of 51.2 seconds was used to ensure that the bending moment average would be close to the long-term average.

8.5 Results

Because for these experiments mixed seas were used, Fourier filtering of the torque records is not appropriate. Instead, root-mean-square values were calculated. Figure 8.2 shows the bending moment response of the spine at a stiffness of 100Nm/rad as a plot of the heave and surge average bending moment in the spine (ie the root-mean-square value of all the readings from all the spine joints in the sampling period) plotted against the sea root-mean-square wave height (Hrms). It can be seen that the scatter is substantial, with average bending moment varying by up to a factor of 5 in surge, and 2.5 in heave for seas with very similar values of Hrms.

In Figure 8.3 the equivalent plot for a stiffness of 1000Nm/rad is shown. The stiffness has increased by a factor of 10, and the bending moments accordingly have increased by about $\sqrt{10}$. The scatter is very slightly lower than at the lower stiffness. But it is clear that sea Hrms is a very poor indicator of spine bending moment.

Figure 8.2

Spine average bending moment against H_{rms}.

Spine stiffness 100Nm/rad.

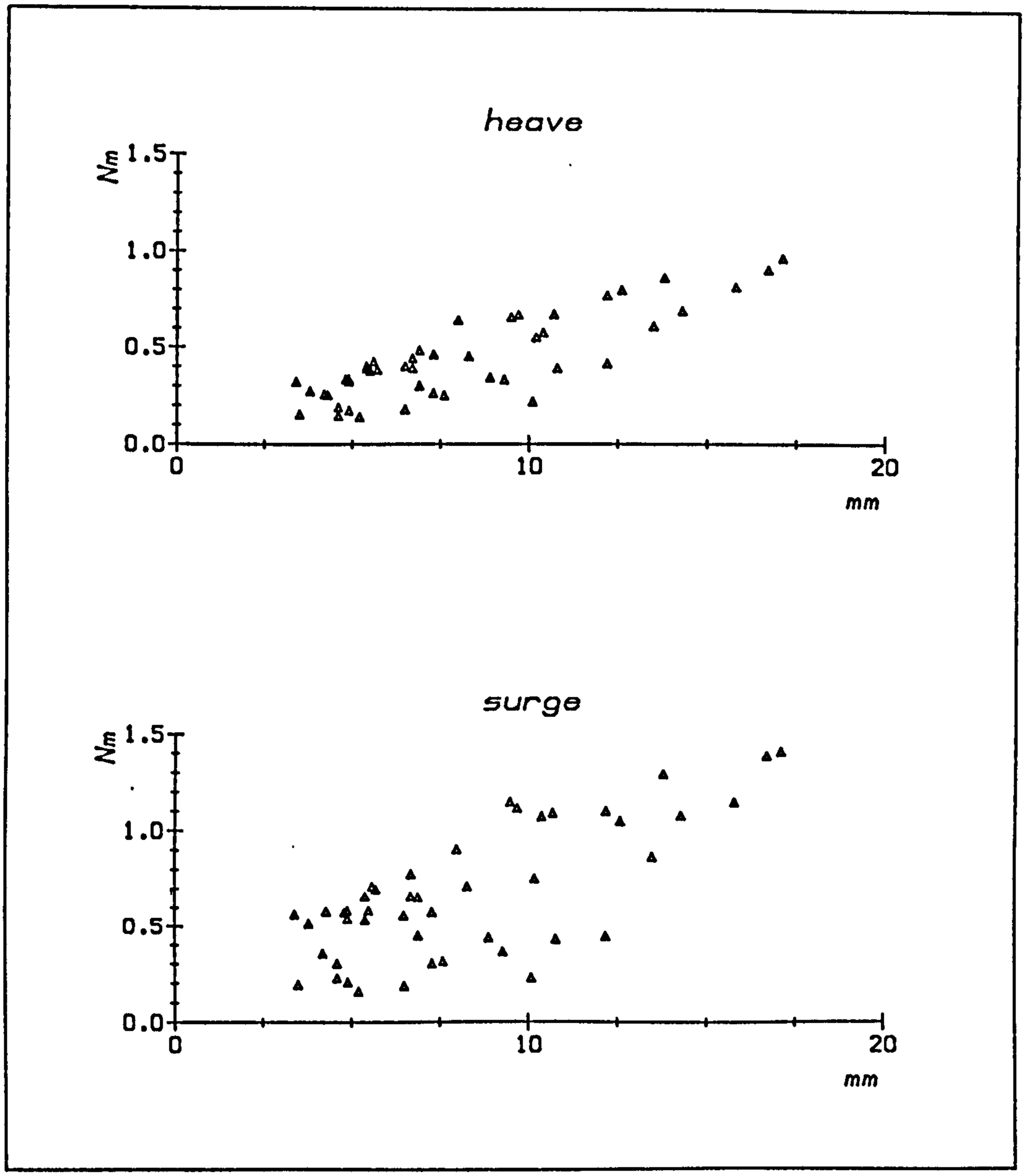

Figure 8.3
Spine average bending moment against H_{rms}.
Spine stiffness 1000Nm/rad.

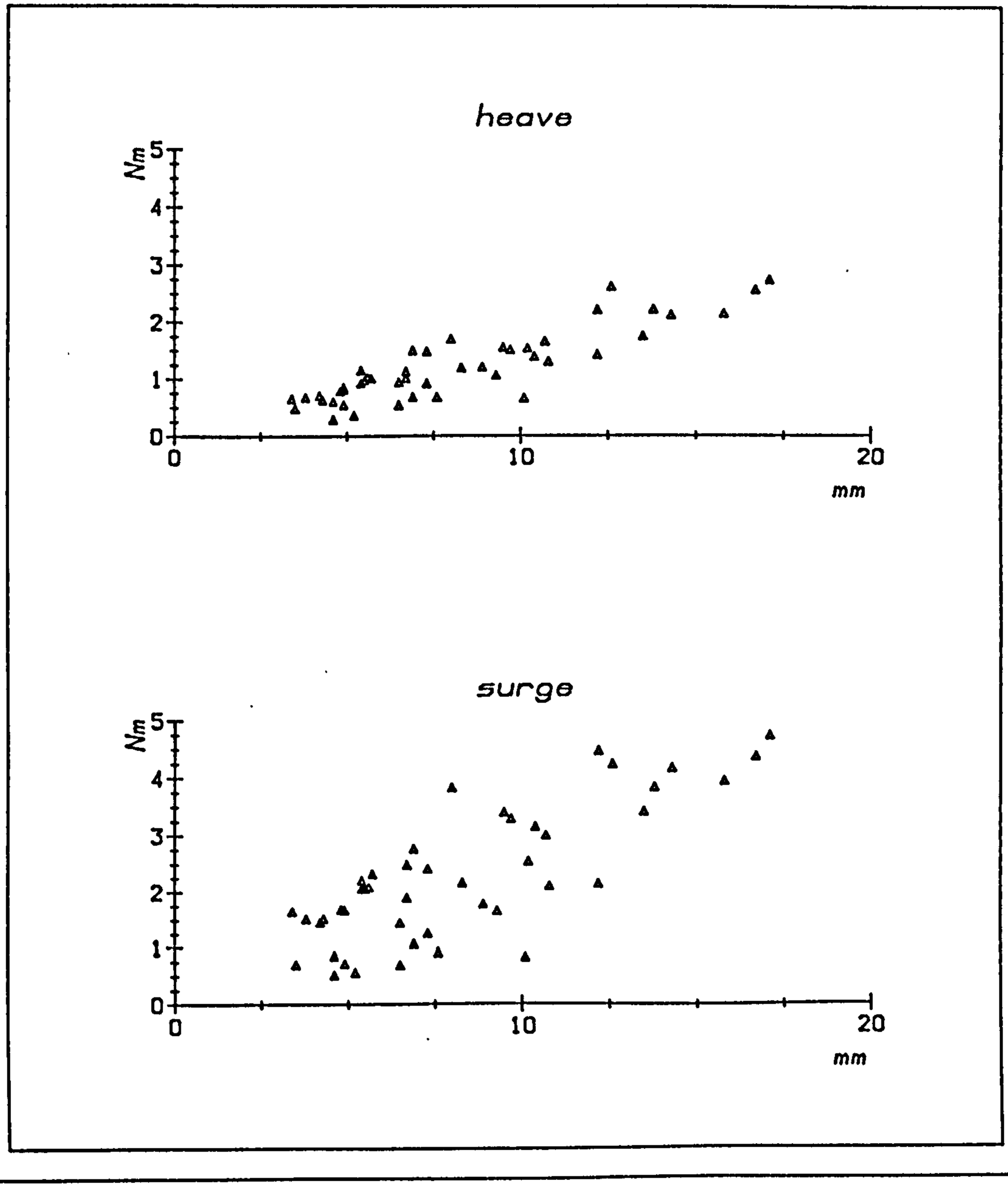

Figure 8.4 shows bending moment spatial plots in the 46 spectra for the spine at a stiffness of 100Nm/rad. The rms value of bending moment for each joint is plotted against joint position. Both heave and surge are plotted; the heave bending moment curve is invariably the lower one, about half the magnitude of surge. The plots are very varied, not only in overall size, but also in shape. For example, for sea 360 the plots are almost flat, barely changing down the length of the spine. For sea 359 there is strong tilt and peakiness. Surge plots seem to show slightly more tilt and peakiness than heave. They tend to be about twice the size of heave, but increase more slowly than heave as the seas increase in size.

When the plots are compared with the wavefront plots of figure 8.1 several interesting correlations appear. When the bending moment plots show a marked tilt, for example 359, the corresponding sea state shows a strong asymmetry. As we would expect from the results for regular waves from chapter 4, when the angle of offset of the sea-state is towards positive angles, then the bending moment plot is higher at the positive end.

When the wavefront plot shows a more or less uniform spread with angle, for example, 089, 200, 268, then the bending moment plots are level. Sea 352 has two tight swells, approximately balancing each other, and the bending moment plot is again level.

The exceptionally low bending moments - 201, 210, 212, 223, 249, 348 for example - arise in seas with tight swells, usually placed around 0 degrees, well away from the region of spine resonance. And conversely, seas with a large number of components in the resonance region - eg 324, 347, 352 - show high bending moments.

Figure 8.5 shows the equivalent results for the spine at a stiffness of 1000Nm/rad. The results, though higher in general, show the same discrimination in response to sea type. The plots tend to show larger broader peaks and more tilt. This agrees with the differences between the high and low stiffness cases for regular waves in chapter 4.

Figure 8.4

Spine bending moments in the 46 spectra.

Spine stiffness 100Nm/rad.

Bending moments 0–2.5Nm against position 0–16m.

Surge top trace, heave bottom trace.

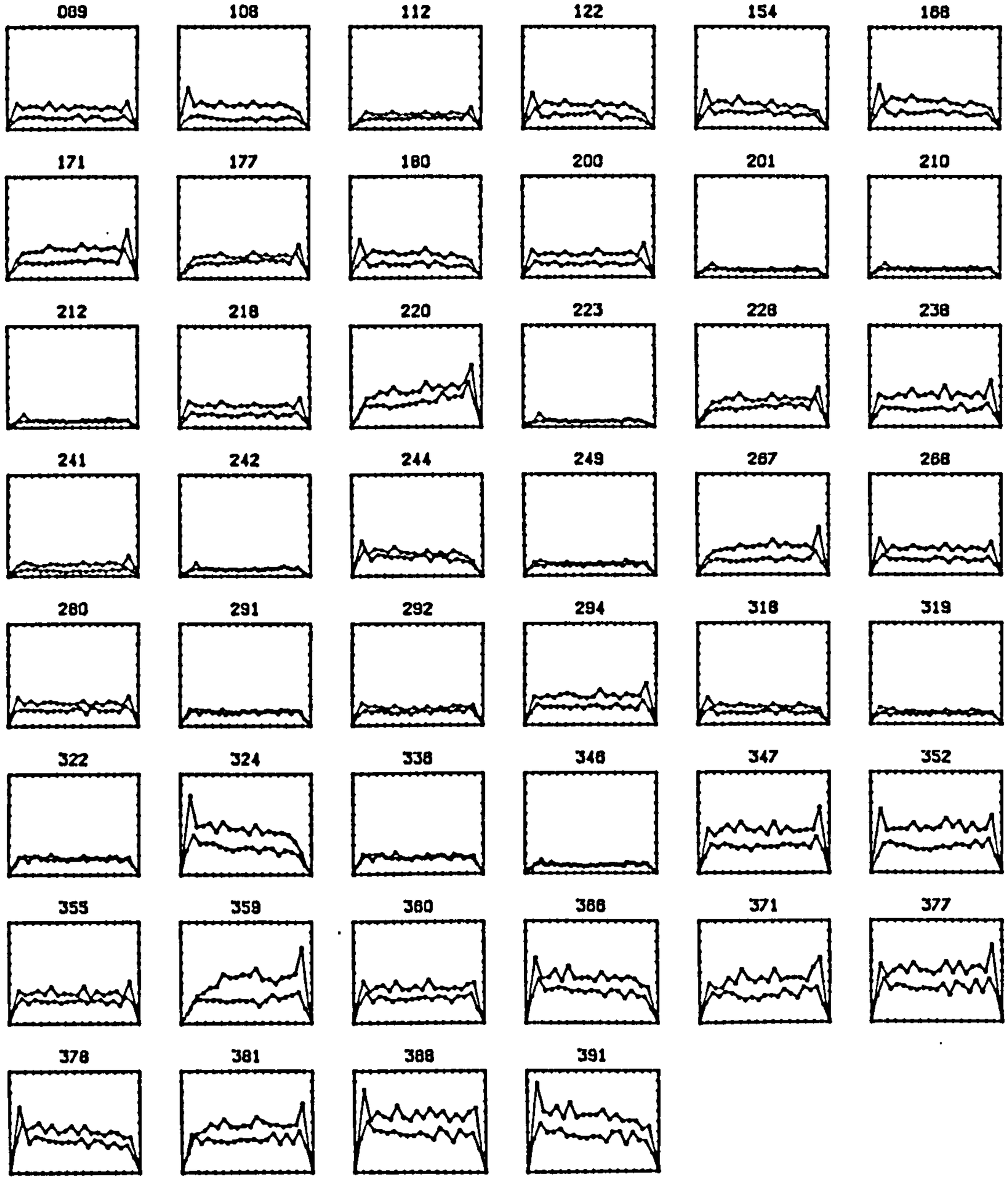

Figure 8.5 :

Spine bending moments in the 46 spectra.

Spine stiffness 1000Nm/rad.

Bending moments 0–10Nm against position 0–16m.

Surge top trace, heave bottom trace.

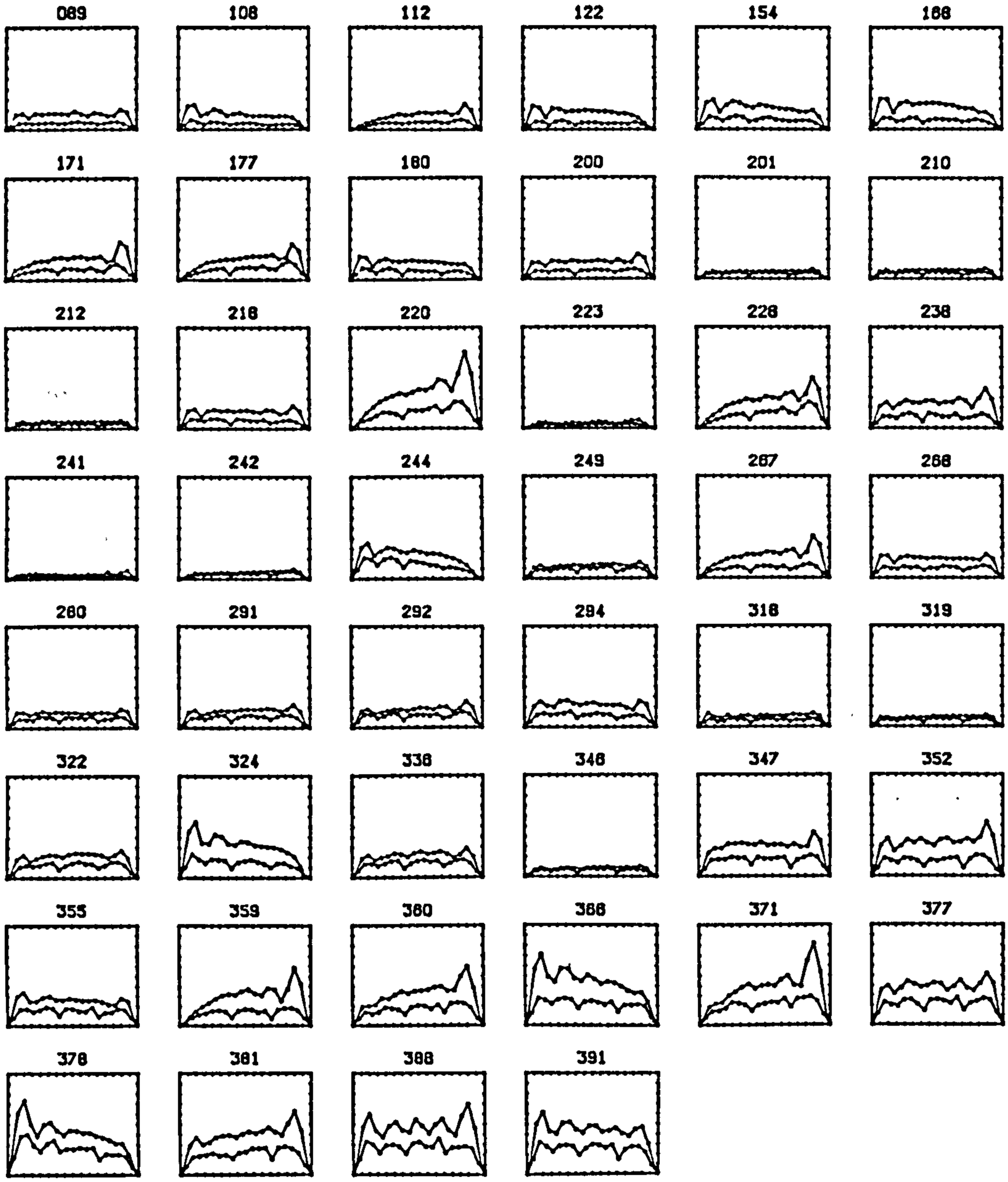

8.6 Prediction of spine bending moments

In this section the bending moments of the spine in the 46 spectra are predicted using the nodal beam model of chapter 6, and superposing the effects of the individual wavefronts which make up each spectrum. In each of the 46 spectra the bending moment for each spine joint is determined by calculating the beam response to each wavefront, whose parameters of amplitude, frequency, angle and phase are recovered from the spectrum specification. Because there is only one wavefront at each frequency it is possible to add the calculated beam responses as uncorrelated inputs: that is, to take the square root of the sum of the squares of the bending moments at each frequency for each joint. The joint bending moments are then plotted against joint position.

The resultant spatial plots for the spine at a stiffness of 100 in heave are shown in figure 8.6. They are plotted as lines, and the experimental data from figure 8.4 are overplotted as points. The predictions match the data very well, both in the magnitude and shape of the plots. In general, the predicted plots are very smooth, being the sum of so many contributions. By contrast, the experimental data tend to show greater peakiness. It is noticeable that theory underpredicts bending moments in the cases where there is a strong swell around zero degrees. In Chapter 4 it was noted that the spine experienced bending moments even in zero angled regular waves, due to the presence of reflections in the tank. It is likely that here too reflections are causing the experimental bending moments to be higher than the predictions. The same could be happening for sea 359, where the bending moment prediction, though high, is still less than the data.

Figure 8.6

Predicted discrete beam bending moments in the 46 spectra, overplotted with experimental data points.
Spine stiffness 100Nm/rad.
Heave bending moments 0–2Nm.

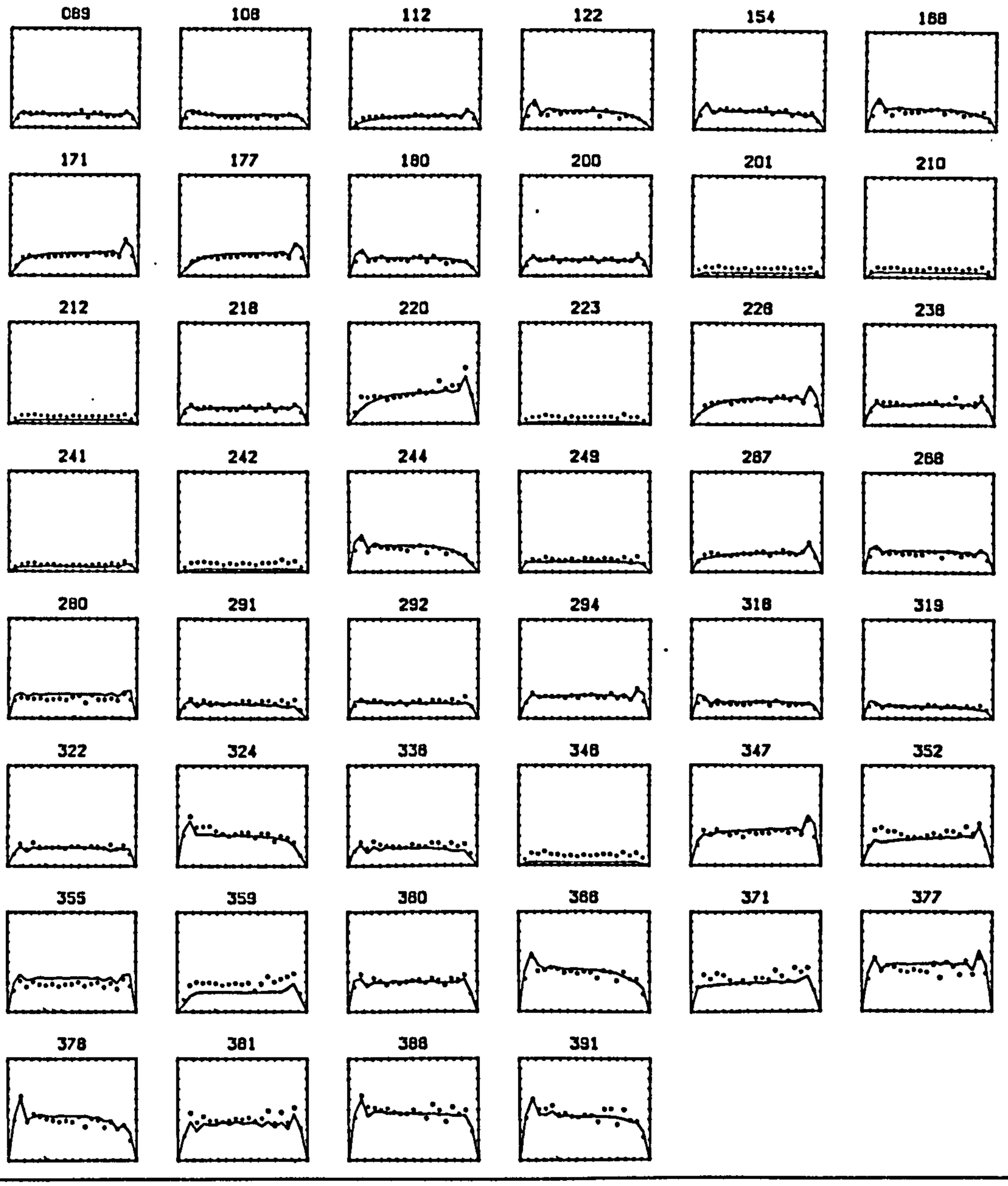

Figure 8.7 shows the equivalent plots for surge. Again for most of the range the fit is excellent. However, in the larger seas, theory is tending to overpredict the bending moment. Or at least to overpredict the *average* bending moment; the peaks are almost exactly predicted in every case. The effect is probably allied to the non-linearity due to wave overlapping described in Chapter 7. The bending moment peaks, which are correctly predicted, occur towards the ends of the spine. In these regions the spine is less constrained by its own stiffness and tends to move more nearly with the waves. In consequence there will be less overlapping of the waves here than in the middle of the spine, which perhaps accounts for the higher bending moments.

Figure 8.7

Predicted discrete beam bending moments in the 46 spectra, overplotted with experimental data points.
Spine stiffness 100Nm/rad.
Surge bending moments 0–3Nm.

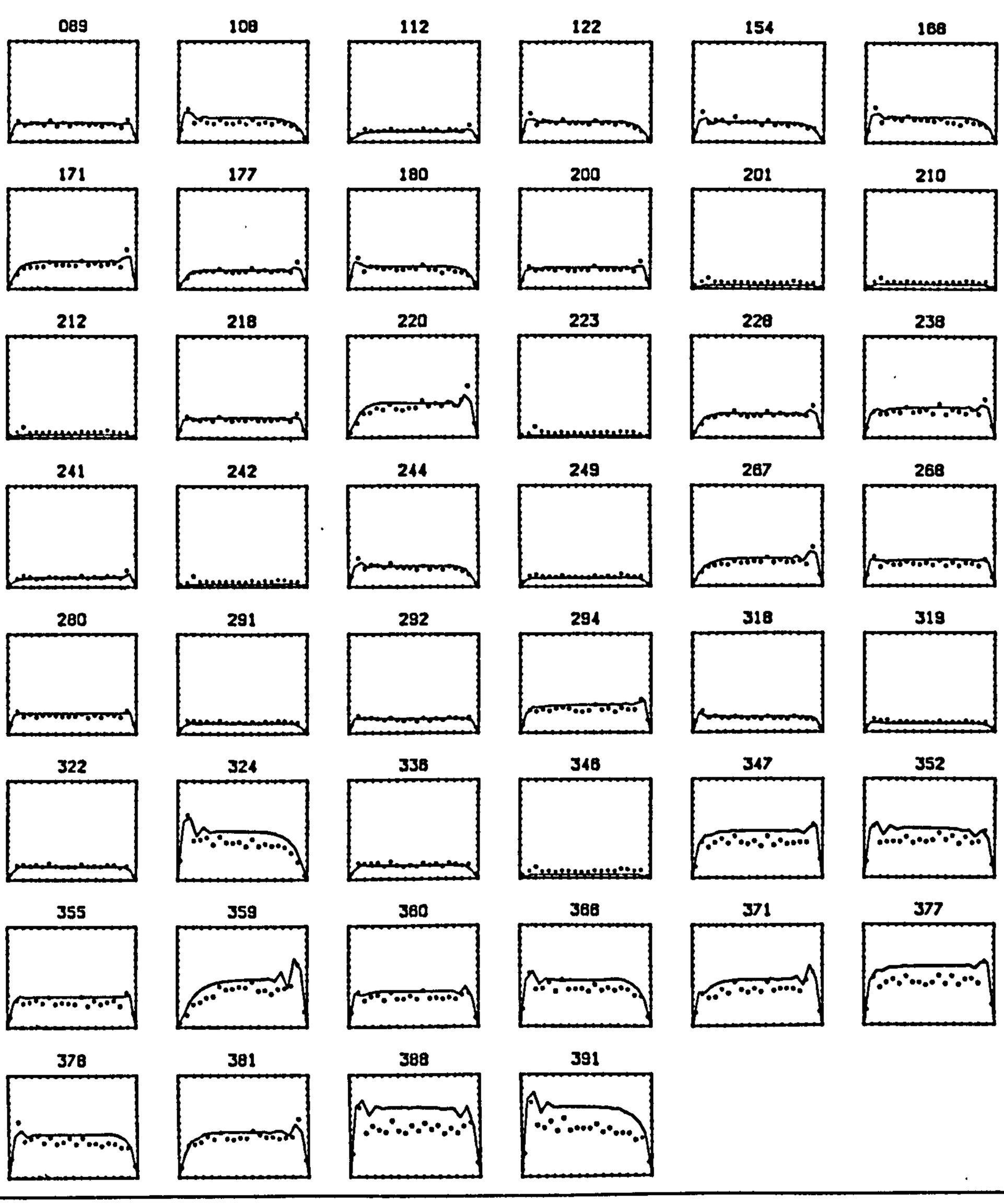

Figure 8.8 shows the results for heave at a stiffness of 1000Nm/rad. The signals are generally larger here, and the noise problem—the mismatch of theory and data for small bending moments—does not arise. In general the agreement is close, though not quite as good as for the low stiffness case. Here the predicted plots show more peakiness than those at the lower stiffness, but still not as much peakiness as the data. it is clear that some spine joints, for example those at 6.4m and 11.2m, consistently produce lower bending moments than either their neighbours or the predicted plot.

Figure 8.8

Predicted discrete beam bending moments in the 46 spectra, overplotted with experimental data points.
Spine stiffness 1000Nm/rad.
Heave bending moments 0–10Nm.

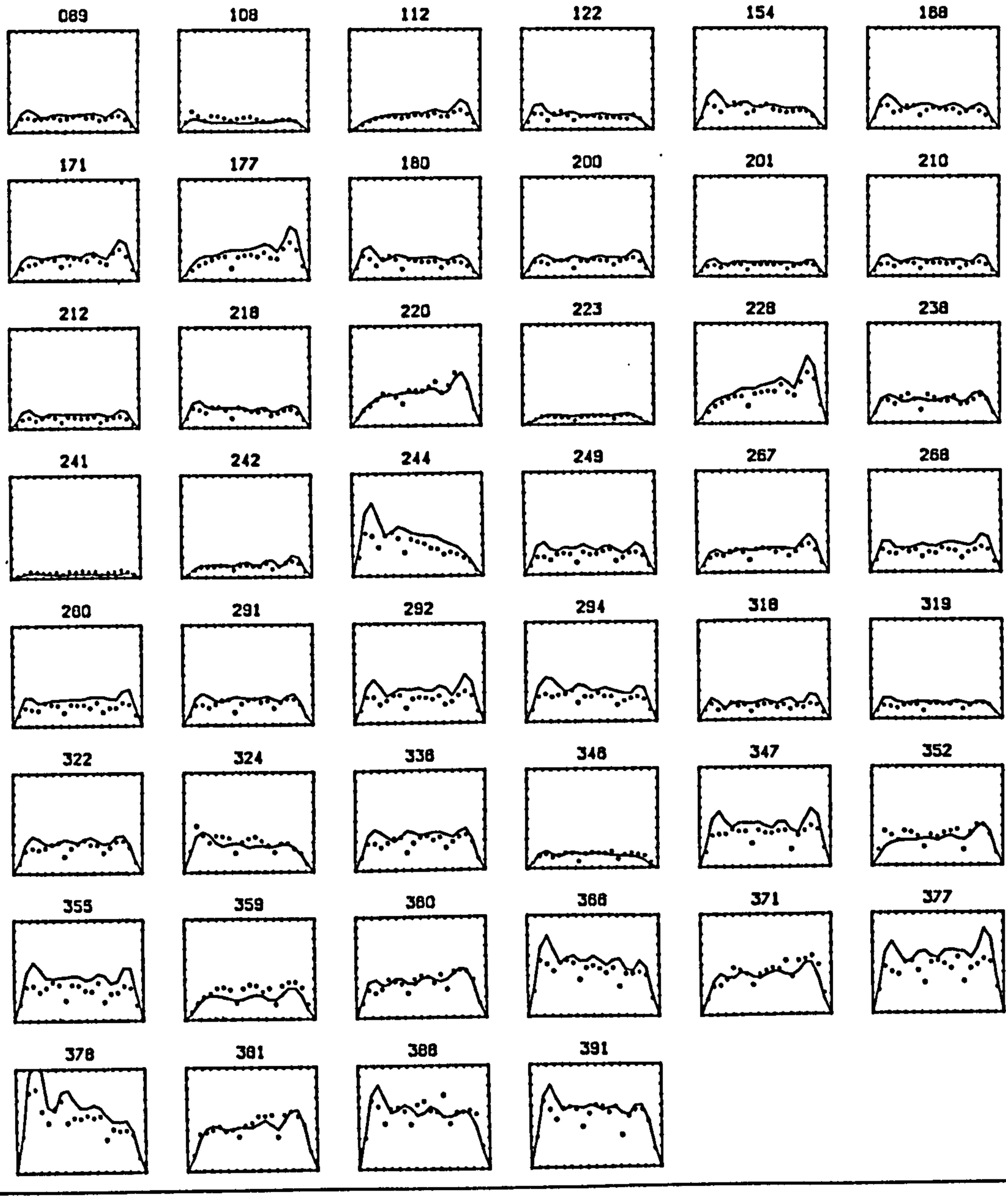

Figure 8.9 shows the results at 1000Nm/rad in surge. For the quarter of the plots depicting the largest bending moments theory overpredicts the bending moments by 40–80%.

However, the prediction of plot *shapes* is very good. There is no anomalous behaviour from particular spine joints. At this higher stiffness the spine joints are considerably more constrained—spine curvature will be $\sqrt{10}$ less than at the lower stiffness—and all segments will experience a more similar degree of wave overlapping. Hence the consistency of the predicted shape with the data.

8.7 Conclusions

These figures show that the nodal beam theory works well to predict spine response in mixed seas. In heave, bending moment is accurately predicted both in overall magnitude and in variation along the length of the spine. In surge, magnitudes are overpredicted for the higher bending moments, but the shape of the response is accurate. Given some further development in the understanding of the effects of wave overlapping, the combined use of nodal beam theory with tested or calculated hydrodynamic data for cylinders is promising.

Figure 8.9
Predicted discrete beam bending moments in the 46 spectra, overplotted with experimental data points.
Spine stiffness 1000Nm/rad.
Surge bending moments 0–15Nm.

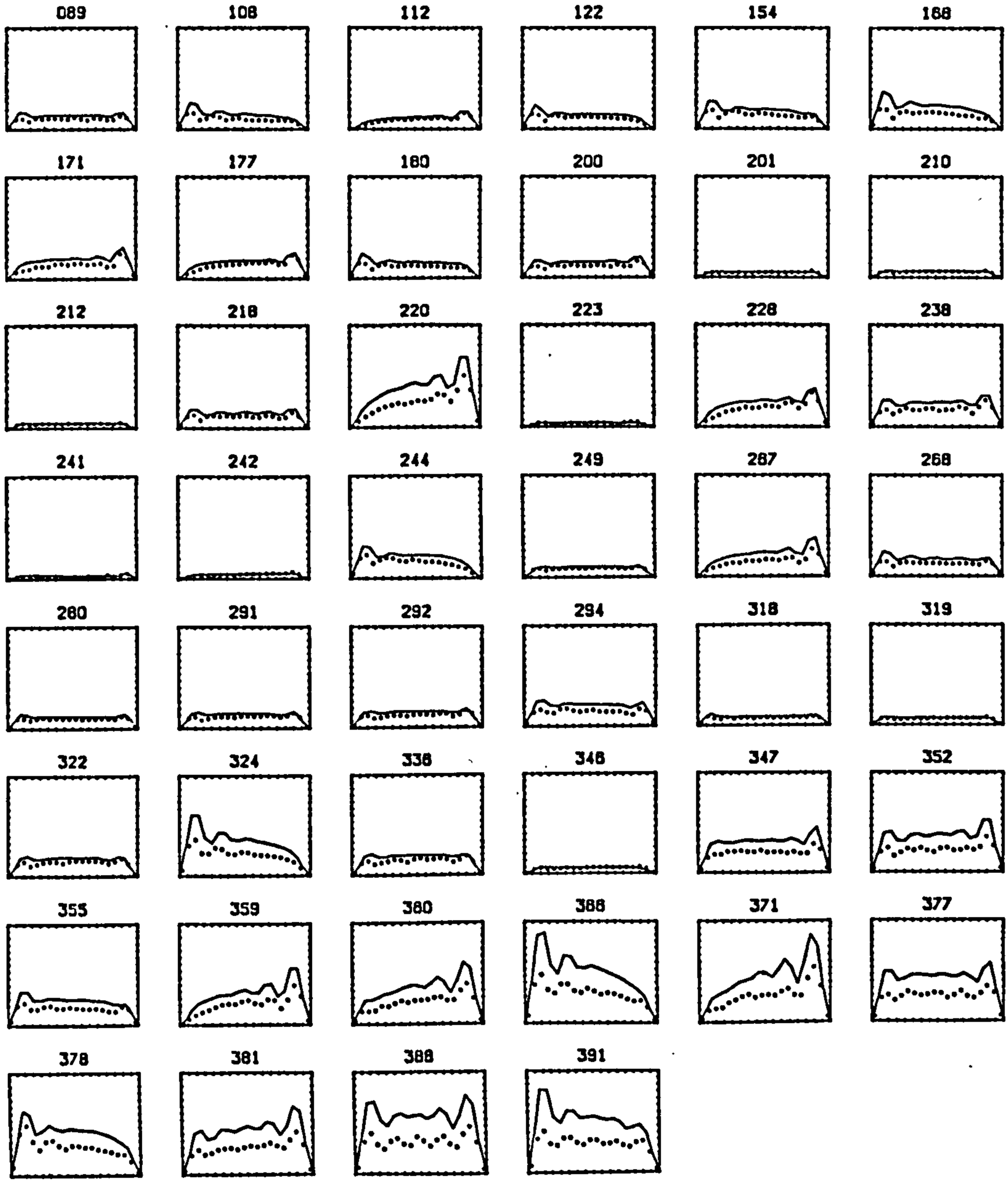

Chapter 9

Conclusions

For convenience the conclusions throughout the thesis are drawn together in this chapter.

1. Spine experiments

When the spine model is tested in regular waves, at any frequency there is a particular angle of incidence at which resonance occurs. This resonance angle increases as wave frequency decreases, that is, the wave crests become more nearly parallel with the spine. The variation of bending moment down the length of the spine is dependent upon the frequency and angle of the wave.

As spine stiffness increases the bending moments increase and the resonance shifts to smaller wave angles. Also the number of peaks in the bending moment down the length of the spine decreases.

Surge bending moments are greater than heave by about a factor of two. The variation of magnitude of the response with frequency is different in heave and surge.

When the spine is tested in mixed seas the bending moments are very poorly correlated with the root-mean-square wave height, and show great variation in bending moment along the spine.

2. Cylinder measurements in two-dimensional waves

A rig was used to measure the forces on and velocities of a cylinder when driven in the water and exposed to waves in a wave tank. The forces and velocities can be combined with measurements of the ambient wave field in a matrix

operation which yields the wave force coefficient W, and the hydrodynamic impedance Z free of the effects of wave reflection in the tank. Three different cylinder diameters were tested over a range of submergences.

The results show that the parameters for heave and surge are only similar at deep submergences. As the surface is approached both W and Z change radically, and differently in heave and surge. The effects in surge are greatest when the upper surface of the cylinder is tangent to the water surface. In heave the changes are heavily dependent on the buoyancy induced by the waterline area, which increases as the cylinder freeboard increases. Because of the cancellation of the inertial force of the wave on the cylinder by the buoyancy force, the value of W across the frequency range is generally less for a surface-piercing cylinder in heave than in surge.

3. CONTINUOUS BEAM THEORY

Continuous beam theory correctly accounts for the presence of a spine resonance at all frequencies, and shows how the wave angle at the resonance peak increases as frequency decreases. It shows how the resonance shifts to smaller angles as spine stiffness increases, and thus accounts for the resonance shift to smaller angles due to buoyancy. It predicts that the bending moment at resonance rises as the square root of beam stiffness.

In an infinite beam the bending moment magnitude would not change down the beam length. However, for a finite beam, the end-conditions generate variations — peakiness — in the bending moment down the beam.

When the theory fails to match the experimental data for the spine model, it is because it predicts a larger number of peaks in the bending moment down the length of the spine than the segmented spine model is capable of resolving.

4. NODAL BEAM TIIEORY

The predictions from nodal beam analysis match those from the continuous beam but provide a far more accurate fit to the experimental data in the cases where the continuous beam theory overpredicts the number of peaks in bending moment down the spine.

At very low frequencies however, the match with data is poor. This is

probably due to the existence of spurious damping in the spine model which is substantially greater than the hydrodynamic damping.

5. NON-LINEARITY

Experiments on fixed cylinders and on the spine show that the forces on the spine in waves are non-linear. The wave force coefficients for heave and surge on a fixed cylinder were found to be frequency and amplitude dependent, and the effect appears to be associated with wave-overlapping, that is, waves passing over the spine, sometimes breaking.

Experiments on the spine which is allowed to move also show a non-linearity for a regular wave, and the results concur with the fixed cylinder results. In a mixed sea there was little non-linearity in heave, but substantial amounts in surge, the forces at 20mm H_{rms} being about half that expected from a linear extrapolation from waves around 5mm.

6. MIXED SEA PREDICTIONS

The bending moment response of the spine in a mixed sea may be predicted by calculating the bending moments by nodal beam theory in each of the component wavefronts of the mixed sea and adding the results as uncorrelated forces.

The spine was tested in 46 spectra representative of North Atlantic conditions and the results compared with theory. In heave, bending moment is accurately predicted both in overall magnitude and in variation along the length of the spine. In surge, the shape of the response is accurate but, due to the non-linear effects of wave overlapping, magnitudes are overpredicted for the higher bending moments.

The 46 spectra used account for more than three quarters of the annual energy of the North Atlantic wave climate. In most of the sea states the nodal analysis predicts the spine response accurately; in about a quarter of the cases theory overpredicts bending moments by between 40 and 80%, an amount which compares favourably with engineering safety margins.

DISCUSSION

The purpose of this thesis has been to devise an analysis capable of predicting the dynamics of a full scale spine in mixed seas. Model experiments show that the spine exhibits bending moment magnitudes in mixed seas which correlate poorly with the root-mean-square wave height of the sea state. Experiments in regular angled waves reveal the presence of a spine resonance. Two linear theories are developed: one assuming the spine to be a continuous beam; the other is a nodal analysis. Both combine dynamic equations for the spine structure with hydrodynamic equations for the wave loading, and both accurately predict the size and position of the spine resonance with respect to the frequency and angle of the waves. The nodal method is computationally more expensive, but gives a better account of the variation of the bending moment down the length of the spine. At model scale, the nodal analysis gives a very close fit to the shape of the spine response in mixed seas.

Assuming dynamic similarity between the model and full scale, it is possible to predict full scale quantities from model quantities by using the appropriate scale factor. In this case, mass varies with the cube of scale, and from the dispersion relation, equation 1.18, time varies as the square root of scale. From these relationships for mass, length and time all other quantities can be determined. For example, bending moment rises as the fourth power of scale.

In chapter 3, the quantity kD was used as the axis of the non-dimensionalized plots of wave force coefficient and impedance for the short cylinders in waves. The superposability of the plots for different cylinder sizes showed that scaling held over the range of cylinder size tested, and in small waves.

It is pointed out in section 1.6 that the full scale Reynolds number will be 1000 times that for the model. It was suggested that this would not matter because the Keulegan-Carpenter number was so low that a wake would not have time to develop around the cylinder. However, in chapter 7, the wave amplitude experiments showed dramatic departures from linearity for surge forces due to waves overlapping the spine producing a strong vortex in the cylinder lee. At the top of the amplitude range tested this halved the inertial forces.

The implication of these two sets of results is that scaling is valid providing vortex generation is small. This will be the case for a full-scale spine with ducks mounted on it because the ducks absorb energy from waves, preventing

overlapping for all but the very largest waves.

The effect of spine length is not considered in this thesis. Experiments performed by Taylor (1984) indicate that for a given sea state, a constant spine stiffness, and a constant orientation of the spine to the principal direction of that sea state, large changes occur with spine length. The wave crest length is the average distance between crests in a direction normal to the principal direction. When the spine length is small compared with the crest length, then the maximum bending moment found in the spine is small. A large increase in the bending moment occurs when the spine length is comparable to the crest length, reaching a maximum at two crest lengths. Beyond that, a plateau is reached and bending moments do not increase no matter how long the spine is made.

The Clam spines are made stiff, and short compared with the average North Atlantic crest length. The use of the continuous beam equation would be appropriate for calculating the bending moments; they will be small because the spine is not crest spanning. Consequently it is easy to make a rigid support for the Clam air bags. Because the spine is not crest-spanning it will undergo large displacements. These too are calculable from the continuous beam theory, and can be used to determine the consequences for the air bags and hence for Clam efficiency.

The Duck spine is well above the critical length, and bending stresses are very much greater than for the Clam. It is therefore made flexible. Short stiff post-tensioned concrete segments are connected by joints whose stiffness is controlled by hydraulic rams. The technique can provide stiffnesses of up to 10kNm/rad at the model scale of this thesis. More stiffness can be provided, but at higher cost.

However, while increasing the stiffness increases the crest-averaging qualities of the spine, this is not necessary for the ducks, which contain their own gyroscopic references. Moreover, this thesis demonstrates that the position of the spine resonance with respect to wave frequency and angle changes little with increase of stiffness, and in fact, to shift the resonance away from the wave frequencies and angles which carry the bulk of the power, the stiffness should actually be reduced.

In any case, it should not be assumed that because the spine resonance

results in high bending moments and reduced crest averaging it is necessarily a liability. As remarked in the Introduction, wavepower devices are unique amongst marine structures in that they are designed to be dynamic not static in waves. When damping is applied to the spine, either by its hydraulic rams or by the ducks, power is extracted from the waves, and spine motion and bending moments are reduced.

Experiments on a duck model in the 2D wave tank indicate the value of duck pitch compliance and of the mounting compliance in heave and surge required to maximize duck efficiency. The values are frequency dependent. The mounting compliance value can be converted to an equivalent value for spine stiffness; and the duck efficiency with frequency at that spine stiffness can be used to calculate the damping of spine motion by the duck. The nodal analysis of the spine dynamics developed in this thesis can then be used to calculate the spine stresses and fatigue cycles over its projected life in a representative set of appropriately weighted sea-states. Spine costs rise with stiffness because of the increased bending moments; duck value rises with productivity. The nodal analysis allows trade-offs to be quantified and a cost-effective choice to be made.

In 1982 the Department of Energy ceased funding for the wavepower research program. The subsequent report (Davies, 1985) concluded that electricity from 2GW arrays for most of the devices would cost between 8 and 20 pence per kWh, compared with the current cost of supply by power stations of around 2.5 pence. The wavepower resource is free: the cost per unit of electricity is mainly the result of the depreciation of a high capital cost.

Costs of less than 4p/kWh have been claimed for two prototype wavepower devices in Norway. Because they were shore-based, construction costs were relatively low. By contrast, the big British projects, most of them placed well out to sea, would have construction costs comparable with offshore industry, and the emplacement of some components, anchors or underwater power take-off devices for example, would incur sub-sea costs.

It is a rule of thumb in the offshore industry that the cost of a process — welding for example — increases by a factor of about 10 in going from land to offshore. The cost rises by a further factor of 10 in going sub-sea. It should be noted that human deaths and injuries also rise by similar factors in these environments.

Oil rigs and platforms have huge capital costs (North Sea investment is reckoned in tens of billions of pounds) but the payback time is extraordinarily short, often of the order of a year or so. By contrast, the billions of pounds for a wavepower station are recovered over the design life of 25 years. Even though the resource is free, the payback is long. In the UK no industrial backers appeared when the wavepower program was cancelled.

Viable wavepower awaits an adequate combination of the following: a technological breakthrough which dramatically lowers the cost of construction; a presumably gradual reduction of offshore costs; the combination of wavepower with some other profitable activity.

Specifics of the first category are hard to guess. Over the 8 years of funding, estimated costings for wavepower devices dropped by a factor of 5; even after the funding stopped, device teams were still producing cost-cutting ideas.

Offshore costs can be expected to decline slowly as the engineering becomes refined and the knowledge base increases. The use of robots for arduous or dangerous tasks will make operations cheaper and more reliable.

Combining activities offshore may also improve the economics. Allowing for rail and road links on a tidal barrage can increase the utility; and some solar and insulation retrofits to domestic dwellings have payback times which rival the oil industry's. Perhaps it will be appropriate to combine wavepower with other technologies which make use of the ocean: subsea mining; desalination; fish farming. Such projects are likely to have power requirements far below the 2GW of a full size wavepower station, so even if a duck were chosen as the appropriate device, it would not need a spine.

Given that the construction of full-scale spines is unlikely, can the analysis presented in this thesis be put to any other purposes?

In the offshore oil industry cylinders are a basic structural component. They are used, in a variety of diameters, for vertical items such as caissons and risers, and for horizontal items such as bracing elements, pontoons and pipelines. Designers work hard to keep these cylinders away from waves in general and the splash zone in particular, but sometimes such locations are unavoidable: pipelines must be lowered through the surface, and indeed it may be economic to tow them out at the surface. Risers of necessity pierce the surface. The continuous beam equation is appropriate for the calculation of forces on such

structures. For the horizontal pipelines the wave loading can be expressed the same way as in this thesis, that is, as a constant wave amplitude changing in phase with distance down the pipeline axis. For risers, the wave loading should use the vertical wave field varying in amplitude with depth. It may also be necessary to change the spatial end-conditions: risers and pipelines are fixed at one or both ends. Additionally, dynamic conditions can be included, such as the motion of the vessel to which they are attached. It should be noted that the solution offered in this thesis is linear: for slender cylinders such as pipelines and risers for which the Keulegan-Carpenter number is large the non-linear forces due to drag must explicitly be added, in which case the equations must be solved by time-stepping.

The nodal analysis was used to solve the case of the segmented spine. Because each segment and joint was identical an analytic solution of a finite difference equation would have been possible. However, the matrix technique is much more general. The matrix describing the spine was very regular, with five diagonal lines of elements and zero values elsewhere. In the general case every element can be used — ie, the interaction of all nodes can be considered and the nodes can be made highly disparate. Applications include multi-hulled ships, hydrofoils and control surfaces, and elaborate oil platform designs.

Perhaps the most exciting use of the generalized matrix solution is for robots which are necessarily composed of joints and links. The robot's task may be repetitive, in which case a steady-state solution may be possible; it is however more likely to be adaptive, in which case a time-stepping solution is required and initial conditions — position, velocity etc — must be incorporated in the matrix.

Note that while in this thesis known wave forces are applied to the spine and the displacement of its segments then calculated, the problem can easily be reversed. A displacement goal for the robot may be specified, and the forces required to meet that goal are then calculated. Constraints such as maximum acceleration or maximum jerk can also be applied.

Interaction between the robot's links will be determined by their connectivity, and also for marine robots, because the water surrounding them can transmit force, by proximity. These latter interactions will be determined by the linkage kinematics and can be entered as appropriate cross-terms in the

matrix.

The dynamic response of the robot can therefore be constructed as a matrix, and used to devise appropriate control tactics — for example, the avoidance of modal vibration or the calculation of minimum action.

Future uses of the oceans can only be guessed at, but the dependence on technology is certain. Understanding of hydrodynamics and structural dynamics is already shaping the offshore industry; the application of marine robotics with its reliance on kinematics, dynamics and control theory will provide a rich field for research. The techniques developed in this thesis are a useful and general addition to the portfolio of the marine engineer.

Notation

A	wave amplitude
D	diameter
F	force
J	moment of inertia
K	Keulegan-Carpenter number
M	moment
N	number of segments
R	hydrodynamic moment
Re	Reynolds number
S	surface area
T	hydrodynamic force
U	body velocity
W	wave force coefficient
Z	impedance
g	acceleration of gravity
h	spine segment spacing; water depth
i	$\sqrt{-1}$
k	wavenumber
m	mass
n	normal vector
p	pressure
t	time
u, v, w	velocities
x, y, z	Cartesian coordinates

list continues

Δ	finite difference operator
$\sum$	finite sum operator
α	wave angle
β	spine segment relative angle
δ	spine damping; wavemaker phase angle
θ	spine segment angle; wave angle
λ	wavelength
μ	spine segment mass
ν	viscosity
π	3.141592...
ρ	density
σ	spine stiffness
τ	torque
ϕ	velocity potential
ψ	stream potential
ω	angular frequency

References

Battjes J, 1982
Effects of short-crestedness on wave loads on long structures.
Applied Ocean Research, Vol 4, No 3

Bearman P W, Graham J M R, Obasaju E D, 1984
A model equation for the transverse forces on cylinders in oscillatory flow.
Applied Ocean Research, Vol 6, No 3

Bearman P W, Downie M J, Graham J M R, Obasaju E D, 1985
Forces on cylinders in viscous oscillatory flow at low Keulegan-Carpenter numbers.
JFM Vol 154, pp337-356

Bellamy N W, Peatfield A M, 1984
Further development of the SEA Clam wave energy converter.
IEE Energy Options Conference publication no. 233

Brevig P, Greenhow M, Vinje T, 1981
Extreme wave forces on submerged cylinders.
Proc BHRA, Second Int Symp on Wave and Tidal Energy, Cambridge.

Bryden I G, 1983
PhD thesis
University of Edinburgh

Bryden I G, Greated C A, 1981
Dynamics of semi-submerged cylinders in waves.
Numerical methods for Coupled Problems, ed Hinton E, Betters P, Lewis R W

Chakrabarti S K, 1985
Recent advances in high-frequency wave forces.
4th OMAE Symposium, 1985

Chaplin J C, 1984
Nonlinear forces on a horizontal cylinder beneath waves.
J Fluid Mech, vol 147 449-464

Chaplin J C, 1985
Loading on a cylinder in uniform elliptical orbital flow.
Department of Civil Engineering, University of Liverpool, Report MCE/JUL/85

Chaplin J C, 1985
Morison inertia coefficients in orbital flow.
ASCE, J Waterways, Ports, Coastal and Ocean Division, Vol 111

Chaplin R V, French M J, 1980
Aspects of the French flexible bag device.
Power from Sea Waves, ed. B Count, Academic Press, London.

Chung J S, 1977
Forces on submerged cylinders oscillating near a free surface.
Journal of Hydronautics, Vol 11, No. 3

Cokelet E D, 1979
Breaking waves: the plunging jet and the interior flow field
Mechanics of Wave-induced Forces on Cylinders, ed T L Shaw, Pitman

Crabb J, 1980
Synthesis of a directional wave climate.
Power from Sea Waves, ed Count B, Academic Press, London.

Curran S C, Curran J S, 1979
Energy and Human Needs Scottish Academic Press, Edinburgh

Davies P G, Cloke M S, Major K A, Page D I, Taylor R J, 1985
Wave energy
ETSU R26, UK Department of Energy

Dean R G, 1970
Relative validities of water wave theories
ASCE, J Waterways, Ports, Coastal and Ocean Division, Vol 96, No WW1

Dixon A G, Greated C A, Salter S H, 1979
Wave forces on partially submerged cylinders.
Journal of the Waterway, Port, Coastal and Ocean Division, ASCE
Vol 105, No WW4, Proc Paper 14996, pp421-438

Ellix D M, Arumugam K, 1985
Second order wave loading on surface piercing cylinders.
BOSS

Evans D V, Jeffrey D C, Salter S H, Taylor J R M, 1979
Submerged cylinder wave energy device: theory and experiment.
Applied Ocean Research, Vol 1, No 1

Evans D V, 1979
Some theoretical aspects of three-dimensional wave energy absorbers.
Symposium on ocean wave energy utilization. Gothenburg, Sweden.

Evans D V, 1981
Power from water waves.
Annual Review of Fluid Mechanics, Vol 13, 157-187

Faltinsen O, Kjaerland O, Noltveit A, Vinje T, 1977
Water impact loads and dynamic response of horizontal circular cylinders in offshore structures.
OTC 2741

Frank W, 1967
Oscillation of a cylinder in or below the free surface of deep fluids.
Naval Ship Research and Development Center, Navy Dept Rept 2357

Fryer D K, Wilkie M J, 1975
The simulation in the laboratory of random seas and their effects.
Instrumentation in Oceanography, Conf Proc, Bangor, North Wales.

Garrison C J, 1978
Hydrodynamic loading of large offshore structures: three-dimensional source distribution methods.
Numerical Methods in Offshore Engineering, ed O C Zienciewicz et al, Wiley

Garrison C J, 1980
A review of drag and inertia forces on circular cylinders.
OTC 3760

Garrison C J, 1984
Interaction of oblique waves with an infinite cylinder
Applied Ocean Research Vol 6, No 1

Grass A J, Simons R R, Cavanagh N J, 1985
Fluid loading on horizontal cylinders in wave type orbital oscillatory flow.
ASME paper No. OMAE-262, Proc. Fourth Offshore Mechanics and Arctic Engineering Symp. Dallas

Greenhow M, Vinje T, Brevig P, Taylor J, 1982
A theoretical and experimental study of the capsize of Salter's duck in extreme waves.
JFM Vol 118, pp 221-239

Greenhow M, Li Yanbao, 1987
Added masses for circular cylinders near or penetrating fluid boundaries: review, extension, and application to water entry, exit and slamming.
Ocean Engineering Vol 14 pp 325-348

Guilloud J C, Vignat P, 1979
Motion and deformation of a pipe submerged in waves.
Mechanics of Wave-induced Forces on Cylinders, ed T L Shaw, Pitman

Hasselmann K, Ross D B, Miller P, Sell W, 1976
A parametric wave prediction model.
J Phys Oceanography

Hogben N, 1974
Fluid loading on offshore structures, a state of the art appraisal: wave loads.
Marine Technology Monograph. The Royal Institute of Naval Architects.

Hogben N, 1976
Wave loads on structures
BOSS

Hogben N, 1977
Hydrodynamics in marine technology, an introductory review.
NMI R19

Isaacson M, 1979
Wave induced forces in the diffraction regime.
Mechanics of Wave-induced Forces on Cylinders, ed T L Shaw, Pitman

Isaacson M, Nwogu O, 1986
Wave loads and motions of long structures in directional seas.
Proc. Fifth Offshore Mechanics and Arctic Engineering Symp. Tokyo Vol. 1

Jefferys E R, 1980
Device characterisation.
Power from Sea Waves, ed. B Count, Academic Press, London.

Jefferys E R, 1983
Interpolation and extrapolation of hydrodynamic coefficients.
Applied Ocean Research, Vol 5, No. 3

Jeffrey D C, et al, 1978
Edinburgh Wave Power Project, 4th Year Report
Report to WESC, Edinburgh

Jeffreys H, 1924/5
On the formation of waves by wind.
Proc Royal Society A 107, A110

Keulegan G H, Carpenter L H, 1958
Forces on cylinders and plates in an oscillating fluid.
J Res Nat Bur of Stand, 60(5), 423-440

Kim W D
On the harmonic oscillations of a rigid body on a free surface.
JFM 21 427-451

Lighthill M J, 1978
Waves in Fluids
CUP

Lighthill M J, 1979
Waves and wave loading.
BOSS

Longuet-Higgins M S, 1977
The mean forces exerted by waves on floating or submerged bodies with application to sand bars and wave power machines.
Proc Roy Soc London A 352, 463-480

Madsen OS, 1986
Hydrodynamic force on circular cylinders.
Applied Ocean Research, Vol 8, No 3

Martin P A, Dixon A G, 1983
The scattering of regular surface waves by a fixed, half-immersed, circular cylinder.
Applied Ocean Research, Vol 5, No 1

Matten R B, Hogben N, Ashley R M, 1978
A circular cylinder oscillating in still water, in waves and currents.
Mechanics of Wave-induced Forces on Cylinders, ed T L Shaw, Pitman

Maull D J, Milliner M G, 1978
Sinusoidal flow past a circular cylinder.
Coastal Engineering, Vol 2

Maull D J, Milliner M G, 1979
The forces on a circular cylinder having complex periodic motion.
Mechanics of Wave-induced Forces on Cylinders, ed T L Shaw, Pitman

Mehlum E, 1980
A circular cylinder in water waves.
Applied Ocean Research, Vol 2, No 4

Mitsuyasu H, 1975
Observations of the directional spectra of ocean waves using a cloverleaf buoy.
J Phys Oceanography 5 750-760

Mollison D, 1983
Wave energy losses in intermediate depths.
Applied Ocean Research 5 234-237

Mollison D, 1985
Wave climate and the wave power resource.
IUTAM Symposium, ed. Evans D V, Falcao A, Lisbon

Morison J R, O'Brien M P, Johnson J W, Schoof S A, 1950
The force exerted by surface waves on piles.
Petr Trans, AIME, 189, 149-154

Newman J N, 1975
Interaction of waves with two-dimensional obstacles: a relation between the radiation and the scattering problems
JFM Vol 71, pp 273-282

Newman J N, 1977
Marine hydrodynamics.
MIT Press

Ogilvie T F, 1963
First and second order forces on a cylinder submerged under a free surface.
J Fluid Mechanics 16, 451-472

Pierson W J, Moskowitz L, 1964
A proposed spectral form for fully developed wind seas based on the similarity theory of S A Kitaigorodsku.
J Geophys Res 69, 5181-5190

Retzler C-H, 1986
The long spine mooring
Report to the Wave Energy Steering Committee, Edinburgh

Rienecker M M, Fenton J D, 1981
A Fourier approximation method for steady water waves.
JFM 104, 119-137

Roberts A J, 1983
Highly non-linear short-crested water waves.
JFM 135, 301-321

Salter S H, 1985
Progress on Edinburgh Ducks
IUTAM Symp: Hydrodynamics of Ocean Wave-Energy Utilization, Lisbon

Sarpkaya T, Garrison C J, 1963
Vortex formation and resistance in unsteady flow.
ASME, J Applied Mechanics, 85, p16

Sarpkaya T, 1975
Forces on cylinders and spheres in a sinusoidally oscillating fluid.
J Applied Mechanics, ASME 42, 32-37

Sarpkaya T 1976
Forces on cylinders near a plane boundary in a sinusoidally oscillating fluid.
J Fluids Engineering, ASME 98, 499-505

Sarpkaya T, 1977
Hydroelastic response of flexibly mounted cylinders in harmonic flow.
OTC, 2897, Houston.

Sarpkaya T, 1978
Wave impact loads on cylinders.
OTC 3065

Sarpkaya T, Isaacson M, 1981
Mechanics of wave forces on offshore structures.
San Francisco, Van Nostrand Reinhold Company

Sarpkaya T, 1986
Force on a circular cylinder in viscous oscillatory flow at low Keulegan-Carpenter numbers.
JFM, Vol 165, pp 61-71

Skyner D J, 1987
Solo Duck linear analysis
Report to Wave Energy Steering Committee, Edinburgh

Standing R G, 1978
Applications of wave diffraction theory.
NMI R32

Standing R G, 1980
Use of potential flow theory in evaluating wave forces on offshore structures.
Power from Sea Waves, ed Count B, Academic Press, London.

Standing R G, 1981
Wave loading on offshore structures: a review.
NMI R102

Taylor J R M, 1984
Bending moments in long spines.
Report to WESC, UK DoE.

Timoshenko S, Young DA, Weaver W, 1974
Vibration problems in engineering.
Wiley

Ursell F, 1949
On the heaving motions of a circular cylinder on the surface of a fluid.
Quart J of Mech and Applied Math 11(2), 218-231

Vada T, 1987
A numerical solution of the second-order wave-diffraction problem for a submerged cylinder of arbitrary shape.
J Fluid Mech, vol 174, 23-37

Verley R L P, Every M J, 1979
Wave-induced vibrations of flexible cylinders.
OTC 2899, Houston.

Vugts J H, 1968
The hydrodynamic coefficients for swaying, heaving and rolling cylinders in a free surface.
Int. Shipb. Progr., vol 15, pp 251-276

Wiegel R L, 1964
Oceanographical Engineering.
Prentice-Hall, New Jersey.